NUMERICAL SIMULATIONS OF TWO-DIMENSIONAL SATURATED GRANULAR MEDIA

Thesis by

Phalkun Tan

In Partial Fulfillment of The Requirements

for the Degree of

Doctor of Philosophy

California Institute of Technology

Pasadena, California

1990

(Submitted October 31, 1989)

This is dedicated to the Ones I love:
my Parents,
Mealdey & Thida

ACKNOWLEDGEMENTS

In Cambodia where I was born, we were taught quite early in life that each person has to be thankful to their two sets of parents: the first one being our natural parents for they give us life and raise us and the second one being our "Gurus" (i.e., teachers) for they teach us all the knowledge we need in life. For this reason and many more, I would like to express my deepest gratitude to my advisor, Prof. R.F. Scott for his guidance, patience and most valuable advice during the course of this study. I would like to thank also all my former professors at Caltech and at the Ecole Polytechnique de l'Université de Montréal who opened up my mind by the excellence of their teaching: in particular, I would like to thank Prof. J.K. Knowles who gave me a new perspective on solid mechanics, Prof. J.F. Hall who introduced me to numerical computations and who patiently listened to my numerical problems, Prof. J.L. Beck whose conciseness in teaching Engineering Principles made me better understand the role of mathematics in engineering, Prof. W.D. Iwan whose clarity is legendary in teaching Dynamics and Vibrations, Prof. J.N. Franklin who showed me the human side of mathematics, Prof. F.E. Marble who convinced me that fluid mechanics can be quite interesting, Prof. R.F. Scott who made me appreciate his original concept in teaching soil mechanics and Prof. M. Soulié, my former advisor in Canada who introduced me to the world of research. I am also thankful to Prof. C.E. Brennen who patiently answered my questions in fluid mechanics.

To my parents, for whom I have caused much anxiety during these last six years, I am deeply indebted for their love, devotion, understanding, and sacrifice. I am also grateful to my mother-in-law for her constant encouragement. Thanks are especially due to Mealdey, my dear wife, who cheered up my life and brought us the joy of our life with the birth of our daughter. I admire her patience and understanding, especially when I have to desert her and leave our daughter under her

sole responsibility whenever I need to come to Caltech.

Special thanks are also due to Miss Crista Potter and Mrs. Sharon Beckenbach for their help in the typing of this manuscript.

To my Cambodian fellows whose suffering is a constant reminder of how fortunate I am, I would like to extend my sympathy and my hope that peace will return soon to our homeland.

My sincere thanks also goes to Dr. P. Cundall who made available his computer code without which this work would not be feasible. I gratefully acknowledge the Natural Sciences and Engineering Research Council of Canada, the Government of Québec (Fonds F.C.A.C.), and the U.S. National Science Foundation (NSF Award No. ECE8610887) for their financial support.

This study would not be possible without the availability of the Cray computers at the San Diego Supercomputer Center and at the Jet Propulsion Laboratory to which I would like to express my sincere thanks.

ABSTRACT

The liquefaction phenomenon in soil has been studied in great detail during the past 20 years. The need to understand this phenomenon has been emphasized by the extent of the damages resulting from soil liquefaction during earthquakes. Although an overall explanation exists for this phenomenon through the concept of effective stress, the basic mechanism of loss of strength of the soil skeleton has not been thoroughly examined and remains unclear.

The present study proposes a numerical model for simulations of the behavior of saturated granular media. The model was developed with two main objectives:

1. To represent the mechanical response of an assemblage of discrete particles having the shape of discs.

2. To model and represent the interaction of interstitial pore fluid present with the idealized granular media.

The representation of the solid skeleton is based on Cundall and Strack's distinct element model, in which discrete particles are modelled as discs in two dimensions, each obeying Newton's laws. Interparticle contacts consisting of springs and frictional element dashpots are included. Assuming a Newtonian incompressible fluid with constant viscosity and density, and quasi-steady flow, the fluid phase is described by Stokes' equations. The solution to Stokes' equations is obtained through the boundary integral element formulation. Several validation test cases are presented along with four simple shear tests on dry and saturated granular assemblages. For these last four tests, the numerical results indicate that the model is able to represent qualitatively the behavior of real soil, while at the same time clarifying the processes occurring at the microscale that influence soil response.

Contents

List of Figures

List of Tables

Chapter 1

INTRODUCTION

1.1 Motivations

The extent of damage resulting from the so-called *soil liquefaction* phenomenon during earthquakes (Niigata, Japan, 1964; Alaska, USA, 1964; San Fernando, USA, 1971; and probably during the recent San Francisco earthquake on 10/17/89) emphasizes the need to understand the physical phenomenon that starts this process, whereby the soil skeleton completely loses its strength. During the '60's and early '70's, research interest was mainly focused on phenomenological experiments where it was shown that excess pore pressures were generated during cyclic shearing of a loaded saturated sand. In the extreme case where the soil skeleton loses all its shear strength, the portion of the applied load, which was originally supported by the soil skeleton, is shifted to the liquid phase so that the soil assumes the properties of a dense liquid. Settlement results when the pore pressure dissipates by diffusion to drainage surfaces. In these experimental studies, empirical data were accumulated on the pore pressure generated in a particular soil under a particular applied stress, as a function of the shear stress level and number of shear stress cycles [43,57,61,70,77]. The basic mechanism of loss of strength has not been thoroughly examined and remains unclear.

With the advance of computers, predictions of liquefaction have been conducted mainly by numerical simulations [75,99]. These numerical simulations were performed by considering the soil as a continuum with a coupling relationship between the soil

skeleton and the interstitial pore fluid. The appropriate material properties were obtained empirically. Although these numerical models proved to be quite useful in the predictions of the behavior of soils, they do not help to explain the basic phenomenon that initiates the liquefaction process.

In the quest for understanding soil behavior, some current research interest is focused on the behavior of soil at the microscale [23,89]. From that work, the individual particle behavior can be simply described. In particular, the *distinct element method* (DEM) introduced by Cundall and Strack [23] has shown that even in the simplest case, where the individual particles are modelled as discs in two dimensions and spheres in three dimensions, each obeying Newton's laws and having contacts consisting of springs and frictional element dashpots, the global behavior obtained reasonably simulates the actual behavior of granular media. The shortcoming of this model comes from the large amount of computation time required to perform each simulation. Furthermore and very importantly, the original DEM cannot take into account the fluid phase, which has such a significant effect on soil behavior.

A liquid phase is essential in the modelling of the saturated granular behavior. The modelling of the behavior of particles in a fluid medium is of practical importance in chemistry or biomechanics. However, in those fields contact interaction between particles is not significant and usually a dilute system of particles in a fluid medium is considered. In the case of soil, the interaction between the soil grains is the most important factor controlling the behavior of the saturated soil medium. Therefore, a model of a microscopic granular medium needs to be able to represent both the *solid-solid* and *solid-liquid* interactions.

To model the liquid phase at the microscale, Darcy's law [31], which is generally used to describe liquid flow in a porous media, is no longer sufficient. The derivation of Darcy's law assumes that the medium is a continuum and the relationship obtained

holds on the average. If the fluid is assumed to be Newtonian and incompressible with constant viscosity and density, the description of the motion of the fluid phase is given, in general, by the Navier-Stokes equations. However, fluid flow in granular media occurs at low Reynolds numbers, with this condition, and by assuming furthermore that quasi-study flow occurs, the description of the motion of the liquid phase can be given by Stokes' equations.

With the combination of the microscopic solid model, that is the DEM, and a liquid behavior representation, it is then possible to model the behavior of a saturated granular medium. Because of the complexity of the combined solid-solid and solid-fluid interactions and the lengthy calculations involved in the numerical solution of the behavior of the liquid phase in particular, no such attempt at modelling the saturated granular medium at the microscale has been attempted before. Owing to the widespread availability of supercomputers, such a simulation is now feasible and has been implemented here.

1.2 Outline of the Present Work

As mentioned above, the main purpose of this research is to develop a numerical model that can represent both the solid-solid and solid-liquid interactions at the microscale. To this end, a numerical simulation tool, NePTune, was developed based on the microscopic solid-solid model pioneered by Cundall and Strack [23]. The description of this model is presented in chapter 2.

In chapter 3, the derivation of Stokes' equations is given. The main purpose is to introduce the underlying assumptions that lead to these equations which describe the solid-liquid interaction.

Several numerical methods exist for solving Stokes' equations; however because of the complexity of the shape of the liquid domain, the finite element method proved

to be impractical because the domain needs to be discretized entirely. In this work, the boundary element approach is chosen because of its simplicity in representing the liquid domain where the knowledge of the liquid boundaries is sufficient for the description of the geometry of the problem. Although the formulation of the boundary element method is elegant and simple, its numerical implementation proves to be difficult, particularly when singular functions are involved. By comparison with the finite element method, the boundary element method is not necessarily more advantageous because the matrix obtained is full and non-symmetric. In light of the complex shape of the liquid domain present in the particulate problem, use of the finite element method will also produce a large size of matrix; however, its numerical implementation is more straightforward than that of the boundary element method. The boundary integral formulation and its numerical implementation are discussed in chapter 4 along with some validation examples.

Further test and validation cases involving solid and fluid interactions are presented in chapter 5. Of particular interest, four simple shear tests have been performed (two for a loose array of particles and two for a dense array). Because of the limited resource available on the Cray, only a limited number of particles has been used in these four simulations. Nevertheless, we were able to obtain interesting and reasonable results for these limited configurations. In particular, the model shows that it is able to represent qualitatively the behavior of a real soil, while at the same time indicating the processes occuring at the microscale that influence soil response.

Finally, certain conclusions and recommendations for future work are summarized in chapter 6.

Chapter 2

NUMERICAL MODELLING OF THE SOLID PHASE

2.1 Different Concepts for Modelling Granular Media

2.1.1 The Continuum Approach

In engineering applications, the response behavior of any materials can be studied at a macroscopic level without considering atomic or molecular structures. This continuum concept lends itself naturally to homogeneous materials such as metals, but the same approach has also been used by geotechnical engineers to model soil, an aggregate of highly inhomogeneous particles. From a practical point of view, the continuum approach has provided geotechnical engineers with a working hypothesis in which a soil mass can be simplified and idealized. However, engineers must be fully aware of the uncertainties involved and they must anticipate the differences between real soil and the idealized materials used in their design. Safety factors are used extensively to overcome uncertainties. In the overall, the continuum approach has been used quite successfully in Soil Mechanics as can be proved by the large number of standing man-made earthworks and few failures of structures supported by soil.

One main advantage of the continuum concept comes from the fact that we can establish a mathematical model that describes the behavior of the materials. Several constitutive models have been developed to idealize the mechanical properties of different soils [36]. The establishment of constitutive models is based on experimental

observations at a macroscopic level.

However, the identification of the relevant constitutive variables for a certain material could become a difficult task. Also, the selection of pertinent properties often may have to be done only by experience and intuition. Depending on the complexity of the models, the amount of internal variables used is quite large. Due to the limited amount of available standard tests in Soil Mechanics, the determination of some of these internal variables is not easy and requires special experimental apparatus. Furthermore, constitutive models must obey certain principles or axioms that govern the physical phenomena. These axioms are classified as follows:

- Axiom of determinism:

  Future response is determined by the state (or history) of the body up to the present time. This is also called the "principle of heredity."

- Axiom of causality:

  Mathematical models describing the internal constitution of matter are developed after selecting suitable constitutive variables. The axiom of causality provides a selection or identification rule to distinguish dependent constitutive variables from independent ones. (For example, deformation (effects) do not occur without an external force (cause)).

- Axiom of objectivity:

  The constitutive response functionals must be form-invariant under arbitrary rigid motions of spatial frame of reference and a constant shift of the origin of time.

- Axiom of neighborhood:

  This axiom, which was presented by Eringen [41,42], is also known as the "axiom of local action." This axiom states that the values of response functions at a point

are affected less and less by the conditions far away from that point. In other words, the axiom of neighborhood is used to exclude from constitutive equations "actions at a distance."

- Axiom of fading memory:

  The values of present constitutive variables are affected less and less by the values of constitutive variables at distant past. This is the counterpart of the axiom of neighborhood in the time domain.

- Axiom of equipresence:

  This axiom, as stated by Eringen [42] is:

  "At the outset all constitutive response functionals are to be considered to depend on the same list of constitutive variables until the contrary is induced."

  The principle of equipresence says that all the constitutive variables should be included in every equation, unless the presence of a certain variable violates a basic principle of mechanics or thermodynamics, or another axiom. However, when there are too many variables in the constitutive equation, the problem of retaining them becomes complicated.

- Axiom of admissibility:

  The constitutive laws will be different for different materials. The physical laws of nature, such as conservation of mass, linear and angular momentum, and laws of thermodynamics, should be satisfied by any system irrespective of the material type. These physical laws lead to the governing equations, such as the continuity equation, equation of motion, symmetry of stress tensor, energy balance, and the entropy inequality. In other words, the axiom of admissibility asserts that constitutive equations must be consistent with the physical laws. Details of these laws are given in various references [16,41,42,65,55,59,92,93].

Nonlinear or general constitutive models added an important step to earlier Soil Mechanics design concepts in which the soil was assumed to be either perfectly elastic or perfectly plastic. However, the utilization of complicated constitutive models proved to give rise to difficulties when local yield occurs in narrow shear zones, resulting in bifurcation behavior, or when significant non-linear soil behavior exists.

As is apparent from the axioms above, the overall macroscopic description of granular materials could rapidly become complicated, although at the microscopic level, the behavior is simply that of an aggregate of particles that slip and roll over each other. This suggests that ideally, granular media can be modelled as an assembly of elastic or rigid three-dimensional spheres or two-dimensional discs obeying certain contact laws.

2.1.2 The Discrete Modelling Approach

2.1.2.1 Deterministic Approaches

In this approach, a granular medium is composed of distinct particles that move independently from one another and interact only at their contact points. Although such a model is quite simple to visualize, the overall behavior of the particles can become sophisticated enough to represent the behavior of granular media.

Among the previous work performed in this field, we can distinguish three phases: the analytical, physical, and numerical phase. Analytical works have been restricted to a face-centered cubic array of uniform size spheres. Deresiewicz [35] proposed an analytical model of such an array in which non-linear and hysteretic stress-strain behavior was predicted. Ultimate failure was also accommodated in the formulation. Based on his results, Scott [76, chap.7] gave an interesting observation in which the behavior of real granular soil can be deduced from individual particle behaviors.

Due to the restrictions of the geometry and loading conditions of analytical models, several investigators have turned to physical experiments to study the behavior of granular media. Dantu [30] and Wakabayashi [94] used optically sensitive material for the discs in two-dimensional photo-elastic tests. De Josselin de Jong and Verruijt [33] gave an account of the analyses of such tests where the force distribution was determined. Although this approach is quite general and provides accurate contact forces, displacements, and rotation for individual discs, the process is time-consuming and the preparation and test conditions are elaborate. Nevertheless, Drescher and De Josselin de Jong [37] performed a series of tests in order to confirm De Josselin de Jong's [34] double-sliding free-rotating model formulated for continuum models.

Oda and Konishi [67] presented experimental results of direct shear tests on assemblies of cylinders made of photoelastic material packed at random. The study showed that the two-dimensional model presented the same microscopic characteristics in regard to deformation and strength behavior as those of sand. They concluded from their study that:

1. The direction of the normals to the contact planes tend to concentrate toward the maximum principal stress axis. This tendency of concentration of the direction of these normals is not determined by the magnitude of the applied shear displacement but by the intensity of mobilized stress ratio (τ/σ_N, where τ and σ_N represent, respectively, the applied shear and normal stress).

2. The preferred direction of the contact normals gradually rotates with the rotation of principal stress axes during shear deformation. Thus rotation of the principal stress axis must be taken into account in any granular model.

3. Sliding in microscopic scale at contacts is not, at any one instant, occuring in the majority of contacts in the assembly, but rather is confined to some preferred contacts (i.e., slipping planes).

In their study, the determination of the direction of the normals to the contact planes proved to be tedious work.

With the advance of computers, numerical modelling, the third phase, became the preferred tool used to simulate assemblies of discs and spheres. Several models have been proposed. These models can be divided into two different classes: one (essentially static) representing dense arrays of particles, having multiple contact points, such as soils, and the other (dynamic), simulating rapid shear flow of particles where the number of contact points for each particle is very limited (usually zero or one contact per grain, i.e., a dilute system of particles). Among the models of the first class above, Serrano and Rodriguez-Ortiz [78] and Rodriguez-Ortiz [72] developed a model that simulates aggregates of discs and spheres. Contact forces are determined by incremental displacements of the particle centers. Hertzian-type contact compliances are used for normal forces whereas the effects of tangential forces are considered according to the theory of Mindlin and Deresiewicz [62], and Nayak [64], and shape changes are neglected. In this model, assemblies of discs are represented by the finite element method. A stiffness matrix is computed that takes into account the geometrical arrangement of the particles and the current stiffness at each contact. Incremental displacements can be computed by inverting this stiffness matrix. An iteration procedure is necessary to deal with slip and contacts. Only one contact is allowed to slip at any time. The stiffness matrix needs to be reformulated whenever a contact is made or broken, and this process is time-consuming. Therefore, this model is only able to process a relatively small number of particles.

The second model for a dense configuration of particles was developed by Cundall [20] and expanded by Cundall and Strack [23]. First, it was mainly used for the analysis of rock mechanics problems [20,21] and was named "**distinct element method**" or "**discrete element method**" (**DEM**). It is capable of handling particles of

any shape and size. It is based on an explicit local equilibrium algorithm in which the contacts are monitored and the motions of the individual particles are computed. As such, global equilibrium is not observed. Cundall also introduced several methods of handling data, which reduce the computation time required to locate contacts between particles. Because global equilibrium is not observed, static problems are treated as dynamic cases. For dynamic problems, small time steps are required by the explicit time integration algorithm and the absence of global equilibrium. This method, which is essentially a finite difference approach, will be the one used for the following work and its complete description will be given later.

To simulate rapid shear flows of granular media, Campbell and Brennen [11,12] developed the binary collision model. It has been used mainly to study two-dimensional fluidized behavior of granular materials composed of circular discs. This model assumes that two collisions cannot occur simultaneously so that only two-particle or binary collisions need be considered. Between collisions, each particle follows its own trajectory and the positions and velocities are only functions of time. Trajectories change only at collisions. Therefore, the updating process is performed from collision to collision. The incremental time steps are as long as the interval between collisions. This presents a distinct advantage over Cundall and Strack's model where the time step required is small in order to maintain stability. The binary collision assumption appears to be adequate for the rapid shear flows at relatively low densities studied by Campbell.

2.1.2.2 Probabilistic Approaches

The deterministic approach such as the DEM allows random distribution of particle size, shape, and physical properties. From the physics of the problem, contact forces are determined. For a random distribution of particles used in a deterministic model, the contact forces obtained appear to be erratic and suggest a statistical description

of these forces. This observation leads to the introduction of probabilistic models. Because the determination of contact forces is not easily feasible deterministically, they are assumed to be random variables. Theoretical analyses are conducted to obtain the behavior of these models.

Marsal [60] introduced a model composed of spherical particles made of homogeneous materials. The distribution of the number of particles and dimensions are obtained from the grain-size curve of the soil. As the magnitude of the contact forces between grains depend on:

- the dimensions and shapes of particles
- the mechanical properties of the grains, and
- the particle arrangement in the vicinity of each contact,

the contact forces cannot be evaluated in a deterministic manner and are assumed to be random variables. Similarly, the number of contacts of each grain is also a random, discrete variable. From the known distribution of contact forces and number of contact points, stress distributions were determined as well as stress-strain relationships.

Oda [66] proposed a model of granular material on the basic assumption that sliding at contact among grains is the main mechanism of microscopic deformation and rolling of grains has a negligible effect on the mechanical behavior of the granular material. The mean value of the force acting on a contact is assumed to be a function of the state of principal stresses and the direction of the normal to the principal stress axes. The relation between the mobilized stress ratio and the *"fabric index"* is determined by considering static equilibrium of forces at contact. Several definitions of fabric index have been proposed, however the one used by Oda is defined as the

following ratio:

$$\frac{S_z}{S_x} = \frac{\sigma_1}{\sigma_3} \frac{1}{\tan^2(\frac{\pi}{2} + \frac{1}{2}\phi_\mu)} \tag{2.1}$$

where (S_z/S_x) is the fabric index, (σ_1/σ_3) the mobilized principal stress ratio and ϕ_μ the interparticle friction angle. The probability of sliding at a contact can be calculated by considering that the forces at the contact are random variables having mean values and standard deviations. The rates of strain in the principal directions are theoretically obtained in terms of the frequency and intensity of sliding and the fabric index. Finally, based on the stress-dilatancy relations given by Rowe [74], relations among the fabric index, the dilatancy factor $(= (1 - dv/d\epsilon_1)$, where dv is the volume change and $d\epsilon_1$, the axial strain change) and the mobilized stress ratio are obtained. Comparison made with experimental results by means of the microscope and thin section method showed that this theoretical model agrees well with the experimental results.

Davis and Deresiewicz [32] also studied the compressibility and force transmission in granular media. Their model is composed of a two-dimensional random packing of like spheres in elastic contact. The packing geometry is represented by a stochastic planar graph where the nodes of the graph are taken as centers of the spheres and the branches are made of contacts between adjacent spheres. This stochastic graph is further replaced by a lattice, each of whose branches has a random stiffness modulus assigned to it. For mechanical response calculations, the lattice is treated as an elastic structure with branch stiffness in the form of the Hertz contact law. From their analysis, they observed that a significant fraction of the contacts among the spheres support no load whatsoever, while a few contacts sustain loads many times larger than the average. Such behavior agrees qualitatively with the works of Drescher and De Josselin de Jong [37], and Cundall and Strack [23].

Rodriguez-Ortiz [73] pointed out that even in the simplest case, the hypotheses

introduced in the stochastic approach can deviate from the actual behavior of granular materials. He cited:

- The surface friction of the particles plays an important role in the magnitude and orientation of the stress transmission paths.
- Rotations and tangential forces between particles cannot be neglected.
- The creation and breaking of contacts also play an important role in the overall behavior.
- Actual particles are heterogeneous and of irregular shape.

2.2 The Distinct Element Method

This model was first developed to handle two-dimensional elements of random polygonal shapes, then later discs [22,23], and was subsequently extended to three-dimensional spheres [24]. To date, the model has been used to study mechanisms of deformation in granular media [26,27], constitutive relations for soil [4,25,98], stability of rock masses [21], seismic stability of rock mass [2,68], the eolian saltation process (the transport of sand by the wind) [95,96], and practical applications in Soil Mechanics [88,89].

In this study, we are mainly interested in the microscopic behavior of particles. For example, we would like to understand the behavior at the microscale of particles when a phenomenon like liquefaction occurs. In this respect, the continuum approach is not covenient because only a global and averaged behavior is obtained. Discrete experimental simulations have been ruled out due to the large amount of work required to measure the interparticle contact forces. Most of the statistical models neglect one or more basic features of the granular behavior and because they were developed on too many hypothetical assumptions, their usage will limit the response of the system studied. This then leaves us with the discrete deterministic models. As was discussed

earlier, Serrano and Rodriguez-Ortiz's model can only be used when the number of particles is small, therefore, this model is not useful. We are then left with Cundall and Strack's DEM. It turns out that this model, although very simplistic, is able to model qualitatively well the behavior of real soil. Its main advantage lies in its efficiency in handling a large number of grains through the use of a convenient data structure for storing and retrieving information. However, as will be seen later, this model requires that the time step that is used is small enough to achieve numerical stability. The assumptions and algorithm of the DEM are given in the following.

2.2.1 Assumptions

The particles used in this model are assumed to be dry two-dimensional circular discs. The inclusion of a fluid phase will be described in a later chapter.

In the distinct element method, every particle (or element) in the assembly is identified separately, with its own mass, moment of inertia, and contact properties. The deformations of individual particles are assumed to be small in comparison to the deformation of the assembly as a whole. This global deformation is caused mainly by the rigid body motions of particles. Therefore, in the distinct element model, precise particle deformation is not considered; instead, particles are allowed to overlap one another at contact points. The overlaps, which replace the the particle deformation, are small in relation to the particle sizes. Figure 2.1 shows the mechanism used to model the contact between two particles. The symbols used are defined as follows:

C = Global translational damping coefficient

C^* = Global rotational damping coefficient

k_N = Contact normal spring constant

k_S = Contact shear spring constant

c_N = Contact normal dashpot coefficient

c_S = Contact shear dashpot coefficient

S = Contact shear force

N = Contact normal force

ϕ_μ = Contact friction angle

Normal and tangential springs and dashpots exist at each contact, with a frictional limit on the maximum tangential shear strength. While nonlinear spring and dashpot behavior can be accommodated with this scheme, the present implementation assumes constant spring stiffness and linearly viscous damping values. The magnitude of the contact forces is determined by the overlap between neighboring elements. In other words, an element can be visualized as a rigid disc with a coating of springs and dashpots at the periphery. At the contact point between two elements, the spring and dashpot at that location are activated. In the normal direction, for example, the compression of the contact spring is determined by the overlap between the contacting particles whereas the dashpot compression is determined by the relative velocities between these two particles. In turn, the amount of overlap is directly controlled by the stiffness of the springs. Dashpots are used to dissipate energy. Similarly, in the tangential direction, the relative sliding of two contacting particles determines the motion of the shear spring whereas the relative rotational velocity determines the motion of the shear dashpot. The computed shear force is limited by the Coulomb friction law.

Movements inside the assembly of particles are generated by the propagation, through the medium, of disturbances originating at the boundaries. If the time step can be small enough so that during a single time step disturbances cannot propagate from any disc further than its immediate neighbors, the resultant forces on a disc can be determined simply by its interaction with discs with which it is in contact. However, this local equilibrium could create global inequilibrium at an instantaneous

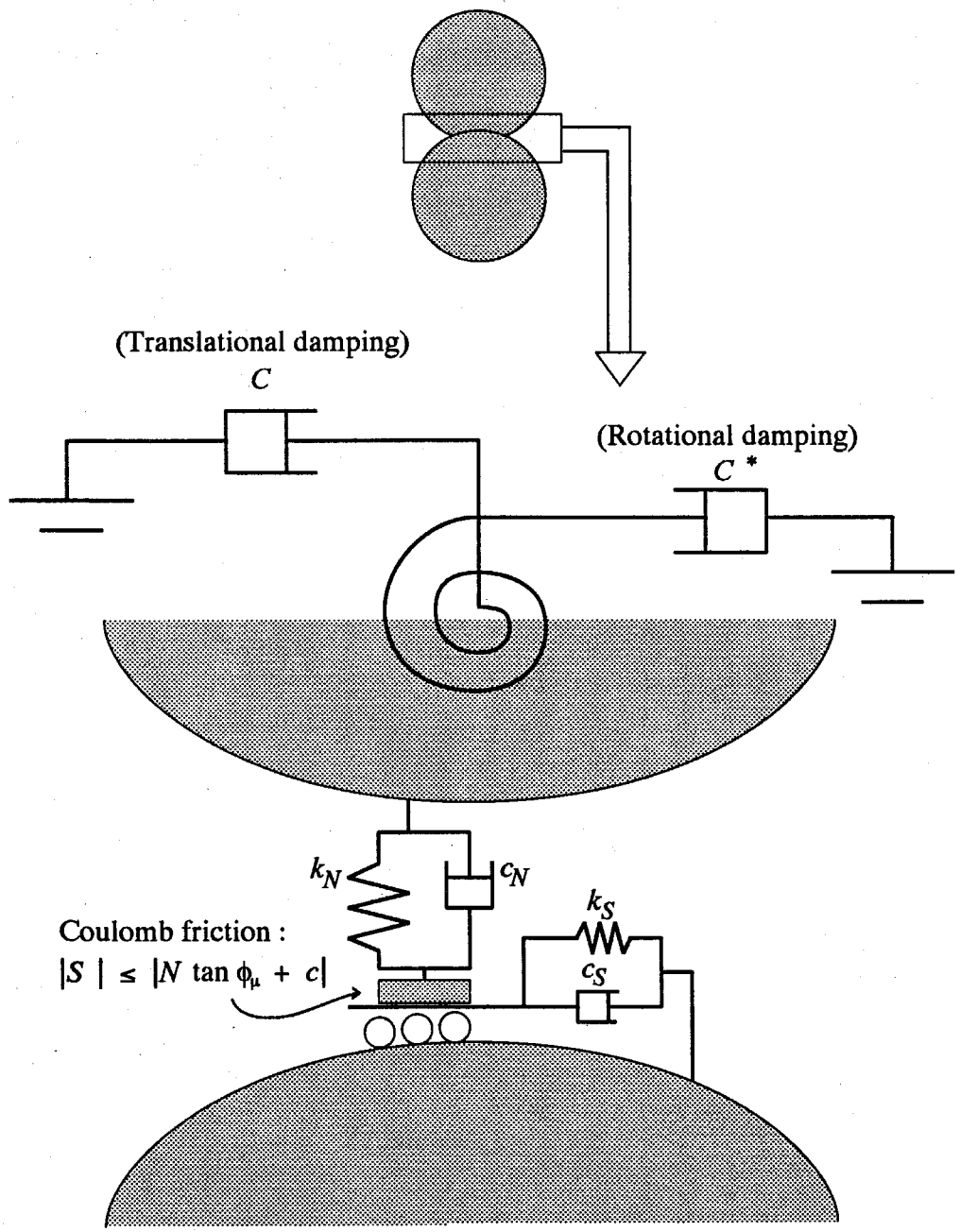

Figure 2.1: Contact model used by the distinct element method

time step. To avoid iterative procedures, an explicit time integration scheme is used. To achieve numerical stability, an explicit scheme requires a judicious choice of time increment. As the time increment chosen is considered small, velocities and accelerations are assumed to be constant over a time step.

2.2.2 Choice of the Distinct Element for the Solid Model

2.2.3 A Simple Example

Typically, the calculation process involved in the distinct element method alternates between the application of Newton's second law and the force-displacement law at the contacts. The motion of the particles is obtained by Newton's second law. As the particles move, contacts are created or broken. If contact occurs, the contact forces are determined by the force-displacement law. Summing all the contact forces on a particle provides the overall forces that are applied at the centroid of that particle. These forces are in turn used to determine the particle motion through Newton's second law.

To illustrate the calculation cycle, Cundall [23] considered the case shown on Figure 2.2. Two discs, labelled α and β, are maintained in the horizontal plane between a pair of rigid walls (i.e., no gravity involved). The walls are moving toward each other at a constant velocity u. In this example, simplifications have been introduced so that only normal contact forces are involved.

At the initial time $t = t_0$, the walls and discs are tangent to each other and no contact exists, i.e., springs at points A, B, and C are at rest (Figure 2.2(a)). At the following time step (see Figure 2.2(b)), $t_1 = t_0 + \Delta t$, the walls have moved inward over a distance $u\Delta t$. Because disturbances are not allowed to travel beyond a single disc during one time step, both discs remain at their initial position. Due to this, overlaps occur at contact points A and C. The overlap magnitude is $\Delta n = u\Delta t$.

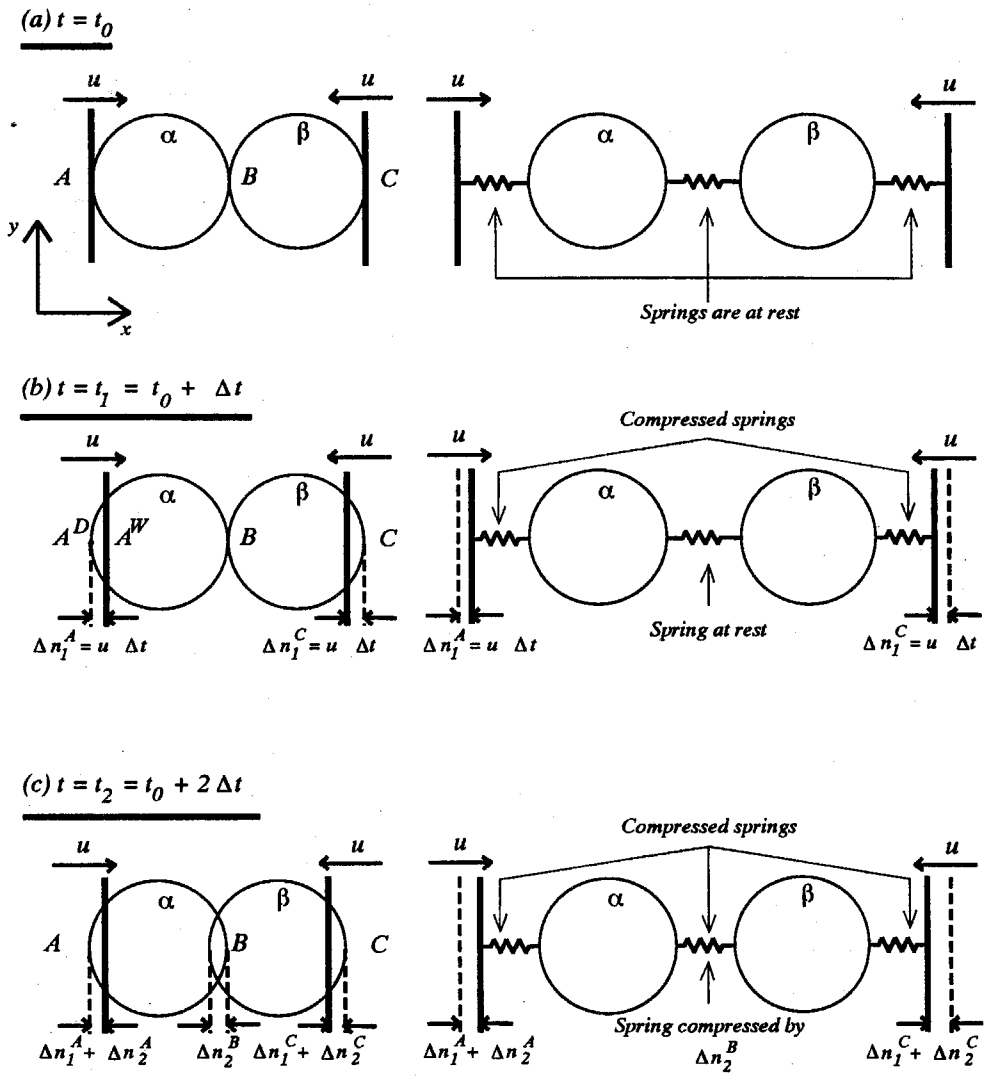

Figure 2.2: A simple example: two discs compressed between rigid walls

In the notation used here, superscripts designate the referenced object (such as the contact point, the disc or the walls) and subscripts indicate the time step, for example, Δn_1^A indicates the relative displacement of contact point A at time step t_1.

Contact point A is defined as the midpoint of segment A^D and A^W where A^D and A^W represent, respectively, points of the disc and wall lying on a perpendicular to the wall through the disc center. The relative displacement, Δn_1^A, at the contact is taken as the relative displacement of point A^W with respect to A^D.

As explained in the assumptions above, the contact springs at points A and C are activated at time t_1 (for the sake of simplicity, dashpots have been omitted here). Figure 2.2(b) shows the compression of the contact springs. Assuming constant spring values, the incremental contact forces at time t_1 at points A and C are given by:

$$\begin{aligned} \Delta N_1^A &= k^A \Delta n_1^A = k^A u \Delta t \\ \Delta N_1^C &= k^C \Delta n_1^C = k^C u \Delta t \end{aligned} \tag{2.2}$$

where k^A and k^C are the normal spring stiffnesses at contact points A and C respectively and compression is taken to be positive. According to the reference frame shown on Figure 2.2(a), the acting forces on discs α and β at time t_1 along the x-axis are:

$$\begin{aligned} F_1^\alpha &= k^A \Delta n_1^A \\ F_1^\beta &= -k^C \Delta n_1^C \end{aligned} \tag{2.3}$$

From Newton's second law, the accelerations of each disc in the x-direction are given by the above forces, namely:

$$\begin{aligned} \ddot{\alpha}_1 &= F_1^\alpha / m^\alpha \\ \ddot{\beta}_1 &= F_1^\beta / m^\beta \end{aligned} \tag{2.4}$$

where $\ddot{\alpha}_1$ and $\ddot{\beta}_1$ stand for the accelerations of disc α and β and m^α and m^β, their respective masses.

Assuming constant accelerations over the interval t_1 and $t_2 = t_0 + 2\Delta t$, velocities at time t_2 can be obtained:

$$\begin{aligned} \dot{\alpha}_2 &= \ddot{\alpha}_1 \Delta t = (F_1^\alpha / m^\alpha)\Delta t \\ \dot{\beta}_2 &= \ddot{\beta}_1 \Delta t = (F_1^\beta / m^\beta)\Delta t \end{aligned} \tag{2.5}$$

Hence, the relative displacement increments at points A, B, and C at time t_2, are determined to be:

$$\begin{aligned} \Delta n_2^A &= [u - \dot{\alpha}_2]\,\Delta t \\ \Delta n_2^B &= \left[\dot{\alpha}_2 - \dot{\beta}_2\right]\Delta t \\ \Delta n_2^C &= \left[\dot{\beta}_2 - (-u)\right]\Delta t \end{aligned} \tag{2.6}$$

Figure 2.2(c) shows the situation at time t_2.

This cycle is repeated, i.e., forces corresponding to displacements are found according to the force-displacement law; the resultant of the contact forces is in turn used in Newton's second law to determine new accelerations and velocities at the following time step. In the general case of an assembly of discs, vectorial forces are acting at each contact point. The equations used in a calculation cycle for a general case are presented in the following section.

2.2.4 General Calculation Cycle

2.2.4.1 Notations and Definitions

Let α and β be two discs in contact as shown in Figure 2.3. The coordinates of the disc centers, according to the reference system are $\boldsymbol{\alpha} = (\alpha_1, \alpha_2)$ and $\boldsymbol{\beta} = (\beta_1, \beta_2)$. Their respective velocities will be denoted by $\dot{\boldsymbol{\alpha}} = (\dot{\alpha}_1, \dot{\alpha}_2)$ and $\dot{\boldsymbol{\beta}} = (\dot{\beta}_1, \dot{\beta}_2)$. Their angular velocities, $\dot{\theta}_{(\alpha)}$ and $\dot{\theta}_{(\beta)}$, are taken positive in the counterclockwise direction. Each disc has been assigned a radius, $R_{(\alpha)}$ and $R_{(\beta)}$; a mass, $m_{(\alpha)}$ and $m_{(\beta)}$; and

a moment of inertia $I_{(\alpha)}$ and $I_{(\beta)}$. If gravity is present, it is represented by vector $\boldsymbol{g} = (g_1, g_2)$. Points $P_{(\alpha)}$ and $P_{(\beta)}$ are defined as the points of intersection of the line connecting the disc centers with the boundaries of discs α and β respectively. The unit vector from the centroid of α to β is represented by $\boldsymbol{\epsilon} = (\cos\gamma, \sin\gamma)$. Its perpendicular unit vector in the clockwise direction is $\boldsymbol{\tau}$.

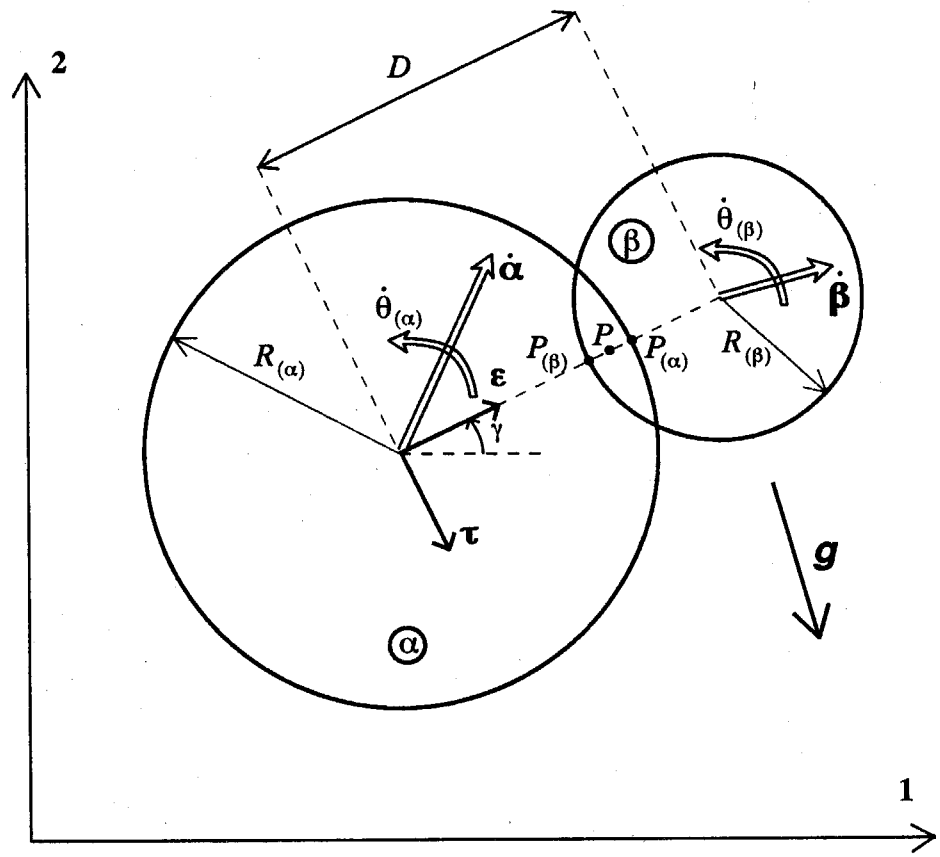

Figure 2.3: Variables used in the force-displacement law

2.2.4.2 Contact Forces Determination

If contact occurs between α and β, D, the distance between their centers is less than the sum of their radii, i.e.:

$$D < \left[R_{(\alpha)} + R_{(\beta)}\right] \tag{2.7}$$

As explained in the previous example, if this condition is verified, the contact point P is defined as the midpoint of $P_{(\alpha)}$ and $P_{(\beta)}$. The relative velocity of $P_{(\alpha)}$ with respect to $P_{(\beta)}$ can be expressed as:

$$\begin{aligned} \dot{\boldsymbol{P}} &= (\dot{P}_1, \dot{P}_2) \\ &= (\dot{\boldsymbol{\alpha}} - \dot{\boldsymbol{\beta}}) - (\dot{\theta}_{(\alpha)} R_{(\alpha)} + \dot{\theta}_{(\beta)} R_{(\beta)})\boldsymbol{\tau} \end{aligned} \tag{2.8}$$

The normal and tangential components of $\dot{\boldsymbol{P}}$, $\dot{n}$ and $\dot{s}$, are obtained by the decomposition of $\dot{\boldsymbol{P}}$ along $\boldsymbol{\epsilon}$ and $\boldsymbol{\tau}$:

$$\begin{aligned} \dot{n} &= \dot{\boldsymbol{P}} \cdot \boldsymbol{\epsilon} \\ &= (\dot{\boldsymbol{\alpha}} - \dot{\boldsymbol{\beta}}) \cdot \boldsymbol{\epsilon} - (\dot{\theta}_{(\alpha)} R_{(\alpha)} + \dot{\theta}_{(\beta)} R_{(\beta)})\boldsymbol{\tau} \cdot \boldsymbol{\epsilon} \\ &= (\dot{\boldsymbol{\alpha}} - \dot{\boldsymbol{\beta}}) \cdot \boldsymbol{\epsilon} \\ &= (\dot{\alpha}_k - \dot{\beta}_k)\epsilon_k \end{aligned} \tag{2.9}$$

$$\begin{aligned} \dot{s} &= \dot{\boldsymbol{P}} \cdot \boldsymbol{\tau} \\ &= (\dot{\boldsymbol{\alpha}} - \dot{\boldsymbol{\beta}}) \cdot \boldsymbol{\tau} - (\dot{\theta}_{(\alpha)} R_{(\alpha)} + \dot{\theta}_{(\beta)} R_{(\beta)})\boldsymbol{\tau} \cdot \boldsymbol{\tau} \\ &= (\dot{\boldsymbol{\alpha}} - \dot{\boldsymbol{\beta}}) \cdot \boldsymbol{\tau} - (\dot{\theta}_{(\alpha)} R_{(\alpha)} + \dot{\theta}_{(\beta)} R_{(\beta)}) \\ &= (\dot{\alpha}_k - \dot{\beta}_k)\tau_k - (\dot{\theta}_{(\alpha)} R_{(\alpha)} + \dot{\theta}_{(\beta)} R_{(\beta)}) \end{aligned} \tag{2.10}$$

Einstein summation convention is assumed only for subscript k. Indices between parentheses do not follow this convention.

By integrating the relative velocity components with respect to time, the relative displacement increments are:

$$\begin{aligned} \Delta n &= \dot{n}\Delta t \\ &= \left[(\dot{\boldsymbol{\alpha}} - \dot{\boldsymbol{\beta}}) \cdot \boldsymbol{\epsilon}\right] \Delta t \end{aligned} \tag{2.11}$$

$$\begin{aligned} \Delta s &= \dot{s}\Delta t \\ &= \left[(\dot{\boldsymbol{\alpha}} - \dot{\boldsymbol{\beta}}) \cdot \boldsymbol{\tau} - (\dot{\theta}_{(\alpha)} R_{(\alpha)} + \dot{\theta}_{(\beta)} R_{(\beta)})\right] \Delta t \end{aligned} \tag{2.12}$$

From the force-displacement law, the normal and tangential incremental forces can be computed as:

$$\Delta N = k_N \Delta n \tag{2.13}$$

$$\Delta S = k_S \Delta s \tag{2.14}$$

where k_N and k_S represent the normal and shear spring stiffnesses.

Finally at each time step, the incremental forces, ΔN and ΔS, are added into the sum of all force increments, N and S, determined from the previous time step:

$$N = N + \Delta N \tag{2.15}$$

$$S = S + \Delta S \tag{2.16}$$

In the above notations, normal and shear forces are assumed to be positive in the direction opposite to vectors $\boldsymbol{\epsilon}$ and $\boldsymbol{\tau}$.

The contact model also includes a Coulomb-type friction; that is, the magnitude of the shear force S must obey the following rule:

$$| S | \leq S_{max}, \ (S_{max} = | N \tan \phi_\mu + c |) \tag{2.17}$$

where ϕ_μ represents the smallest value of the interparticle friction angle and c the smallest value of the cohesion of the two contacting particles because the weakest

particle will control sliding. In the case where S exceeds S_{max} in the absolute value, the value of S is set to S_{max} with the sign preservation of S.

Because the contact model also has provision for damping, friction damping forces at the contact point are also considered. The magnitudes of the damping forces are given by:

$$\begin{aligned} D_N &= c_N \dot{n} \\ &= c_N \left[(\dot{\boldsymbol{\alpha}} - \dot{\boldsymbol{\beta}}) \cdot \boldsymbol{\epsilon} \right] \qquad (2.18) \\ D_S &= c_S \dot{s} \\ &= c_S \left[(\dot{\boldsymbol{\alpha}} - \dot{\boldsymbol{\beta}}) \cdot \boldsymbol{\tau} - (\dot{\theta}_{(\alpha)} R_{(\alpha)} + \dot{\theta}_{(\beta)} R_{(\beta)}) \right] \qquad (2.19) \end{aligned}$$

where c_N and c_S are, respectively, the normal and shear damping coefficients.

The shear forces generate the following moments on each particle:

$$\begin{aligned} M_{(\alpha)} &= \bar{S}_{(\alpha)} R_{(\alpha)} \\ M_{(\beta)} &= \bar{S}_{(\alpha)} R_{(\beta)} \qquad (2.20) \end{aligned}$$

in which $\bar{S}$ represents the sum of the shear force, S, and the damping force, D_S (if shear damping is used, the Coulomb friction law becomes $\mid S + D_S \mid \leq S_{max}$ where S_{max} is as defined in equation (2.17)).

The sums of the normal and shear forces and moment at each contact point provide the forces and moment acting at the centroid of the particle. Resolving the forces into the 1 and 2 directions, the forces at a particle centroid, $\sum \boldsymbol{F}_{(\alpha)}$, are given by $\sum F_{(\alpha)1}$ and $\sum F_{(\alpha)2}$. Similarly, the resultant moment generated is $\sum M_{(\alpha)}$ whereas the contact damping forces, $\sum \boldsymbol{D}_{(\alpha)}$, are $\sum D_{(\alpha)1}$ and $\sum D_{(\alpha)2}$. Although constant springs have been used throughout the derivations, non-linear springs can easily be included in this model.

2.2.4.3 Particle Motion

In addition to local contact damping, global damping is also included in the particle equation of motion. Although it can be used in combination with local contact damping, global damping prevents a ringing effect when no local contact damping is used. It consists of translational and rotational dashpots attaching each particle to the ground. Assuming that C and C^* are the global damping coefficients for the translational and rotational degrees of freedom (cf. Figure 2.1), and with the presence of gravity, $\boldsymbol{g}$, the equations of motion of disc α are given by Newton's second law:

$$m_{(\alpha)}\ddot{\boldsymbol{\alpha}} + C\dot{\boldsymbol{\alpha}} = \sum \left[\boldsymbol{F}_{(\alpha)} + \boldsymbol{D}_{(\alpha)}\right] + m_{(\alpha)}\boldsymbol{g} \tag{2.21}$$

$$I_{(\alpha)}\ddot{\theta}_{(\alpha)} + C^*\dot{\theta}_{(\alpha)} = \sum M_{(\alpha)} \tag{2.22}$$

As stated earlier, a central difference scheme [18] is used to integrate equations (2.21) and (2.22). In this scheme, the velocities at time step t_i are evaluated halfway through the time step, i.e.,

$$\dot{\boldsymbol{\alpha}}_i = \frac{1}{2}(\dot{\boldsymbol{\alpha}}_{i-\frac{1}{2}} + \dot{\boldsymbol{\alpha}}_{i+\frac{1}{2}}) \tag{2.23}$$

$$\dot{\theta}_i = \frac{1}{2}(\dot{\theta}_{i-\frac{1}{2}} + \dot{\theta}_{i+\frac{1}{2}}) \tag{2.24}$$

The translational and rotational accelerations at time t_i can now be written as:

$$\ddot{\boldsymbol{\alpha}}_i = (\dot{\boldsymbol{\alpha}}_{i-\frac{1}{2}} + \dot{\boldsymbol{\alpha}}_{i+\frac{1}{2}})/\Delta t \tag{2.25}$$

$$\ddot{\theta}_i = (\dot{\theta}_{i-\frac{1}{2}} + \dot{\theta}_{i+\frac{1}{2}})/\Delta t \tag{2.26}$$

Combining equations (2.21), (2.22), (2.23), (2.24), (2.25), and (2.26), the velocities at time $t_{i+\frac{1}{2}}$ can be obtained:

$$\dot{\boldsymbol{\alpha}}_{i+\frac{1}{2}} = \frac{\dot{\boldsymbol{\alpha}}_{i-\frac{1}{2}}\left[1 - \frac{C\Delta t}{2m_{(\alpha)}}\right] + \sum \left[\boldsymbol{F}_{(\alpha)} + \boldsymbol{D}_{(\alpha)}\right]_i \frac{\Delta t}{m_{(\alpha)}} + \boldsymbol{g}\Delta t}{\left[1 + \frac{C\Delta t}{2m_{(\alpha)}}\right]} \tag{2.27}$$

$$\dot{\theta}_{i+\frac{1}{2}} = \frac{\dot{\theta}_{i-\frac{1}{2}}\left[1 - \frac{C^*\Delta t}{2I_{(\alpha)}}\right] + \sum \left[M_{(\alpha)}\right]_i \frac{\Delta t}{I_{(\alpha)}}}{\left[1 + \frac{C^*\Delta t}{2I_{(\alpha)}}\right]} \tag{2.28}$$

The velocities are then integrated to yield the particle displacements at the next time step, t_{i+1}:

$$\boldsymbol{\alpha}_{i+1} = \boldsymbol{\alpha}_i + \dot{\boldsymbol{\alpha}}_{i+\frac{1}{2}} \Delta t \tag{2.29}$$

$$\theta_{i+1} = \theta_i + \dot{\theta}_{i+\frac{1}{2}} \Delta t \tag{2.30}$$

It should be noted that in equation (2.27), the discretization of the damping forces can be performed as follows:

$$\begin{aligned} (D_N)_i &= c_N \dot{n} \\ &= c_N \left[\dot{\boldsymbol{\alpha}} - \dot{\boldsymbol{\beta}}\right]_{i-\frac{1}{2}} \cdot \boldsymbol{\epsilon} \end{aligned} \tag{2.31}$$

$$\begin{aligned} (D_S)_i &= c_S \dot{s} \\ &= c_S \left[(\dot{\boldsymbol{\alpha}} - \dot{\boldsymbol{\beta}}) \cdot \boldsymbol{\tau} - (\dot{\theta}_{(\alpha)} R_{(\alpha)} + \dot{\theta}_{(\beta)} R_{(\beta)})\right]_{i-\frac{1}{2}} \end{aligned} \tag{2.32}$$

An error of half a time step is introduced in the calculation of D_N and D_S. Cundall [23] indicated that this error is found to be negligible.

From the equations of motion, we can see that energy is dissipated through friction, local contact damping, and global damping. If neither local contact or global damping is used in static problems, the system would never reach equilibrium.

2.2.4.4 Choice of Time Step

Explicit time integration is only conditionally stable. To insure numerical stability, the time step, Δt, should be chosen smaller than the critical time step, Δt_{crit} ($\Delta t < \Delta t_{crit}$) [3, chap.9]. Because the equilibrium of each particle is only satisfied locally, it is impossible to obtain the critical time step of the global system, which is determined by the highest natural frequency (or eigenvalue) of the system. However, the critical time step can be estimated based on the oscillation of a single degree of freedom system of a mass m attached to a spring of stiffness k. For this system, the critical time step is $(2\sqrt{(m/k)})$. The critical time step estimated by the solid phase

algorithm is based on the lowest particle mass and the highest stiffness in the problem. The actual time step used by the algorithm is chosen as a fraction of this estimated critical time step. Cundall [22] recommended the use of 10% of the estimated critical time step as a safe choice for the actual time step. This choice is found to be adequate for the present work.

2.2.4.5 Contact Determination

If contact between two particles occurs, equation (2.7) needs to be checked for every pair of particles. It is obvious then that the number of computations required would be of the order of N^N where N is the total number of particles in the simulation. This number could be reduced to $O(N!)$ if we do not test twice for each pair of particles; i.e., if the contact between two particles α and β has been tested, we would not check again the contact between β and α. At any rate, the number of computations required is so large that this algorithm is not acceptable for any practical purpose. To eliminate the contact search between distant particles, Cundall [22] devised a scheme in which the global area under study is divided into smaller ones called "boxes." As illustrated in Figure 2.4, the box size is chosen in such a way that the largest disc diameter is less than one box width or height. Based on this constraint, the scan for contacts is reduced to a partial search in the disc vicinity only. Consider, for example, disc α on Figure 2.4; because its immediate bounding square lies inside boxes B_5 and B_6, we only need to consider discs inside these two boxes to test for contact condition. This technique of "Divide and Conquer" significantly reduces the computation time.

In some cases such as the one shown in Figure 2.5, the immediate bounding square of a disc fails to determine all the particles that would be in contact with that disc. In this particular case, disc α lies solely inside box B_n. Now, because its immediate bounding square is fully contained by box B_n, disc β will not be included in

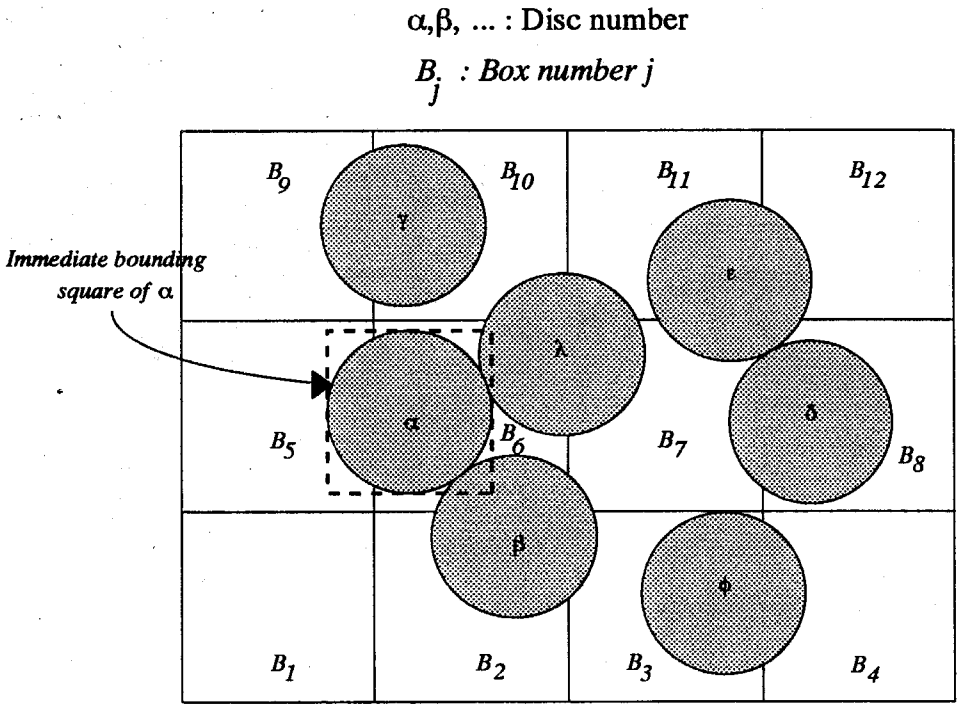

Figure 2.4: Division of the area into boxes

the search during the contact scan. To circumvent this weakness of the scan method, a bigger bounding square is used. A margin length, $DNTOL/2$, is set outside the immediate square to determine all the boxes in which a particle lies (cf. Figure 2.6). The value of $DNTOL$ is chosen so that the following condition is satisfied:

$$\left[2\max(R_{(\alpha)}) + DNTOL\right] \;<\; 2 \times (Box\ Dimension),\ \forall\alpha \qquad (2.33)$$

The above condition ensures that a contact scan for a disc will not include more than the discs inside 4 adjacent boxes.

2.2.4.6 Compliances of the DEM with the Axioms of Continuum Mechanics

At the grain size level, all particles follow all the axioms stated earlier in the continuum approach, namely:

- Axiom of determinism: the motion of a particle depends only on the state at the previous time step.

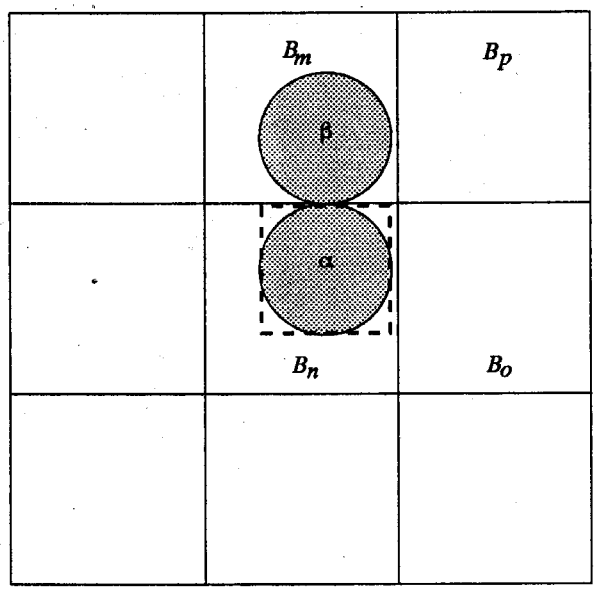

The immediate bounding square of disc α lies solely inside box B_n so that disc β will never be tested for possible contact with α.

Figure 2.5: Case where the immediate bounding square fails to produce all possible contacts

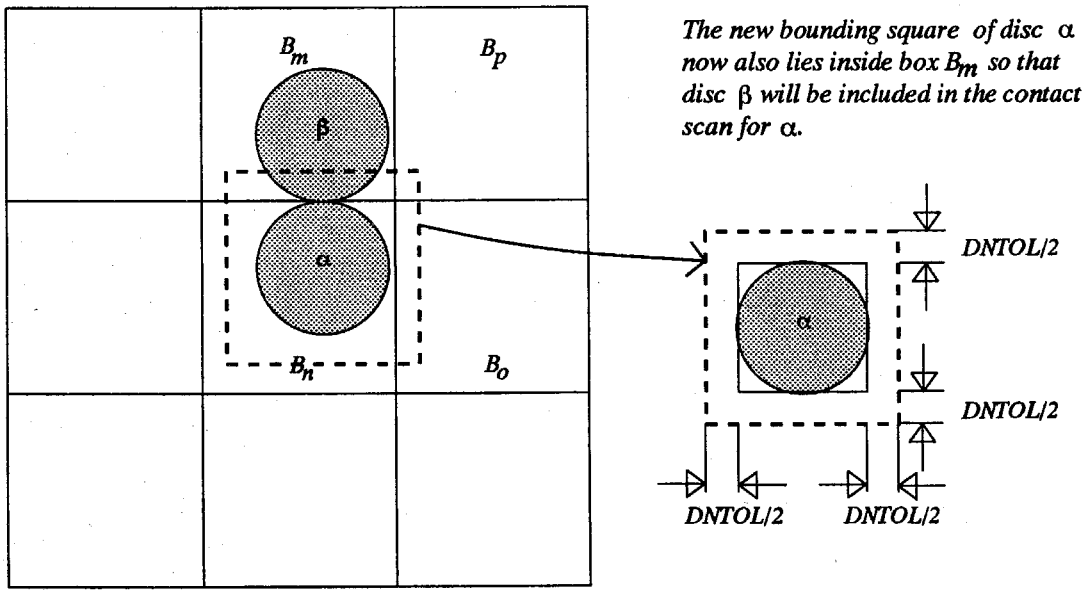

The new bounding square of disc α now also lies inside box B_m so that disc β will be included in the contact scan for α.

Figure 2.6: Margin length sets so that the contact search will find all the contacting discs

- Axiom of causality: the cause and effect that determine the motion of the assembly of particles are clearly identified as the propagation through the medium of disturbances originating at the boundaries. Hence all the variables used in this model are clearly identified.

- Axiom of objectivity: it is obvious from the description of the DEM that under rigid body motions or a constant shift of time, the results obtained are identical.

- Axiom of neighborhood: as explained earlier, the response of a particle is only affected by directly adjacent particles or objects (such as wall boundaries).

- Axiom of fading memory: the motions of a particle are affected by the response of the previous time step. Therefore, the DEM follows a special case of this axiom.

- Axiom of equipresence: the basic equations of motion of the DEM include all the physical variables and do not violate any principle of mechanics or thermodynamics, or another axiom.

- Axiom of admissibility: the governing equations of the DEM satisfy all the physical laws of nature at the grain size level. However, due to the iterative procedure used in static problems, global imbalance of forces could occur during iterations. For dynamic problems, force imbalance is minimized by the use of small time steps that are also dictated by the explicit time integration scheme.

2.2.4.7 Comments about the DEM

In general, the DEM is quite flexible because it can accommodate different particle sizes and material properties. However, the specification of material properties is not easy for dynamic problems. *For static or quasi-static problems (such as monotonic loading), the material properties used do not affect the results because equilibrium is*

always achieved. For dynamic problems, the contact spring and dashpot constants cannot be measured directly. For these cases, the value of the normal contact spring constant can be obtained by condering the geometry of the contact between two identical particles each having a radius R (see Figure 2.7). The overlap between the particles, δ, determines the strain, $\epsilon = \delta/2R$. The stress generated by the contact force, F, is assumed to act over the chord length, l; hence, the contact stress per unit length is given by:

$$\sigma = \frac{F}{l} \tag{2.34}$$

Furthermore, if E represents Young's modulus of the particles, assuming linear relationship between the stress and strain gives:

$$\frac{F}{l} = E\frac{\delta}{2R} \Rightarrow F = \frac{El}{2R}\delta \tag{2.35}$$

Let

$$k_N = \frac{El}{2R} \tag{2.36}$$

then the relationship between the force and overlap distance is obtained as:

$$F = k_N\delta \tag{2.37}$$

The dependence of l on δ ($l = 2\sqrt{R^2 - (R-\delta)^2}$) shows that even in this simple-minded model, the relationship between contact forces and overlap length is nonlinear. To simplify the problem, the value of δ is chosen so that it will not exceed a prescribed value (usually between 1 to 5% of the minimum radius). This maximum value of δ is used to determine the maximum value of the contact chord. Finally, the value of the normal contact spring constant given by equation (2.36) is used for all range of overlap length.

The study of Hertzian contact theory for elastic spheres by Mindlin and Deresiewicz [62] showed that the tangential stiffness at a contact may vary between 2/3

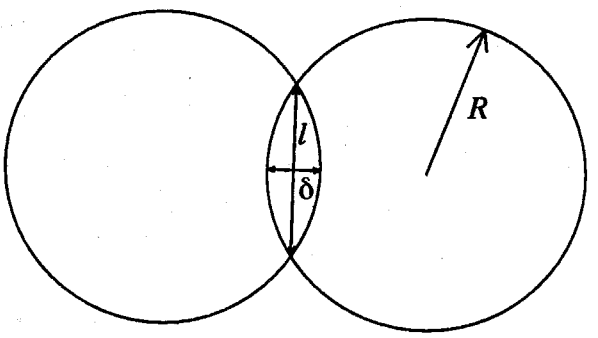

Figure 2.7: Definition of parameters used to define k_N

and 1 times the normal stiffness. No such information is readily available for two-dimensional discs, therefore, such a range of values can only be assumed.

The normal contact damping is directly related to the coefficient of restitution of the particle. Because it is mainly used as a dissipator of energy, its function is identical to the coefficient of restitution. The value of the normal contact damping can be selected so that it matches the value of the coefficient of restitution. To establish the correlation between these two variables, a test can be devised in which a disc is dropped onto a rigid, flat surface. The ratio of the initial dropping height over the bouncing height determines the coefficient of restitution. In most studies involving the DEM, the value of the shear damping has been arbitrarily selected so that its ratio over the shear stiffness is the same as that of the normal damping over the normal stiffness.

One way of determining the global translational damping, C, is obtained by considering the hysteretic stress-strain relationships such as the one shown on Figure 2.8. These relationships are obtained in the laboratory by means of triaxial compression tests, simple shear tests or torsional shear tests conducted under cyclic loading conditions.

The damping ratio, C is defined as [49]

$$c = \frac{A_1}{4\pi A_2} \tag{2.38}$$

where A_1 = area of abcdefa, and A_2 = area of Oag.

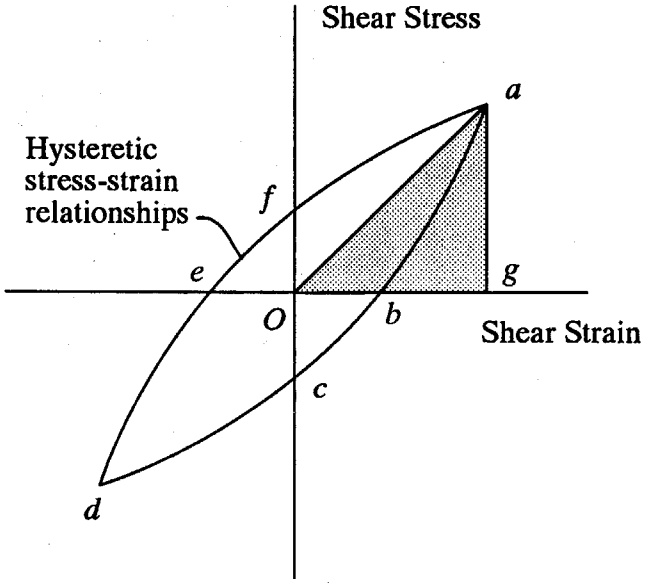

Figure 2.8: Hysteretic stress-strain relationships

Alternatively, the translational global damping, C, is assumed to have a value ranging from 1 to 5% of the value of the critical damping of a single degree of freedom system having the particle mass and normal spring stiffness. Similarly, the rotational global damping C^* can be arbitrarily selected.

The values of the material parameters can thus be fine-tuned by devising special experiments to obtain appropriate concordance with measurable physical quantities.

Due to the small size of the particles, the moment of inertia, $I_{(\alpha)}$, should not play an important role in the deformation of an actual system of particles. However, its inclusion in the equation of motion is required for a complete description of the motion of each particle.

Although in principle any type of loading could be applied to the boundary (i.e., specified displacement, force, or stress boundary), a specified displacement boundary

is the most practical one to be used with the DEM. If force or stress is applied to a boundary, their distribution to directly adjacent particles presents some ambiguities.

In conclusion, the richness of information provided by the DEM proves to be also one of its weaknesses. The wealth of information about each particle at each time step gives rise to a dilemma: either statistical information should be compiled out of these discrete results, in which case all the microscopic behaviors become fuzzy; or global information should be analyzed, in which case all the information could not be easily absorbed unless only a small portion of the system is considered.

2.2.4.8 Summary of the Distinct Element Method Algorithm

The distinct element method algorithm can be summarized as follows:

read simulation parameters and initial conditions
for all time t_i steps **do**
    for each disc α **do**
        assemble the disc contact list, i.e., all objects in contact with α
        for each object of the contact list **do**
            compute outward normal vector
            compute incremental velocities at contact
            compute contact forces and update contact information
        compute accelerations for disc α at time t_i
    for each disc α **do**
        integrate for velocities at time $t_{i+\frac{1}{2}}$
        integrate for displacements and rotations at time t_{i+1}
    update disc information array
    update list of contacts made or broken
    update wall motion and wall information array
end of simulation

2.2.5 Algorithm Validation

2.2.5.1 Static Test: One Disc under Gravity Loading

The following test was performed mainly to show the different types of damping used in the DEM. In this example, a disc having a radius of 1 m and a density of

$\rho_s = 2400\ kg/m^3$ (i.e., having a mass $m = 7539.823\ kg$), supported by a horizontal plate, is subjected to a vertical gravity field of intensity $g = 10\ m/sec^2$ (see Figure 2.9(a)). Friction, shear contact spring and dashpot have been omitted. The value of the normal contact spring constant is assumed to be $k_N = 10^7\ N/m$.

Four cases have been studied: case 1 considers only the normal contact spring (Figure 2.9(b)); in case 2, both the normal contact spring and global translational dashpot are included in the analysis (Figure 2.9(c)); for the third case, the normal contact spring is combined with the normal contact dashpot (Figure 2.9(d)); and in case 4, the normal contact spring and dashpot, and the global translational dashpot are all used (Figure 2.9(e)). The different values of spring and dashpot constant used in each case are given in Table 2.1.

Case	k_N Normal Contact Spring (N/m)	c_N Normal Contact Dashpot $(N/(m/sec))$	C Translational Dashpot $(N/(m/sec))$	Final Contact Force (at $t = 5sec$) (N)	Absolute Force Error $(\%)$
1	10^7	0	0	[1]	[1]
2	10^7	10^5	0	72703.36	3.5742
3	10^7	0	1.0×10^4	75398.66	0.0006
4	10^7	10^5	4.5×10^5	75397.49	0.0010

Table 2.1: Values of spring and dashpot constant used for each case

Due to the simplifications made here, the only contact force involved in all these four cases is the normal contact force between the disc and the plate. Figure 2.10 shows the normal reaction force on the plate with respect to time for each case studied. Because no damping is considered in case 1, the reaction force is simply oscillating around the weight of the disc (75398.23 N). The equation of motion of case 2 can be expressed as :

[1]Not included due to oscillation in the response.

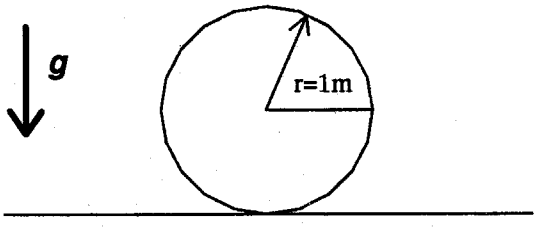

(a) Physical Model

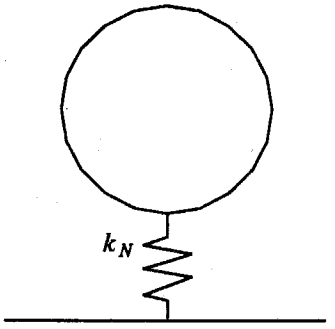

(b) Case 1: No Damping

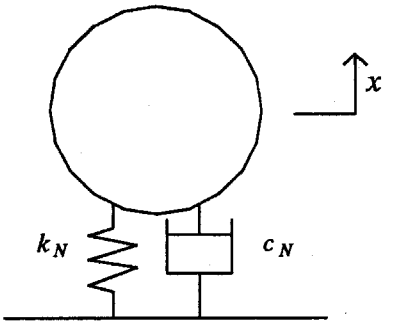

(d) Case 3: Contact Damping Only

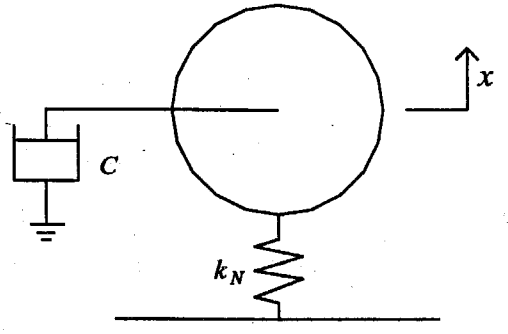

(c) Case 2: Global Damping Only

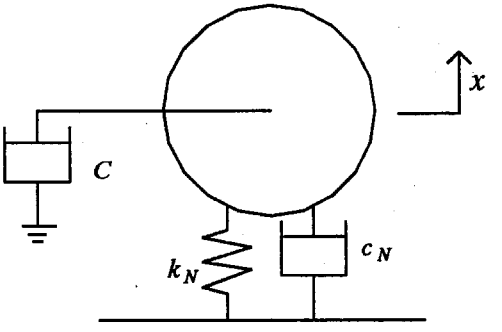

(e) Case 4: Contact and Global Damping

Figure 2.9: Different cases studied for the settling of a disc on a flat plate under gravity loading

$$m\ddot{x} + C\dot{x} + k_N x = mg \tag{2.39}$$

where C is the global translational damping, x, the displacement of the disc relative to its initial position, $\dot{x}$ and $\ddot{x}$ are respectively the velocity and acceleration of the disc.

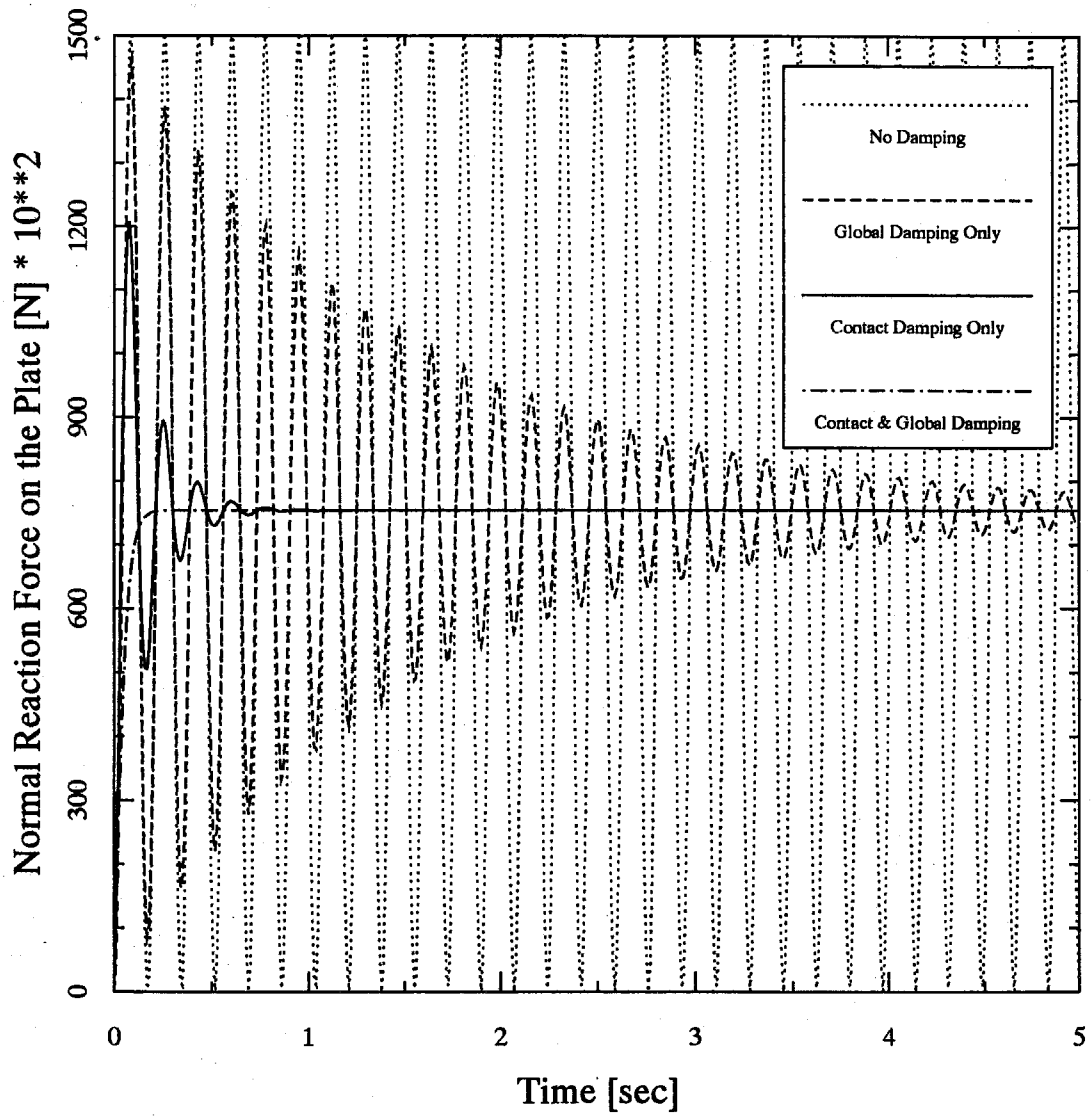

Figure 2.10: Normal reaction force on the plate

Likewise, the equation of motion of case 3 is given by:

$$m\ddot{x} + c_N\dot{x} + k_N x = mg \tag{2.40}$$

where c_N is the normal contact damping value.

The similarity of the equations of motion of cases 2 and 3 is caused by the simplicity of the model presented. In cases where a disc is also in contact with another disc, the velocity used in equation (2.40) would be the relative velocity of the contact point rather than the velocity of the disc itself.

Finally, the equation of motion of case 4 is:

$$m\ddot{x} + (C + c_N)\dot{x} + k_N x = mg \tag{2.41}$$

As shown in Table 2.1, the magnitude of the damping used in case 2 is 10 times smaller than the one used in case 3. Consequently, the response of case 3 reaches equilibrium faster. In case 4, the combination of normal contact damping and global translational damping is such that their sum yields the critical damping ratio of this simple degree of freedom system. Hence, no oscillation is observed for this later case as the normal reaction force reaches the weight of the disc (i.e., when equilibrium is achieved). Table 2.1 also gives the value of the normal reaction force on the plate at the end of the 5000 steps simulation (i.e., at $t = 5$ *sec*). The deviation of the normal force from the weight of the disc is also shown on this table. In general, the magnitude of the error tends to decrease as the amount of damping increases. When higher damping is used, the disc reaches equilibrium faster. When no damping is included, the disc will oscillate indefinitely; therefore, depending on the time when the contact force is selected, its value can vary from 0 to twice the weight of the disc, which is why the contact force has been omitted from Table 2.1.

The contact force between the disc and the plate of case 4 is shown on Figure 2.11. Here, the thickness of the line gives the intensity of the force whereas its direction is given by the direction of the contact force line. It should be noted that since the disc and plate are frictionless, the contact force is acting along the perpendicular to the plate. This graphical representation of the contact force can be

associated with the fringes observed in pictures of photoelastic material testing.

2.2.5.2 Static Test: Five Discs under Gravity Loading

This test was performed to verify the accuracy of the contact forces under static loading. Here, 5 discs, each having a radius of 1 m and a mass of 7539.823 kg, are allowed to settle in the presence of gravity ($g = 10\ m/sec^2$) (see Figure 2.12(a)). The discs are assumed to be frictionless (i.e., only normal contact spring and dashpot, and global translational dashpot are present). The parameter used for both the disc–disc and disc–wall contact are:

$$\begin{aligned} k_N &= 10^7 N/m \\ c_N &= 10^5 N/(m/sec) \\ C &= 4.5 \times 10^5 N/(m/sec) \end{aligned}$$

Table 2.2 shows the predicted value of the normal contact force at the end of the simulation ($t = 5\ sec$) at each contact point, along with the theoretical contact forces calculated from force equilibrium of each disc, and the error introduced by the algorithm.

Contact between	Predicted Force (N)	Theoretical Force (N)	Error %
Disc 1 – Wall 1	188492.5	188495.6	0.002
Disc 1 – Wall 2	133648.0	128247.7	4.21
Disc 2 – Wall 1	188491.3	188495.6	0.002
Disc 2 – Wall 3	133647.8	128247.7	4.21
Disc 3 – Disc 1	175075.0	170996.9	0.52
Disc 3 – Disc 2	175079.4	170996.9	0.52
Disc 3 – Disc 4	115750.6	113997.9	1.54
Disc 3 – Disc 5	115760.0	113997.9	1.55
Disc 4 – Wall 2	87832.7	85498.4	2.73
Disc 5 – Wall 3	87828.2	85498.4	2.72

Table 2.2: Comparison of the predicted contact force values with the theoretical values

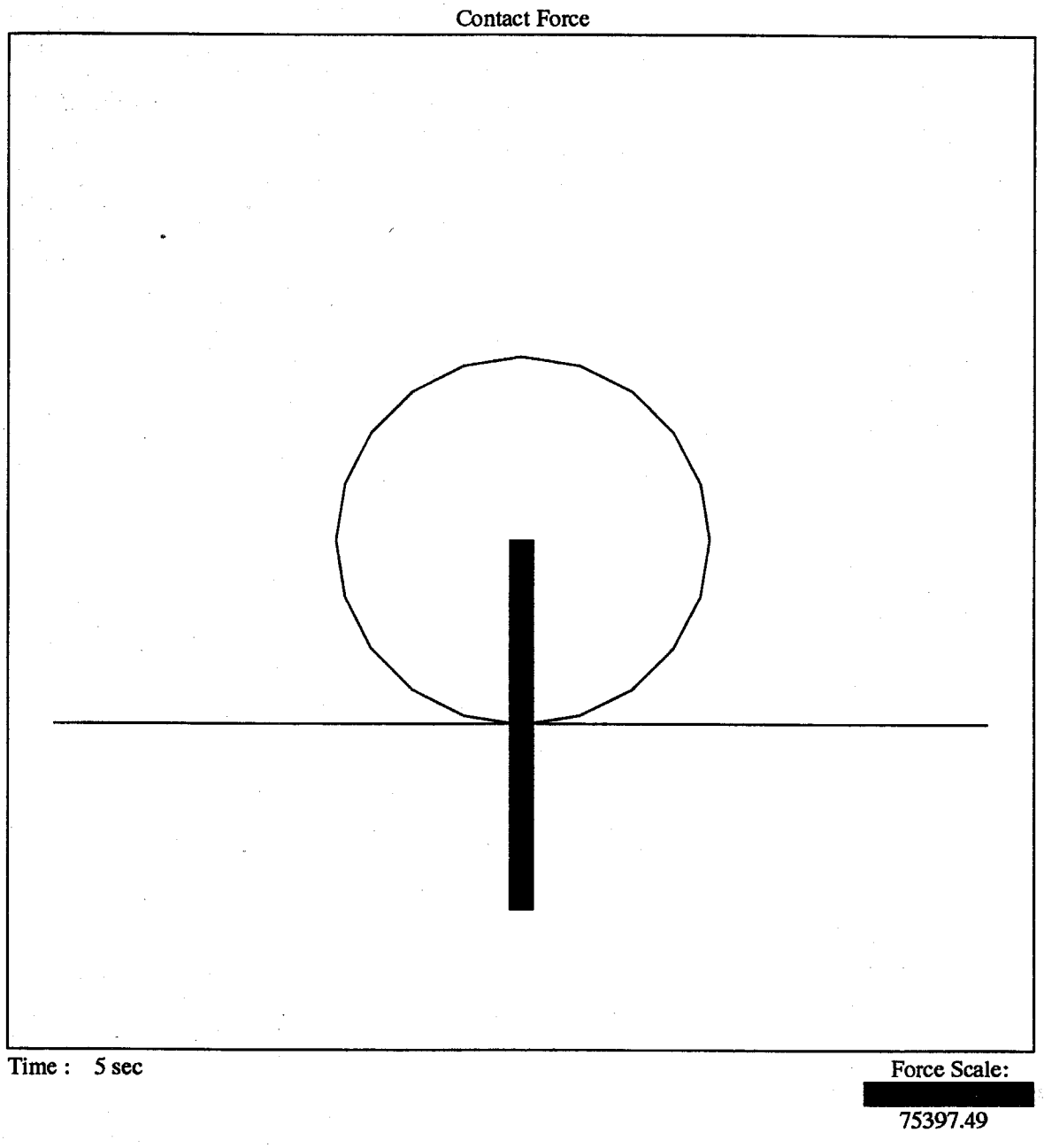

Figure 2.11: Graphical representation of the contact force for case 4 at the end of simulation

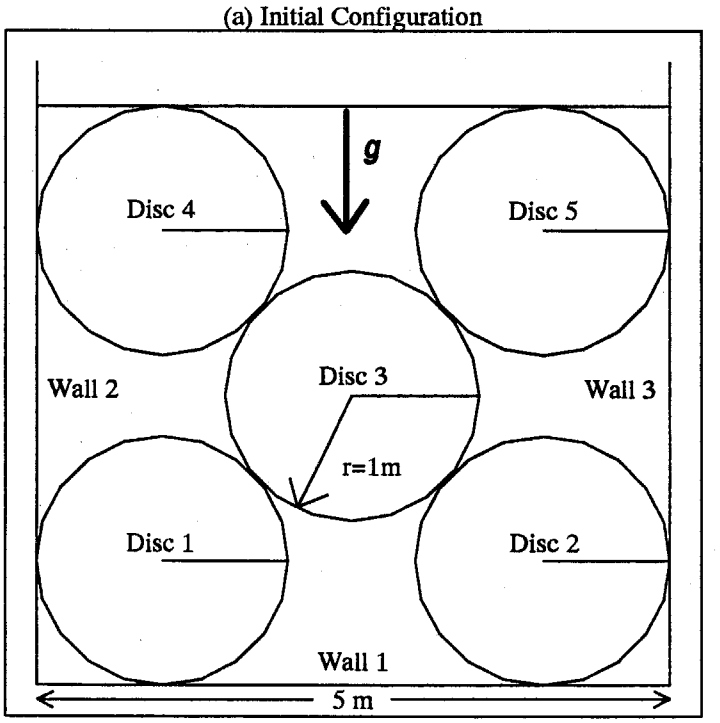

Figure 2.12: Initial and final geometry for the settling of 5 discs under gravity loading

The maximum error found is about 4%. This error is caused mainly by the difference in geometry used to calculate the theoretical force where the discs are assumed rigid. As is apparent from Figure 2.12(b), due to the disc overlap allowed by the DEM, a re-arrangement of the configuration occurred by the end of the simulation whereas in the theoretical computation, the final configuration is identical to the initial configuration.

Figure 2.13(a) shows the contact force at each contact point at the end of the simulation. For all practical purposes, the distribution of the contact force is symmetrical with respect to the vertical passing through the center of disc 3. The velocity vectors of each disc at the end of the simulation are presented on Figure 2.13(b). The small magnitude of the velocity of each disc indicates that they have reached equilibrium.

The normal reaction force on walls 1, 2, and 3 as a function of time is given in Figure 2.14. Due to the high values of damping used, no oscillation is observed as the reaction forces reach their equilibrium value.

When friction and shear contact springs and dashpots are used, the results predicted by the algorithm differ from that of frictionless materials. In the following case, the friction angle at a contact point between two discs or between a disc and a wall is assumed to be $\phi = 15°$. The shear contact spring is given a value of $k_S = 7 \times 10^6\ N/m$, whereas the shear contact dashpot and rotational dashpot constant take respectively a value of $c_S = 7 \times 10^4\ N/(m/sec)$ and $C^* = 4.5 \times 10^5\ N/(m/sec)$ (i.e., these values have been chosen arbitrarily such that $c_S \approx 2/3 c_N$ and $C^* = C$). Figure 2.15(a) shows the final position of the discs at the end of the simulation at 5 *sec.* Discs 4 and 5 have slightly rotated from their initial positions as shown by the slight inclination of their radius indicators (see Figure 2.15(a)). Also, because of the settlement of the discs, the final configuration differs slightly from the original one.

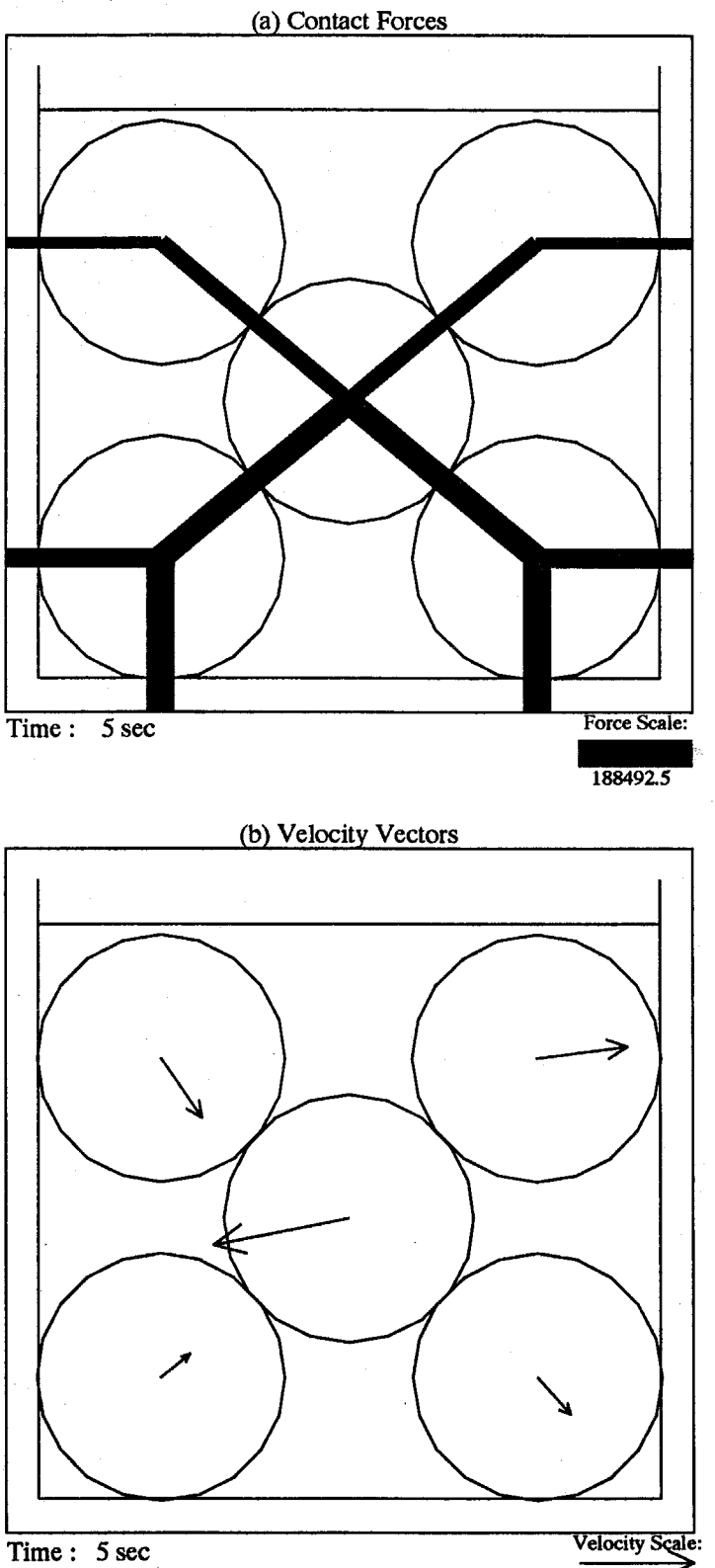

Figure 2.13: Contact force and velocity distribution at the end of the simulation

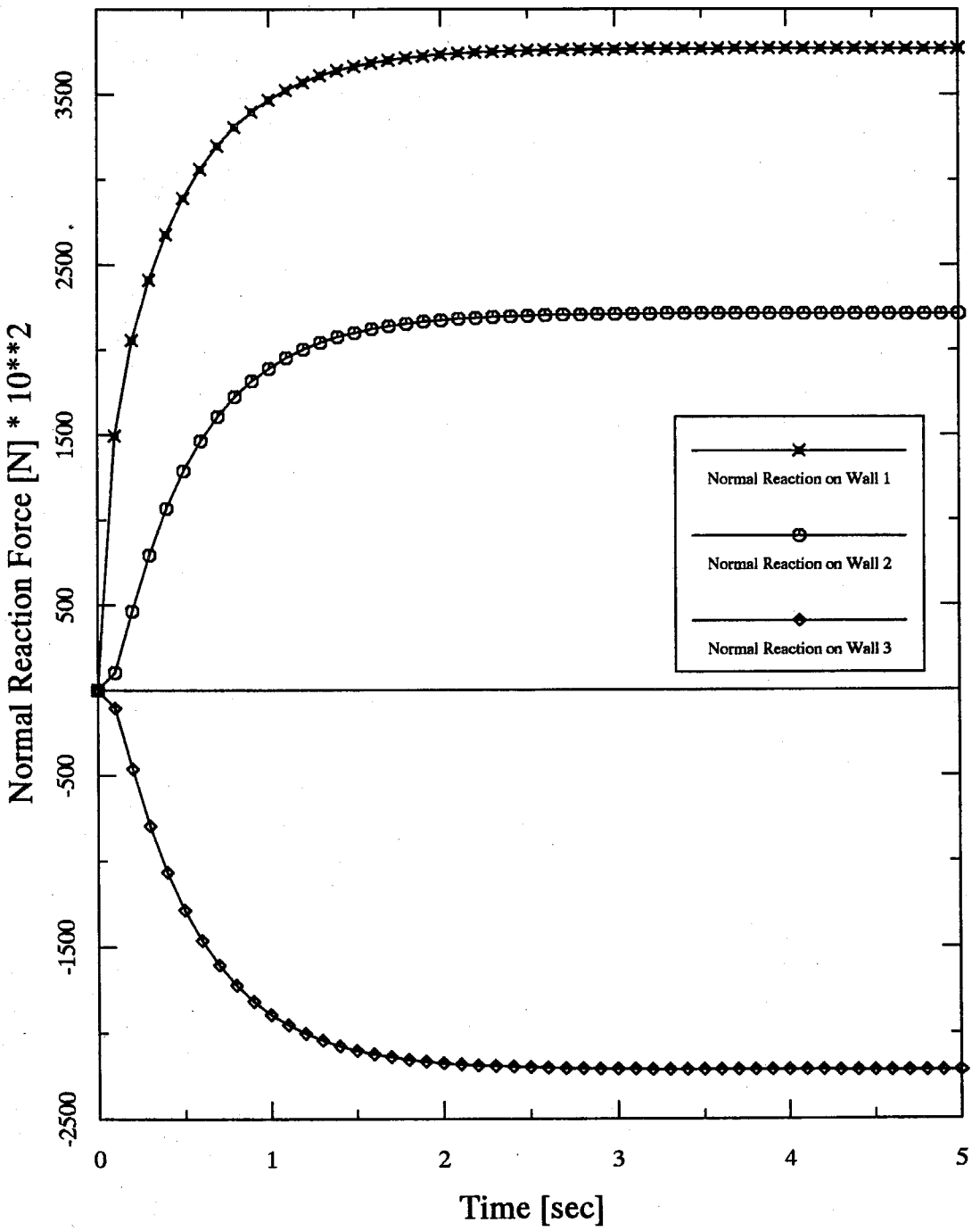

Figure 2.14: Normal Reaction Forces on Wall 1, 2, and 3

The distribution of contact forces is presented in Figure 2.15(b). Due to the friction, the contact forces are no longer normal to the walls and they do not pass through the centers of two contacting discs. From this figure, it is clear that the distribution of the contact forces is again symmetrical with respect to a vertical passing through the center of disc 3.

The values of the components of the contact forces for each contact point are given in Table 2.3. The orientation of axes x and y is given in Figure 2.15(b).

Contact between	F_x (N)	F_y (N)
Disc 1 – Wall 1	167269.7	38775.2
Disc 1 – Wall 2	28609.2	-7665.5
Disc 2 – Wall 1	167269.7	-38774.5
Disc 2 – Wall 3	28610.1	7664.9
Disc 3 – Disc 1	116104.0	-31109.8
Disc 3 – Disc 2	116103.1	31109.6
Disc 3 – Disc 4	78747.3	13561.1
Disc 3 – Disc 5	78749.6	-13561.0
Disc 4 – Wall 2	50610.7	-13561.0
Disc 5 – Wall 3	50611.1	13561.0

Table 2.3: Components of the contact forces for material with friction

The sum of the horizontal and vertical reaction forces on walls 1, 2, and 3 yield $\sum F_x = -0.5\ N$ and $\sum F_y = 376991.7\ N$. The value of $\sum F_y$ closely approaches the value of the weight of the five discs (which is 376991.2 N). Similarly, the value of $\sum F_x$ is almost zero, indicating the symmetry of the distribution of the contact forces with respect to a vertical passing through the center of disc 3.

2.2.5.3 Dynamic Test: Impact of Two Discs

This simple experiment was devised to test the algorithm in a dynamic case. Disc 1 has an initial velocity of 6 m/sec in the vertical direction as shown on Figure 2.16. It collides with disc 2 of equal mass and radius and initially at rest. Assuming that

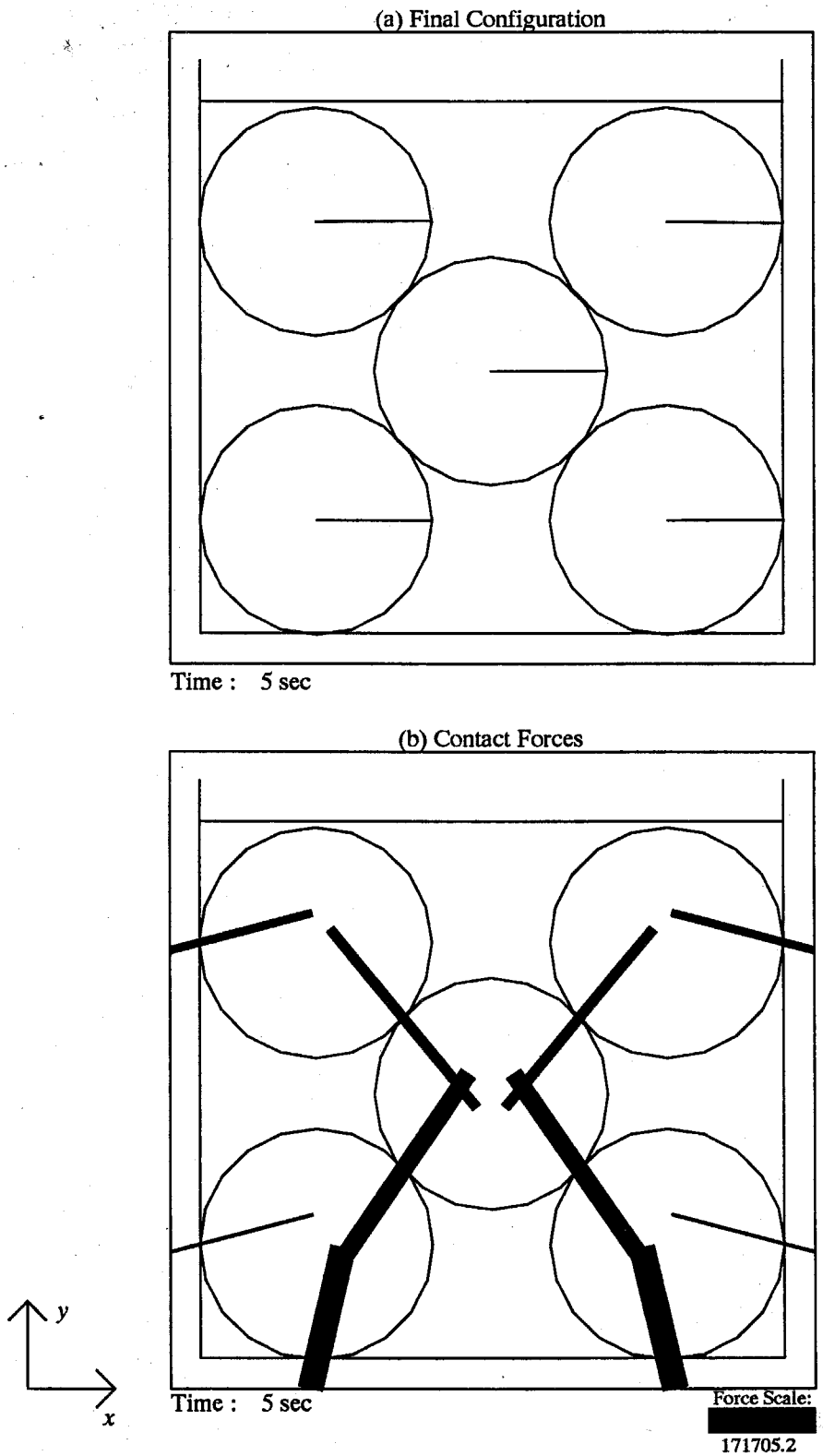

Figure 2.15: Final configuration and contact force distribution for material with friction

there is no loss of energy during the collision, i.e., that there are neither contact nor global rotational dashpots, and that the material is frictionless, the theoretical values of the velocity of each disc can be calculated from the kinematics of the particles (conservation of momentum and coefficient of restitution of 1). The predicted value of the velocity of each disc ((v_{1x}, v_{1y}) for disc 1, and (v_{2x}, v_{2y}) for disc 2) and the theoretical results after the collision are presented in Table 2.4.

Velocity Component	Predicted (m/sec)	Theoretical (m/sec)	Error %
v_{1x}	2.591	2.598	0.27
v_{1y}	1.514	1.500	0.93
v_{2x}	−2.591	−2.598	0.27
v_{2y}	4.486	4.500	0.31

Table 2.4: Comparison of predicted and calculated velocities after collision

In general, the maximum error is less than 1 %. Therefore, the predicted results agree well with the theoretical values. The position of the discs at impact, and at time $t = 1$ *sec* along with the trajectory and final velocity of each disc are also shown on Figure 2.16.

It should be noted, however, that for this particular test, the only material parameter involved is the normal contact spring constant, which was chosen to be $k_N = 10^7$ N/m. In the theoretical solution of the problem, the mass of each disc is irrelevant, however, in the DEM, a mass has to be assigned for each disc. Here the mass is assumed to be $m = \pi$ kg for each disc. Due to the small mass used, the value of the critical time step is roughly of the order of 10^{-3} *sec*. To be able to capture all the features of the impact, the time interval is chosen to be 10^{-5} *sec*. The impact occurs roughly between $t = 44$ *msec* and $t = 46$ *msec*. The magnitude of the contact force is presented on Figure 2.17. The impulse–type force can be viewed as consisting of two sections. The first one covers the period of compression from first contact until maximum deformation of the two bodies (for the DEM, this corresponds to maximum

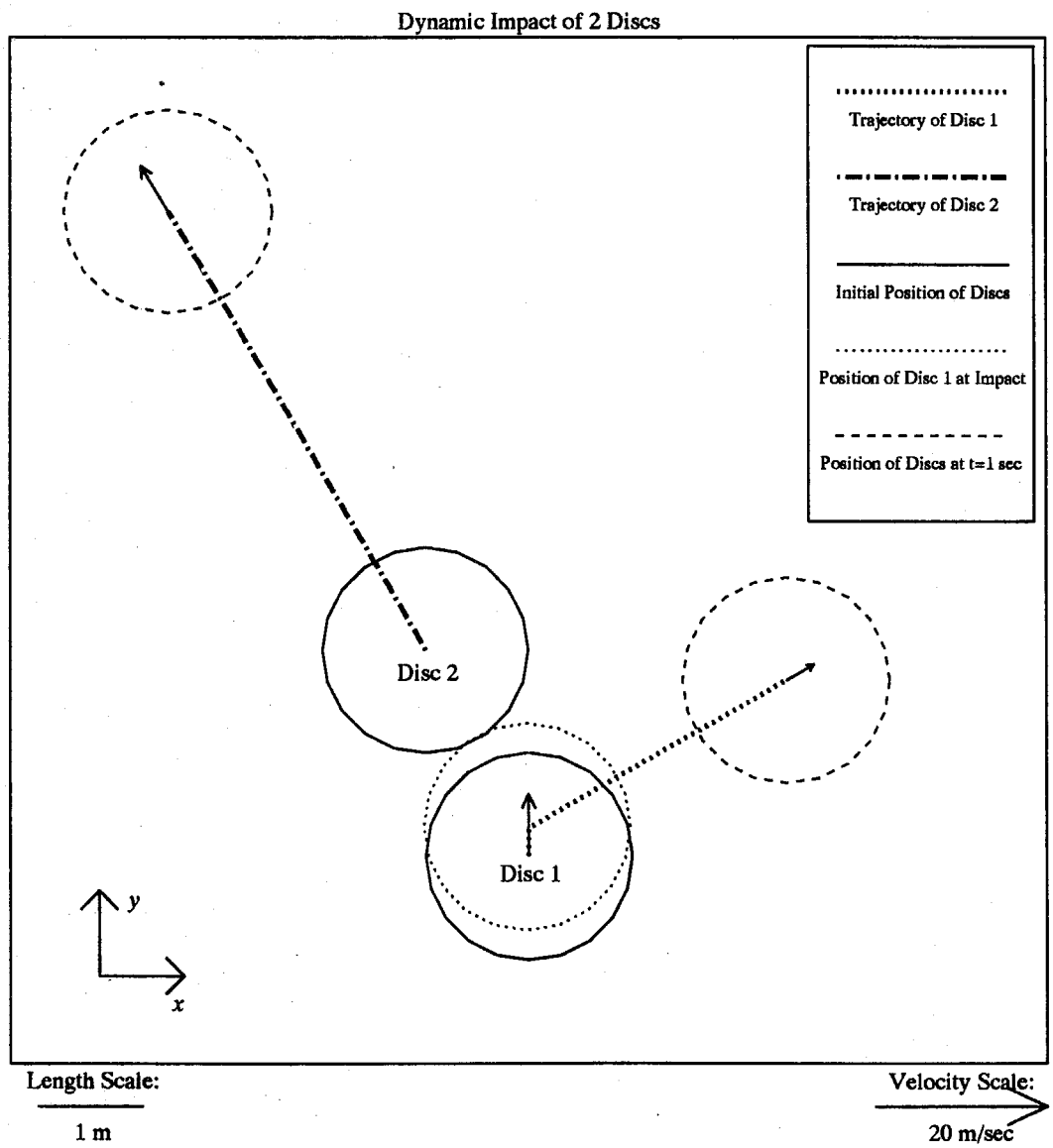

Figure 2.16: Geometry, trajectories and velocities of the collision of two discs

overlap between the two discs). At the end of this period, the relative velocity of the two bodies is zero. The second interval comprises the period of restitution from maximum deformation until cessation of contact. The symmetrical shape of the contact force clearly indicates that the deformation is purely elastic.

This concludes the description of the solid phase used in this work. The modelling of the fluid phase is given in the following chapter.

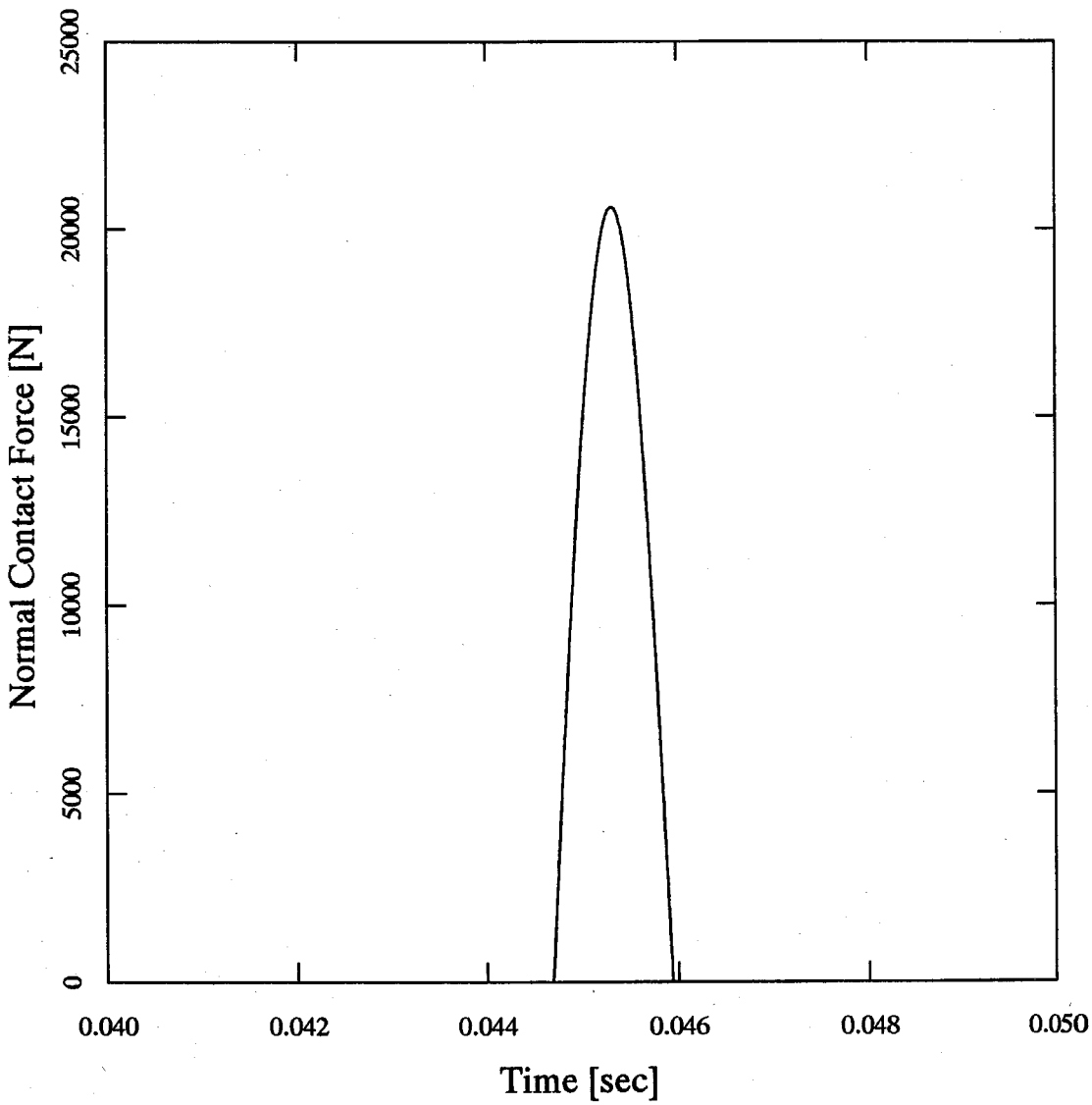

Figure 2.17: Normal contact force for the collision of two discs

Chapter 3

MODELLING THE FLUID PHASE

3.1 Historical Review

The following gives a short review of the historical developments of flow through porous media. For a complete review of major historical works in this field, the reader is referred to Happel and Brenner's book [48].

Flow through porous media has probably been considered throughout history; however, the first scientific results were obtained only about one hundred and fifty years ago. Flow through porous media had attracted the attention of several engineers at the *"Corps des Ponts et Chaussées"* in France during the first half of the nineteenth century. Darcy, while director of public works at the city of Dijon, performed a series of research on the flow of water through sand bed filters. From the results of these studies, he developed a law for flow through porous media [31], named Darcy's law. This law simply stated that the superficial velocity of flow is directly related to the pressure gradient through the bed of fine particles by a constant of proportionality that includes both the soil and water properties. This law is widely used for investigating the behavior of water flow through porous media, such as underground flow to wells, flow in soils being irrigated, and flow through earth dams. Flow of oil in underground formations has also been found to follow Darcy's law. Dupuit, another member of the *"Corps des Ponts et Chaussées,"* continued Darcy's work on flow through porous media and published his work in a book on the transportation

and distribution of water [38].

The expression of Darcy's law is obtained by considering water flow through soil as a continuum. In other words, this law averages all the motions of the fluid inside the pores of the soil continuum. Hence, Darcy's law represents an average of the microscopic behavior of flow in the soil continuum. Furthermore, Darcy's law is valid only for a range of slow velocity flows that are usually found in soil (i.e., for flow for which Reynolds number, Re, is smaller than 1). For large Reynolds number flow, the linear relationship given by Darcy's law is no longer valid.

In 1899, Slichter [79] studied geometrical arrangements of spheres in order to reduce the hydraulics of a complex soil to an idealized system. He also made the first attempt to derive the porosity function for beds of uniform spheres, by making the simplifying assumption that the average cross-sectional area for a flow would be triangular. Applying the equivalent of Poiseuille's law for a flow through a tube of triangular section, he obtained Darcy's permeability equation. Unfortunately, Slichter's basic formula proved to be inadequate due to its oversimplification. Nevertheless, his study provided the starting point for many subsequent works.

In parallel to the experimental studies of flow through granular media, theoretical developments on slow flow of fluids have also been accomplished. One of the earliest was performed by Stokes on the resistance of a solid body moving relative to a fluid. For this study, fluid viscosity was taken into account. In 1851, he published a paper [83] in which the so-called linearized form of the general equations of motion of a viscous incompressible fluid, i.e., a time-dependent form of the creeping motion equations, was used to estimate the frictional damping of the motion of a spherical pendulum bob due to air resistance. The resistance to fall of a spherical body was also presented in this paper. The relationship between the drag force and the radius and velocity of a falling sphere that he developed, known as Stokes' law, is still used

in estimating the size distribution of grains in a soil. Stokes' law applies only to situations where the particles are far enough so that the motion of each one is not affected by the motion of its neighbors.

Lorentz [58], following the method developed by Stokes [82], determined the motion of a sphere in the presence of a plane wall. The technique used involved *reflection* of the original motion produced by the body from the surface of the wall and back again. Smoluchowski, a Polish mathematician, employing the same technique of reflection, was able to study the effects of hydrodynamic interaction between two spheres moving in a viscous fluid [80] and the sedimentation of an assembly of spheres [81]. Cunningham [28] studied the sedimentation of a cloud of particles in a closed vessel, employing a *cell model.* His estimate of the decrease in terminal settling velocity due to particle interaction was based on the approximate assumption that each particle moves, on the average, as if it were contained in a rigid spherical envelope of radius equal to half the distance to its nearest neighbors. Many of the early contributions to low Reynolds number hydrodynamics can also be found in Oseen's book [69].

It is also interesting to note that Einstein's doctorate thesis was concerned, among other things, with a new method for determining the size of molecules of chemical substances. In order to accomplish this, he developed a theory for the resistance to shear of a suspension of small spherical particles immersed in a continuous fluid, as a model for large molecules in solution. He showed theoretically that the apparent increase in viscosity of the suspending liquid could be related to the volumetric concentration of solid particles (or solute molecules) by a simple proportionality constant [40]. Einstein's law for suspension viscosity has been used as the basis for almost all theories of the behavior of suspensions in shearing fields of flow. Like Stokes' law, Einstein's law applies to cases where the suspended particles are far

enough apart on the average that their motion is not influenced by mutual interaction of the disturbances produced by individual particles.

Recent developments in flow through porous media have been more varied and more numerous. These developments were motivated by the needs of different scientific communities. The various disciplines that have studied fluid flow through porous media comprise:

- Chemical engineering: In this field, usually interaction of particles is neglected so that the fundamentals of single particle motion apply, and this application refers essentially to dilute systems of particles.

- Civil engineering: Although the infiltration of water and oil through soil has been studied routinely by assuming the validity of Darcy's law, no work has been performed to study the microscopic behavior of flow through an assembly of particles. For dilute systems, such as the transport of sediments, the analyses led to microscopic studies. Saltation, the transport of particles (generally sand) by the wind is also of particular interest.

- Biology: Normal blood is a suspension of flexible particulate matter (red cells, white cells, and platelets) in a continuous medium, the plasma. Therefore, microscopic studies are required for a better understanding of the difference between an idealized man-engineered blood system and a real one.

The above branches are not necessarily the only ones interested in fluid flow through porous media. Other scientific fields, such as mining engineering, physical sciences, and earth sciences have also contributed to the study of this topic.

Although Darcy's law has been used with great success for modelling fluid flow through porous media, its development was made by assuming the medium as a continuum. In other words, Darcy's law provides a macroscopic behavior of fluid flow.

To study the details of an incompressible fluid flow through an aggregate of particles, the equations of motion of the fluid phase can be described by the Navier-Stokes equations.

In the classical theory of fluid mechanics, the Navier-Stokes equations proved to be a major achievement to describe the motion of an isothermal, incompressible fluid with constant density and viscosity. However, owing to its nonlinearity, the solutions of these equations under given boundary conditions are difficult to obtain. Furthermore, due to their generality, the Navier-Stokes equations have proved to be cumbersome in describing fluid flow through porous media. By reducing the Navier-Stokes equations to the so-called creeping motion equations, or Stokes' equations, the equations of motion of fluid flow become linear and are easier to handle. At the fundamental microscale, Stokes' equations provide a complete description of the entire flow field. By performing appropriate volume averages of Stokes' equations, Darcy's law, which was established empirically at the macroscopic level, can be obtained. Therefore, Stokes' equations give an adequate description of the fluid flow at the microscopic level.

In the following, first, the derivation of the Navier-Stokes equations will be presented, however, due to the complexity in solving these equations, they will be simplified by assuming quasi-steady flow and neglecting the inertial term. This then leads to the Stokes' equations.

3.2 The Navier-Stokes Equations

3.2.1 Development of the Navier-Stokes Equations

Assuming *isothermal flow of a homogeneous viscous fluid*, the equation of continuity is obtained from the conservation of mass of a small stationary volume element within

a flowing fluid. In vector form, this equation is given by:

$$\frac{\partial \rho}{\partial t} = -\nabla \cdot (\rho \mathbf{u}) \tag{3.1}$$

where ρ is the local density of the fluid, $\mathbf{u}$ is the local mass average fluid velocity, and $\partial/\partial t$ refers to the time rate of change at a fixed point in the fluid. The quantity $\nabla \cdot (\rho \mathbf{u})$, which is called the divergence of $\rho \mathbf{u}$, expresses the net rate of mass efflux per unit volume. In other words, the continuity equation (equation (3.1)) states that the sum of the rate of change of mass inside a control volume and the net rate of mass efflux through the control volume is zero.

An alternative form of the continuity equation is given by:

$$\frac{D\rho}{Dt} = -\rho \nabla \cdot \mathbf{u} \tag{3.2}$$

where the operator D/Dt, called the *substantial derivative* or Stokes operator, is defined as:

$$\frac{D}{Dt} = \frac{\partial}{\partial t} + \mathbf{u} \cdot \nabla \tag{3.3}$$

This later form of the equation of continuity describes the rate of change of density as measured by an observer moving along with the fluid.

If the fluid is also assumed to have constant density ρ (i.e., incompressible), the continuity equation simply reduces to:

$$\nabla \cdot \mathbf{u} = 0 \tag{3.4}$$

The equation of conservation of linear momentum is obtained by the application of Newton's laws of motion to a differential volume of fluid. These laws may be interpreted as stating that the external force acting on a stationary fluid element is equal to the time rate at which momentum is being created within the element. There are two external forces acting on the fluid element: (a) the surface or contact forces exerted by the fluid stresses acting over the surface of the element and (b) the volume

or body forces exerted on the element (such as gravity). The rate of creation of momentum in the volume is given by the sum of the rate of accumulation or increase of momentum in the volume and the net rate of efflux of momentum out of the volume element through its surface. Hence, the equation of linear momentum is given by:

$$\frac{\partial(\rho \mathbf{u})}{\partial t} + \nabla \cdot (\rho \mathbf{u} \otimes \mathbf{u}) = \nabla \cdot \mathbf{T} + \rho \mathbf{X} \tag{3.5}$$

The left-hand side of equation (3.5) expresses the rate of creation of momentum per unit volume, which is the sum of the rate of increase of momentum per unit volume $(\partial(\rho \mathbf{u})/\partial t)$ and the rate of momentum loss by convection though the surface, per unit volume $(\nabla \cdot (\rho \mathbf{u} \otimes \mathbf{u}))$. The right-hand side of the above equation relates to the external forces per unit volume. The quantity $(\nabla \cdot \mathbf{T})$ gives stresses on the surface per unit volume, whereas $(\rho \mathbf{X})$ are the external body forces on the element per unit volume.

The second rank stress tensor $\mathbf{T}$ is defined according to the usual convention, that is, if $d\mathbf{S}$ is a directed element of surface area, $d\mathbf{S} \cdot \mathbf{T}$ is the contact force exerted by the fluid into which the vector $d\mathbf{S}$ is directed on the fluid on the opposite side of the surface element. If $\mathbf{T}$ is assumed to be symmetric, its nine components, σ_{ij}, are reduced to only six independent ones (i.e., $\sigma_{ij} = \sigma_{ji}$).

The external body force, $\mathbf{X}$, is a force per unit mass. Typically it arises from the action of gravity. For example, if $\mathbf{g}$ is the acceleration of the gravity vector, then $\mathbf{X} = \mathbf{g}$.

Also, in equation (3.5), $\nabla \cdot (\rho \mathbf{u} \otimes \mathbf{u})$ represent a vector due to the *dyadic* product of the velocity vector $\mathbf{u}$ (i.e., $\mathbf{u} \otimes \mathbf{u}$ represent a tensor of rank 2). Similarly, $\nabla \cdot \mathbf{T}$ is also a vector because $\mathbf{T}$ is a tensor.

By combining equations (3.4) and (3.5), and after rearrangement, equation (3.5) becomes:

$$\rho \frac{D\mathbf{u}}{Dt} = \nabla \cdot \mathbf{T} + \rho \mathbf{X} \tag{3.6}$$

Here, the substantial derivative of the velocity vector is defined as:

$$\frac{D\mathbf{u}}{Dt} = \frac{\partial \mathbf{u}}{\partial t} + \mathbf{u} \cdot (\nabla \mathbf{u}) \tag{3.7}$$

Note here that the quantity $\nabla \mathbf{u}$, which represents the gradient of the velocity vector, is a tensor of rank 2.

As expressed in equation (3.6), the left-hand side gives the mass-per-unit volume times the acceleration, whereas the right-hand side represents the sum of the stresses and body forces on the element, per unit volume. In this form, the equation of momentum is referred to a small volume element moving with the fluid and accelerated by forces acting upon it.

Referring to an orthonormal system of axes (x_1, x_2, x_3), equation (3.6) can be written explicitly as:

$$\rho \frac{\partial u_i}{\partial t} + \rho u_k \frac{\partial u_i}{\partial x_k} = \frac{\partial \sigma_{ji}}{\partial x_j} + \rho X_i \tag{3.8}$$

The components of the velocity vector, $\mathbf{u}$, and the body force, $\mathbf{X}$, are respectively (u_1, u_2, u_3) and (X_1, X_2, X_3). Before equation (3.6) can be used to solve problems, suitable expressions for the stresses must be obtained in terms of the velocity field.

Assuming Newtonian fluid, i.e., the stress is proportional to the rate of shearing strain (angular deformation rate). The stresses may be expressed in terms of velocity gradients and fluid properties as follows:

$$\mathbf{T} = -p\mathsf{I} + 2\mu\Delta \tag{3.9}$$

where p is the local thermodynamic pressure, μ is the shear viscosity or *dynamic viscosity*, I the unit tensor (or identity matrix, $[\delta_{jk}]$) and the tensor Δ is defined as:

$$\Delta = \frac{1}{2}[(\nabla \mathbf{u}) + (\nabla \mathbf{u})^t] - \frac{1}{3}(\nabla \cdot \mathbf{u})\mathsf{I} \tag{3.10}$$

Here, $(\nabla \mathbf{u})^t$ represents the transpose of $\nabla \mathbf{u}$. The pressure is given by:

$$p = -\frac{1}{3}\sigma_{ii} \tag{3.11}$$

Substituting the expression of $\mathbf{T}$ from equation(3.9) into equation (3.6), the general equation of motion for an incompressible newtonian fluid is given by:

$$\rho\frac{D\mathbf{u}}{Dt} = -\nabla p+\mu\nabla^2\mathbf{u}+\frac{1}{3}\mu\nabla(\nabla\cdot\mathbf{u})+2(\nabla\mu)\cdot\nabla\mathbf{u}+(\nabla\mu)\times(\nabla\times\mathbf{u})-\frac{2}{3}(\nabla\mu)(\nabla\cdot\mathbf{u})+\rho\mathbf{X} \tag{3.12}$$

This equation, along with the continuity equation and the equation of state $p = p(\rho, T)$ (where T represents the temperature), the density dependence of the dynamic viscosity $\mu = \mu(\rho, T)$ and the boundary and initial conditions, determines completely the pressure, density, and velocity components of a flowing isothermal fluid.

When the gradients of temperature and pressure are small, terms in $\nabla\mu$ may be omitted, i.e., the dynamic viscosity is assumed to be constant.

Finally, for constant density ρ, i.e., incompressible fluids ($\nabla\cdot\mathbf{u} = 0$) and constant dynamic viscosity, equation (3.12) reduces to the so-called Navier-Stokes equations:

$$\rho\frac{D\mathbf{u}}{Dt} = \rho(\frac{\partial\mathbf{u}}{\partial t} + \mathbf{u}\cdot\nabla\mathbf{u}) = -\nabla p + \mu\nabla^2\mathbf{u} + \rho\mathbf{X} \tag{3.13}$$

which were first derived by Navier in 1827 [63] and modified by Stokes in 1845 [82].

Assuming an orthonormal coordinate system, the equations of continuity and motion of an incompressible fluid with constant density and viscosity are given explicitly as:

$$\frac{\partial u_i}{\partial x_i} = 0 \tag{3.14}$$

and

$$\frac{\partial u_i}{\partial t} + u_j\frac{\partial u_i}{\partial x_j} = -\frac{1}{\rho}\frac{\partial p}{\partial x_i} + \nu\nabla^2 u_i + X_i \tag{3.15}$$

where $\nu = \mu/\rho =$ *kinematic viscosity.*

The components of the symmetric stress tensor, $\mathbf{T}$, are given explicitly as:

$$\sigma_{ij} = \sigma_{ji} = -p\delta_{ij} + \mu(\frac{\partial u_i}{\partial x_j} + \frac{\partial u_j}{\partial x_i}) \tag{3.16}$$

Note that in equation (3.16), δ_{ij} represents the Kronecker symbol ($\delta_{ij} = 1$ if $i = j$ and $\delta_{ij} = 0$ if $i \neq j$).

When $\mu = 0$, the Navier-Stokes equations (equation (3.13)) reduce to the well-known *Euler equation* for a frictionless or ideal fluid. In the case of irrotational motion, i.e., $\nabla \times \mathbf{u} = 0$, the equations of *potential flow* is obtained. These form the basis for most of the classical hydrodynamic theory. Because steady potential streaming flows exert no force on stationary solid bodies, the theory is useful mostly for predicting fluid flow patterns at a distance from boundaries.

Due to their nonlinearity, solutions of the Navier-Stokes equations are difficult to obtain both analytically and numerically. Further assumptions are required in order to obtain a simpler form for the equations of motion. This leads to Stokes' equations, which are described in the following.

3.3 The Stokes' Equations

3.3.1 Development of the Stokes' Equations

One common way of simplifying the Navier-Stokes equations is to assume that the flow is *quasi-steady*, i.e., that the dependence on time, $\partial\mathbf{u}/\partial t$, can be neglected. This assumption is acceptable for the range of small velocity found in flow through granular media. This means essentially that for a dynamic problem, the instantaneous drag force acting on an object is a function of the geometry of the problem at that particular instant of time only. Furthermore, the *inertial term*, $\rho\mathbf{u} \cdot \nabla\mathbf{u}$, is assumed to be small compared to the *viscous term*, $\mu\nabla^2\mathbf{u}$, and therefore is omitted from the Navier-Stokes equations. These two assumptions lead to the so-called *creeping motion* or Stokes' equations. Thus for a quasi-steady incompressible isothermal fluid with constant

viscosity, the equations of motion are given by:

$$\nu\nabla^2\mathbf{u} - \frac{1}{\rho}\nabla p + \mathbf{X} = 0 \tag{3.17}$$

$$\nabla \cdot \mathbf{u} = 0 \tag{3.18}$$

By neglecting the inertial term and the time dependence term, the equations of motion have now become linear. If, in a given flow problem, l and U represent respectively the characteristic length and velocity, then the inertial term and viscous term are respectively proportional to $(\rho U^2/l)$ and $(\mu U/l^2)$. Assuming that $\rho\mathbf{u}\cdot\nabla\mathbf{u} \ll \mu\nabla^2\mathbf{u}$ is equivalent to saying that $(\rho U^2/l)/(\mu U/l^2) \ll 1$ or $(\rho U l/\mu) \ll 1$. This last ratio is the Reynolds number. Thus, the smaller the Reynolds number, the better the approximation of the Navier-Stokes equations by equations (3.17) and (3.18). For the type of flow through porous media that are dealt with in this study, the assumption of small Reynolds number ($Re \ll 1$) is appropriate.

3.3.2 Stokes' Paradox

In the case of two-dimensional flow that is studied in this work, it is interesting to note Stokes' paradox, which was pointed out by Stokes himself. He stated that it is impossible to find a steady two-dimensional solution that satisfies equations (3.17) and (3.18) and boundary conditions. Three-dimensional solutions do not have this problem. Stokes' paradox can be illustrated with a dimensional argument: if inertia is negligible, the force, F, acting on a cylinder, placed perpendicular to a two-dimensional streaming motion, and having a radius R must depend only upon free stream velocity U, fluid viscosity μ, and characteristic length R:

$$F = f(U, \mu, R) \tag{3.19}$$

From dimensional analysis, it can be shown that:

$$\frac{F}{\mu U} = constant \tag{3.20}$$

This second equation is quite unrealistic as verified by numerous experiments. It means that the drag force on the cylinder would be independent of the radius R of the cylinder. Thus when the radius of this cylinder approaches zero, the force would not vanish, as it must in reality. It follows that if the inertial term is not negligible, there must always be a density effect in plane creeping motion, i.e.,

$$F = f(\rho, U, \mu, R)$$

or

$$\frac{F}{\mu U} = f(\frac{\rho U R}{\mu}) \tag{3.21}$$

This relation no longer conflicts with physical plausibility, providing that the function vanishes when $(\rho UR/\mu) \rightarrow 0$. Mathematically, Stokes' paradox means that a plane creeping solution will produce a logarithmic singularity at infinity unless inertia terms are accounted for.

Fortunately, two-dimensional solutions of Stokes' equations exist in the case of bounded regions.

3.3.3 Stream Function Formulation of Stokes' Equations

It is sometimes convenient to formulate Stokes' equations in terms of stream functions. This transformation is given as follows.

If the body force is present and if it can be expressed as a gradient of a field, then the body force term can be combined with the pressure term. Thus the equation of motion becomes homogeneous. In the following, the equation of motion is assumed to be homogeneous, that is, the body force term is either simply neglected or combined with the pressure term.

Assuming that $\mathbf{u} = (u_1, u_2)$ defines the velocity in the (x_1, x_2) plane, the vorticity vector is defined as:

$$\mathbf{V} = \frac{1}{2}\nabla \times \mathbf{u} \tag{3.22}$$

In two-dimensions, **V** is a vector perpendicular to the (x_1, x_2) plane. Its coordinate along the axis perpendicular to this plane is given by:

$$\omega = \frac{1}{2}(\frac{\partial u_2}{\partial x_1} - \frac{\partial u_1}{\partial x_2}) \tag{3.23}$$

The equations of motion are given explicitly as:

$$-\frac{1}{\rho}\frac{\partial p}{\partial x_1} + \nu(\frac{\partial^2 u_1}{\partial x_1^2} + \frac{\partial^2 u_1}{\partial x_2^2}) = 0 \tag{3.24}$$

$$-\frac{1}{\rho}\frac{\partial p}{\partial x_2} + \nu(\frac{\partial^2 u_2}{\partial x_1^2} + \frac{\partial^2 u_2}{\partial x_2^2}) = 0 \tag{3.25}$$

Differentiating equation (3.24) with respect to x_2 and equation (3.25) with respect to x_1 and subtracting one from another, yields:

$$\nabla^2 \omega = 0 \tag{3.26}$$

By defining the velocities in terms of stream functions, ψ,

$$\begin{aligned} u_1 &= \frac{\partial \psi}{\partial x_2} \\ u_2 &= -\frac{\partial \psi}{\partial x_1} \end{aligned} \tag{3.27}$$

such that the continuity equation is automatically satisfied, and by substituting these velocities into equation (3.23), we obtain:

$$\nabla^2 \psi = -\omega \tag{3.28}$$

Combining equations (3.28) and (3.26), we finally get:

$$\nabla^4 \psi = 0 \tag{3.29}$$

That is, the stream function, ψ, satisfies the two-dimensional bi-harmonic equation. Although in some instances, this form of the Stokes' equations can be conveniently used, the boundary conditions , especially for the vorticity term, are difficult to define. This form is used for numerical solution of the Stokes flow because it is analogous to the solution of the well-known elastic plate equation.

3.3.4 Relationship between Stokes' Equations and Darcy's Law

The one-dimensional empirical relationship discovered by Darcy has served as the starting point for numerous applications. While the original conditions studied by Darcy are found in many practical situations, it is the extensions to more general cases that are especially deserving of theoretical analysis because they usually represent situations in which experiments are difficult to perform. The extension to three dimensions of Darcy's law would be practical because it covers many types of real groundwater flows or oil recovery processes. While Darcy's law is being used with great frequency for three-dimensional flow, no experimental verification of the obvious tensorial representation of Darcy's empiricism seems to exist. On the other hand, there are many theoretical treatments that lead to this result (cf. Gray and O'Neil [45], and summaries of the subject are also given by Bear [5]). However, in all of these developments, one or several constitutive assumptions were made to obtain the final conclusion. The only exceptions appear in the works of Brenner [9] and Whitaker [97].

In Brenner's work, Stokes flow in a spatially periodic porous medium was analyzed in order to produce Darcy's law for the case in which the volume-averaged velocity is constant. Whitaker's approach, which is also devoid of any constitutive model, considers the momentum balance equation (i.e., equations of motion) of the fluid phase only, regarded as a continuum. Accordingly, he derived the equation of motion for the fluid phase present in the void space of a porous medium by taking an appropriate volume average of the equations of motion of this phase. By assuming that (a) the inertial effects, and (b) the internal friction inside the fluid are negligible in comparison to the drag produced at the fluid-solid interface, Whitaker proved that Darcy's law can be obtained from this process of averaging the Stokes' equations. Whitaker's work presents the following advantage over Brenner's work: (a) spatial

periodicity and (b) homogeneity of the porous media are not required in the analysis.

From these theoretical works, it can be concluded that Darcy's law depicts the macroscopic behavior of the flow whereas Stokes' equations give the details (i.e., microscale) of the fluid flow considered as a continuum.

3.4 Continuum Approach to Fluid Flow in Porous Media

Assuming that Stokes' equations hold for the fluid phase of a porous medium, it becomes clear from these equations that if the velocity is known, the pressure, and therefore the drag force exerted by the fluid, can be obtained. If an assembly of particles, such as the one represented by the Distinct Element Method in the previous chapter, is submerged in a fluid phase, then the drag force acting on each particle can be determined because the velocity of each particle is known. This drag force can be added to the interparticle contact forces resulting from the solid-solid interactions to produce the global forces acting on each particle. This global force is used to determine the new velocity of the particle, which in turn will determine the new boundary conditions for the fluid phase and the creation or breaking of solid-solid contacts. Thus, the simulation of a bi-phase system in which *solid-solid* and *solid-fluid* interactions are considered can be simulated.

The assumptions applying to the fluid phase that lead to this model are listed as follows:

1. Isothermal flow: the flow occurs at constant temperature.

2. Incompressible fluid: the density of the fluid phase is assumed constant.

3. Constant viscosity.

4. Newtonian liquid.

5. Quasi-steady flow: the drag force acting on a particle is only a function of the geometry of the problem at that instant of time. This assumption is valid for the range of low Reynolds number flow studied here.

6. Omission of the inertia term: for low Reynolds number flow ($Re \ll 1$) found in practical underground flow, this assumption is acceptable.

Additional assumptions are required before the complete description of the bi-phase model can be given.

In three dimensions, the fluid phase of an aggregate of polyhedral or spherical shaped particles is a continuum, that is, the fluid phase constitutes a single domain. This is not always the case in two dimensions. As illustrated in Figure 3.1, the fluid phase could be divided into several pockets of fluid trapped in between particles and outer boundary walls. In principle, the velocity at the boundary of each pocket can be easily obtained from the velocity of the particles and walls that form the boundary of that pocket. Therefore each pocket can be treated as separate bodies of fluid to be handled individually. The fluid force acting on a particle is obtained by summing all the contributions from different fluid pockets with which the boundary of the particle is in contact. The problem that arises from this solution method is the delineation of the fluid pockets. Although this delineation can be easily done visually, an algorithm performing this task would be very complicated. This division of the fluid domain into pockets can be completely avoided if we assume that the fluid phase occupies only a single domain. For this, we allow the particle to shrink slightly so that all the fluid pockets become interconnected (see Figure 3.2). The fluid phase can now be visualized as a single domain with multiple holes (i.e., a swiss cheese-like geometry). At the boundary of each hole, particle velocities are prescribed. Under this assumption, the modelling of the fluid phase is far easier than the one with different fluid pockets. This idealization is similar to a three-dimensional model where

the fluid phase is a continuum. However, this model requires the specification of a minimal gap between the particles.

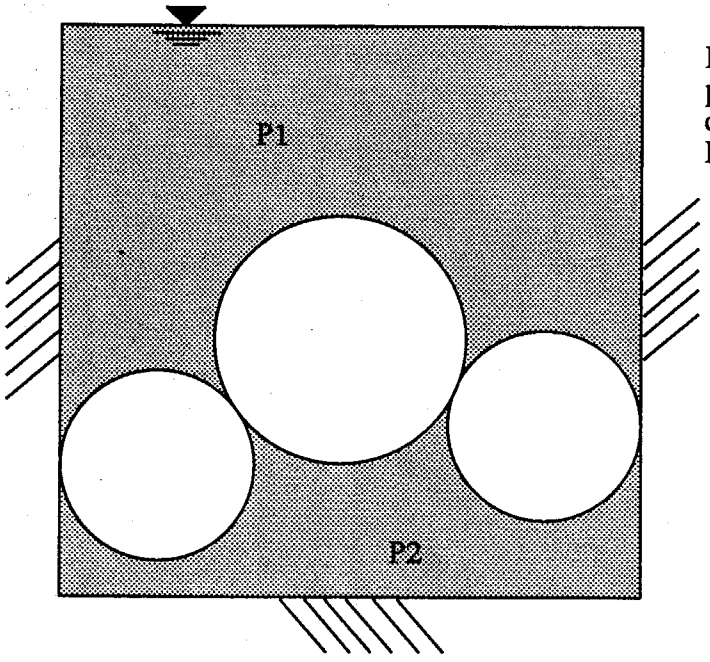

Figure 3.1: Fluid pockets inside a 2D saturated assembly of particles

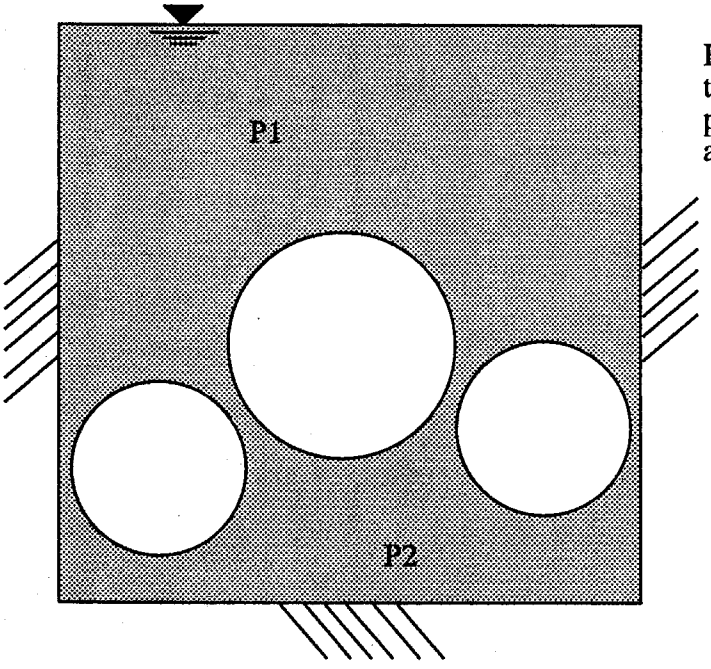

Figure 3.2: Shrinkage of particles to produce a single domain fluid phase

Finally, for the sake of simplicity, all particles are assumed to be completely submerged in the fluid phase (i.e., the study considers a *saturated* granular medium). Thus the capillary effect can be ignored. Furthermore, the outside boundary of the fluid domain can be simply determined because no particles are allowed to cross this boundary.

In summary, the model that will be used to simulate a saturated granular medium consists of:

1. A solid phase with contacting particles.

2. A continuum fluid phase with multiple holes at the location of each particle. To obtain this geometry, the particle size is allowed to shrink enough so that interconnection of fluid pockets that used to be trapped between particles and boundary walls become interconnected. In this case, the fluid is allowed to flow in between the gap. The quantity of fluid flow through this gap is controlled by the gap width. If this width is chosen small enough, the flow could become negligible.

The algorithm used in the computer program NePTune (**Ne**w **P**rogram by **T**an for **u**seful **n**umerical **e**xperiments) obtained by introducing a fluid phase to the DEM algorithm is as follows:

read simulation parameters and initial conditions
for all time t_i steps **do**
    shrink the radius of the particles until all fluid pockets become interconnnected
    solve for the fluid force acting on each particle from known
        velocities of particles and walls
    for each disc α **do**
        assemble the disc contact list, i.e., all objects in contact with α
        for each object of the contact list **do**
            compute outward normal vector
            compute incremental velocities at contact
            compute contact forces and update contact information
        compute accelerations for disc α at time t_i by
            considering contact forces and fluid forces acting on the disc
    for each disc α **do**
        integrate for velocities at time $t_{i+\frac{1}{2}}$
        integrate for displacements and rotations at time t_{i+1}
    update disc information array
    update list of contacts made or broken
    update wall motion and wall information array
end of simulation

From this algorithm we observe that the boundary conditions used for solving the fluid phase are out of phase from that of the solid phase by half a time step. Performed numerical simulations have shown that the error introduced is negligible, especially when the time step required is small.

The numerical treatment of Stokes' equations will be presented in the following chapter. Owing to the complexity of the fluid domain, the boundary element method is used to model the fluid phase.

Chapter 4

NUMERICAL SOLUTIONS OF STOKES' EQUATIONS

In this chapter, the numerical implementation of Stokes' equations is given. The boundary element method [1,8,7] is chosen to model the fluid phase based on its flexibility in discretizing the domain. Three test cases have been included to verify the validity of the numerical formulation.

4.1 Governing Equations of Motion

Recalling from the preceding chapter, the governing equations of motion of a Newtonian, incompressible fluid in a cartesian coordinate system can be summarized as follows:

- Conservation of linear momentum:

$$\sigma_{jk,k} + \rho X_j = 0 \tag{4.1}$$

- Conservation of mass:

$$u_{k,k} = 0 \tag{4.2}$$

- Constitutive equation:

$$\sigma_{jk} = -p\delta_{jk} + 2\mu d_{jk} \tag{4.3}$$

where

$$d_{jk} = \frac{1}{2}(u_{j,k} + u_{k,j}) \tag{4.4}$$

where σ_{jk} is the stress tensor, u_k are the velocity components, ρ is the fluid density, X_j are the body force components per unit mass, p is the pressure, δ_{jk} is the Kronecker symbol, μ is the constant viscosity and d_{jk} is the rate of strain tensor. The tensors σ_{jk} and d_{jk} are both symmetric tensors. The above equations are assumed to be satisfied in a domain Ω, the domain of the problem.

These governing equations must satisfy the following boundary conditions:

$$\begin{aligned} u_j &= \bar{u}_j, \text{ on } \Gamma_1 \\ t_j &= \sigma_{jk} n_k = \bar{t}_j, \text{ on } \Gamma_2 \end{aligned} \tag{4.5}$$

where t_j are the component of the traction vector, n_k are the components of the unit outward vector normal to Γ, $\bar{u}_j$ and $\bar{t}_j$ are the components of the specified velocity and traction vectors on Γ_1 and Γ_2, respectively, and Γ_1 and Γ_2 are parts of the boundary of the domain Ω. Furthermore, it is assumed that $\Gamma_1 \cup \Gamma_2 = \Gamma$, where Γ constitutes the complete boundary of region Ω.

Equations (4.1) - (4.4) and the boundary conditions (equation (4.5)) determine completely the pressure, density, and velocity components of an incompressible viscous flow field.

4.2 Different Approaches for Solving Stokes' Equations

The most common approach used for solving Fluid Mechanics problems is the *finite difference method* [13,71]. Due to the simplicity of formulation, the use of finite differences allows concentration on the particular nature of the flow problem rather than on the numerical tool used for solving it. However, the main difficulty in the use of finite differences lies in the incorporation of the boundary conditions. In the analysis, because the differential equations of equilibrium of the system are approximated directly by the difference scheme, it is necessary in the differencing to satisfy both

the essential and natural boundary conditions. This can be difficult to achieve at arbitrary boundaries, because the topology of the finite difference mesh restricts the form of differencing that can be performed. Also, the matrix formed by this method is not always symmetric and requires lengthy operations for inverting it.

To overcome the difficulties introduced by the finite difference method, the *finite element* approach has been used increasingly in fluid flow analysis. Taylor and Hood [86] presented two approaches for solving the Navier-Stokes equations (i.e., including convection and time-dependence terms). In their first formulation, the velocity and pressure are the physical variables used for solving the problem. Using this approach, the boundary conditions are easily defined because the variables used are directly related to physical variables. In their second formulation, the Navier-Stokes equations are transformed to include the stream function and the vorticity. However, the solution method in this second approach is not straightforward because generally the vorticity is not known on boundary walls, and the specification of boundary conditions on pressure, except for the simplest problems, is practically impossible. Nevertheless, this second approach has also been adopted by Tong and Fung [90] to solve biomechanics problems involving slow particulate viscous flow in channels and tubes.

The numerical implementation of both the finite difference and finite element approaches are relatively straightforward. However, due to their discretization of the physical domain, these solution techniques are not the most convenient ones for modeling the fluid phase in this study. For example, to obtain the solution of a particular problem, the physical domain needs to be discretized into a mesh for the finite difference method or several elements in the case of the finite element method; thus, solving fluid flow through pores of an assembly of particles requires the discretization of a domain with a complicated shape. Furthermore, these techniques

also provide solutions at locations not directly adjacent to a particle (i.e., inside the fluid medium itself), which are not required to obtain the solution of the problem. In fact, what are needed are only the solutions at the periphery of a particle because these completely determine the reaction force of the fluid on the particle. Therefore, knowledge of the solutions at points inside the fluid phase other than those at the periphery of a particle is not necessary. In other words, the motion of a particle is only a function of the inter-particle contact forces (solid-solid interaction) and the *drag* force generated by its motion inside a viscous, incompressible fluid (solid-fluid interaction).

Because solutions are needed only at the boundaries of solid particles, this suggests that the *boundary element method* (**BEM**) [1,8,7] might be the most convenient one to use for solving flow of the fluid phase. The BEM reduces the dimensions of the problem by one through re-formulating the problem in the form of boundary integral equations. This method is well suited for solving the fluid phase problem because the two-dimensional domain occupied by this phase is now reduced to curves along the boundaries of particles and walls. Although the formulation of the BEM is quite straightforward, its implementation is usually complicated because it involves non-singular functions. Furthermore, the matrix that arises from the BEM formulation is non-symmetric and full. To obtain the solution of the problem, this matrix needs to be inverted at each time step and this requires lengthy computations.

Like the finite element method, Stokes' equations can be solved by two different approaches using the BEM. In the first formulation, Stokes' equations are transformed by introducing the stream function. In this case, the bi-harmonic equation (equation (3.34)) is obtained and solved. Bézine and Bonneau [6] presented a formulation based on this approach. They adopted this method because of its similarity to the equations of plate bending problems. Like the finite element method,

the difficulty of this approach lies in the specification of boundary conditions. A second approach using physical variables, i.e., velocity and pressure, was presented by several authors [10,56,91]. This formulation is probably the most useful one because the physical variables used here have direct significance and can be easily specified. The velocity-pressure approach will be the method used for solving the fluid phase flow and its formulation is presented in the following.

4.3 Boundary Integral Formulation

Let $\hat{u}_j$, $\hat{p}$, and $\hat{\sigma}_{ij}$ be a set of arbitrary velocity, pressure, and stress weighting fields (weighting functions). If u_j, p, and σ_{ij} *do not identically satisfy* equations (4.1) and (4.2) in Ω, the following weighted residual statement can be written:

$$\int_\Omega \left[\sigma_{jk,k} + \rho X_j\right] \hat{u}_j d\Omega + \int_\Omega u_{k,k} \hat{p} d\Omega = 0 \tag{4.6}$$

Integrating by parts the term involving $\sigma_{jk,k}$, equation (4.6) becomes:

$$-\int_\Omega \sigma_{jk} \hat{u}_{j,k} d\Omega + \int_\Gamma \sigma_{jk} n_k \hat{u}_j d\Gamma + \int_\Omega \rho X_j \hat{u}_j d\Omega + \int_\Omega u_{k,k} \hat{p} d\Omega = 0 \tag{4.7}$$

From the definition of traction (equation (4.5)), it follows that equation (4.7) can be written as:

$$-\int_\Omega \sigma_{jk} \hat{u}_{j,k} d\Omega + \int_\Gamma t_j \hat{u}_j d\Gamma + \int_\Omega \rho X_j \hat{u}_j d\Omega + \int_\Omega u_{k,k} \hat{p} d\Omega = 0 \tag{4.8}$$

Because $\hat{u}_j$, $\hat{p}$, and $\hat{\sigma}_{ij}$ can be chosen arbitrarily, they can be selected to be Newtonian, incompressible fields, i.e.,

$$\begin{aligned} \hat{u}_{k,k} &= 0 \\ \hat{\sigma}_{i,j} &= -\hat{p}\delta_{ij} + \hat{\mu}\hat{d}_{ij} \\ \hat{d}_{ij} &= \frac{1}{2}(\hat{u}_{i,j} + \hat{u}_{j,i}) \\ \hat{\mu} &= \text{viscosity of the weighting field} \end{aligned} \tag{4.9}$$

From the symmetry of σ_{jk} and $\hat{d}_{jk}$,

$$\int_\Omega \sigma_{jk}\hat{u}_{j,k}d\Omega = \int_\Omega \sigma_{jk}\hat{d}_{jk}d\Omega \tag{4.10}$$

Using the constitutive equation (4.3) and considering the incompressibility of the weighting field, equation (4.10) can be rewritten as:

$$\begin{aligned}\int_\Omega \sigma_{jk}\hat{u}_{j,k}d\Omega &= \int_\Omega \sigma_{jk}\hat{d}jkd\Omega \\ &= -\int_\Omega p\delta_{jk}\hat{d}_{jk}d\Omega + \int_\Omega 2\mu d_{jk}\hat{d}_{jk}d\Omega \\ &= -\int_\Omega p\hat{d}_{kk}d\Omega + \int_\Omega 2\mu d_{jk}\hat{d}_{jk}d\Omega \\ &= \int_\Omega 2\mu d_{jk}\hat{d}_{jk}d\Omega \end{aligned} \tag{4.11}$$

Similarly,

$$\int_\Omega \hat{\sigma}_{jk}u_{j,k}d\Omega = -\int_\Omega \hat{p}\delta_{jk}d_{jk}d\Omega + \int_\Omega 2\hat{\mu}\hat{d}_{jk}d_{jk}d\Omega \tag{4.12}$$

The value of $\hat{\mu}$ is chosen such that:

$$\hat{\mu} = \mu \tag{4.13}$$

Combining equations (4.11) - (4.13) yields:

$$-\int_\Omega \sigma_{jk}\hat{u}_{j,k}d\Omega = -\int_\Omega \hat{\sigma}_{jk}u_{j,k}d\Omega - \int_\Omega u_{k,k}\hat{p}d\Omega \tag{4.14}$$

This last equation is also known as the *reciprocal theorem* for incompressible viscous flow.

Substituting equation (4.14) into equation (4.8), we obtain:

$$-\int_\Omega \hat{\sigma}_{jk}u_{j,k}d\Omega + \int_\Gamma t_j\hat{u}_j d\Gamma + \int_\Omega \rho X_j\hat{u}_j d\Omega = 0 \tag{4.15}$$

Integrating by parts the term involving $\hat{\sigma}_{jk}$ and retaining the other terms give:

$$-\int_\Omega \hat{\sigma}_{jk,k}u_j d\Omega = \rho\int_\Omega X_j\hat{u}_j d\Omega - \int_\Gamma \hat{t}_j u_j d\Gamma + \int_\Gamma t_j\hat{u}_j d\Gamma \tag{4.16}$$

The left-hand side of equation (4.16) can be further reduced by an appropriate choice of the weighting field. This reduction is explained in the two following sections.

4.3.1 Choice of the Fundamental Solutions or Kernels

The weighting field is chosen such that:

$$\hat{\sigma}_{jk,k}(Q) + \Delta(P,Q)\delta_{ij} = 0 \tag{4.17}$$

where $\Delta(P,Q)$ is the Dirac delta function. This function has the following properties:

$$\begin{aligned} \Delta(P,Q) &= 0, \text{ if } P \neq Q \\ \Delta(P,Q) &= \infty, \text{ if } P = Q \\ \int_\Omega f(Q)\Delta(P,Q)d\Omega(Q) &= f(P) \end{aligned} \tag{4.18}$$

The components of velocity and traction of the weighting field at any point of the domain are given by:

$$\begin{aligned} \hat{u}_j(Q) &= \sum_i u^*_{ij}(P,Q) \\ \hat{t}_j(Q) &= \sum_i t^*_{ij}(P,Q) \end{aligned} \tag{4.19}$$

where u^*_{ij} and t^*_{ij} represent respectively the j component of velocity and traction generated at point Q by a unit load at P in the i direction. In other words, the components of the velocity and traction can be visualized as the sum of the individual j components of the velocity and traction generated by unit point loads in two or three directions for two- or three-dimensional space.

In the case of an incompressible fluid flow, the $(.)^*$ field, which is also known as the *fundamental solution* or *kernel*, is given by the so–called Stokeslet [14,47]. In two dimensions, it is defined as follows:

$$u^*_{ij}(P,Q) = \frac{1}{4\pi\mu}\left\{\ln(\frac{1}{r})\delta_{ij} + r_{,i}r_{,j}\right\} \tag{4.20}$$

$$t^*_{ij}(P,Q) = -\frac{1}{\pi r}\left\{\frac{\partial r}{\partial n}r_{,i}r_{,j}\right\} \tag{4.21}$$

where $r = r(P,Q) = \|\vec{PQ}\|$, is the distance between the source point P and the field point Q, and n is the unit outward normal vector. The derivatives are taken with

reference to the coordinates of the field point, Q, i.e.,

$$\begin{aligned} r &= \sqrt{r_i r_i} \\ r_i &= x_i(Q) - x_i(P) \\ r_{,i} &= \frac{\partial r}{\partial x_i(Q)} = \frac{r_i}{r} \end{aligned} \tag{4.22}$$

These fundamental solutions satisfy Stokes' equations in an infinite domain with a unit point source in the i direction at P. With this choice of fundamental solutions, equation (4.16) can be reduced as follows:

4.3.2 Boundary Integral Formulation for a Point Inside the Domain

Given a point P inside the domain Ω, substituting equation (4.17) into (4.16) yields:

$$u_i(P) = \rho \int_\Omega X_j u^*_{ij}(P,Q) d\Omega(Q) - \int_\Gamma t^*_{ij}(P,Q) u_j(Q) d\Gamma(Q) + \int_\Gamma u^*_{ij}(P,Q) t_j(Q) d\Gamma(Q) \tag{4.23}$$

This last equation is similar to Somigliana's identity in solid mechanics.

4.3.3 Boundary Integral Formulation for a Point On the Boundary

If $P \in \Gamma$, equation (4.23) is still valid; however, the second and third terms of the right-hand side of this equation include singular terms (i.e., $u^*_{ij} = f_1(1/r)$ and $t^*_{ij} = f_2(1/r)$; when $P = Q, r = 0$, and thus u^*_{ij} and t^*_{ij} become singular). Assuming that the boundary is smooth at P, we can represent it by a half circle (see Figure 4.1) centered around P and having a radius ϵ. By taking $\epsilon \to 0$, this half circle tends, in the limit, to point P.

In this case, the second term of the right-hand side of equation (4.23) can be written as:

$$\int_\Gamma t^*_{ij} u_j d\Gamma = \lim_{\epsilon \to 0} \left\{ \int_{\Gamma - \Gamma_\epsilon} t^*_{ij} u_j d\Gamma + \int_{\Gamma_\epsilon} t^*_{ij} u_j d\Gamma \right\} \tag{4.24}$$

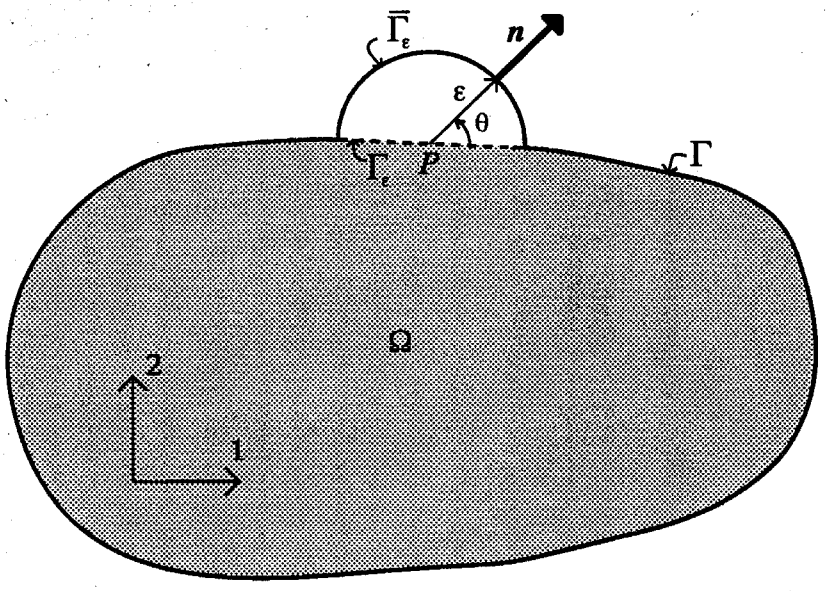

Figure 4.1: Singular point replaced by a half circle

Considering only the $\bar{\Gamma}_\epsilon$ integral, we obtain:

$$\begin{aligned} I_i^t &= \lim_{\epsilon \to 0} \left\{ \int_{\bar{\Gamma}_\epsilon} t_{ij}^* u_j d\Gamma \right\} \\ &= \lim_{\epsilon \to 0} \left\{ \int_{\bar{\Gamma}_\epsilon} -\frac{1}{\pi r} \left[\frac{\partial r}{\partial n} r_{,i} r_{,j} \right] u_j d\Gamma \right\} \end{aligned} \tag{4.25}$$

Along $\bar{\Gamma}_\epsilon$, we have:

$$r \equiv \epsilon$$

$$n_1 = \cos\theta, \quad n_2 = \sin\theta \tag{4.26}$$

$$r_{,1} = \cos\theta, \quad r_{,2} = \sin\theta$$

therefore,

$$\frac{\partial r}{\partial n} = r_{,l} n_l = 1 \tag{4.27}$$

hence,

$$I_i^t = \lim_{\epsilon \to 0} \left\{ \int_{\bar{\Gamma}_\epsilon} \left[-\frac{1}{\pi r} r_{,i} r_{,j} \right] u_j d\Gamma \right\} \tag{4.28}$$

When $i = 1$ for example, using the geometry shown on Figure 4.1, I_1^t becomes:

$$\begin{aligned} I_1^t &= \lim_{\epsilon \to 0} \left[-\frac{1}{\pi r} \int_0^\pi (r_{,1} r_{,1} u_1 + r_{,1} r_{,2} u_2) r d\theta \right] \\ &= \lim_{\epsilon \to 0} \left[-\frac{1}{\pi} \int_0^\pi (\cos^2 \theta u_1 + \cos\theta \sin\theta u_2) d\theta \right] \\ &= -\frac{1}{2} u_1 + 0 u_2 \end{aligned} \tag{4.29}$$

Similarly,

$$I_2^t = 0 u_1 - \frac{1}{2} u_2 \tag{4.30}$$

Finally,

$$\int_\Gamma t_{ij}^* u_j d\Gamma = -\frac{1}{2} \delta_{ik} u_k + \int_\Gamma t_{ij}^* u_j d\Gamma \tag{4.31}$$

It is understood that the second term in the right-hand side of the above equation is defined in the sense of *Cauchy Principal Value.*

Performing the same procedures for the third term of the right-hand side of equation (4.23), we obtain:

$$\int_\Gamma u_{ij}^* t_j d\Gamma = \lim_{\epsilon \to 0} \left\{ \int_{\Gamma - \Gamma_\epsilon} u_{ij}^* t_j d\Gamma + \int_{\bar{\Gamma}_\epsilon} u_{ij}^* t_j d\Gamma \right\} \tag{4.32}$$

Considering only the $\bar{\Gamma}_\epsilon$ integral, we obtain:

$$\begin{aligned} I_i^u &= \lim_{\epsilon \to 0} \left\{ \int_{\Gamma_\epsilon} u_{ij}^* t_j d\Gamma \right\} \\ &= \lim_{\epsilon \to 0} \left\{ \int_{\Gamma_\epsilon} \frac{1}{4\pi\mu} \left[\ln(\frac{1}{r}) \delta_{ij} + r_{,i} r_{,j} \right] t_j d\Gamma \right\} \end{aligned} \tag{4.33}$$

When $i = 1$, for example, I_1^u is given by:

$$\begin{aligned} I_1^u &= \lim_{\epsilon \to 0} \left\{ \epsilon \int_0^\pi \left[\ln(\frac{1}{\epsilon}) t_1 + \cos\theta \sin\theta t_2 + \cos^2\theta t_1 \right] d\theta \right\} \\ &= 0 \end{aligned} \tag{4.34}$$

Similarly,

$$I_2^u = 0 \tag{4.35}$$

The singularity found in the third term of equation (4.23) does not present the strong singularity type encountered in the second term.

Defining,

$$c_{ij}(P) = \frac{1}{2}\delta_{ij}, \tag{4.36}$$

the integral equation for a point on a smooth boundary is given by:

$$\begin{aligned} c_{ij}(P)u_j(P) &= \rho\int_\Omega u^*_{ij}(P,Q)X_j(Q)d\Omega(Q) + \int_\Gamma u^*_{ij}(P,Q)t_j(Q)d\Gamma(Q) \\ &\quad -\int_\Gamma t^*_{ij}(P,Q)u_j(Q)d\Gamma(Q) \end{aligned} \tag{4.37}$$

If the location of point P is not smooth, i.e., P is at a sharp corner of Γ, the tensor $[c_{ij}(P)]$ is given by [46,53]:

$$[c_{ij}(P)] = \frac{1}{4\pi}\begin{bmatrix} 2\theta + (\sin 2\theta_1 - \sin 2\theta_2) & (\cos 2\theta_2 - \cos 2\theta_1) \\ (\cos 2\theta_2 - \cos 2\theta_1) & 2\theta - (\sin 2\theta_1 - \sin 2\theta_2) \end{bmatrix} \tag{4.38}$$

in which the angles θ, θ_1, and θ_2 are shown positively on Figure 4.2.

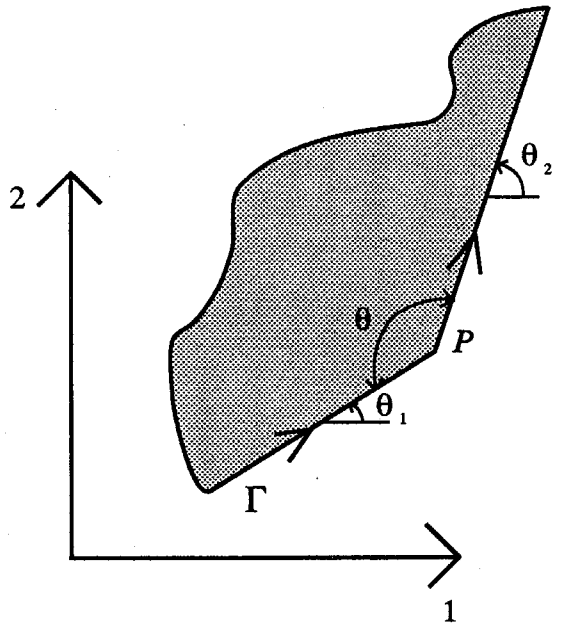

Figure 4.2: Definition of angles used in tensor $[c_{ij}(P)]$

4.3.4 Numerical Implementation of the Boundary Integral

The integral equation (4.26) involves an integration over the domain Ω; therefore the domain must also be discretized. However, if the body force is simply that of gravity, this integral can be handled separately. We are then left with integrals involving only the boundary Γ. The following gives the numerical implementation of the boundary integral equation and the special handling of the body force term.

4.3.4.1 Body Force Term

If the body force consists only of the gravity field (i.e., $\mathbf{X} = \mathbf{g}$), the linearity of Stokes' equations requires the solution to the equation motion to correspond to the *static pressure*. The force generated by the gravity field on an immersed particle is simply the *buoyancy force*, i.e.,

$$\mathbf{B} = -\rho A \mathbf{g} \tag{4.39}$$

where $\mathbf{B}$ is the buoyancy force, and A the area of the particle. This force can be computed explicitly and need not be integrated numerically.

In this case, the boundary integral equation remaining to be solved is reduced to:

$$c_{ij}(P)u_j(P) = \int_\Gamma u^*_{ij}(P,Q)t_j(Q)d\Gamma(Q) - \int_\Gamma t^*_{ij}(P,Q)u_j(Q)d\Gamma(Q) \tag{4.40}$$

4.3.4.2 Vectorial Notation

For the sake of simplicity in the numerical implementation, a vectorial formulation will be used instead of the indicial notation.

Let $\mathbf{x}$, $\mathbf{u}$, and $\mathbf{t}$ be respectively the position, velocity, and traction vectors,

$$\mathbf{x} = \left\{ \begin{array}{c} x_1 \\ x_2 \end{array} \right\}, \ \mathbf{u} = \left\{ \begin{array}{c} u_1 \\ u_2 \end{array} \right\}, \ \mathbf{t} = \left\{ \begin{array}{c} t_1 \\ t_2 \end{array} \right\} \tag{4.41}$$

Also, by defining the following matrices:

$$\mathbf{u}^* = \begin{bmatrix} u^*_{11} & u^*_{12} \\ u^*_{21} & u^*_{22} \end{bmatrix}, \ \mathbf{t}^* = \begin{bmatrix} t^*_{11} & t^*_{12} \\ t^*_{21} & t^*_{22} \end{bmatrix}, \ \mathbf{c}^* = \frac{1}{2}\begin{bmatrix} 1 & 0 \\ 0 & 1 \end{bmatrix} \tag{4.42}$$

the integral equation (4.40) for a point on a smooth boundary is given by:

$$\mathbf{c}(P)\mathbf{u}(P) + \int_\Gamma \mathbf{t}^*(P,Q)\mathbf{u}(Q)d\Gamma(Q) = \int_\Gamma \mathbf{u}^*(P,Q)\mathbf{t}(Q)d\Gamma(Q) \tag{4.43}$$

It is in this form that the integral equation will be implemented numerically.

4.3.4.3 Numerical Implementation Steps

In order to solve the integral equation numerically, the following approach is used:

1. The boundary Γ is discretized into a series of elements over which velocities and tractions are chosen to be piecewise interpolated between the elements' *nodal points.*

2. Equation (4.40) is applied in discretized form to each nodal point P of the boundary Γ and the integrals are computed (usually by a numerical quadrature scheme) over each boundary element. A system of linear equations can then be obtained.

3. Boundary conditions are prescribed that complete the system of linear equations obtained in step 2. This system of equations is solved by standard methods to obtain the unknown boundary values.

4. If solution at a point inside the domain is required, equation (4.23) is used where the integrals are evaluated numerically.

4.3.4.4 Discretization of the Boundary

The boundary Γ is divided into N_e segments or *boundary elements* as shown on Figure 4.3. Several types of elements are used in the BEM, the most common ones

being the *constant, linear*, and *quadratic* elements. For the constant element, the only node of each element is located at the middle of the element. Because each element has only one node, there can be no variation of variables along an element. In other words, the value of each variable is constant throughout the element. For a linear element, each element contains two nodes and variables are assumed to vary linearly between the nodal values. The quadratic element consists of three nodal points per element; therefore, variables along each element are obtained by using quadratic interpolation functions. The choice of the type of element to be used depends on the type of problem to be solved. However, it is quite obvious that the higher the order of the element used, the more accurate the solution can be obtained because higher order elements allow more flexible interpolation of the element variables. On the other hand, the higher the order of the element, the greater the memory storage and the larger the computation time. The numerical implementation used to model the fluid flow in this work will be based on the *linear element.* Also, the so-called *discontinuous* element will be used (see Figure 4.3(c)). The choice of this type of element will be discussed later.

The interpolation functions used in the BEM are identical to those used in the finite element method. The value of a variable along an element, Γ_k, is expressed as a function of the nodal values, i.e.,

$$\mathbf{u} = \mathbf{N}\mathbf{u}_k,\ \mathbf{t} = \mathbf{N}\mathbf{t}_k,\ \mathbf{x} = \mathbf{N}\mathbf{x}_k, \tag{4.44}$$

$$\mathbf{N} = \begin{bmatrix} N_1 & 0 & N_2 & 0 \\ 0 & N_1 & 0 & N_2 \end{bmatrix}, \tag{4.45}$$

$$\mathbf{x}_k = \begin{Bmatrix} x_1(P_1) \\ x_2(P_1) \\ x_1(P_2) \\ x_2(P_2) \end{Bmatrix},\ \mathbf{u}_k = \begin{Bmatrix} u_1(P_1) \\ u_2(P_1) \\ u_1(P_2) \\ u_2(P_2) \end{Bmatrix},\ \mathbf{t}_k = \begin{Bmatrix} t_1(P_1) \\ t_2(P_1) \\ t_1(P_2) \\ t_2(P_2) \end{Bmatrix}, \tag{4.46}$$

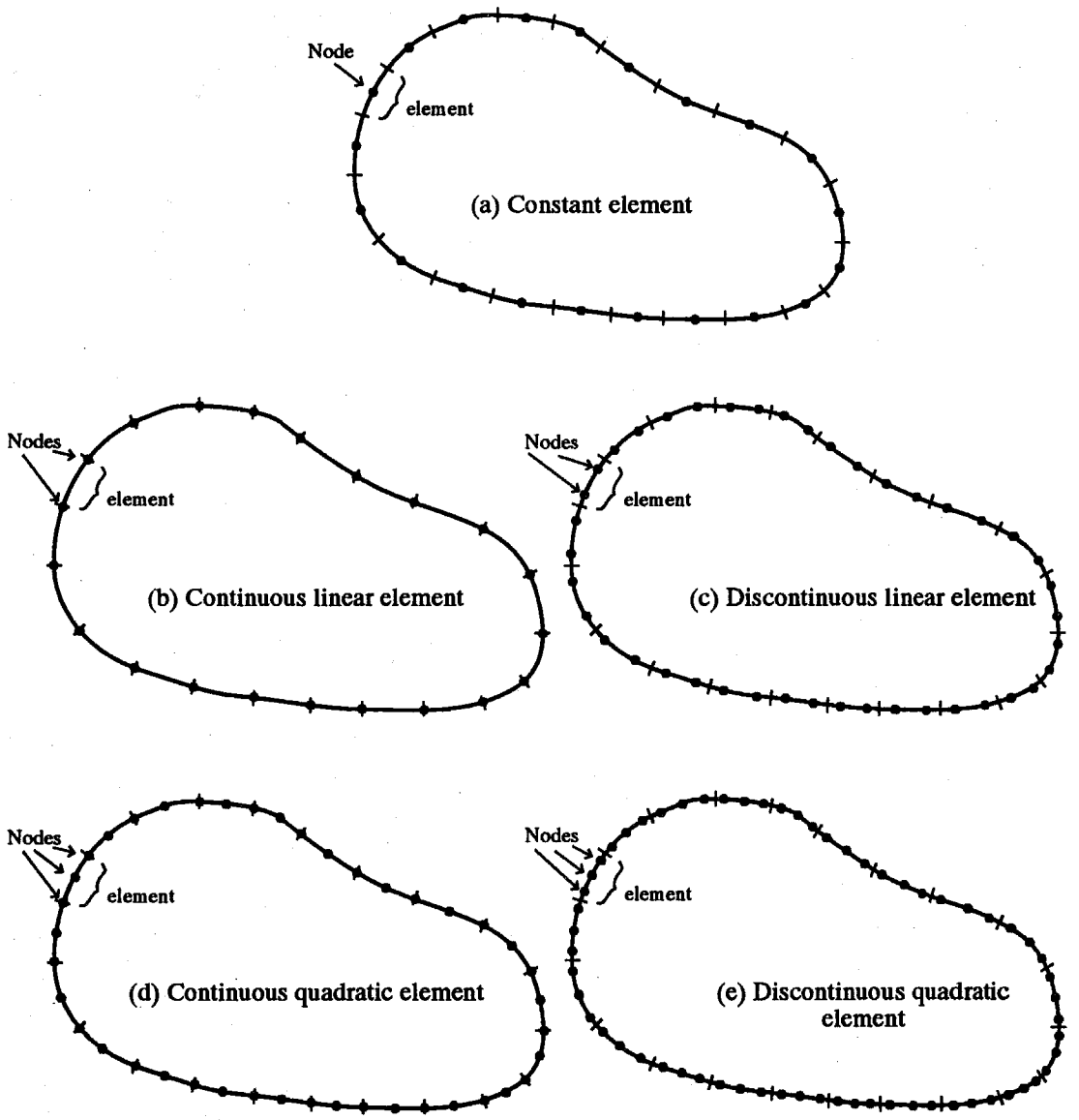

Figure 4.3: Boundary Discretization

and P_1 and P_2 are the nodal points of element Γ_k.

For the continuous linear element, the interpolation functions are functions of the homogeneous coordinate η and are given by:

$$\begin{aligned} N_1 &= \frac{1}{2}(1-\eta) \\ N_2 &= \frac{1}{2}(1+\eta) \end{aligned} \tag{4.47}$$

The interpolation functions of the discontinuous linear element are:

$$\begin{aligned} N_1 &= (\frac{1}{2}-\eta) \\ N_2 &= (\frac{1}{2}+\eta) \end{aligned} \tag{4.48}$$

Figure 4.4 shows the interpolation functions for each type of linear element.

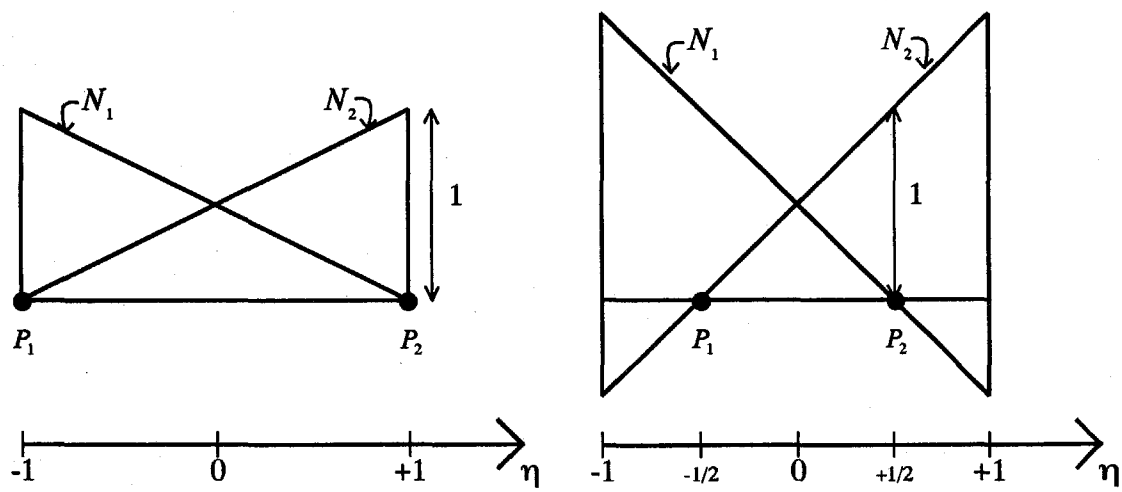

(a) Continuous linear element (b) Discontinuous linear element

Figure 4.4: Interpolation functions for linear elements

Substituting equation (4.44) into equation (4.43) and assuming that nodal point P corresponds to node number i, we obtain:

$$\mathbf{c}_i\mathbf{u}_i + \sum_{k=1}^{N_e}\left\{\int_{\Gamma_k}\mathbf{t}^*\mathbf{N}d\Gamma\right\}\mathbf{u}_k = \sum_{k=1}^{N_e}\left\{\int_{\Gamma_k}\mathbf{u}^*\mathbf{N}d\Gamma\right\}\mathbf{t}_k \tag{4.49}$$

Let:

$$\mathbf{H}^*_{ik} = \int_{\Gamma_k} \mathbf{t}^* \mathbf{N} d\Gamma, \ \mathbf{G}^*_{ik} = \int_{\Gamma_k} \mathbf{u}^* \mathbf{N} d\Gamma \tag{4.50}$$

we then define:

$$\hat{\mathbf{H}}_{ik} = \mathbf{H}^*_{ik} + \mathbf{c}_i \delta_{ik}, \ \hat{\mathbf{G}}_{ik} = \mathbf{G}^*_{ik}, \tag{4.51}$$

and equation (4.49) can now be written as:

$$\sum_{k=1}^{Ne} \hat{\mathbf{H}}_{ik} \mathbf{u}_k = \sum_{k=1}^{Ne} \hat{\mathbf{G}}_{ik} \mathbf{t}_k \tag{4.52}$$

Selecting each node alternately as the source point, a system of linear equations can be formed:

$$[H]\,\mathbf{U} = [G]\,\mathbf{T} \tag{4.53}$$

where $[H]$ and $[G]$ are obtained by assembling each of the individual $\hat{\mathbf{H}}_{ij}$ and $\hat{\mathbf{G}}_{ij}$ submatrices. $[H]$ and $[G]$ each has dimension $2N_n \times 2N_n$ where N_n is the total number of nodal points. Vectors $\mathbf{U}$ and $\mathbf{T}$ are defined as follows:

$$\mathbf{U} = \begin{Bmatrix} u_1(P_1) \\ u_2(P_1) \\ \vdots \\ u_1(P_{N_n}) \\ u_2(P_{N_n}) \end{Bmatrix}, \ \mathbf{T} = \begin{Bmatrix} t_1(P_1) \\ t_2(P_1) \\ \vdots \\ t_1(P_{N_n}) \\ t_2(P_{N_n}) \end{Bmatrix}, \tag{4.54}$$

with P_1 to P_{N_n} the nodal points.

If the boundary conditions are applied, the system of equations (equation (4.53)) can be ordered as follows:

$$[A]\,\mathbf{Y} = \mathbf{R} \tag{4.55}$$

where $[A]$ contains all the coefficients of $[H]$ and $[G]$ related to unknown variables, $\mathbf{Y}$ is the vector consisting of all the unknown variables, and $\mathbf{R}$ is the vector formed by the product of the coefficients of $[H]$ and $[G]$ and the known variables.

4.3.4.5 Traction Discontinuities at Corner Points

If the velocities are defined at a node located on a sharp corner (see Figure 4.5), and the tractions are unknown both before and after the node, then this situation gives rise to the so–called *traction discontinuity problem.* In this case, the two sets of tractions before and after the node are not necessarily identical, and there is a jump or discontinuity in the traction field. If only one node is assigned at the sharp corner, equation (4.52) involves both of these two sets of tractions. In other words, we can only form two equations involving four unknowns. Therefore, another set of 2 equations is needed for solving the problem. If two sets of tractions are specified and the velocities are unknown, the system of equations is complete with only one node at the corner (i.e., the two required extra conditions simply consist of identical velocities at the intersection of the two elements).

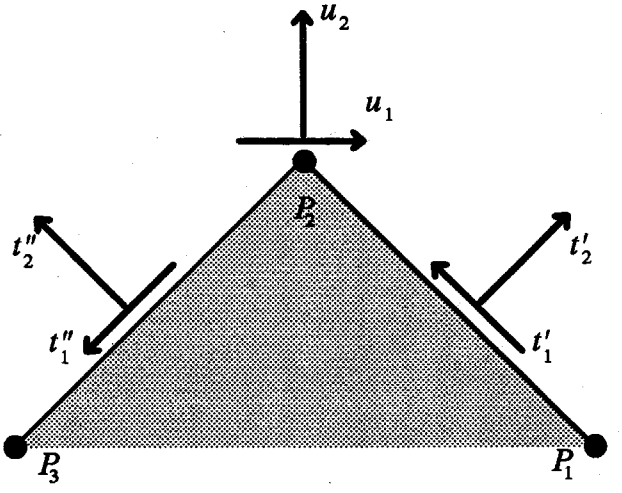

Figure 4.5: Corner node with traction discontinuities

Several methods exist for handling this problem [7, pp.165–167]. The different possibilities are:

1. Corner with gap: in this method, two separate nodes are used at each sharp corner. Each node is assigned only a set of two traction components (cf. Figure 4.6(a)). A gap is left in between the two nodes. The length of this gap must

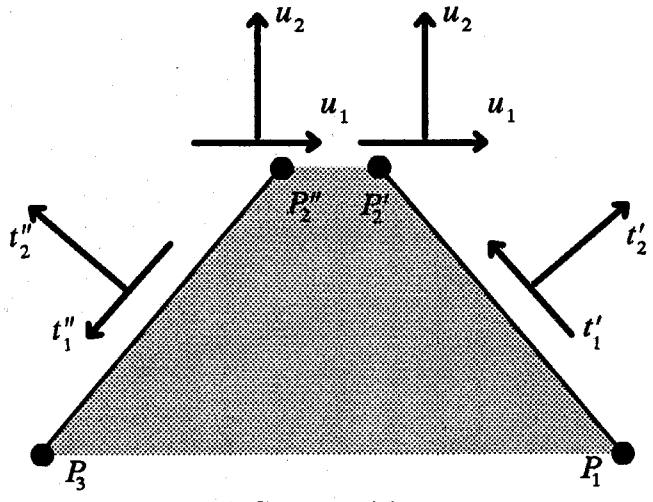

(a) Corner with gap

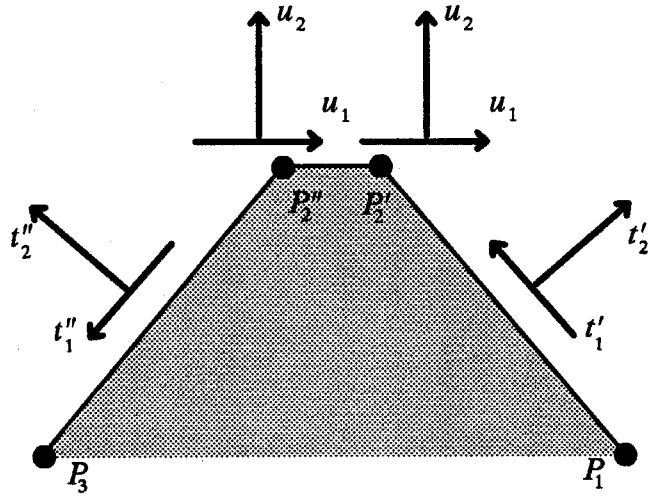

(b) Corner with small element

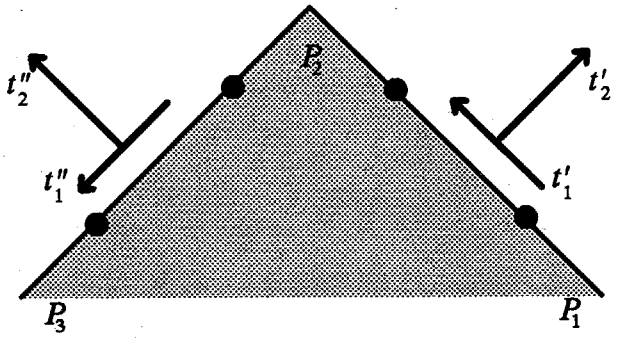

(c) Discontinuous element

Figure 4.6: Treatment of corner node with traction discontinuities

be small enough to limit the error introduced. However, a too small gap could cause numerical instabilities because the coefficients of the two sets of generated equations are very close to each other.

2. Corner with small element: this second method is conceptually the same as the first one. The only difference is that the small element instead of a gap is inserted between the nodes. The disadvantages of this method are the same as in the previous method.

3. Discontinuous element: probably the most general approach to this type of problem is obtained by using discontinuous elements. The deficiency of the boundary element method to handle the traction discontinuities arises from the insistence of locating the nodal points at the end of each element, i.e., by forcing the continuity of the tractions across elements. If we allow the tractions to be discontinued, i.e., if we move the nodal points inside the elements, this problem does not occur. As a matter of fact, the constant element is nothing more than the most simple type of discontinuous element. Here, variables are constant within the element and no continuity is assured across elements. Higher order elements presenting discontinuities are obtained by defining two or more nodal points per element. However, because the interpolating points are no longer located at the end of each element, the interpolating functions have to be modified slightly to reflect this change (cf. equation (4.48)). The main disadvantage of the discontinuous elements comes from the higher number of nodal points used in a problem when compared to the one having the same number of elements but using continuous elements.

Due to the generality of the formulation using discontinuous elements, they will be used in the numerical implementation of the fluid phase.

4.3.4.6 Numerical Integration for Source Points Not on the Field Element

When the source point, P, is not located on the field element, i.e., $P \notin \Gamma_k$, conventional Gauss quadrature can be used to integrate each term of the submatrices $\mathbf{H}^*_{ik}$ and $\mathbf{G}^*_{ik}$. Because the interpolation functions are expressed in term of the heterogeneous coordinate, η, it is necessary to transform the element of surface $d\Gamma$ from the local cartesian system to this intrinsic system of coordinates. This is performed through the following relation:

$$d\Gamma = |J|\, d\eta \tag{4.56}$$

where the Jacobian of the transformation is given by:

$$|J| = \sqrt{(\frac{dx_1}{d\eta})^2 + (\frac{dx_2}{d\eta})^2} \tag{4.57}$$

Hence, using a Gauss quadrature, we obtain:

$$\begin{aligned} I_k(u_{ij}) &= \int_{\Gamma_k} u^*_{ij}\mathbf{N}\, d\Gamma \\ &= \int_{-1}^{+1} u^*_{ij}\mathbf{N}\,|J|\, d\eta \\ &\simeq \sum_{l=1}^{N_g} |J|_l w_l \left\{u^*_{ij}\mathbf{N}\right\}_l \end{aligned} \tag{4.58}$$

$$\begin{aligned} I_k(t_{ij}) &= \int_{\Gamma_k} u^*_{ij}\mathbf{N}\, d\Gamma \\ &= \int_{-1}^{+1} t^*_{ij}\mathbf{N}\,|J|\, d\eta \\ &\simeq \sum_{l=1}^{N_g} |J|_l w_l \left\{t^*_{ij}\mathbf{N}\right\}_l \end{aligned} \tag{4.59}$$

where N_g is the number of Gauss quadrature points and w_l the weighting factor [84]. The choice of the number of quadrature points is based on the following parameter:

$$\varrho = \frac{r_{min}}{L} \tag{4.60}$$

where r_{min} is the distance from the source point to the field element, and L the length of the field element. Based on the value of ϱ, N_g is selected according to the rule shown on Table 4.1.

According to this table, the closer the source point is to the field element, the larger the number of quadrature points is to be used.

ϱ	N_g
$200 < \varrho$	1
$20 < \varrho \leq 200$	2
$2 < \varrho \leq 20$	4
$0.1 < \varrho \leq 2$	16
$\varrho \leq 0.1$	32

Table 4.1: Rule for selecting N_g, the number of Gauss quadrature points

4.3.4.7 Numerical Integration for Source Points on the Field Element

When $P \in \Gamma_k$, a special treatment is required in order to handle the singularities found in the integrands (i.e., the kernel functions). The integrations of the velocity and traction kernels are performed as follows:

1. Velocity Kernel

   Let:

$$\begin{aligned} I_k(u_{ij}) &= \int_{\Gamma_k} u^*_{ij}\mathbf{N}\,d\Gamma = \int_{-1}^{+1} u^*_{ij}\mathbf{N}\,|J|\,d\eta \\ &= \int_{-1}^{+1} \frac{1}{4\pi\mu}\left\{\ln(\frac{1}{r})\delta_{ij} + r_{,i}r_{,j}\right\}\mathbf{N}\,|J|\,d\eta \\ &= \int_{-1}^{\eta_s} \frac{1}{4\pi\mu}\left\{\ln(\frac{1}{r})\delta_{ij} + r_{,i}r_{,j}\right\}\mathbf{N}\,|J|\,d\eta \\ &\quad + \int_{\eta_s}^{+1} \frac{1}{4\pi\mu}\left\{\ln(\frac{1}{r})\delta_{ij} + r_{,i}r_{,j}\right\}\mathbf{N}\,|J|\,d\eta \\ &= I^1_k(u_{ij}) + I^2_k(u_{ij}) \end{aligned} \tag{4.61}$$

   where η_s is the homogeneous coordinate of the singular point.

   We define:

$$\xi = -\frac{\eta - \eta_s}{\eta_s + 1} \tag{4.62}$$

   Hence,

$$\eta = \eta_s - (1 + \eta_s)\xi,\ d\eta = -(1 + \eta_s)d\xi \tag{4.63}$$

Performing this change of variable, $I_k^1(u_{ij})$ becomes:

$$I_k^1(u_{ij}) = \int_0^1 \frac{1}{4\pi\mu}\left\{\ln(\frac{1}{r})\delta_{ij} + r_{,i}r_{,j}\right\}\mathbf{N}\,|J|\,(1+\eta_s)d\xi \tag{4.64}$$

Next, we split $I_k^1(u_{ij})$ into two parts:

$$I_k^1(u_{ij}) = I_k^3(u_{ij}) + I_k^4(u_{ij}) \tag{4.65}$$

where,

$$I_k^3(u_{ij}) = \int_0^1 \frac{1}{4\pi\mu}\left\{\ln(\frac{\xi}{r})\delta_{ij} + r_{,i}r_{,j}\right\}\mathbf{N}\,|J|\,(1+\eta_s)d\xi \tag{4.66}$$

$$I_k^4(u_{ij}) = \int_0^1 \frac{1}{4\pi\mu}\left\{\ln(\frac{1}{\xi})\delta_{ij}\right\}\mathbf{N}\,|J|\,(1+\eta_s)d\xi \tag{4.67}$$

Each term of $I_k^3(u_{ij})$ is smooth and well behaved, in particular, the term involving $\ln(\frac{\xi}{r})$ because $r \to 0$ when $\xi \to 0$. Therefore, $I_k^3(u_{ij})$ can be evaluated using standard Gauss quadrature. However, we first need to perform another change of variable:

$$\gamma = 2\xi - 1 \tag{4.68}$$

then:

$$\begin{aligned} I_k^3(u_{ij}) &= \int_{-1}^{+1} \frac{1}{4\pi\mu}\left\{\ln(\frac{\xi}{r})\delta_{ij} + r_{,i}r_{,j}\right\}\mathbf{N}\,|J|\,\frac{(1+\eta_s)}{2}d\gamma \\ &= \sum_{l=1}^{N_g} \frac{1}{4\pi\mu} w_l \left\{\left[\ln(\frac{\xi}{r})\delta_{ij} + r_{,i}r_{,j}\right]\mathbf{N}\,|J|\right\}_l \frac{(1+\eta_s)}{2} \end{aligned} \tag{4.69}$$

Similarly, $I_k^4(u_{ij})$ can be evaluated numerically using a suitable logarithmic quadrature [84], i.e.,

$$\begin{aligned} I_k^4(u_{ij}) &= \int_0^1 \frac{1}{4\pi\mu}\ln(\frac{1}{\xi})\delta_{ij}\mathbf{N}\,|J|\,(1+\eta_s)d\xi \\ &= \sum_{l=1}^{N_g'} \frac{1}{4\pi\mu} w_l' \left\{\delta_{ij}\mathbf{N}\,|J|\right\}_l (1+\eta_s) \end{aligned} \tag{4.70}$$

Likewise, the integration of $I_k^2(u_{ij})$ is obtained by first performing the following change of variable:

$$\zeta = \frac{\eta - \eta_s}{1 - \eta_s} \tag{4.71}$$

Following the same procedure as explained above, we obtain:

$$I_k^2(u_{ij}) = I_k^5(u_{ij}) + I_k^6(u_{ij}) \tag{4.72}$$

where,

$$I_k^5(u_{ij}) = \sum_{l=1}^{N_g} \frac{1}{4\pi\mu} w_l \left\{ \frac{1}{4\pi\mu} \left[\ln(\frac{\xi}{r})\delta_{ij} + r_{,i}r_{,j} \right] \mathbf{N}|J| \right\}_l \frac{(1-\eta_s)}{2} \tag{4.73}$$

$$I_k^6(u_{ij}) = \sum_{l=1}^{N_g'} \frac{1}{4\pi\mu} w_l' \{\delta_{ij}\mathbf{N}|J|\}_l (1-\eta_s) \tag{4.74}$$

In summary, we have:

$$I_k(u_{ij}) = I_k^3(u_{ij}) + I_k^4(u_{ij}) + I_k^5(u_{ij}) + I_k^6(u_{ij}) \tag{4.75}$$

where,

$$I_k^3(u_{ij}) = \sum_{l=1}^{N_g} \frac{1}{4\pi\mu} w_l \left\{ \frac{1}{4\pi\mu} \left[\ln(\frac{\xi}{r})\delta_{ij} + r_{,i}r_{,j} \right] \mathbf{N}|J| \right\}_l \frac{(1+\eta_s)}{2} \tag{4.76}$$

$$I_k^4(u_{ij}) = \sum_{l=1}^{N_g'} \frac{1}{4\pi\mu} w_l' \{\delta_{ij}\mathbf{N}|J|\}_l (1+\eta_s) \tag{4.77}$$

$$I_k^5(u_{ij}) = \sum_{l=1}^{N_g} \frac{1}{4\pi\mu} w_l \left\{ \frac{1}{4\pi\mu} \left[\ln(\frac{\xi}{r})\delta_{ij} + r_{,i}r_{,j} \right] \mathbf{N}|J| \right\}_l \frac{(1-\eta_s)}{2} \tag{4.78}$$

$$I_k^6(u_{ij}) = \sum_{l=1}^{N_g'} \frac{1}{4\pi\mu} w_l' \{\delta_{ij}\mathbf{N}|J|\}_l (1-\eta_s) \tag{4.79}$$

2. Traction Kernel

Let:

$$\begin{aligned} I_k(t_{ij}) &= \int_{\Gamma_k} t^*_{ij}\mathbf{N}\,d\Gamma \\ &= \int_{-1}^{+1} t^*_{ij}\mathbf{N}\,|J|\,d\eta \\ &= \int_{-1}^{+1} -\frac{1}{\pi r}\left\{r_{,m}n_{,m}r_{,i}r_{,j}\right\}\mathbf{N}\,|J|\,d\eta \\ &= \int_{-1}^{\eta_s} -\frac{1}{\pi r}\left\{r_{,m}n_{,m}r_{,i}r_{,j}\right\}\mathbf{N}\,|J|\,d\eta \\ &\quad + \int_{\eta_s}^{+1} -\frac{1}{\pi r}\left\{r_{,m}n_{,m}r_{,i}r_{,j}\right\}\mathbf{N}\,|J|\,d\eta \\ &= I^1_k(t_{ij}) + I^2_k(t_{ij}) \end{aligned} \tag{4.80}$$

Because $r_{,m}n_m \rightarrow 0$ as $t \rightarrow 0$, then $(r_{,m}n_m/r)$ is smooth and well behaved and therefore can be integrated numerically using standard Gauss quadrature. Performing the same transformations as those used for the velocity kernels, we obtain:

$$I^1_k(t_{ij}) = \sum_{l=1}^{N_g} -\frac{1}{\pi}w_l\left\{\frac{r_{,m}n_m}{r}r_{,i}r_{,j}\mathbf{N}\,|J|\,\frac{1+\eta_s}{2}\right\}_l \tag{4.81}$$

$$I^2_k(t_{ij}) = \sum_{l=1}^{N_g} -\frac{1}{\pi}w_l\left\{\frac{r_{,m}n_m}{r}r_{,i}r_{,j}\mathbf{N}\,|J|\,\frac{1-\eta_s}{2}\right\}_l \tag{4.82}$$

4.3.5 Comparison with Plane Strain Elastostatic Problems

If we consider the two-dimensional plane strain elastostatic problem, the equations of motion are given by:

$$\sigma_{jk,k} + b_j = 0 \tag{4.83}$$

where σ_{jk} are the components of the stress tensor and b_j is the body force per unit volume. The constitutive model in this case is:

$$\sigma_{jk} = \frac{2\mu'\nu'}{1-2\nu'}\delta_{jk}u_{l,l} + 2\mu' d_{jk} \tag{4.84}$$

where u_l are the components of the displacement vector, μ' is the shear modulus, ν' is the Poisson's ratio, and

$$d_{jk} = \frac{1}{2}(u_{j,k} + u_{k,j}) \tag{4.85}$$

If we solve this problem using the BEM, the fundamental solutions or kernels are given by:

$$u^*_{ij} = \frac{1}{8\pi(1-\nu')}\left[(3 - 4\nu'\ln(\frac{1}{r})\delta_{ij} + r_{,i}r_{,j}\right] \tag{4.86}$$

$$t^*_{ij} = -\frac{1}{4\pi(1-\nu')r}\left\{\frac{\partial r}{\partial n}\left[(1-2\nu')\delta_{ij} + 2r_{,i}r_{,j}\right] + (1-2\nu')(n_i r_{,j} + n_j r_{,i})\right\} \tag{4.87}$$

If we select ν' to have a value of $1/2$ (i.e., incompressible), the fundamental solutions reduce to those of the incompressible, viscous fluid.

For a point inside the domain Ω, the displacements are given by:

$$u_i(P) = \int_\Omega b_j u^*_{ij}(P,Q)d\Omega(Q) - \int_\Gamma t^*_{ij}(P,Q)u_j(Q)d\Gamma(Q) + \int_\Gamma u^*_{ij}(P,Q)t_j(Q)d\Gamma(Q) \tag{4.88}$$

Substituting equation (4.88) into the constitutive equation (4.84), we finally obtain:

$$\sigma_{ij} = \int_\Gamma D_{kij}t_k d\Gamma - \int_\Gamma S_{kij}u_k d\Gamma + \int_\Omega D_{kij}b_k d\Omega \tag{4.89}$$

where,

$$D_{kij} = \frac{1}{4\pi(1-\nu')r}\left\{(1-2\nu')\left[\delta_{ki}r_{,j} + \delta_{kj}r_{,i} - \delta_{ij}r_{,k}\right] + 2r_{,i}r_{,j}r_{,k}\right\} \tag{4.90}$$

$$\begin{aligned} S_{kij} = \frac{\mu'}{2\pi(1-\nu')r^2}\Bigg\{ & 2\frac{\partial r}{\partial n}\left[(1-2\nu')\delta_{ij}r_{,k} + \nu'(\delta_{ik}r_{,j} + \delta_{jk}r_{,i} - 4r_{,i}r_{,j}r_{,k})\right] \\ & +2\nu'(n_i r_{,j}r_{,k} + n_j r_{,i}r_{,k}) + (1-2\nu')(2n_k r_{,j}r_{,k} + n_j\delta_{ik} + n_i\delta_{jk}) \\ & -(1-4\nu')n_k\delta_{ij}\Bigg\} \end{aligned} \tag{4.91}$$

It should be noted that when $\nu' = 1/2$ (i.e., incompressible), equation (4.84) is not defined; however, stresses inside the domain can still be computed using equation (4.89) because the expressions of D_{kij} and S_{kij} are perfectly well defined for this value of ν'.

4.3.6 Results for Internal Points

Once the values of the velocities and tractions are known on the boundary, the values of the velocities and stresses at any interior point can be computed. The velocities are given by equation (4.23), which in discretized form is:

$$\mathbf{u}(P) = \sum_{k=1}^{N_e} \left\{ \int_{\Gamma_k} \mathbf{u}^* d\Gamma \right\} \mathbf{t}_k - \sum_{k=1}^{N_e} \left\{ \int_{\Gamma_k} \mathbf{t}^* d\Gamma \right\} \mathbf{u}_k + \sum_{k=1}^{M_e} \left\{ \rho \int_{\Omega_k} \mathbf{u}^* \mathbf{X} d\Omega \right\} \tag{4.92}$$

where M_e is the total number of subdivisions of the domain Ω. The right-hand side terms of this equation can be integrated numerically as explained in section 4.3.4.6.

The stresses at a point inside the domain are given in the same manner as those used for solid mechanics, i.e.,

$$\sigma_{ij} = \int_\Gamma D_{kij} t_k d\Gamma - \int_\Gamma S_{kij} u_k d\Gamma + \int_\Omega D_{kij} b_k d\Omega \tag{4.93}$$

where,

$$D_{kij} = \frac{1}{\pi r} r_{,i} r_{,j} r_{,k} \tag{4.94}$$

$$S_{kij} = \frac{\mu}{\pi r^2} \left\{ \frac{\partial r}{\partial n} (\delta_{ik} r_{,j} + \delta_{jk} r_{,i} - 4 r_{,i} r_{,j} r_{,k}) + (n_i r_{,j} r_{,k} + n_j r_{,i} r_{,k}) + n_k \delta_{ij} \right\} \tag{4.95}$$

When the stresses and velocities are known, the pressure can be computed as follows using the constitutive equations (4.3) and (4.4):

$$\begin{aligned} p &= -\sigma_{11} + 2\mu d_{11} \\ p &= -\sigma_{22} + 2\mu d_{22} \end{aligned} \tag{4.96}$$

4.3.7 Velocities and Stresses along the Boundary

If we consider an element along the boundary according to its local coordinate system as shown on Figure 4.7, the component of the strain tensor along the element axis is easily evaluated as:

$$\epsilon_{11} = u_{1,1} = \frac{2}{L} [u_1(P_2) - u_1(P_1)] \tag{4.97}$$

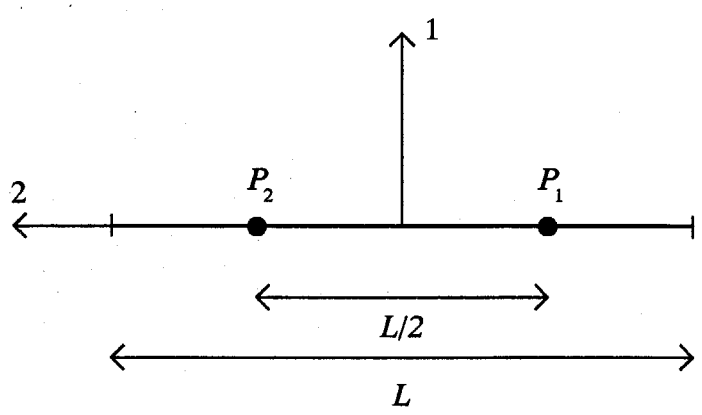

Figure 4.7: Local coordinate system for discontinuous linear element

Using equation (4.44), the tractions can be computed at any point along the element. By using the local coordinate system defined above, the stresses at a point on the boundary element are given by:

$$\sigma_{11} = t_1 \tag{4.98}$$

$$\sigma_{12} = t_2 \tag{4.99}$$

From the equation of conservation of mass (equation (4.2)), we have

$$u_{1,1} + u_{2,2} = \epsilon_{11} + \epsilon_{22} = 0 \tag{4.100}$$

which yields:

$$\epsilon_{22} = -\epsilon_{11} \tag{4.101}$$

Using the constitutive equation (4.3), the stresses are:

$$\sigma_{11} = -p + 2\mu\epsilon_{11} \tag{4.102}$$

$$\sigma_{22} = -p + 2\mu\epsilon_{22} \tag{4.103}$$

Subtracting equation (4.103) from (4.102), and combining the result with equation (4.101), we finally obtain:

$$\sigma_{11} = 4\mu\epsilon_{11} + \sigma_{22} \tag{4.104}$$

Finally, the presssure is given by:

$$p = -\sigma_{22} + \mu\epsilon_{22} \tag{4.105}$$

4.3.8 Multi-boundary Domain

The fluid problem that needs to be solved has more than one surface as shown on Figure 4.8, with internal and external boundary surfaces. Both types of boundary can be differentiated by identifying the direction of the normals. This can easily be done by adopting the rule that the numbering on the external surface is done counterclockwise and the one on the internal surface is carried out in the clockwise direction. From these rules, the normal is perfectly well defined and is always pointing outward from the fluid material domain.

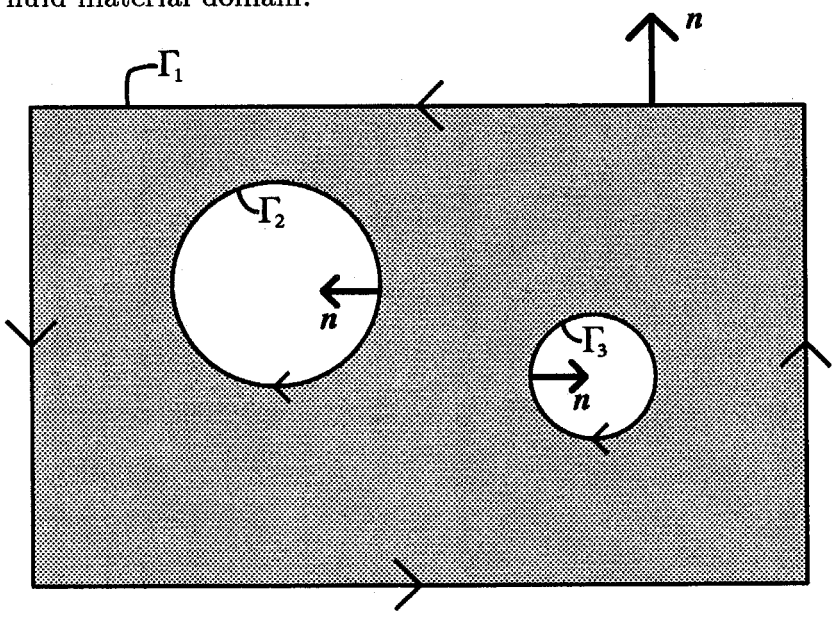

Figure 4.8: Multi-boundary region definition

4.3.9 Force and Moment on the Boundaries

Because the formulation of the BEM used here is employed to compute directly the tractions on the boundaries of the problem, the force and moment acting on a bound-

ary can be obtained as follows :

$$F_x(\Gamma) = \sum_{j=1}^{N_\Gamma} \frac{(t_x(P_1^j) + t_x(P_2^j))}{2} L^j \tag{4.106}$$

$$F_y(\Gamma) = \sum_{j=1}^{N_\Gamma} \frac{(t_y(P_1^j) + t_y(P_2^j))}{2} L^j \tag{4.107}$$

$$M(\Gamma) = \sum_{j=1}^{N_\Gamma} \left\{ \frac{(t_x(P_1^j) + t_x(P_2^j))}{2} d_y^j + \frac{(t_y(P_1^j) + t_y(P_2^j))}{2} d_x^j \right\} L^j \tag{4.108}$$

where, F_x and F_y are the components of the force acting on surface Γ, N_Γ is the number of elements constituting Γ, t_x and t_y are the components of the traction vector, P_1^j and P_2^j are the two nodes of the j-th element of Γ, L_j is the element length, and d_x^j and d_y^j are respectively the horizontal and vertical distance from the center of the element to the moment center. In an actual problem involving particles of microscopic size, d_x^j and d_y^j are *negligible* and therefore the moment can be *neglected.* This is the assumption used in the solid-fluid algorithm.

4.4 Algorithm Validation

In order to verify the validity of the boundary element formulation, three problems have been solved and the results are compared with known solutions found in various publications. The three cases studied are described here.

4.4.1 Flow around an Infinite Length Fixed Cylinder, Located between Two Fixed Planes

The geometry of the problem is given in Figure 4.9. The boundary conditions are:

- Velocities are zero along the top and bottom walls and around the cylinder.
- The velocity profiles at both inlet and outlet are given by:

$$\begin{aligned} u &= \frac{3}{2} U \left[1 - (\frac{Y}{5R})^2 \right] \\ v &= 0 \end{aligned} \tag{4.109}$$

where U is the mean velocity of the flow and R the cylinder radius.

The velocity distribution of the flow is presented in Figure 4.10. The force per unit thickness acting on the cylinder is obtained by integrating the tractions around the cylinder. In the present case, the non-dimensional force is:

$$T/\mu U = 24.20 \tag{4.110}$$

This result compares favourably with Bézine and Bonneau's boundary element result (24.15) [6], Harrison's semi-analytical result (24.55) [52] and Takaisi's semi-analytical value (24.23) [85]. Owing to the symmetry of the problem, this force has a horizontal component only; the vertical component being zero.

4.4.2 Flow around a Steady Infinite Length Cylinder between Two Moving Planes

The geometry and boundary conditions of the problem are shown in Figure 4.11. The following boundary conditions are prescribed:

- Uniform velocity on the top and bottom wall, and on the inlet and outlet of the flow, i.e.,

$$\begin{aligned} u &= U \\ v &= 0 \end{aligned} \tag{4.111}$$

- Velocities are zero along the surface of the cylinder.

The computed velocity distribution is shown in Figure 4.12. Because velocities are specified at each corner of the outer boundary, traction discontinuities occur at these locations. The traction field on the fluid obtained by using discontinuous elements is shown in Figure 4.13. As expected, the results obtained indicate symmetry with respect to the horizontal passing through the center of the cylinder.

Values of the velocity along this symmetry axis are compared with numerical values given by Bouard [19] and the comparison is shown on Figure 4.14. There is a good agreement between the two results. The horizontal force per unit length acting on the cylinder is obtained by integrating the tractions around the cylinder. This value is:

$$T/\mu U = 97.29 \tag{4.112}$$

This result compares favourably with the boundary element results of Bézine and Bonneau (98.8) [6] and Bouard's numerical value of 99.4 [19].

4.4.3 Flow with a Rectangular Particle Floating Freely in a Channel

As shown on Figure 4.15, a denotes the height of the rectangular particle, which is the half-width of the channel. The boundary conditions shown on Figure 4.16 are:

- Velocity is zero along the top and bottom walls.
- Axial velocity is chosen as a two-dimensional Poiseuille profile, i.e.,

$$\begin{aligned} u &= \frac{3}{2}U\left[1-(\frac{Y}{a})^2\right] \\ v &= 0 \end{aligned} \tag{4.113}$$

- The horizontal velocity of the particle is unknown and has to be determined so that the forces acting on it are zero, i.e., the particle is floating freely in the channel. Because of the symmetry of the problem, the vertical component of the particle velocity is simply zero.

This problem is solved by superposing two basic solutions:

1. The particle is moving with a unit horizontal velocity, U_p, in a quiescent fluid.
2. The particle remains fixed while the fluid moves with a unit mean velocity, U.

For each case, the axial force acting on the particle is computed by integrating the tractions around the particle and then the solutions are combined linearly to give a zero axial force on the particle. The ratio of the velocities is:

$$U_p/U = 1.3017 \tag{4.114}$$

This result compares closely to the one obtained by the boundary element formulation of Bézine and Bonneau (1.3041) [6], and the finite element result of Tong and Fung (1.31) [90]. The shear stress distribution along the top wall of the channel is shown on Figure 4.17. Once again, the results are in good agreement with those of Tong and Fung. Using equations (4.97) – (4.105), the distribution of the pressure on the walls and the particle can be obtained. This distribution is shown on Figure 4.18.

In conclusion, the boundary integral method turns out to be an effective approach for numerical analysis of fluid dynamic problems. Furthermore, because only the boundary has to be discretized, this method presents a distinct advantage over the finite element or finite difference method where the complete domain needs to be discretized. Therefore the use of this method to model the fluid phase becomes perfectly evident in the case of fluid flow past moving particles where the discretization of the complex domain is by itself a complicated problem.

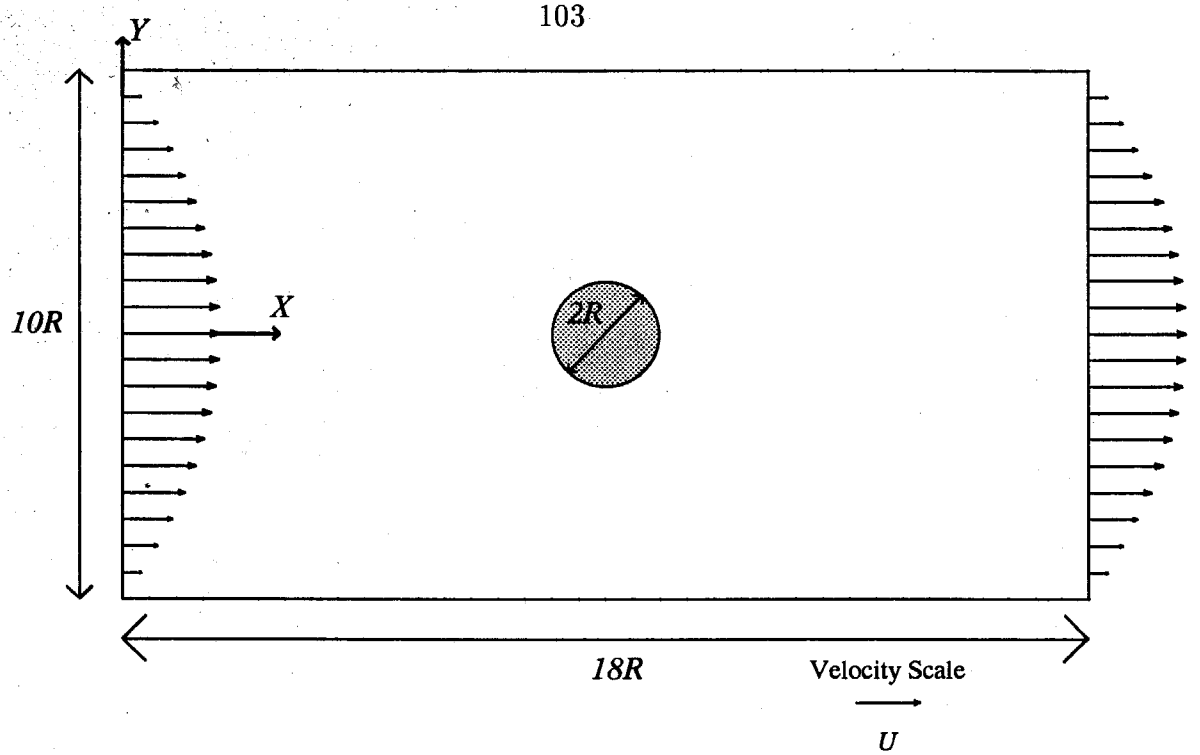

Figure 4.9: Two-dimensional channel flow around a fixed cylinder: Boundary conditions

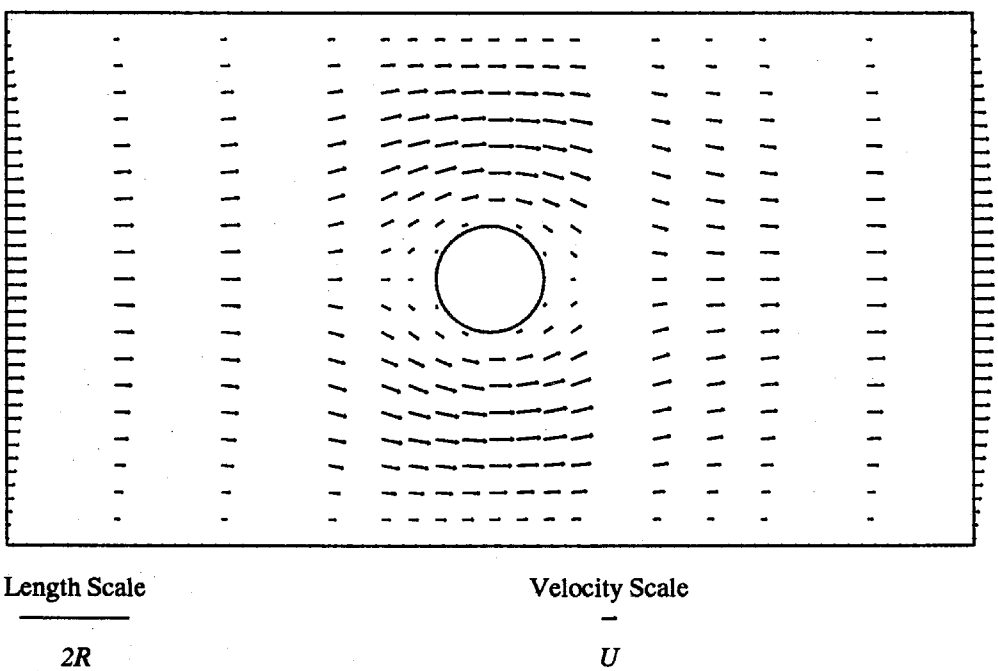

Figure 4.10: Two-dimensional channel flow around a fixed cylinder: Velocity distribution

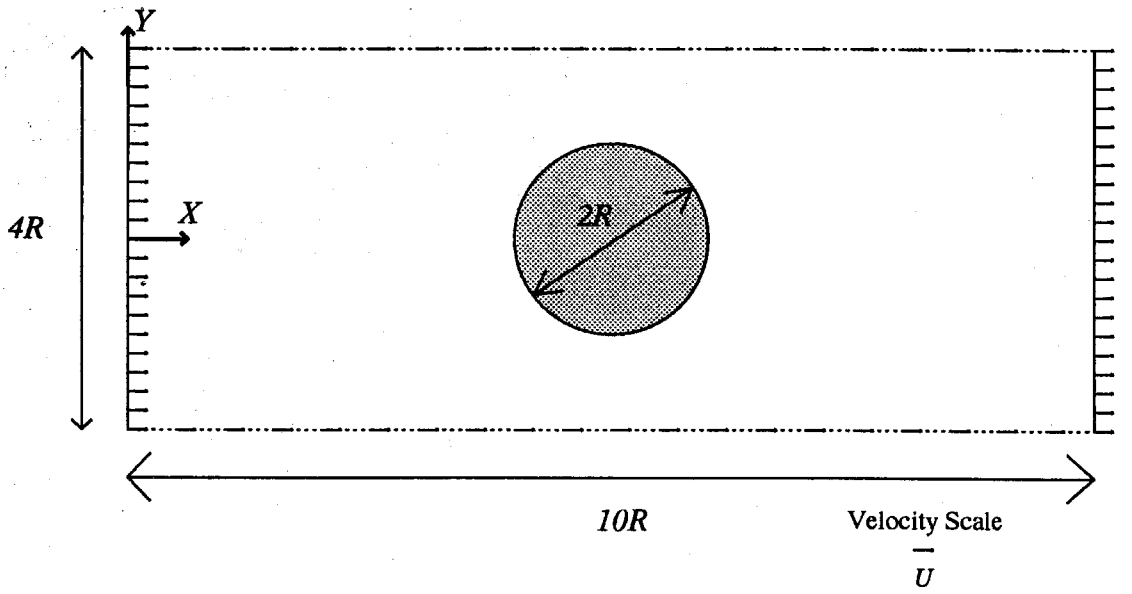

Figure 4.11: Two-dimensional channel flow around a stationary infinite cylinder between two moving planes: Geometry and boundary conditions

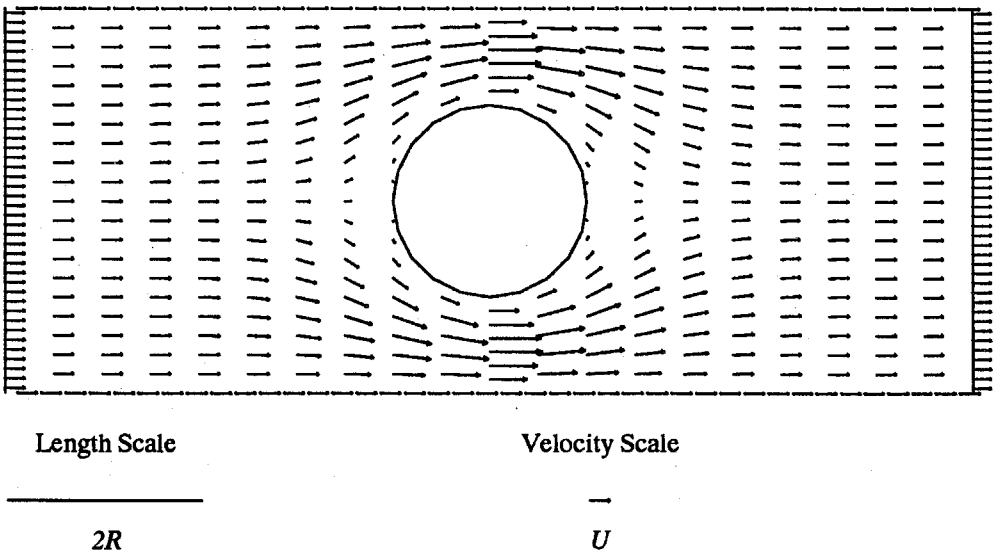

Figure 4.12: Two-dimensional channel flow around a stationary infinite cylinder between two moving planes: Velocity distribution

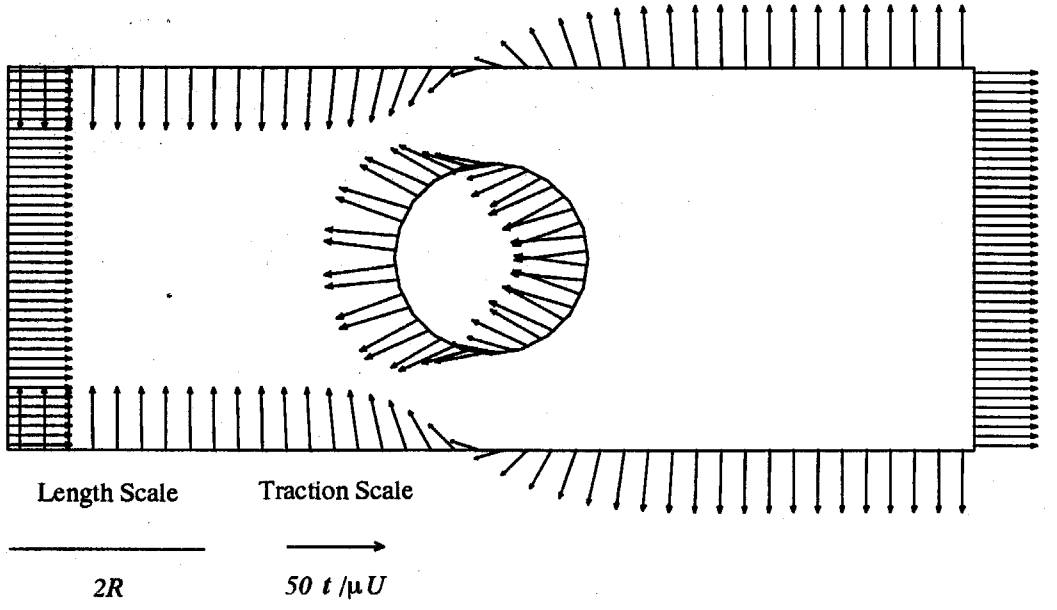

Figure 4.13: Two-dimensional channel flow around a stationary infinite cylinder between two moving planes: Traction field

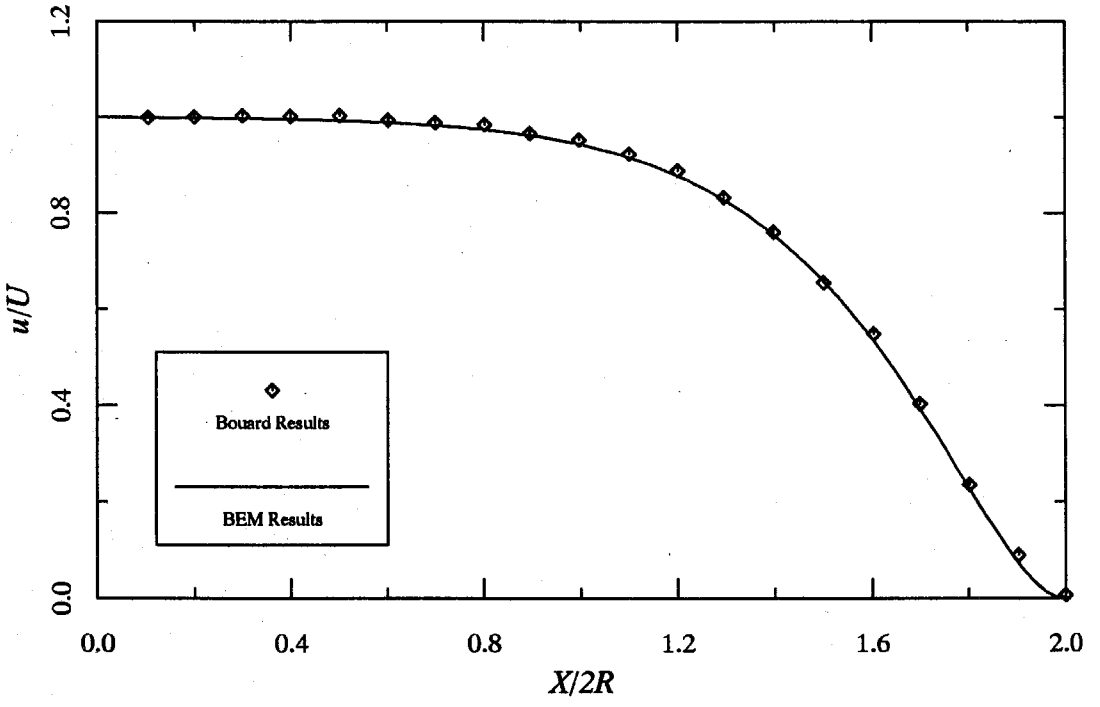

Figure 4.14: Two-dimensional channel flow around a stationary infinite cylinder between two moving planes: Velocity distribution on the symmetry axis

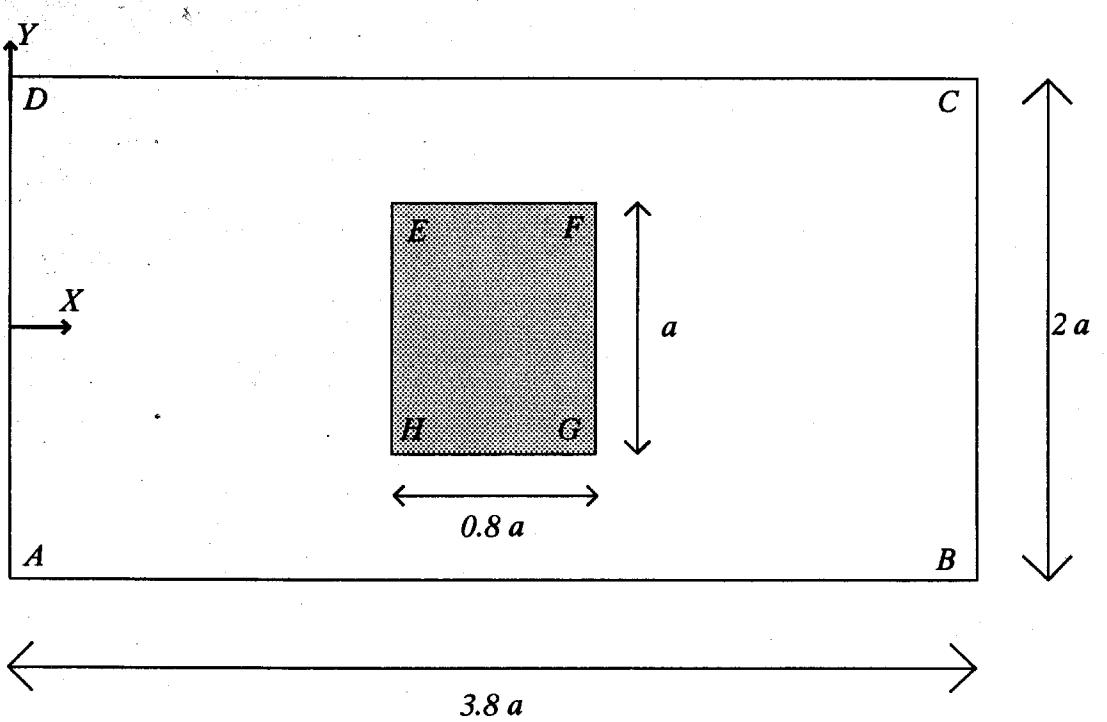

Figure 4.15: Two-dimensional channel flow with one rectangular particle floating freely along the axis: Geometry of the problem

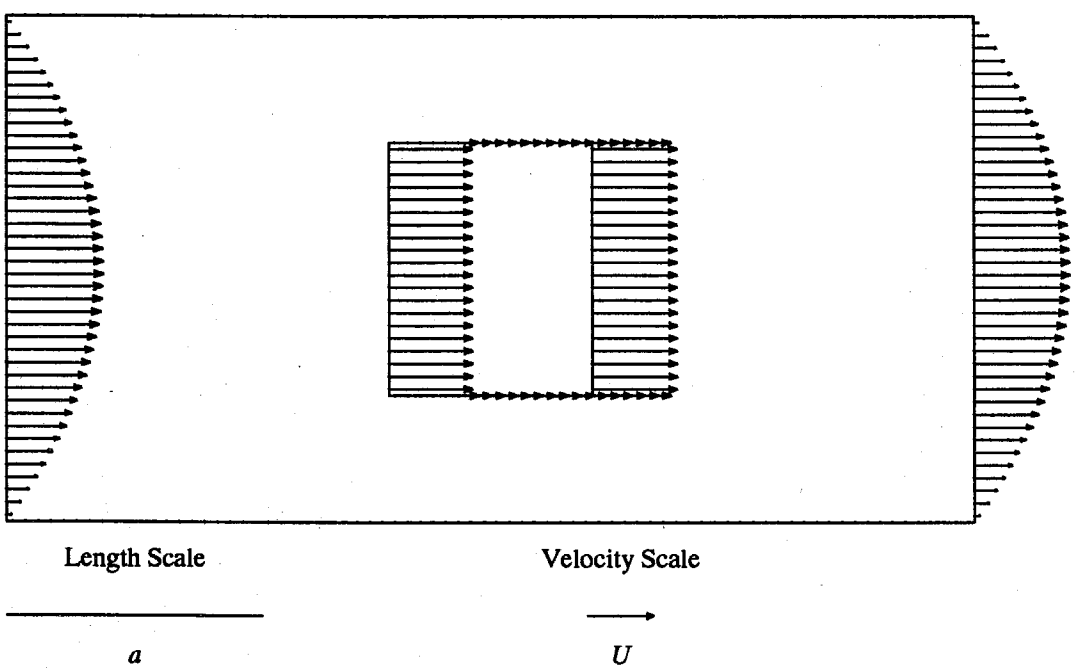

Figure 4.16: Two-dimensional channel flow with one rectangular particle floating freely along the axis: Boundary conditions

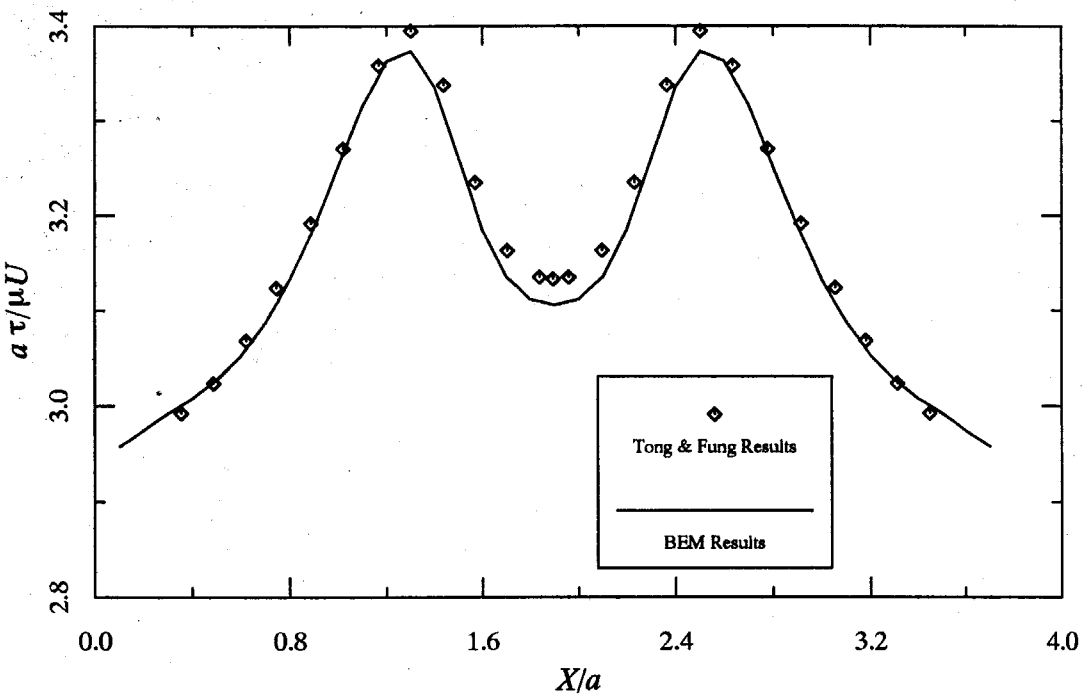

Figure 4.17: Two-dimensional channel flow with one rectangular particle floating freely along the axis: Shear stress distribution along the top wall

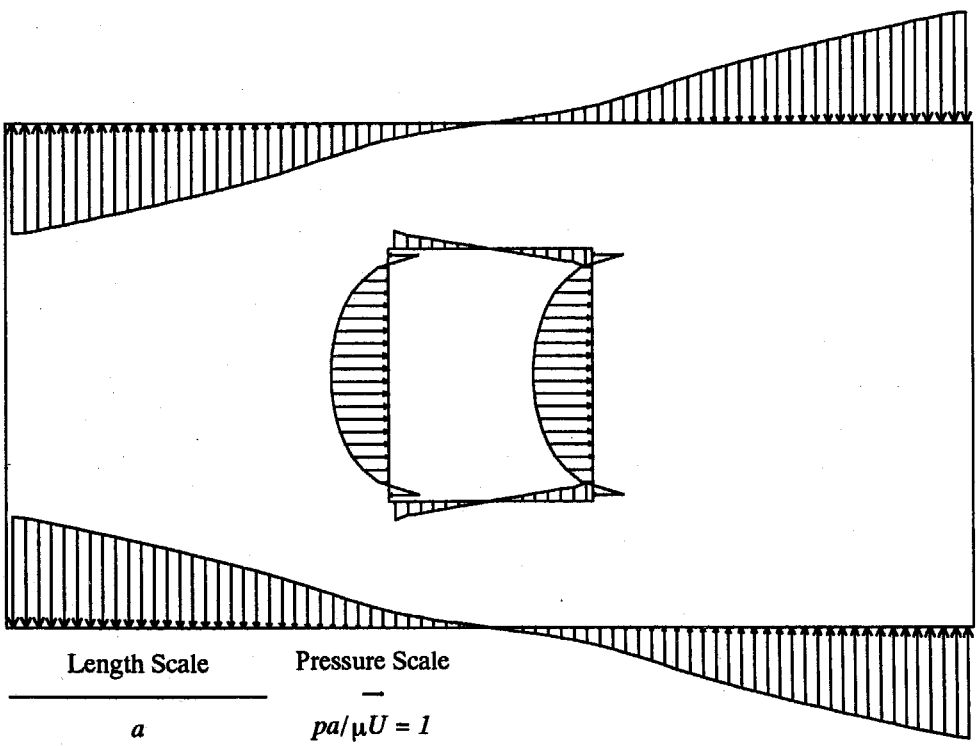

Figure 4.18: Two-dimensional channel flow with one rectangular particle floating freely along the axis: Pressure distribution on the walls and particle boundary

Chapter 5

RESULTS OF NUMERICAL SIMULATIONS

In this chapter, several examples are presented. The first three cases validate the computer program. They will also explain some of the details that were left out of the previous chapters for the sake of clarity. In the final four cases, soil-like systems will be used to demonstrate the capability of the algorithm.

5.1 One Disc Falling Symmetrically in a Viscous Fluid between Two Parallel Walls

Consider the problem as shown on Figure 5.1: a disc of radius $r = 0.5\ cm$ and having a density $\rho_s = 2\ g/cm^3$ is placed exactly mid-way between two parallel walls. The horizontal distance separating the two walls is $2b = 5\ cm$ and the length of each wall, h equals 40 cm. The disc is placed exactly at mid-height of the wall. The space between the walls is filled with a liquid of density $\rho_l = 1\ g/cm^3$ and viscosity $\mu = 50\ g/(cm{-}s)$. This value of the viscosity is chosen arbitrarily. The initial velocity and acceleration of the disc are zero. It is assumed that the thickness of the system is 1 cm perpendicular to the paper. The system is then placed under the action of gravity, $g = -980\ cm/s^2$. The aim of this problem is to find out the terminal velocity of the disc as it moves inside the fluid. This problem is similar to that of a sphere falling in a liquid (i.e., a sedimentation process).

5.1.1 Semi-analytical Solution

Based on the image method, Takaisi [85] obtained an expression for the drag force on the disc as:

$$\begin{aligned} D &= \left\{ \frac{\pi\mu\left[8-4(\frac{r}{b})^2\right]}{2\ln(\frac{b}{r})+3.4486(\frac{r}{b})^2-1.8312} \right\} U \\ &= KU \end{aligned} \tag{5.1}$$

where

μ = viscosity of the liquid

U = velocity of the disc

r = radius of the disc

b = half width between the parallel walls

K = is the expression between braces

This solution is only an approximation of order $(r/b)^2$ of the exact solution. This drag proved to be very close to the BEM solution as shown in the previous chapter. Assuming this drag force, the equation of motion of the disc is given by:

$$m\ddot{x} + A\rho_l g - K\dot{x} = mg \tag{5.2}$$

where

m = $\rho_s \times A \times 1$ = mass of the disc

A = πr^2 = area of the disc

x = as defined in Figure 5.1

g = acceleration of gravity

Equation (5.2) can be further simplified as

$$\ddot{x} = (1-\frac{\rho_l}{\rho_s})g - (\frac{K}{A\rho_S})\dot{x} \tag{5.3}$$

This can be solved as follows: let

$$\begin{aligned} \alpha &= 1 - \frac{\rho_l}{\rho_s} \\ \beta &= \frac{K}{A\rho_s} \end{aligned} \tag{5.4}$$

and initial conditions:

$$\begin{aligned} x(t=0) &= 0 \\ \dot{x}(t=0) &= 0 \end{aligned} \tag{5.5}$$

the terminal velocity is given by:

$$\begin{aligned} v_\infty &= \frac{\alpha}{\beta} \\ &= \frac{\pi g r^2(\rho_s - \rho_l)}{K} \end{aligned} \tag{5.6}$$

For the problem studied here, $g = -980\ cm/s^2$, $r = 0.5\ cm$, $\rho_s = 2\ g/cm^3$, $\rho_l = 1\ g/cm^3$, $\mu = 50\ g/(cm - s)$, $b = 2.5\ cm$, and the terminal velocity is:

$$v_\infty = -0.9535 cm/s$$

5.1.2 Numerical Result

The velocity profiles of the analytical and our numerical results are shown in Figure 5.2. The value of the terminal velocity obtained from the numerical solution is:

$$v_\infty = -0.9306 cm/s$$

This differs from the analytical result by approximately 2%. In general, there is a good agreement between the behaviors and the two final results. The accelerations given by the numerical and analytical results are compared in Figure 5.3. Again, good agreement is observed.

Because the problem is perfectly symmetric, the velocity and acceleration in the horizontal direction should be zero. Figures 5.2 and 5.3 also show the horizontal velocity and acceleration. For all practical purposes, the numerical solution yields a zero horizontal velocity and acceleration.

5.2 Sedimentation of Three Discs

Durlofsky *et al.* [39] studied the sedimentation process of three identical *spheres* in an infinite fluid domain. They also imposed the constraint that the spheres remain in the same vertical plane while falling (i.e., a two-dimensional problem). However, because NePTune was developed only for handling two-dimensional problems, we selected to simulate the same process as that of Durlofsky *et al.* Here, discs are being used instead of spheres. Furthermore, because only finite space can be modelled numerically here, the three discs are placed in a large container. With the presence of the boundaries of the container, boundary effect will play a certain role in the solution obtained and differences between the two solutions are expected. The geometry of the two-dimensional problem is given in the following.

Three identical discs of radius $r = 1\ cm$, density $\rho_s = 1\ g/cm^3$ and unit thickness, are placed in a container filled with a liquid of density $\rho_l = 1\ g/cm^3$ and viscosity $\mu = 100\ g/(cm - s)$. The choice of this high value of viscosity will be discussed later. The lateral distance between the leftmost disc (labelled 1) and the left wall is 116 cm and its lateral distance to the second disc (labelled 2) is 5 cm. Finally, the distance from the rightmost disc (labelled 3) to the right wall is 72 cm while its distance to disc 2 is 7 cm. The three discs are placed at an elevation of 810 cm from the bottom wall. The system is then subjected to a gravity field with the initial velocity and acceleration of the three discs being zero. The geometry of the problem is illustrated in Figure 5.4. The geometry is chosen intentionally asymmetric in order

to observe the boundary effect of the walls on the particles. Because the particles do not collide against each other or any walls, the contact springs and dashpots are of no significance here, and the problem is one of solid-fluid interaction only.

The trajectories of the discs calculated numerically by the present program are shown in Figure 5.5. Notice that the scale in the horizontal direction is highly exaggerated to show clearly these trajectories. If no scale exaggeration is used, the discs look as if they are falling straight down.

Durlofsky, *et al.* [39] used a mobility matrix formulation where the relationship between the velocity and drag force on a sphere are given by:

$$U = MF \tag{5.7}$$

where

U = vector consisting of translational and rotational velocities

F = vector consisting of force and moment

M = mobility matrix

The mobility matrix is obtained through an expansion of the integral equation of Stokes flow. It can also be viewed as the inverse of the resistance matrix, R, if we express the above relationship as:

$$F = RU \tag{5.8}$$

That is, the force vector, F, is proportional to velocity vector through the resistance matrix. Hence $M = R^{-1}$. The lateral distances between each sphere are the same ones as those used in our simulation. The trajectories obtained by these researchers are shown in Figure 5.6 for the case when they used their most accurate method (i.e., one that takes into account lubrication forces when the particles come close to each other). The parameters x and y are non-dimensional because they were normalized by the uniform radius of the spheres.

Comparing their results with those obtained by NePTune, we notice that they both present the same oscillation-type trajectories. However, it seems that the results obtained by the method given here show a higher frequency of oscillation. This could simply be the effect of the right wall on the particles. It is surprising that Durlofsky *et al.* did not mention the value of the viscosity that they used in their study! The differences in the trajectories can be attributed to a difference in viscosity used in each analysis. However, the appearances of the trajectories are quite similar.

Although Figure 5.5 shows that the trajectories of particles 2 and 3 are intertwined, at no instant of time do the particles touch each other. This is shown in Figure 5.7 where the x and y position of each disc is plotted versus time *(note the scale difference between the plots of the x and y position versus time)*. When the x positions of discs are identical, their y positions are different and we can then conclude that no collison occurs. Finally, the horizontal and vertical velocities of each disc are shown in Figure 5.8. As the particles get closer to the bottom wall, their vertical velocities decreased eventually to reach zero when they hit the bottom wall. However, because of the smaller time step required when the particle approaches the bottom wall, the simulation is aborted at approximately 43 s after it starts. The maximum y velocity of each particle is about 20 cm/s, which gives an approximate Reynolds number of 0.4. Therefore a smaller value of μ will increase the maximum y velocity thereby increasing the Reynolds number and hence the flow will no longer be Stokes flow.

To capture all the details of the particles coming to a stop, smaller time steps are required because the forces exerted by the fluid on the particles become extremely large. The use of a large time step in this case can cause numerical instability as the particles will move in large increments of velocity. Therefore, they generate large drag forces even high enough to push the particle upward. This gives rise to an oscillation,

which is then repeated indefinitely. To avoid this problem, artificial damping can be used to attach the particle to the ground and prevent the oscillation. The damping used in this manner does not correspond to an actual physical value.

As mentioned above, too large a time step cannot be used with this algorithm. At present, no exact method can be used to determine the vertical time step beyond which numerical instability occurs. One simple-minded way of determining this critical time step is to assume that at any instant of time, the velocity of the particles could not be larger than the terminal velocity. Because the geometry of the problem is known, the terminal velocity can be approximated by the expression given in equation (5.6), thus we impose that:

$$\ddot{x}\Delta t \leq v_{\infty} \tag{5.9}$$

This then gives us a value for the critical time step. However, this technique of determining the time step proves to be inaccurate when more than one particle is present. Consequently, the critical time step has been determined by a trial and error method.

5.3 An Artificial Liquefaction Simulation

5.3.1 The Liquefaction Phenomenon

It has been observed [54,57,70] that a loose sand subjected to vibration decreases in volume. The pore pressure increases if it is saturated with drainage restricted (such as in the case of an earthquake). This phenomenon can be explained by the effective stress concept [87], which is defined as:

$$\sigma' = \sigma - u \tag{5.10}$$

where

σ' = effective stress

σ = total overburden pressure

u = pore water pressure.

When the soil grains lose their load-supporting role, the value of σ', which represents the portion of the total overburden pressure carried by the solid phase, becomes zero. Simultaneously, the pore pressure rises to that of the overburden pressure. Therefore, the soil becomes a suspension of solid grains in fluid, or is said to have liquefied.

For liquefaction to occur, three conditions are necessary:

1. an overburden load or stress
2. a solid particulate phase that loses its strength
3. a fluid phase that will absorb the imbalanced force when the solid phase loses its strength.

According to these specifications, we are now able to define a mechanism that can simulate liquefaction.

5.3.2 Saturated Granular Medium Simulation

To fulfill the first requirement, all we need is a constant load that is applied to the granular medium. As we mentioned in chapter 2, the formulation of the DEM is more convenient when applied strain conditions are used because it is easier to define the motion of the particles. However, when an applied stress condition is used, a technique must be developed for the numerical system to support this load. One way of solving this problem when the medium is dry is to allow the walls on which the load is applied to move in the direction required to achieve contact reaction forces on

the wall equal and opposite to the applied force. To illustrate this idea, consider the case shown in Figure 5.9(a). Here, three particles labelled A, B, and C are arranged in a column without touching each other. No liquid is present. If a vertical load F_y is applied to the top boundary (wall 3), the solution consists of moving this wall down until contacts between particle and wall and particle and particle are formed. The downward motion of the top wall is stopped when the contact force between the top wall and particle C reaches F_y (Figure 5.9(b)).

If we suppose that, when the motion of the top wall is stopped, liquid is added to the void space between the particles (Figure 5.9(c)), the particle contacts at this stage still take the vertical load, and the liquid is unstressed. Next we shear the system (Figure 5.9(d)) while preserving its volume, and holding the applied load (F_y) constant. In this case, the top wall has to remain at a fixed distance from the bottom wall. Thus, if the inter-particle contact forces change as the result of this shearing, some other mechanism is required to absorb the unbalanced force that exists at the wall. Because now the system is composed of two phases, i.e., liquid and solid, the unbalanced load will be distributed to the liquid phase, which translates to a change in the pore pressure. If only the solid phase is present, because there is no other phase that can absorb the unbalanced force, the top boundary is required to move up or down to maintain the contact force constant. In this case, there is a volume change in the system. The motion of the wall will be discussed later.

Based on this simple idea, we now have all the ingredients to simulate liquefaction in a saturated granular medium:

1. A top boundary wall with specified constant load.

2. In the saturated case, this load is compared with the contact forces on the wall. If an unbalanced force exists, it is simply distributed to the boundary of the liquid phase that touches the specified load wall. For the liquid phase boundary, this

unbalanced force becomes its applied boundary condition after transforming the load force into tractions. Together with the knowledge of all the other boundary conditions, the solution of the problem of solid/liquid interaction in terms of the liquid phase is given by the BEM, which provides the pore pressure changes at any point in the liquid phase. It also provides the drag-force on the particle, which in turn will be combined with the interparticle contact forces to produce the force applied at the centroid of the particle. The motion of the particle can then be deduced from this force.

3. The solid phase will be simulated using the DEM, which allows us to obtain the contact forces needed at the applied load wall; these are necessary for the computation of the unbalanced force if any. If no contact exists at the applied load wall, the applied load will be distributed entirely to the liquid phase. This condition defines liquefaction.

5.3.3 The Liquefaction Simulation

As explained earlier, the purpose of this simulation is simply to demonstrate the redistribution of load from the solid phase to the liquid phase via our calculation process. Because the example is purely artificial, we will assume that the dimension used is of unit L, the mass of unit M, the force of unit F and time of unit T. From these, all other variables can be deduced.

In this example, three identical frictional particles of radius $r = 5L$ are placed in a container of dimension $30L \times 30L$ with the same arrangement as in Figure 5.9. To achieve eventual instability of the system, disc B is slightly off-center to the left from discs A and B. Next, this dry system is subjected to a vertical loading force $F_y \simeq 10^7 F$. Beyond this value, because disc B is slightly off-center, the column of particles will buckle. At this stage, a liquid of viscosity $\mu = 25\ M/(LT)$ is added to

the void spaces between the particles and walls. The value of the physical parameters used in this example is given as follows:

$$
\begin{aligned}
\mu &= \text{fluid viscosity} = 25M/LT \\
\rho_s &= \text{particle density} = 2400M/L^3 \\
m &= \text{mass of each particle} = 157080M \\
k_N &= \text{normal contact spring constant} = 0.75 \times 10^9 F/L \\
k_S &= \text{shear contact spring constant} = 0.75 \times 10^9 F/L \\
c_N &= \text{normal contact dashpot constant} = 1.5 \times 10^7 F/L \\
c_S &= \text{shear contact dashpot constant} = 1.5 \times 10^7 F/L \\
\phi_{dd} &= \text{disc-disc friction angle} = 22^\circ \\
\phi_{dw} &= \text{disc-wall friction angle} = 10^\circ
\end{aligned}
$$

Because no gravity is present in the problem, the knowledge of the density of the liquid is not necessary. The contact damping ratio in both the normal and shear direction is taken approximately 5% that of the critical damping of a single degree of freedom of a particle of mass m and spring constant k_N. The value of the fluid viscosity is chosen arbitrarily here because our main purpose is to demonstrate the liquefaction mechanism.

A shear rate, $\dot{\gamma}$, of 7×10^{-3} $radian/T$ is applied to the two lateral walls (walls 2 and 4). The velocity of the bottom wall (wall 1) is simply deduced from the motion of the lateral walls because the bottom wall connections are hinged. Shearing is performed until a shear strain, γ, reaches 0.7%. As the shearing process progresses, disc C, due to its friction with the top wall will move in the lateral direction. Therefore, the contact forces diminish gradually (compare the width of the contact force line on Figures 5.10(b) and 5.9(b)). Eventuallly, all contacts are broken (Figure 5.11).

Here, the liquid phase is assumed to be a continuum (i.e., no enclosed pockets of fluid). Therefore gaps ($0.05L$ in size) are artificially generated between the particles to permit fluid flow between regions. Figure 5.12(a) shows the discretization of the fluid phase at $\gamma = 0.35\%$. Because of the unbalanced force at the top wall, the liquid phase has to support this load. The boundary conditions on the lateral and bottom walls are given by the velocity of these walls. On the top wall, applied traction is specified in the vertical direction and specified velocities are prescribed in the horizontal direction. The resulting tractions computed by the BEM are shown on Figure 5.12(b). We notice that the tractions along all four walls are uniform. This is simply the consequence of the incompressibility of the liquid. At the boundary of the particles the tractions are relatively small, suggesting that the velocities of the particles are also very small. Figure 5.12(c) shows the velocity field. We notice that if the top wall consists of a membrane instead of a rigid wall used here, a sloshing effect would occur.

Finally, the boundary element discretization at $\gamma = 0.7\%$ is shown on Figure 5.13(a), the velocity distribution in Figure fig5:13(c) shows that the velocity amplitude is much higher on the left side than on the right side. This is justified by the motion of the particles to the left and the left wall lateral motion to the right, which together produce a squeezing effect on the left side liquid phase. The gap that allows fluid flow between the particles is selected in such a way that the gap width remains constant. Consequently, the fluid phase will see different sizes of the same particle during a simulation. This is illustrated in Figure 5.13(a) where the diameter of particle B has changed. A and C are shrunk because of their close contact with the top and bottom walls. Also because A and C have slightly moved laterally away from B, the distance from B to A or C has increased. Thus by reducing the size of A and C, the gap widths existing between B and A, and B and C are large enough and

therefore B need not be shrunk. The traction field is presented on Figure 5.13(b).

We observe that in Figures 5.12(b) and 5.13(b) that the tractions along the boundary of each disc are almost uniform and that they are not identical to the magnitude of the tractions along the boundary walls. The uniformity of the tractions along each disc indicates simply that the motion of the discs in the viscous fluid does not generate appreciable disturbance. Therefore, the main component of forces generated by the fluid on each disc is simply caused the increase of pore pressure at the wall boundaries. However, because of the multiply connected domain used in this problem, the tractions obtained along each disc are known up to a certain constant to be determined from the boundary tractions. This does not present any ambiguity to the algorithm because the tractions are integrated along the boundary of each disc to obtain the force acting on the centroid of each disc and therefore the knowledge of the boundary constant is not necessary.

The pore pressure change along the top wall (wall 3) indicated by the solid line on Figure 5.14, increases gradually as the contact between disc C and the top wall (wall 3) is broken (indicated by the dotted line). The pressure along the bottom wall (wall 1) (open square) indicates an instantaneous response of the liquid phase when a pressure is applied. As the pore pressure rises to that of the applied vertical stress, the solid phase eventually ceases to support any load. If drainage is allowed at this moment, the top wall will simply collapse. By doing so, it will push all the particles downward until new contacts are created between the walls and discs. Hence a more compact configuration would be generated.

This simulation suggests that the fluid component play a double role:

1. As a transmitting medium for the pressure disturbance created at the boundary by the force unbalance due to the restructuring of the solid particles (**primary effect**).

2. As a viscous medium which resists to the motion of the particles (**secondary effect**).

According to this simulation, we observe that for slow monotonic loading case, the secondary effect is almost negligible. The negligible contribution of the secondary effect can also be caused by the large opening gap between the particles in the fluid phase.

5.4 Simple Shear Simulations – Initial Setup

In this set of simulations, four cases have been studied:

- Dry simple shear of a loose array of particles
- Saturated simple shear of a loose array of particles
- Dry simple shear of a dense array of particles
- Saturated simple shear of a dense array of particles

The results obtained are compared with actual experimental results.

5.4.1 Initial Setup

For all four cases studied, the initial configuration is identical as shown in Figure 5.15. Here, 20 particles having the distribution shown in Table 5.1 are generated randomly inside a box of $1cm$ width and $0.8cm$ height:

Number of Particles	Radius (mm)	Solid Area (mm^2)
3	1.5	21.21
6	1.0	18.85
11	0.5	8.64

Table 5.1: Particle distribution, size, and solid area

The following parameters are used to characterize the properties of these particles:

$$
\begin{aligned}
k_N &= \text{normal contact spring} = 1875 \times 10^3 gF/cm \\
&\quad \text{(both disc–disc and disc–wall)} \\
k_S &= \text{shear contact spring} = 1875 \times 10^3 gF/cm \\
&\quad \text{(both disc–disc and disc–wall)} \\
c_N &= \text{normal contact damping} = 34.323 gF/(cm/s) \\
&\simeq 5\% \text{ average critical damping} \\
c_S &= \text{shear contact damping} = 34.323 gF/(cm/s) \\
\phi_{dd} &= \text{disc–disc friction angle} = 22^\circ \\
\phi_{dw} &= \text{disc–wall friction angle} = 10^\circ \\
\rho_s &= \text{disc density} = 2g/cm^3 \\
\rho_l &= \text{liquid density} = 1g/cm^3 \\
\mu &= \text{liquid viscosity (i.e., water)} = 0.01g/(cm-s)
\end{aligned}
$$

Neither gravity nor global damping is imposed in any of the examples. The value of k_N and k_S are those used by Cundall and Strack's simulations [24]. The contact damping is taken as the average value of 5% that of the critical damping of each disc, each having a mass given on Table 5.1 and a spring constant k_N or k_S.

5.5 Loose Medium

5.5.1 Initial Compression

Before performing the shearing tests, the particles are subjected to an initial compression. This compression is obtained by moving inward walls 2, 3, and 4 (see Figure 5.15). The positions of the particles at the end of the compression are shown

in Figure 5.16(a) and the contact force diagram in Figure 5.16(b). Here, the thickness of the line gives the intensity of the force whereas its direction is given by the direction of the contact force line. This graphical representation of the contact forces can be associated with the fringes observed in pictures of photoelastic material testing.

We observe that after consolidation, the largest contact loads are supported by the biggest particles. Because of the particular configuration used here, the biggest particles located midway between walls 1 and 3 create an arch-like structure and thus prevent particles beneath them from playing an important supporting role. For example, the particle labeled A on Figure 5.15 does not come into contact with any other particles.

To obtain a loose sample, the friction angles have been set at the start of the compression phase. Because of these friction angles, the motions of the particles under the confining loads are more restricted than those obtained when no friction is present.

The width of the compressed box now becomes 0.89 *cm* while the height is reduced to 0.69 *cm* giving rise to a void ratio of $e = 26.11\%$.

At the end of the compression phase, the wall motions are stopped and a period of relaxation is allowed so that static equilibrium can be reached. This equilibrium can be monitored by the sum of the contact forces on all four walls. At equilibrium, these forces become constant with sum zero in the coordinate directions. A slight redistribution of forces is observed at the end of the relaxation period (see Figures 5.16(b) and 5.17(b)) although the particles still remain at the same location and orientation as that of the beginning of the relaxation period (Figures 5.16(a) and 5.17(a)).

Using this later configuration, the system will be sheared either dry or with interstitial pore water. The applied vertical force on wall 3 is taken as the force at

the end of the relaxation period and is fixed throughout the shearing process. This applied vertical force takes a value of $8.1kgF$, which gives a vertical applied stress on the top wall, $\sigma_v = 8.1kgF/(0.89cm \times 1cm) = 9.1kgF/cm^2 = 892.8kN/m^2$.

Before we examine the results obtained by the shearing experiments, we first need to understand the mechanism that maintains the constant force on wall 3 throughout shearing, when no liquid is being used. We have previously explained the mechanism that maintains the load constant when liquid is present in the interstitial pores (cf. section 5.3.2). In this case, the unbalanced force is distributed to the fluid phase.

5.5.2 The Servo Wall Mechanism

Cundall [24], the originator of the DEM, suggested a simple way to maintain the applied force: to obtain a constant force when an unbalanced force exists between the reaction force on the wall resulting from the contact points, F_C, and the applied force, F_A, the wall needs to be moved in the direction of the unbalanced force ($F_A - F_C$). He called this type of wall a "*servo wall*," i.e., like a servo motor, where a sensor constantly monitors the unbalanced force and adjusts the position of the wall accordingly. Using a slightly modified version of Cundall's servo wall, the adjustment of the wall is performed in the following manner:

Let $err = (F_A - F_C)/F_A$ be the error introduced by the unbalanced force, then the most simple way of adjusting the wall is given by the following relation:

$$v_1 = G \times err \tag{5.11}$$

where:

v_1 = velocity by which the wall should be moved

G = gain of the wall

In order to prevent the displacement of the wall from becoming too large, a limit is further imposed on the velocity:

$$v = \min(v_{max}, |v_1|) \times sign(v_1) \tag{5.12}$$

where

v = velocity to be used to displace the wall

v_{max} = maximum imposed velocity

This last equation is also illustrated on Figure 5.18.

Cundall [24] mentioned that if the value of the Gain, G, is too high, the wall might become unstable because a fast motion of the wall to correct the error will create another error in the opposite direction and cause instability. This has also been observed in this study. Furthermore, if the value of G is too small, the response of the servo wall becomes sluggish and hence no constant force can be obtained. The value of G and v_{max} in a particular problem can only be obtained by a trial-and-error process.

Also, to maintain a stable constant force, a slow wall motion is required, which in turn implies a long computational running time. To overcome this problem, we have tried a method in which an additional iterative loop is added to each calculational time step. This method proved to be unsuccessful because the additional iteration loop required a large number of cycles. Furthermore, the adjustment of G and v_{max} becomes almost impossible because the requirements for each time step are different from one another. When fast deformation occurs, the adjustment of the servo wall becomes more difficult to achieve. Although Cundall never mentioned this problem, we came to this conclusion by observing the large number of cycles required in his calculations between two instants of time.

When slow motion is used, no additional iteration loop is required; however, the computation time also increases significantly.

5.5.3 Dry Simple Shear of a Loose Array

5.5.3.1 Simulation Results

Starting from the configuration shown on Figure 5.17(a), a shearing mechanism is applied as shown on Figure 5.19. As explained earlier, to achieve a constant vertical loading force, F_y, wall 3 is allowed to move up or down. For this shear deformation, the value of the required shear force along walls 1 and 3 is obtained from the tangential component of the contact forces of the grains at equilibrium. Notice that there is no joint between wall 3 and the two lateral walls. In other words, this top wall functions just like a lid to the system.

The configuration of the particles and the corresponding contact force diagram at a shear strain of $\gamma = 4.9\%$ and $\gamma = 10.5\%$ are shown respectively on Figures 5.20 and 5.21. As shearing progresses, we observe that the number of particles supporting loads increases. Also, at the end of the simulation, the overall direction of the contact forces is oriented diagonally. This observation agrees with the simulations performed by Cundall [24]. The shear forces (S_1 and S_3) along walls 1 and 3 and their mean value are shown in Figure 5.22. The change of height of the box expressed as a percentage of the initial box height (H) is given in Figure 5.23 where a negative value indicates a decrease in height (i.e., compression). Because the array is always compressing (i.e., densifying) we conclude that the original configuration used was effectively "*loose*."

To insure that the equilibrium is achieved at each time step, the sum of the forces on each wall in the X and Y directions are computed as shown in Figure 5.24. In general, this equilibrium is observed throughout the shearing process. As a consequence of this equilibrium the system behaves statically. Therefore, the velocity and accelerations are small enough so that the inertia terms become negligible. Because no gravity field is present in the problem, this then suggests that a higher value of the disc density can be used in the calculations without changing the behavior of the

system. This implies that a larger time step can be used to speed up the calculation process.

5.5.3.2 Comparison with Experimental Results

Cole [15] performed a series of simple shear tests on dry Leighton Buzzard sand. Typical results of a loosely compacted sand are shown in Figure 5.25. Comparing the numerical simulation shear force in Figure 5.22 and the ratio of τ/σ_N (Figure 5.25) for *shear strain less than* 10%, both cases indicate that the asymptotic plateau value had not yet been reached. Due to the limited amount of particles used in the numerical simulation, the result is not as smooth as that of the experiment. Furthermore, the maximum ratio, S/F_y, obtained in the numerical simulation gives a value of approximately 0.2, which is lower than the experimental results. This value is somewhat higher than the tangent of friction angle of the disc-wall contact but lower than the interparticle friction angle. In other words, the particles serve as a load transmitting medium from the top wall to the bottom wall. The presence of the interparticle friction thus contributes to the rigidity of the system and hence increases somewhat the global friction angle of the system. If a larger number of particles was used, their contribution to the rigidity of the system would be much more significant than the one obtained by this simulation. Consequently, the ratio S/F_y would be increased. Although the number of particles is limited, the qualitative response of this array resembles that of a real soil remarkably well.

When the shearing is pursued further, the dense array obtained from the densification of the loose initial configuration start to dilate. In this case the volume increases, as can be seen in Figure 5.25(b).

5.5.4 Saturated Simple Shear of a Loose Array

5.5.4.1 Simulation Results

Using the same initial configuration as that of the dry simple shear (shown on Figure 5.17(a)), a liquid is added to the interstitial pores. From there, a constant volume shearing mechanism is applied to the system as shown on Figure 5.26. This is achieved by maintaining the height of the box constant.

Unlike the dry simple shear, if unbalanced force exists along the top wall, this force can be supported by the liquid phase and affects the pressure of the liquid. Because no gravity is present here, the liquid density does not play any role in the behavior of the system.

For comparison, the configuration and contact force diagram at a shear strain, $\gamma = 4.9\%$, are shown in Figure 5.27. The contact force diagram shown in Figure 5.27(b) indicates that the contact forces generated during this phase of the shearing process are smaller than those of the dry system. The velocity and fluid force generated on each particle are shown in Figure 5.28. We notice that there is no co-linearity between the particle velocity and the fluid force generated. Therefore the conventional relation between the drag force and the velocity is not valid here. The configuration and contact force diagram at $\gamma = 10.5\%$ are shown in Figure 5.29, and the velocity and fluid force diagram are shown in Figure 5.30. The force generated by the fluid on the particle is smaller than the contact forces. This seems to indicate that either the gap between the particles, which allow fluid flow, is either too big or the viscosity of water is too small. Because of this small value, the liquid plays mainly a role of load transfer material when an unbalanced force occurs. The drag force generated does not play an important role here.

Looking at the contact force diagram sequence, we notice that the intensity of the contact loads has not changed much throughout the shearing. However, we

notice a clear rotation of the direction of the load path. This can be explained as follows: because the volume is kept constant and the value of the void ratio large, the particles do not experience any increase of contact forces because no densification or dilation occur. Therefore the load supported by the skeleton remains almost constant throughout the process. This force is simply rotated as the shearing progresses. Thus, its component in the vertical direction decreases while the horizontal component increases during the shear. This then is translated by an increase in the shear force required to move the system and a decrease of the supporting role of the skeleton in the vertical direction. Because we impose a constant vertical load on the top wall, as the vertical contact force decreases, the liquid phase has to support this unbalanced load so that the top wall remains at a fixed vertical position. Consequently, the pore pressure increases.

By comparison, the dry case where the volume is allowed to change, the contact forces between the particles steadily increases from this densification process while at the same time the load path is rotated from its initial configuration.

The shear forces along walls 1 and 3 and their average values are shown in Figure 5.31. The system does not offer much resistance to shear during the first 4% of shear strain. During this period, an initiation process is required before the loading of the full system occurs. This is probably due to the small number of particles used in this test. If a larger number of particles is used, this initiation process will probably start instantaneously as the shearing is applied.

The pressure change along walls 1 and 3 are shown in Figure 5.32. The results indicate an increase in pore pressure, which is expected. We observe a sharp increase of pore pressure corresponding almost exactly to the period where the shear force starts to increase. As the load supported by the skeleton starts to rotate, the system becomes softer and hence less prone to support any load. Thus the portion of the

load supported by the skeleton decreases sharply, and is accompanied by a sharp increase in pore pressure. However, as the shearing progresses, the skeleton is able to find a more stable position, thereby increasing the portion of the applied load that it supports. Consequently, the pressure decreases. The pore pressure change along the top and bottom wall are quite similar. This is simply the consequence of incompressibilty of the liquid used here.

Finally, Figure 5.33 shows the total components of forces in the horizontal (X) and vertical (Y) directions. In general, we observe that static equilibrium is obtained almost throughout the entire shearing process. Some oscillations occur between the shear strain value of 4 and 7%. This oscillation can be attributed partly to the motion of particle A, which constantly bounces inside the void space it occupies. This observation can only be seen by a rapid animation of the particle motion. The constant oscillation causes the oscillation of the forces measured along the walls. Although the solid-solid contact force is not very important, this bouncing effect could create enough disturbance on the wall. The fluid phase also propagates this effect to other walls as well.

5.5.4.2 Comparison with Experimental Results

Because of the lack of experimental data on undrained monotonic simple shear loading of saturated granular media, we can only make a qualitative comparison between the numerical simulation and undrained triaxial tests on sand. Seed's *et al.* [77] have performed a series of undrained triaxial tests on Sacramento sand. Typical behavior of a loose sand is presented in Figure 5.34. In particular, we notice that the shearing occurs with an increase in pore pressure. For this particular test, we also observe that there is a period where the deviator stress remains almost constant before it starts increasing again until it reaches a plateau value. This seems to corroborate with our numerical results where a period of time is required before the shear force starts to

be mobilized. However, in our numerical results this may simply be caused by the limited number of particles used in the simulation. We conclude that in general, our numerical model is able to represent the qualivative behavior of a loose saturated sand.

5.6 Dense Medium

5.6.1 Dry Simple Shear of a Dense Array

5.6.1.1 Initial Compression

Like the previous cases, prior to performing the shearing tests the particles are subjected to an initial compression. To achieve a dense configuration, during this initial compression case, we imposed a zero friction angle between the particles, and between the particles and walls. Because no friction exists, the particle will offer little resistance to the motion of the walls. This compression is obtained by moving inward walls 2, 3, and 4 (see Figure 5.15) until the width of the box is reduced to 0.89 cm and its height to 0.69 cm. The positions of the particles and the contact force diagram at the end of this initial compression period are shown in Figure 5.35. By comparison to the contact force diagram of the loose case, here the intensity of the contact forces are smaller. This is expected because the particles do not have any friction angles.

To obtain the same vertical loading force as that of the loose case. We replaced the top wall by a servo wall with a specified vertical load force of $8.1kgF$ (i.e., the vertical stress is identical to that of the loose case). When the servo wall has reached the specified load force, a relaxation period is allowed for some period of time for contact force distribution. When the servo wall has reached a stable position, the particle positions and the contact force diagram are shown on Figure 5.36. The height of the box is now reduced to 0.682 cm, giving rise to a void ratio of $e = 24.65\%$.

5.6.1.2 Simulation Results

Using the configuration at the end of the compression phases, a shearing mechanism similar to that of the dry, loose array is used to apply the shearing.

The particle positions and contact force diagram corresponding to a shear strain of 5.0 and 10.5% are shown respectively in Figures 5.37 and 5.38. In contrast to the loose case, the orientation of the load path is clearly shown at a shear strain of 5%. The shear forces along the top and bottom wall shown on Figure 5.39 confirm this observation. The system resists to the shearing motion immediately after it has been started. We also notice that the interparticle contact forces are larger than those found in the loose case. This can be attributed to the dilation of the particles: because the system is dense, as the shearing occurs the particles try to expand in volume; because the volume is fixed the particles are not allowed to dilate, this then results in a net increase of the contact forces.

The change of height of the box, expressed as a percentage of the initial box height (H), is given in Figure 5.40 where a negative value indicates a decrease in height (i.e., compression) and a positive value indicates an increase in height. Here, the volume of the system initially decreases before starting to increase steadily. The increase of volume of the system confirms its dilation and hence the system is "*dense.*" The glitches encountered here are probably due to the small number of particles present. For a system with a higher number of particles, these glitches might be smoothed out.

The sum of forces along the four walls in the X and Y directions are shown in Figure 5.41. Static equilibrium is obtained throughout the shearing. We also note that the vertical force on the top wall (wall 3) remains constant throughout the experiment.

5.6.1.3 Comparison with Experimental Results

Cole [15] has also performed simple shear test experiments on dense Leighton Buzzard sand. A typical behavior of the response of this type of material is given in Figure 5.42. The shape of the shear stress ratio of Cole's experiment presents a remarkable similarity with that of the average shear force obtained by the numerical simulations. However, the maximum ratio of S/F_y (i.e., ratio of shear force over applied vertical load) is approximately 0.19, in comparison to Cole's value of 0.8. As in the loose case, the value of this ratio is only slightly higher than that of the friction angle. Again this indicates that the skeleton serves mainly as a force transmission medium from the top wall to the bottom wall. A higher ratio could probably be obtained by using a higher number of particles. The volume change behaviors are also very similar in both cases.

5.6.2 Saturated Simple Shear of a Dense Array

5.6.2.1 Simulation Results

Using the same initial configuration as that of the dry simple shear (shown on Figure 5.36(a)), a liquid is added to the interstitial pores. From there, a constant volume shearing mechanism similar to the one used for the saturated loose array is applied to the system.

Figure 5.43 shows the particle position and the contact force diagram when the shear strain reaches a value of $\gamma = 5.0\%$. As in the dense, dry case, the rotation of the load path can be seen clearly at this stage. The particle velocity and force generated by the liquid on the particles are shown in Figure 5.44. Like the loose case, we notice here the absence of co-linearity between the velocity vector and the fluid force. Furthermore, the intensity of the fluid forces are relatively small in comparison to that of the contact forces.

The particle position and contact force diagram at 10.5% shear strain are shown in Figure 5.45. Comparing the contact force diagrams at a shear strain of 5% and 10% indicates that the contact forces are steadily increasing. This can be attributed to the dilation of the particles, which is prevented by the imposed constant volume condition. Because the skeleton is able to support a higher portion of applied load, the fluid phase will contribute less to the support of this load, which then results in a decrease in pore pressure. The increase of the contact force intensity is also accompanied by a rotation of the load path.

Figure 5.46 shows the velocity vectors and the fluid force of each particle. We also observe here the absence of the co-linearity between the velocity vector and the fluid force vector. Again, the fluid forces are almost negligible in comparison to the contact forces.

The shear forces along the top and bottom walls (walls 1 and 3) and their average values are shown in Figure 5.47. Unlike the loose case, the shear response is immediate. The pore pressure change along the top and bottom walls is presented in Figure 5.48. A good agreement exists between these two walls. As expected, there is a steady decrease of pore pressure after an initial increase. Finally, the sum of the forces in the X and Y directions is shown in Figure 5.49. Except for a few instances, static equilibrium is observed throughout the simulation.

5.6.2.2 Comparison with Experimental Results

Due to the lack of experimental data on undrained monotonic simple shear loading of granular media, only a qualitative comparison can be made between the numerical simulation and undrained triaxial tests on sand. Seed *et al.* [77] presented some experimental results on undrained triaxial tests performed on Sacramento sands. Typical behavior of deviatoric stress and pore pressure change is shown in Figure 5.50. For the range of shear strain value found in the simulation, Seed's results indicate that

the peak value of stress is not yet reached. This seems to confirm the numerical results where the shear force is still increasing. The pore pressure change exhibits the same behavior as the one obtained by the simulation, that is, the pore pressure rise is immediately followed by a sharp drop.

5.6.3 Conclusions

We have demonstrated here that in general the behavior of the numerical model is qualitatively similar to that of a real granular soil. However, because of the limited computer resources available, we were not able to pursue further simulations with a lager number of grains. Also, due of the lengthy computation time required for each simulation when an interstitial pore liquid is present, we were not able to perform any cyclic shearing.

Although limited, the proposed numerical model contains all the appropriate features for simulating granular media liquefaction. Further conclusions and suggestions for the improvement of the study of discrete saturated granular media are given in the following chapter.

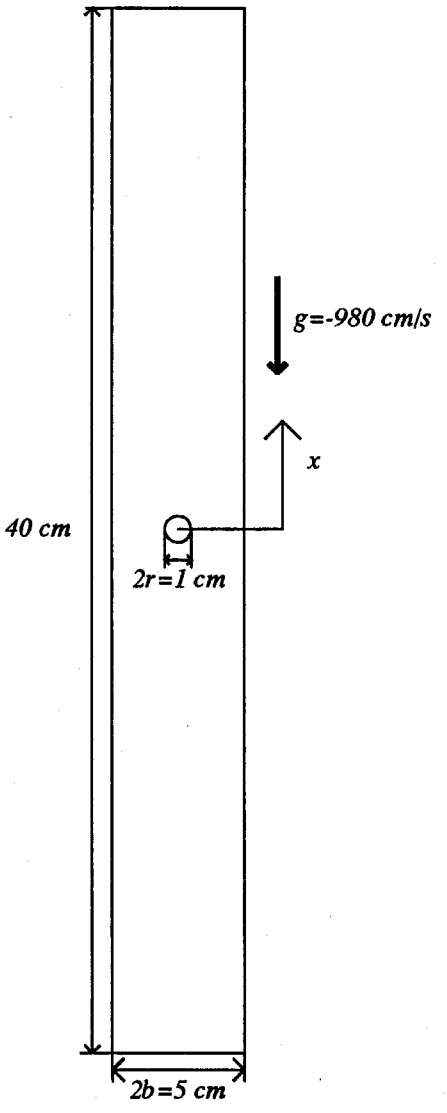

Figure 5.1: One disc falling symmetrically in a viscous fluid between two parallel walls: Geometry

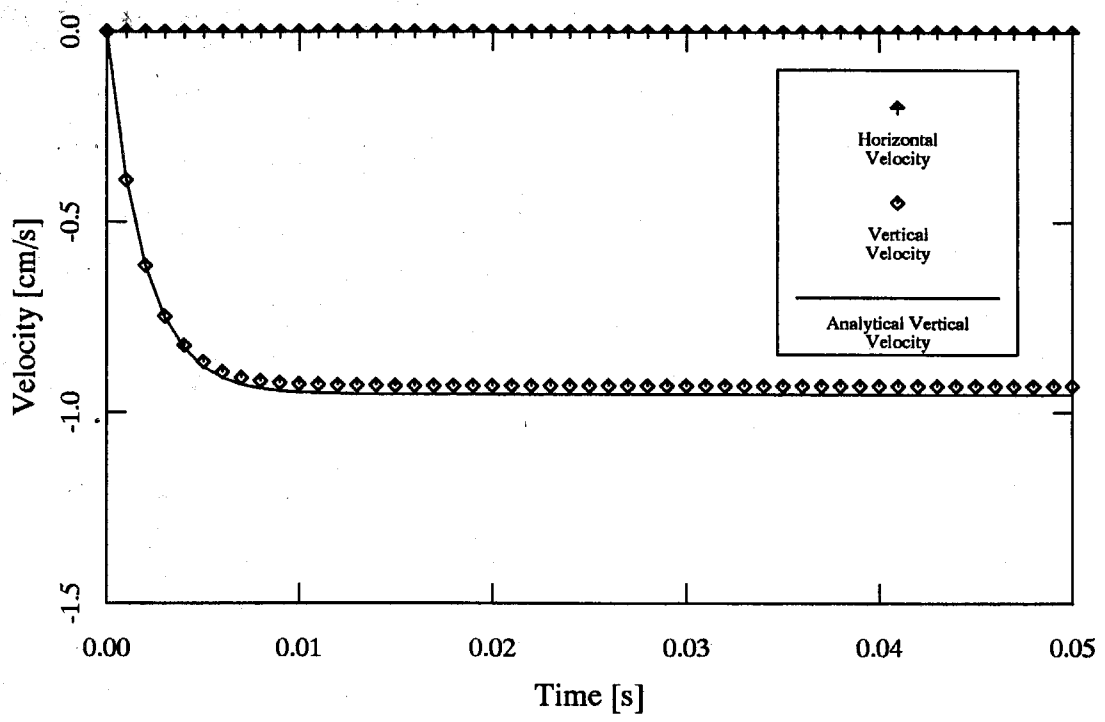

Figure 5.2: One disc falling symmetrically in a viscous fluid between two parallel walls: Disc Velocity

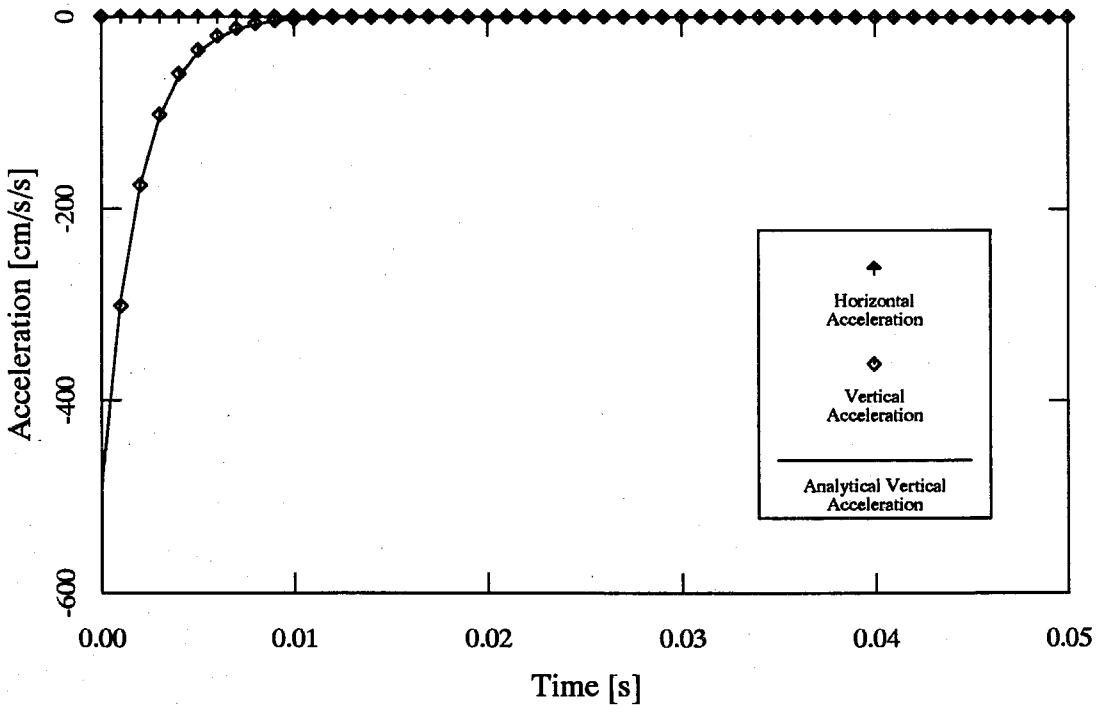

Figure 5.3: One disc falling symmetrically in a viscous fluid between two parallel walls: Disc Acceleration

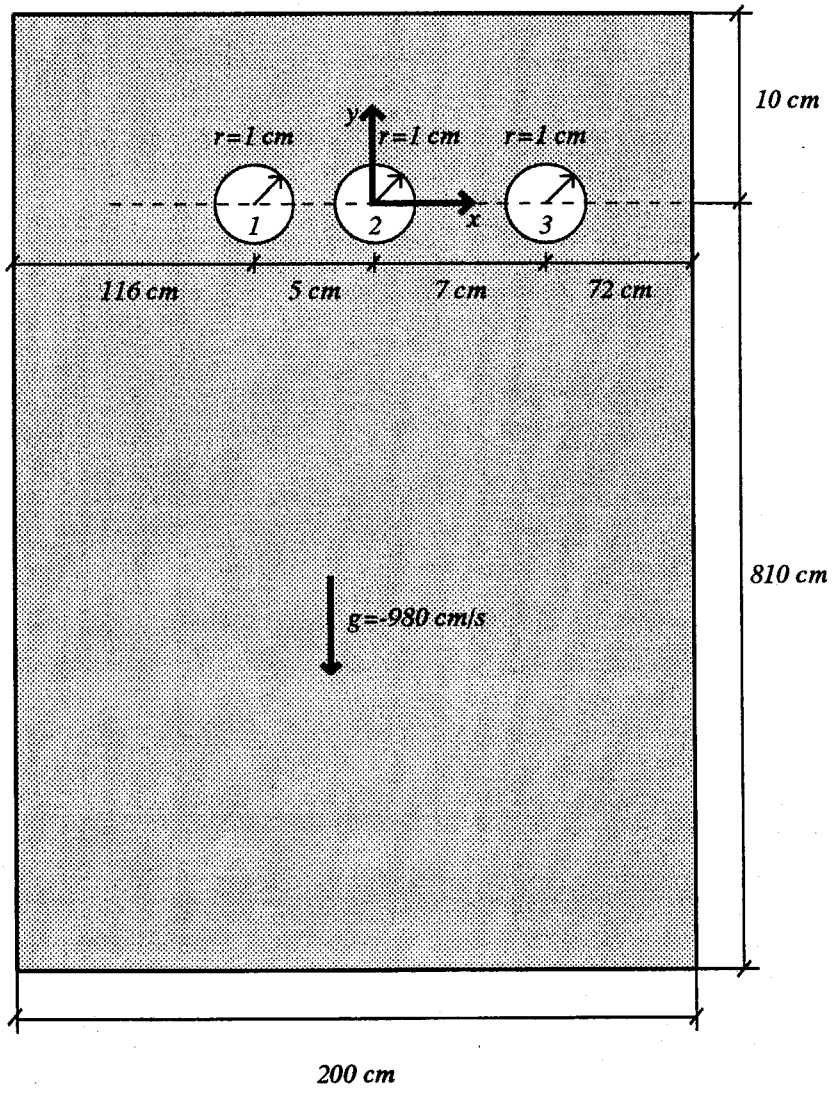

Figure 5.4: Sedimentation of three discs: Geometry (not to scale)

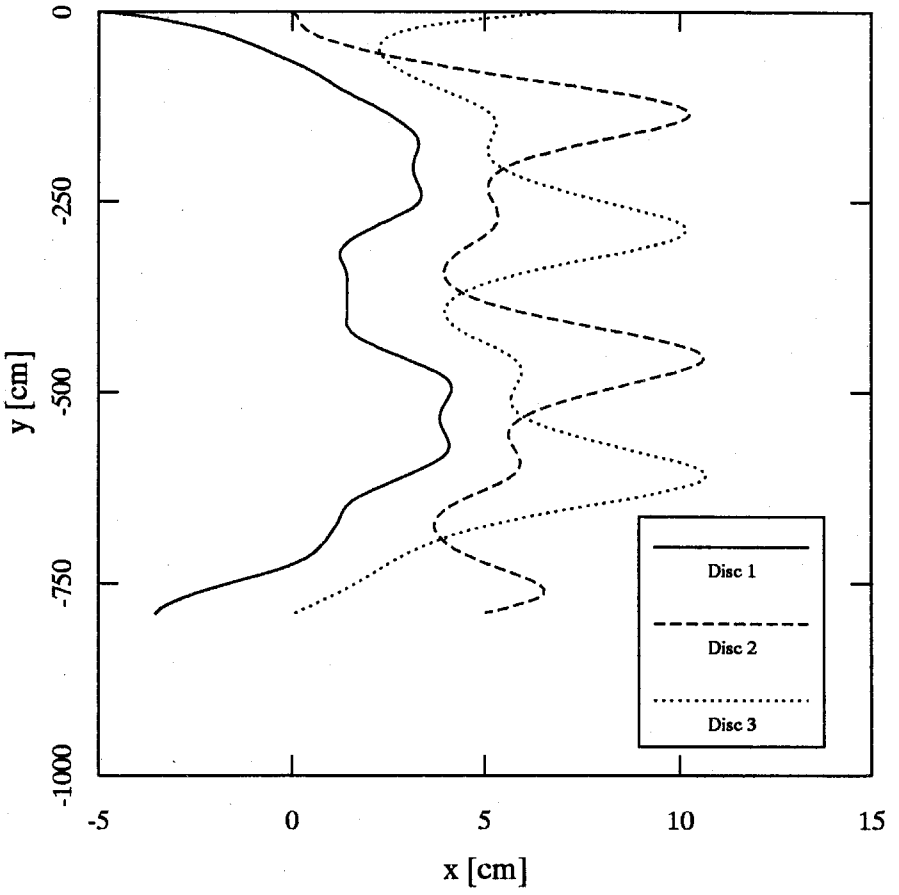

Figure 5.5: Sedimentation of three discs: Trajectories

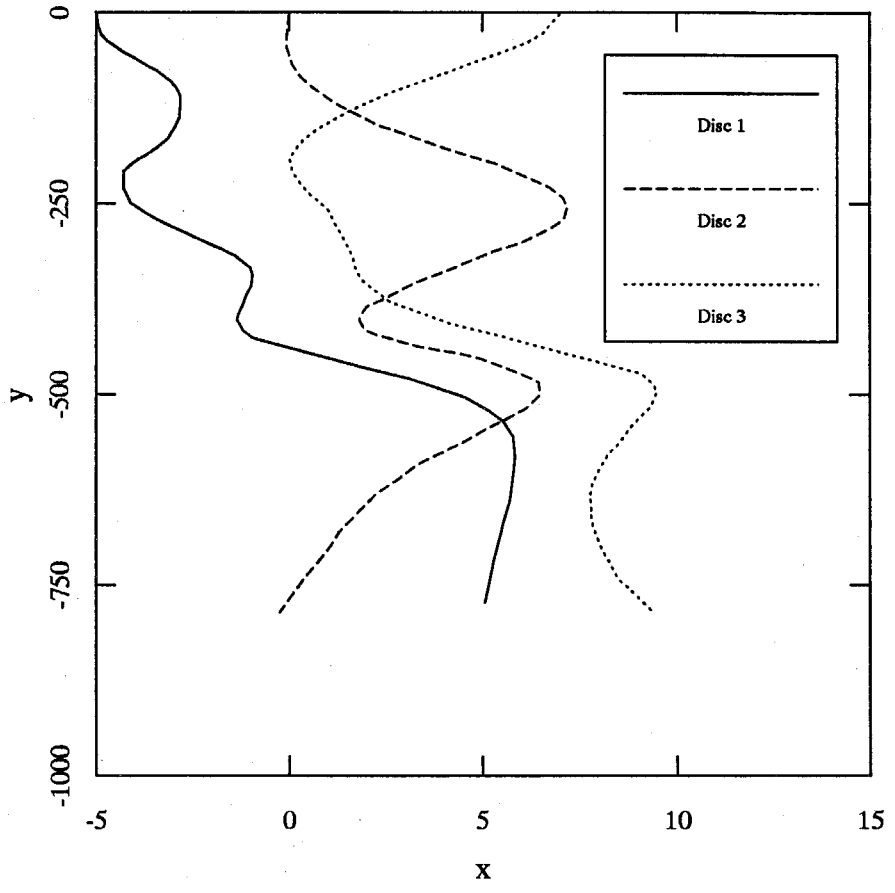

Figure 5.6: Sedimentation of three discs: Trajectories (after Durlofsky, 1987)

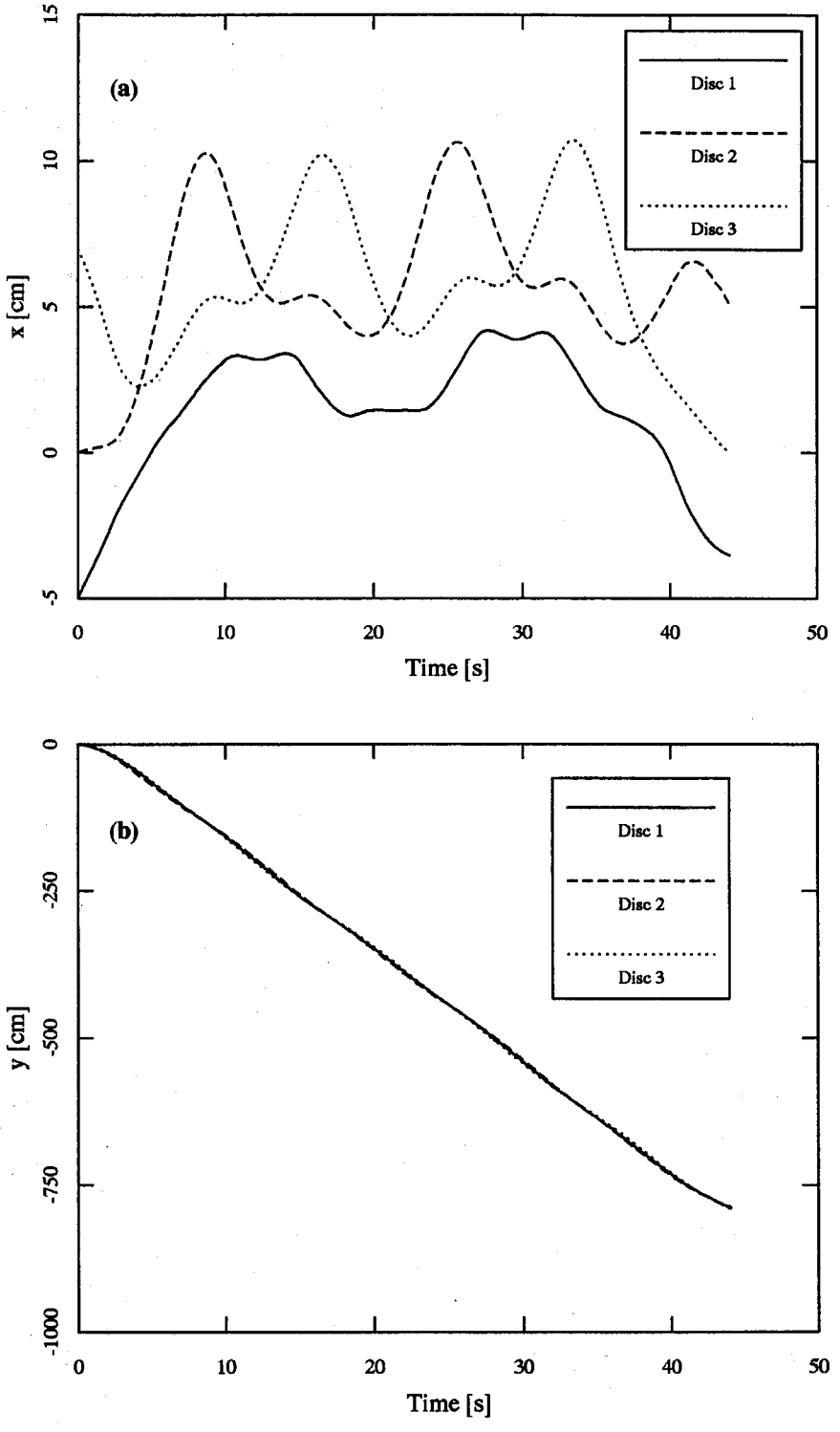

Figure 5.7: Sedimentation of three discs: Position of discs–(a) in the x direction, (b) in the y direction

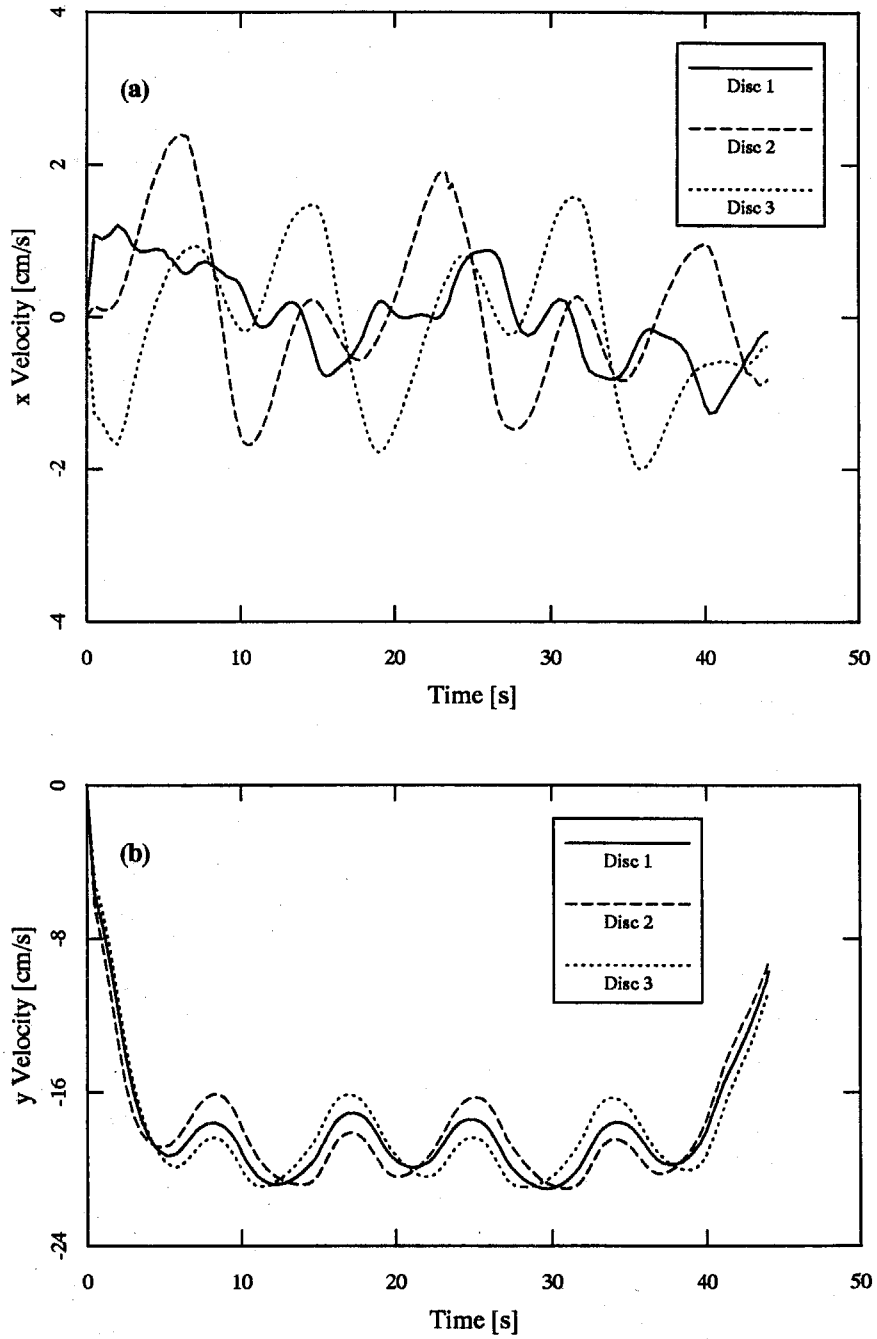

Figure 5.8: Sedimentation of three discs: Velocity of discs–(a) in the x direction, (b) in the y direction

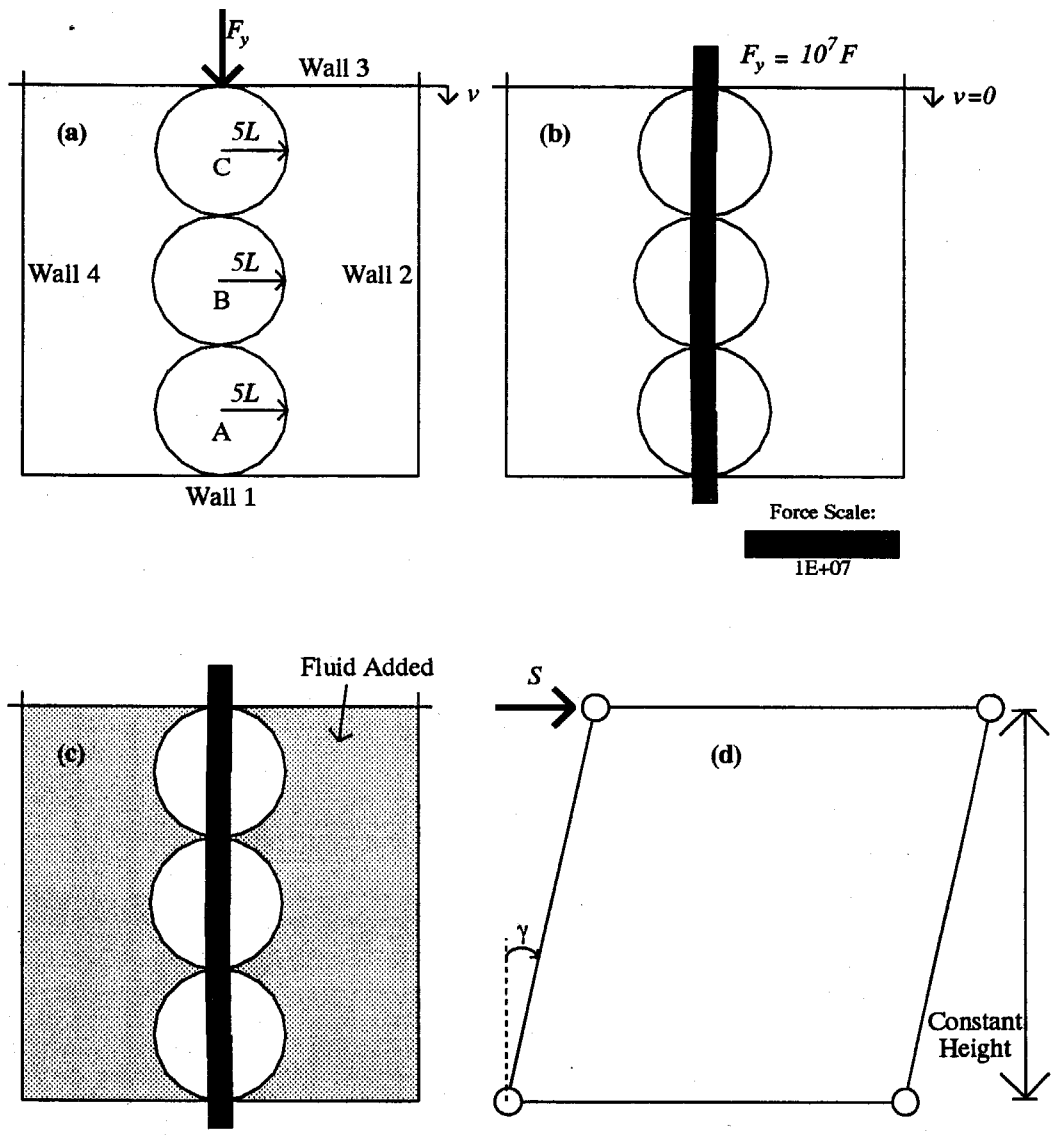

Figure 5.9: Artificial liquefaction simulation: (a) Geometry, (b) Generation of contact forces, (c) Addition of fluid, (d) Shear mechanism

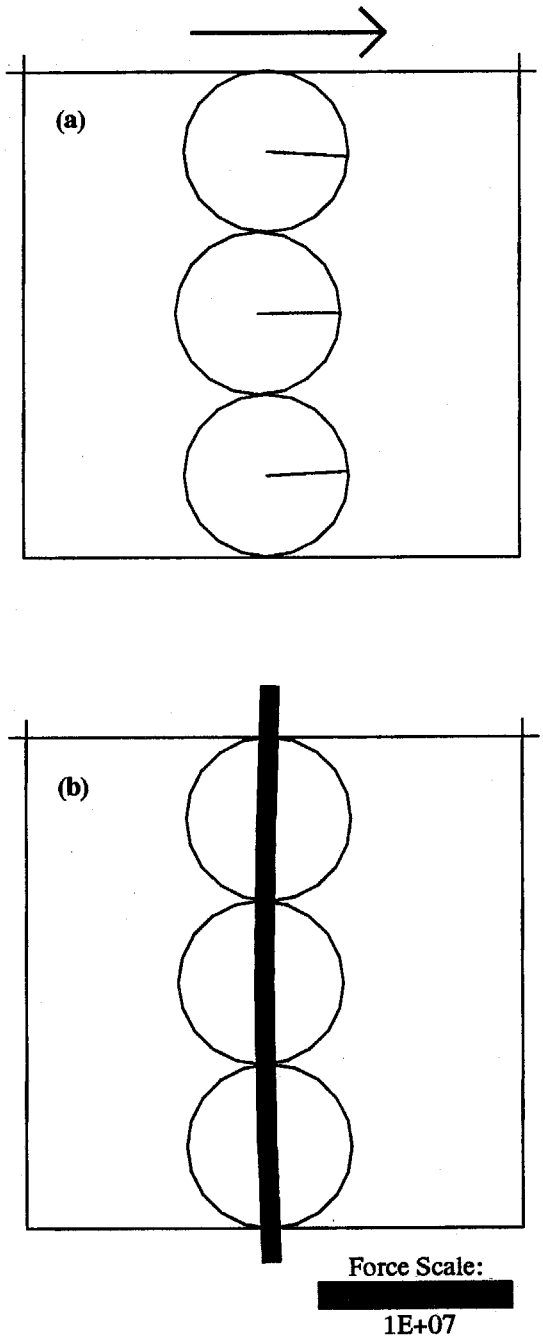

Figure 5.10: Artificial liquefaction simulation (γ=0.35%) : (a) Configuration, (b) Contact forces diagram

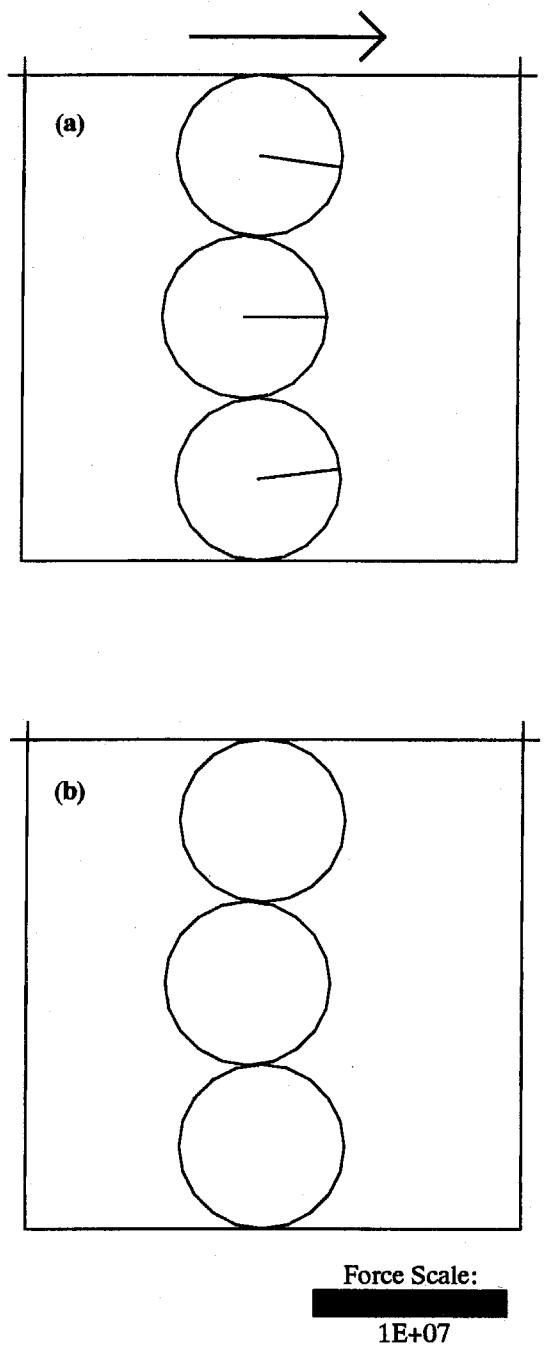

Figure 5.11: Artificial liquefaction simulation (γ=0.7%) : (a) Configuration, (b) Contact forces diagram

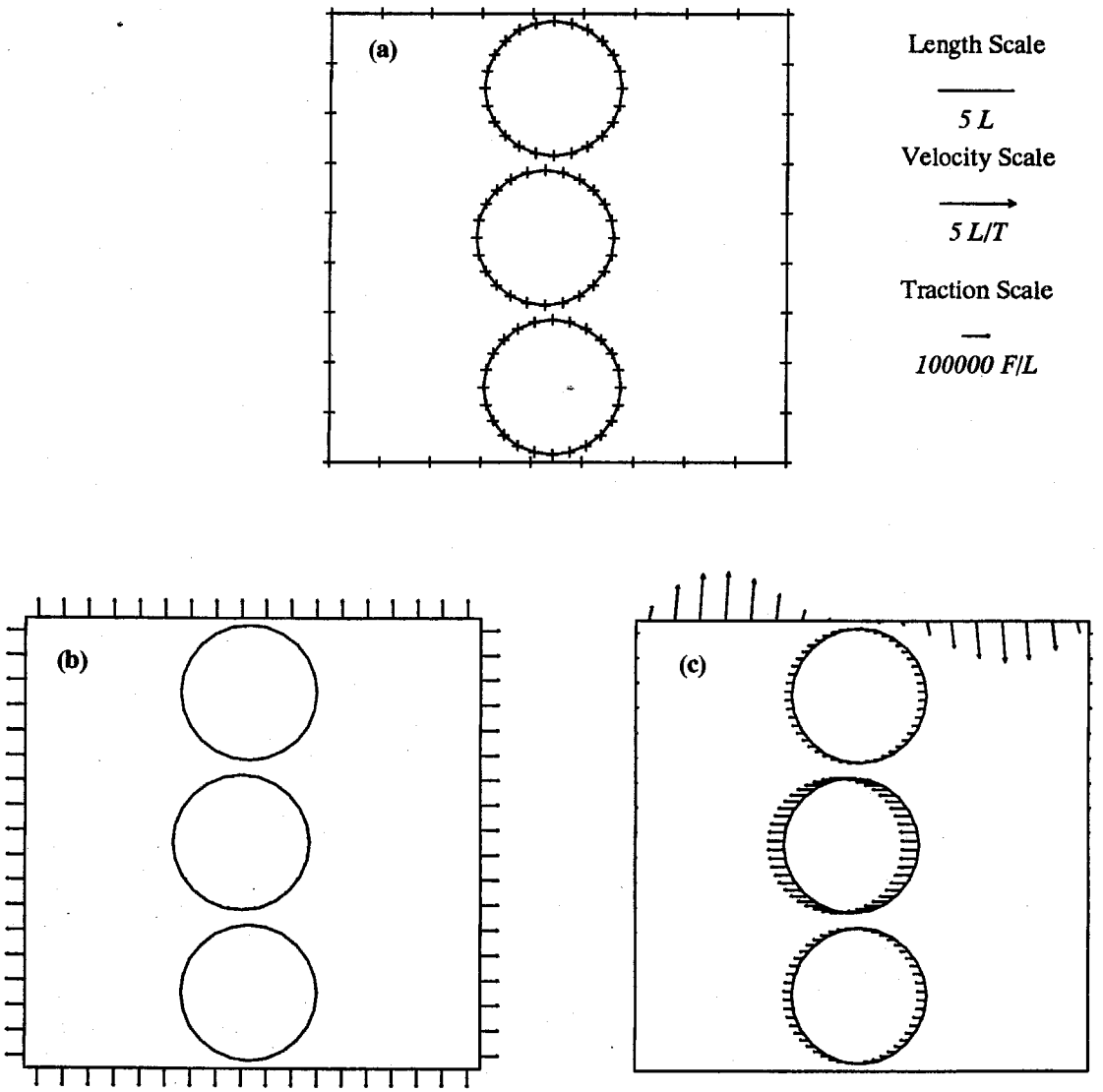

Figure 5.12: Artificial liquefaction simulation (γ=0.35%) : (a) Boundary element discretization, (b) Traction field, (c) Velocity field

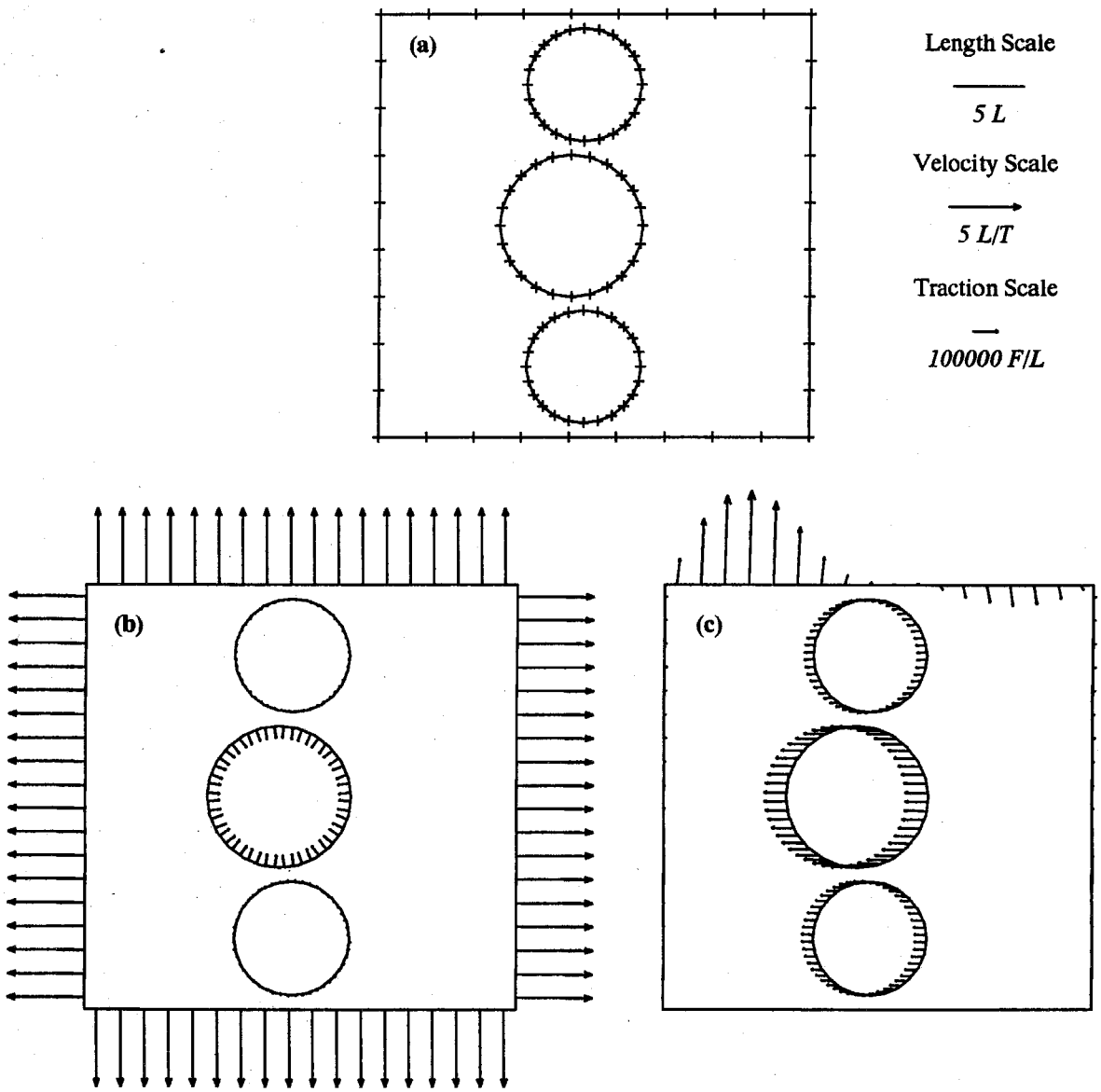

Figure 5.13: Artificial liquefaction simulation (γ=0.7%) : (a) Boundary element discretization, (b) Traction field, (c) Velocity field

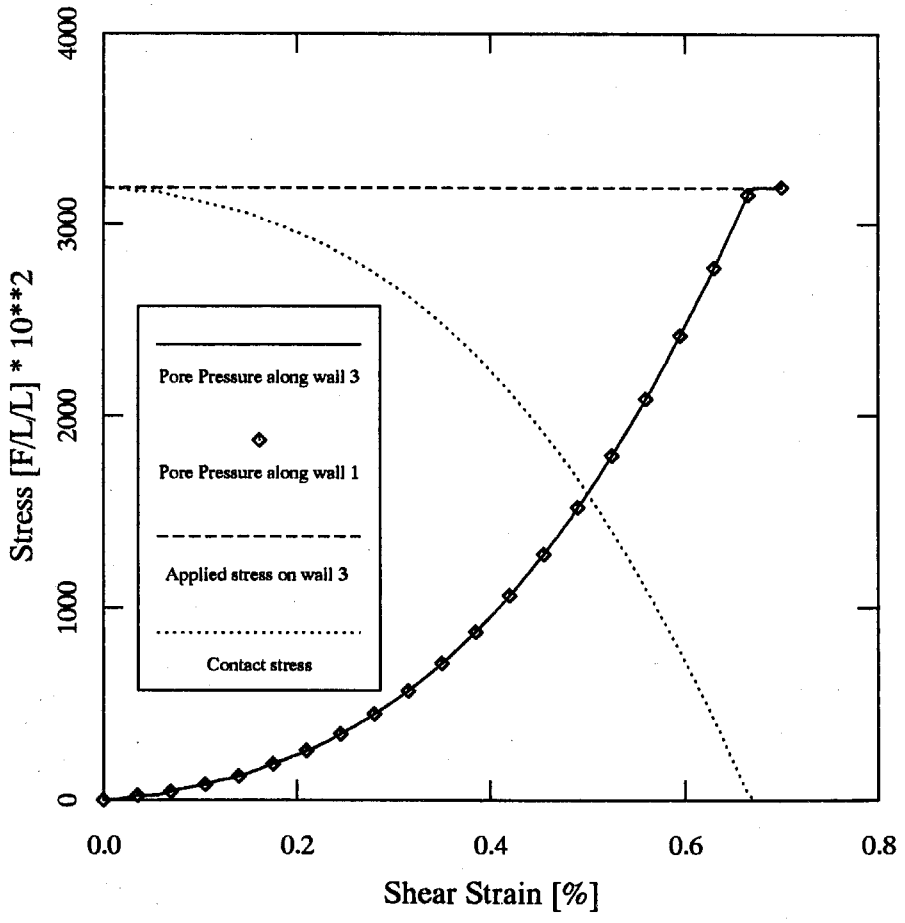

Figure 5.14: Artificial liquefaction simulation (γ=0.7%) : Applied stress, Pressure change along walls 1 and 3, Contact Stress between wall 1 and disc C

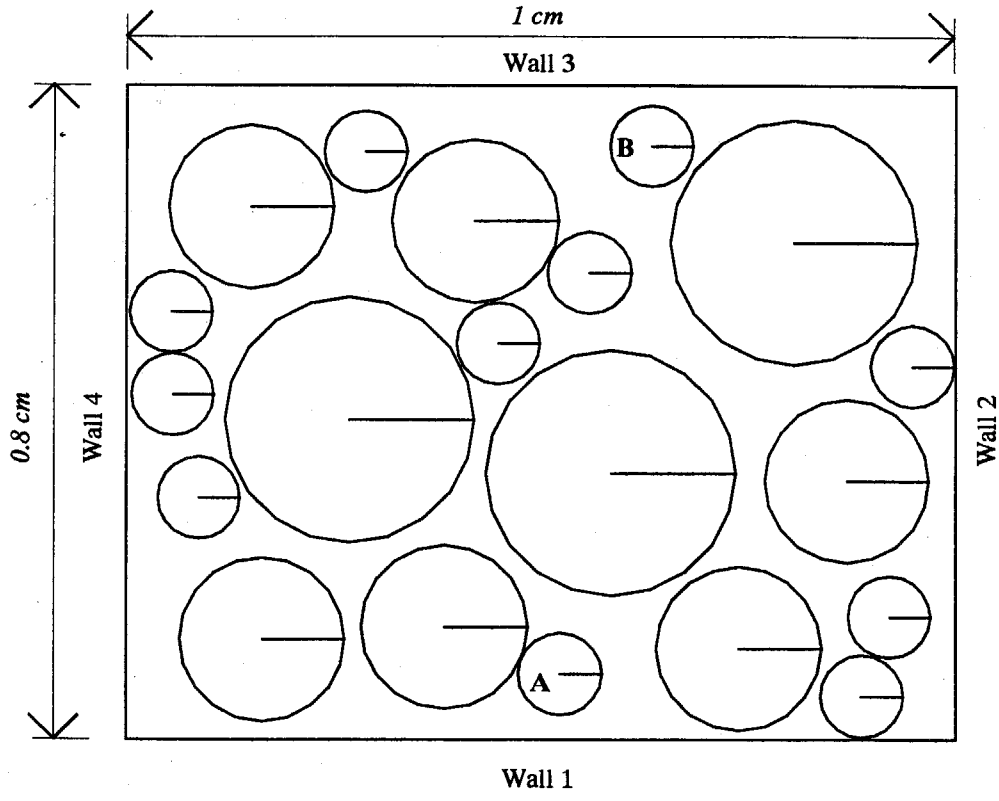

Figure 5.15: Simple shear simulations : initial configuration

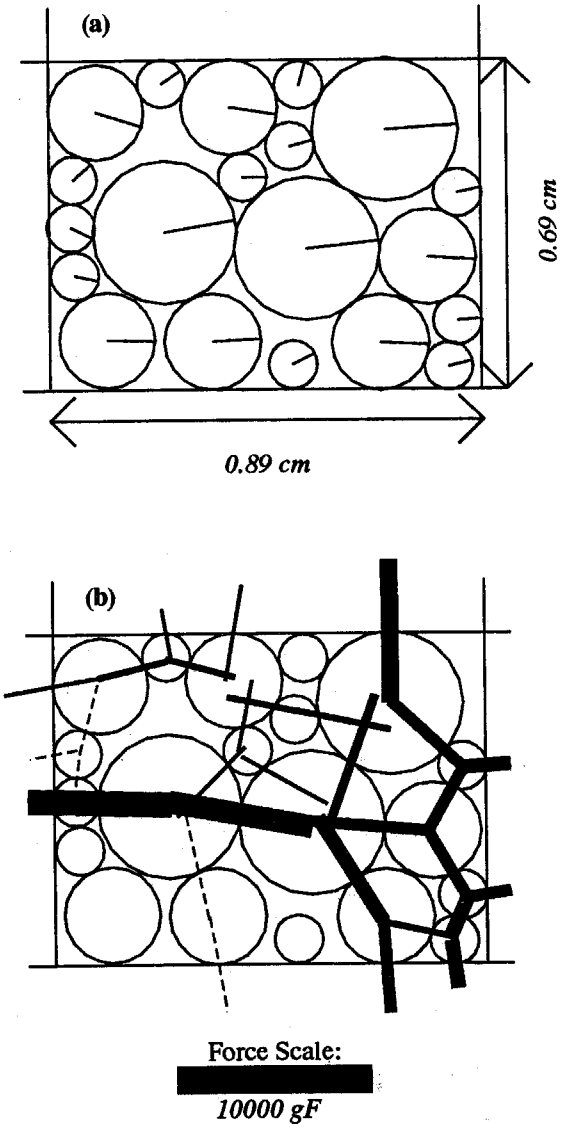

Figure 5.16: Simple shear simulations (dry, loose), end of initial compression–(a) Configuration, (b) Contact force diagram

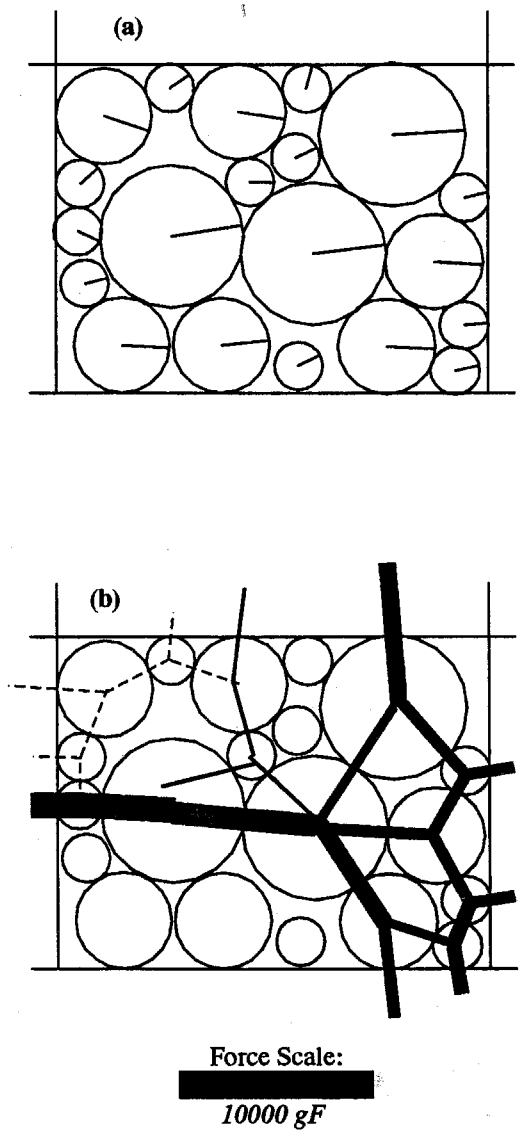

Figure 5.17: Simple shear simulations (dry, loose), end of relaxation period–(a) Configuration, (b) Contact force diagram

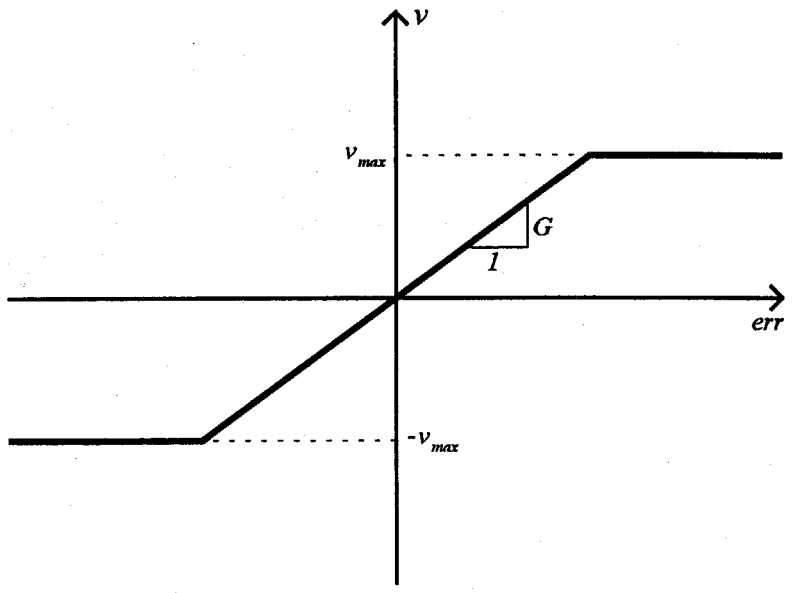

Figure 5.18: Law controlling the velocity of a servo wall

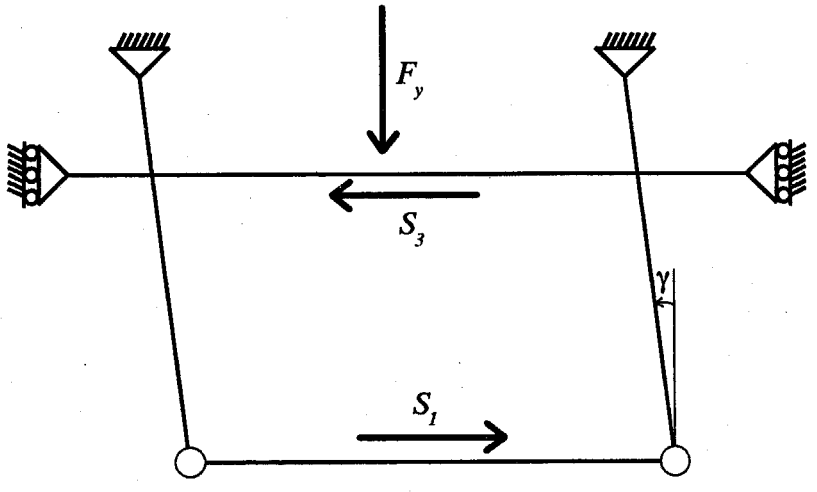

Figure 5.19: Dry simple shear mechanism, with volume change

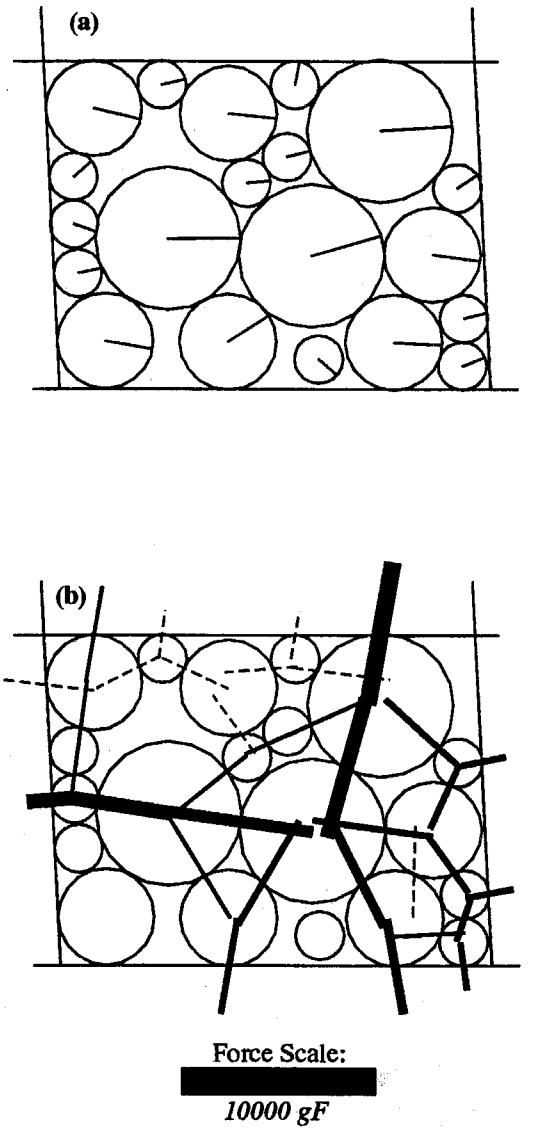

Figure 5.20: Simple shear simulations (dry, loose), γ=4.9%–(a) Configuration, (b) Contact force diagram

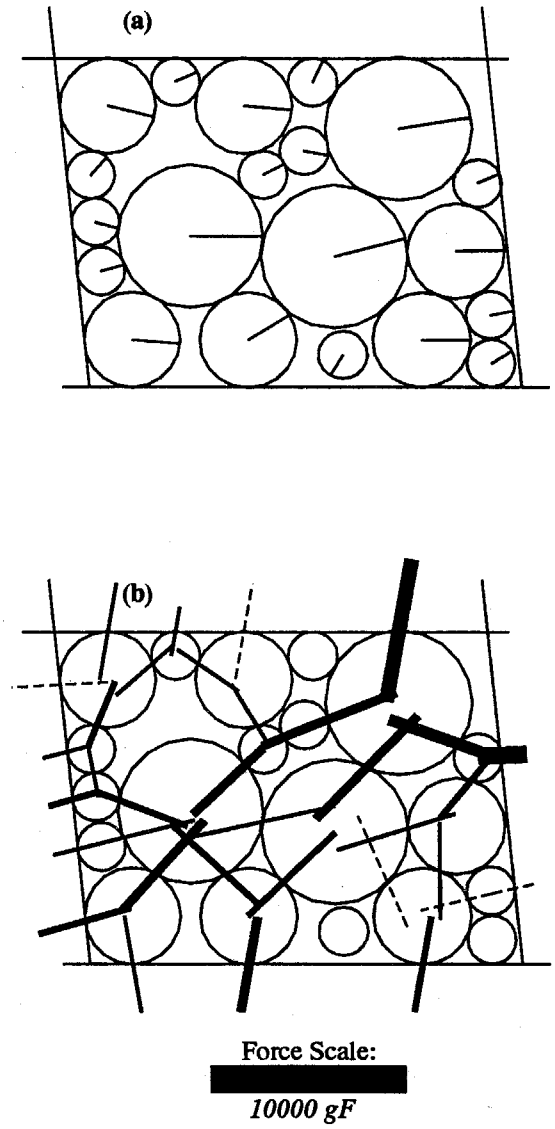

Figure 5.21: Simple shear simulations (dry, loose), γ=10.5%–(a) Configuration, (b) Contact force diagram

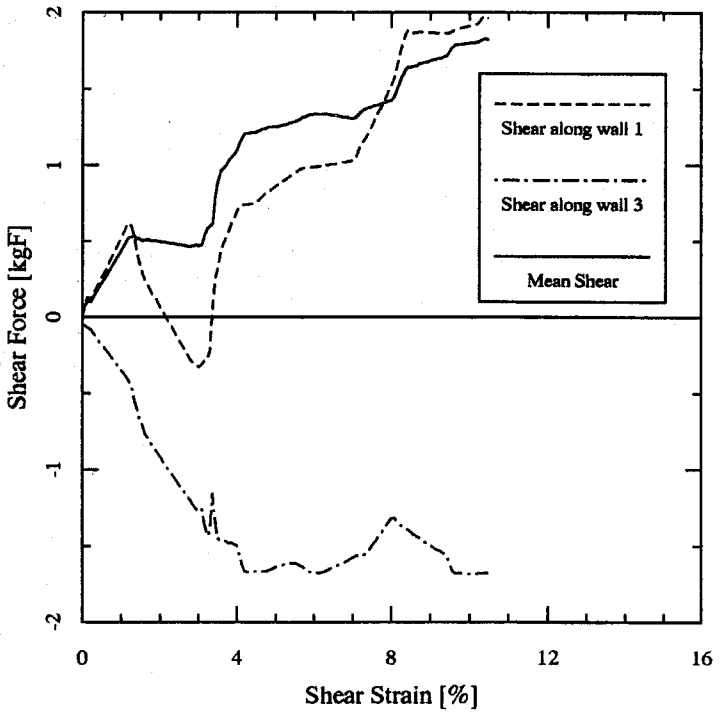

Figure 5.22: Simple shear simulations (dry, loose), Shear force along walls 1 and 3 and their average value

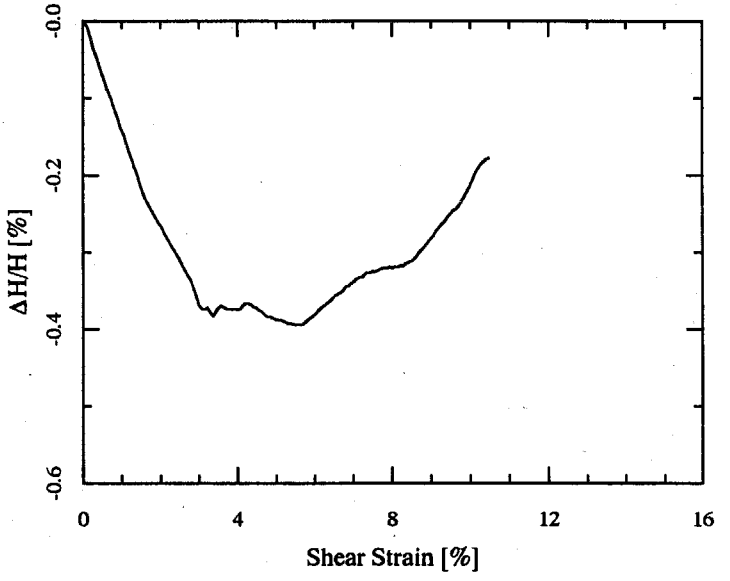

Figure 5.23: Simple shear simulations (dry, loose), Height or volume change

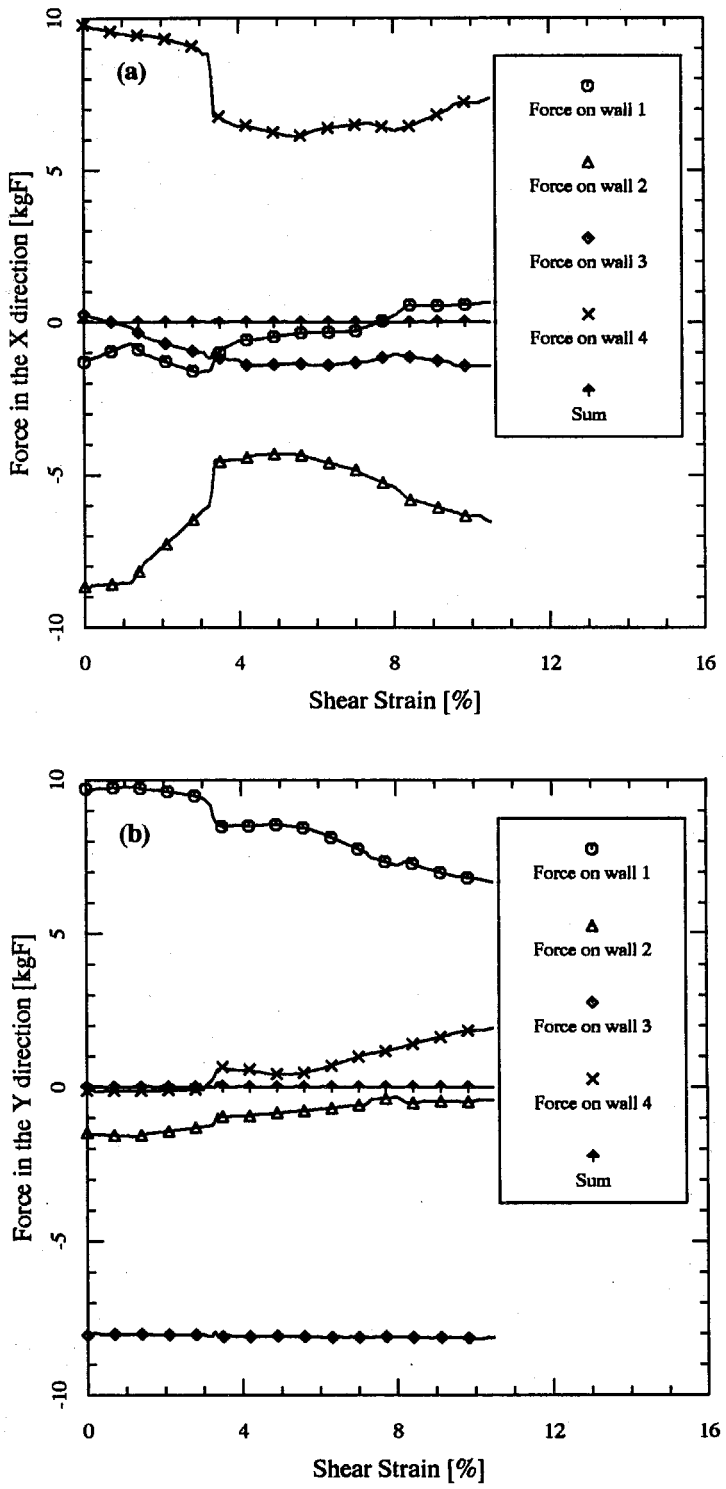

Figure 5.24: Simple shear simulations (dry, loose), Force components along the four walls and their sum–(a) in the X direction, (b) in the Y direction

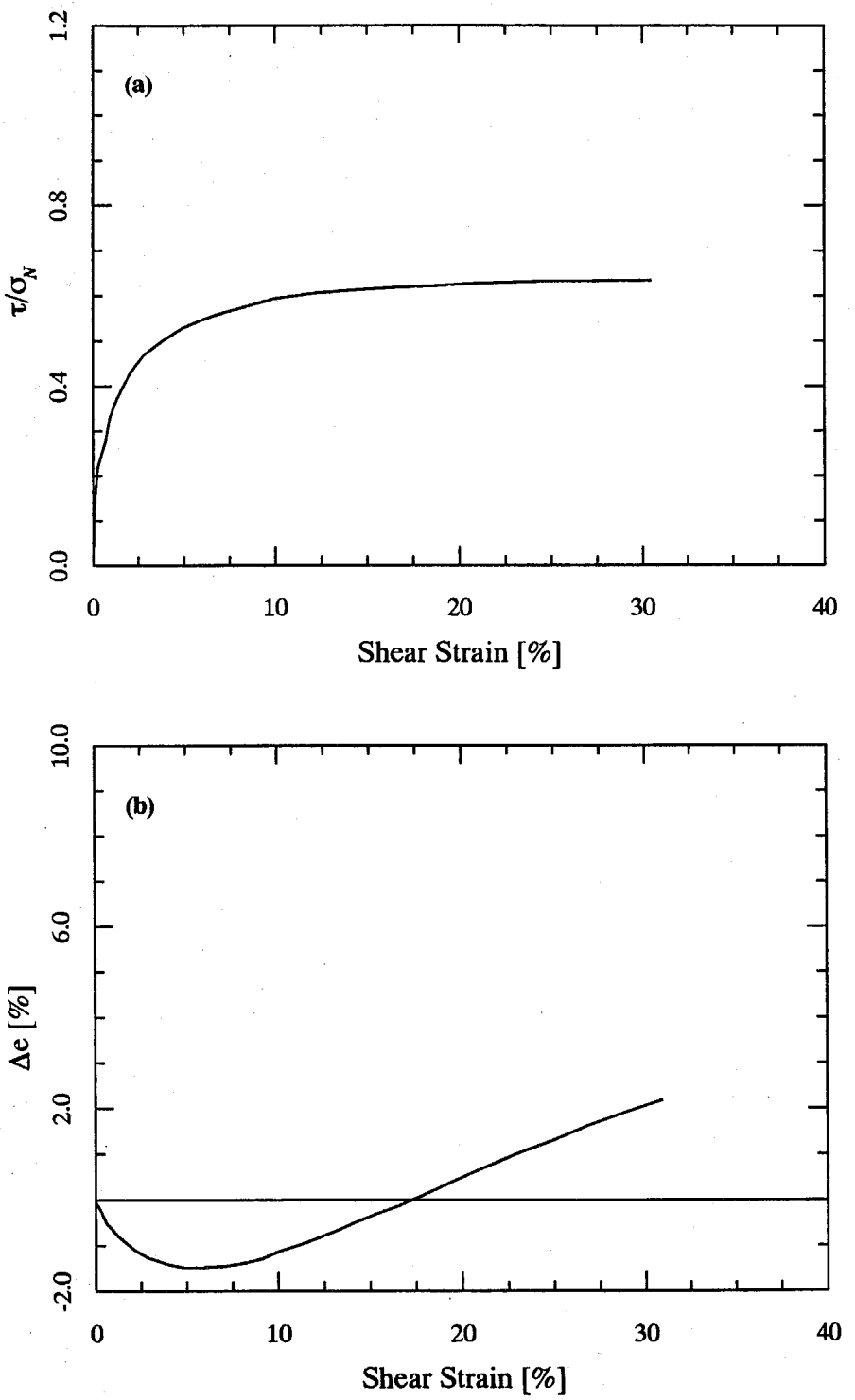

Figure 5.25: Experimental results of simple shear using loose Leighton Buzzard sand–(a) Stress ratio-shear strain relationship, (b) Void ratio change-shear strain relationship (after Cole, 1967

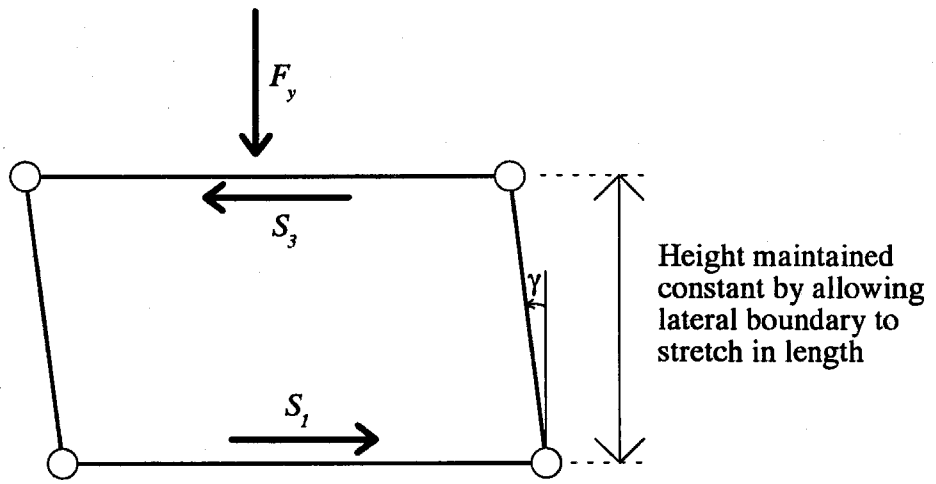

Figure 5.26: Saturated simple shear mechanism (constant volume)

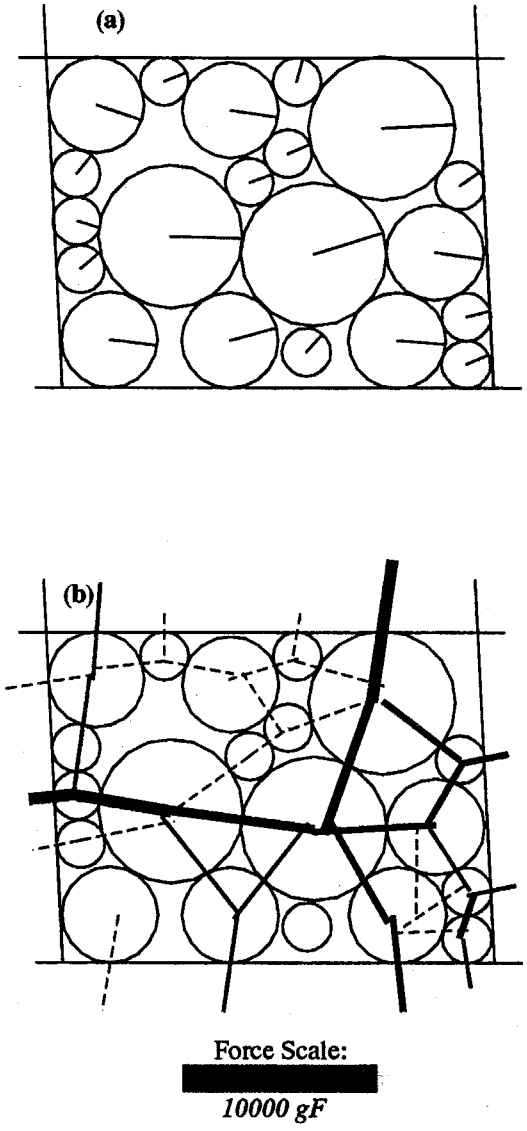

Figure 5.27: Simple shear simulations (saturated, loose), γ=4.9%–(a) Configuration, (b) Contact force diagram

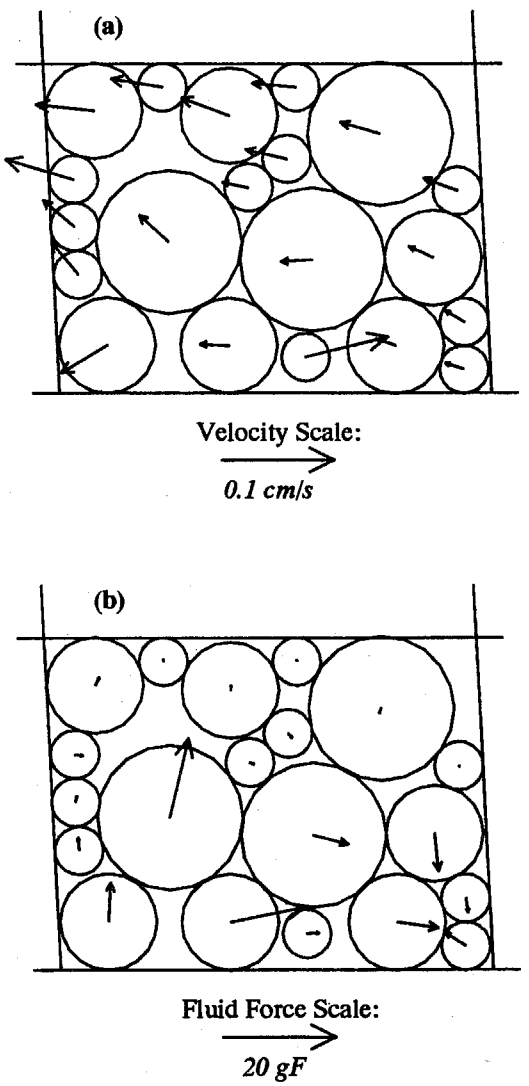

Figure 5.28: Simple shear simulations (saturated, loose), γ=4.9%–(a) Particle velocity, (b) Fluid force on particles

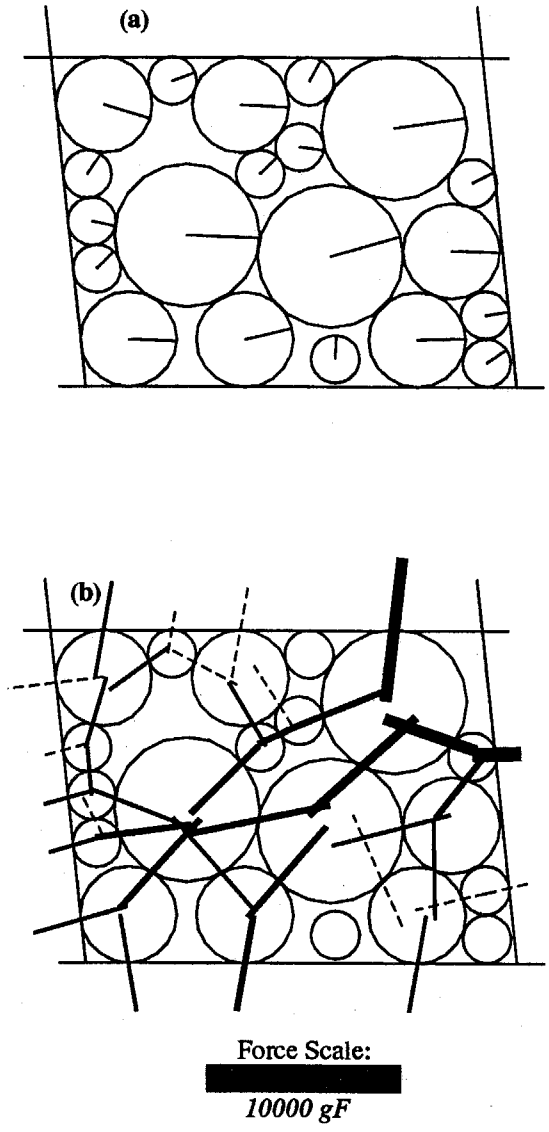

Figure 5.29: Simple shear simulations (saturated, loose), γ=10.5%–(a) Configuration, (b) Contact force diagram

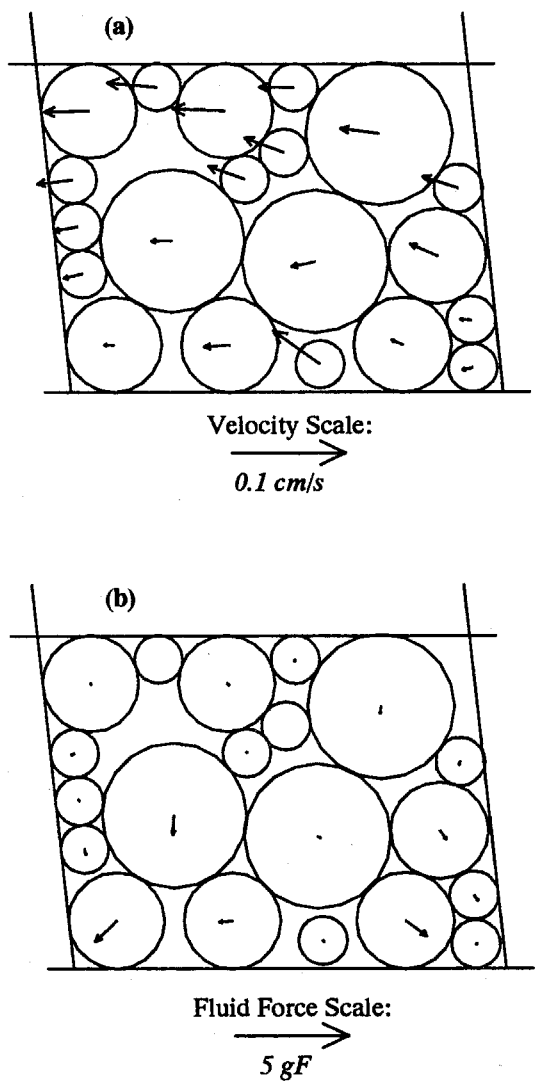

Figure 5.30: Simple shear simulations (saturated, loose), γ=10.5%–(a) Particle velocity, (b) Fluid force on particles

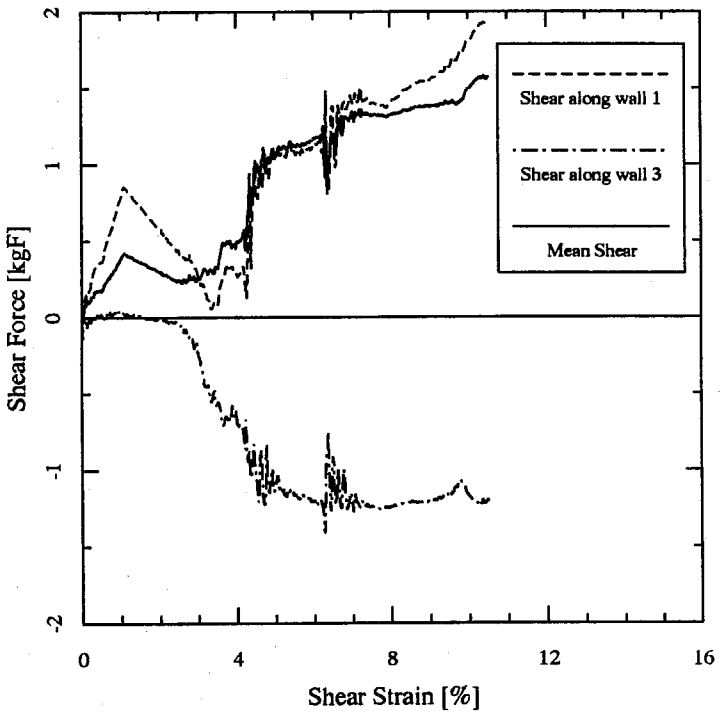

Figure 5.31: Simple shear simulations (saturated, loose), Shear force along walls 1 and 3 and their average values

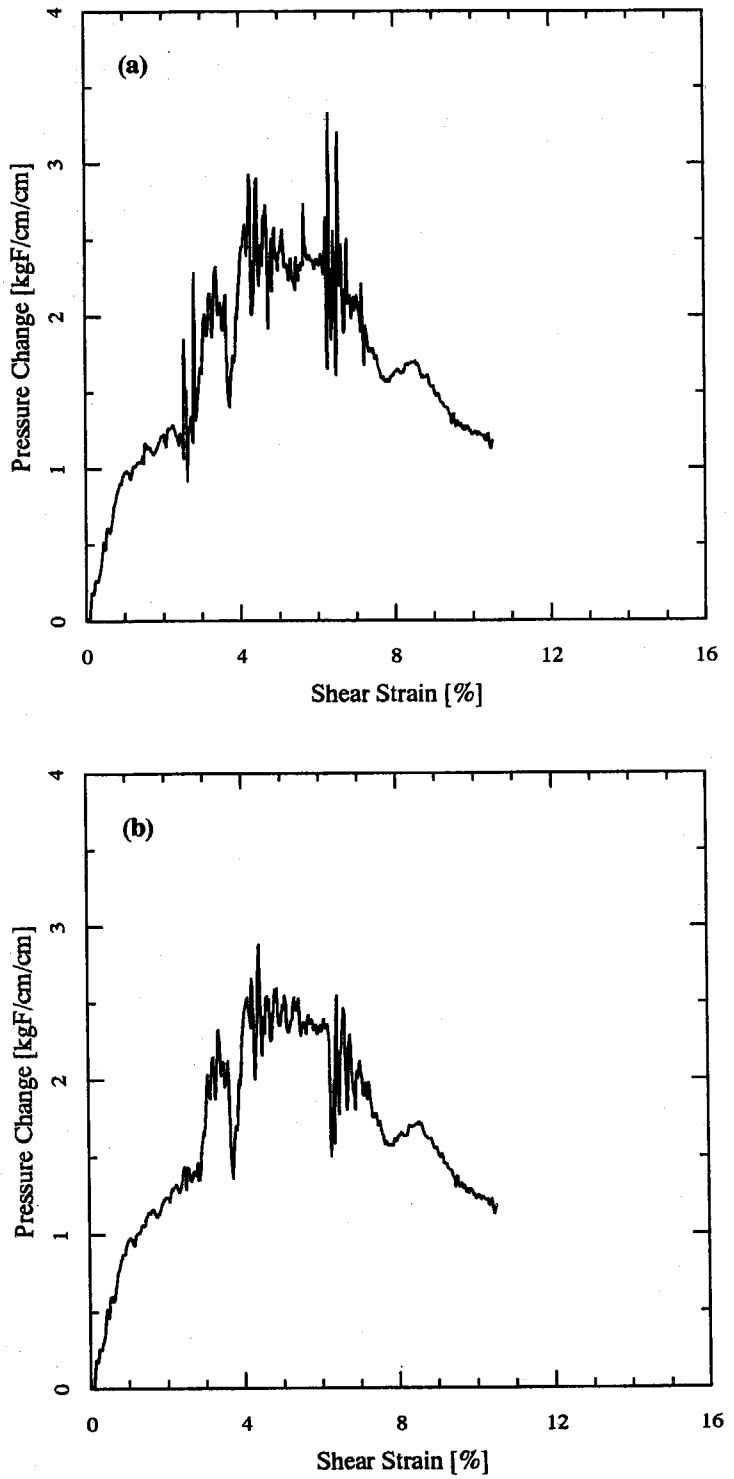

Figure 5.32: Simple shear simulations (saturated, loose), Pore pressure change–(a) along wall 1, (b) along wall 3

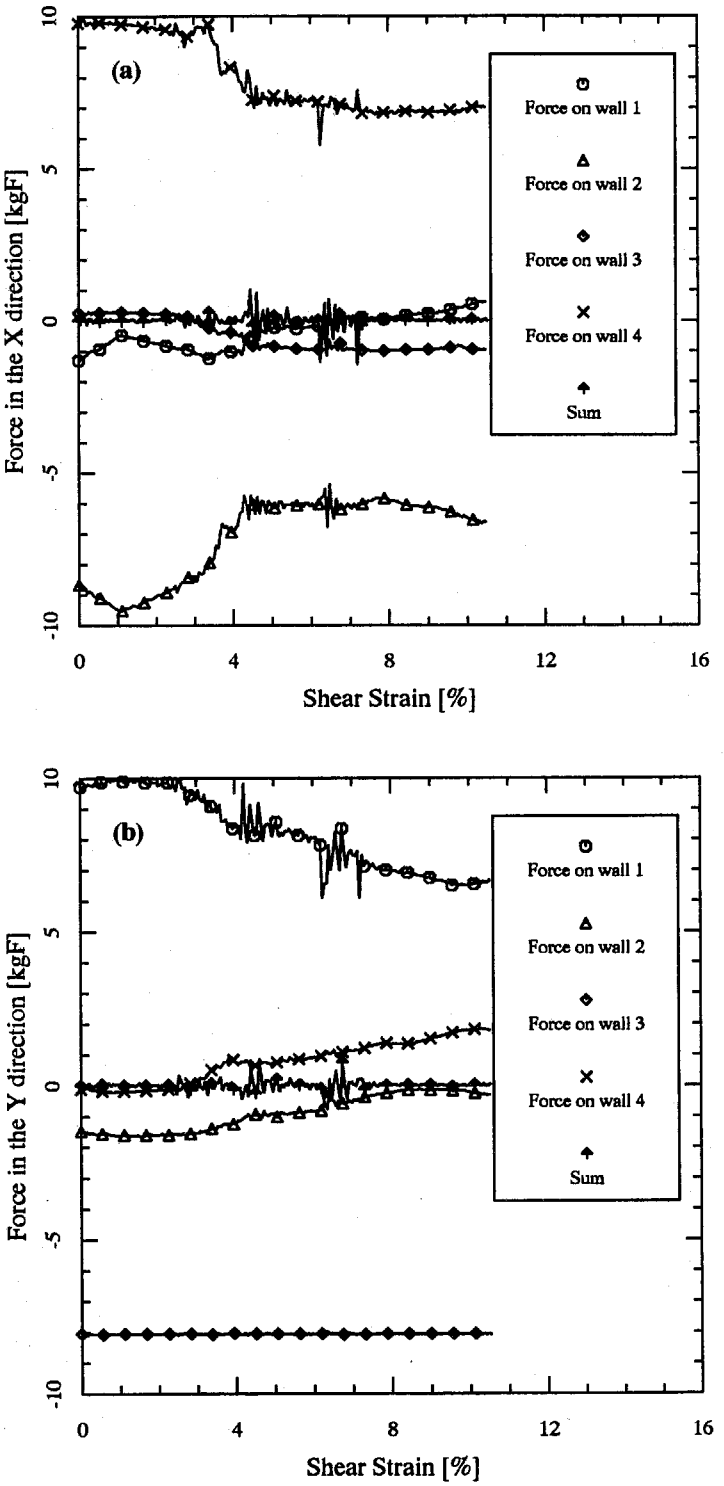

Figure 5.33: Simple shear simulations (saturated, loose), Force components along the four walls and their sum–(a) in the X direction, (b) in the Y direction

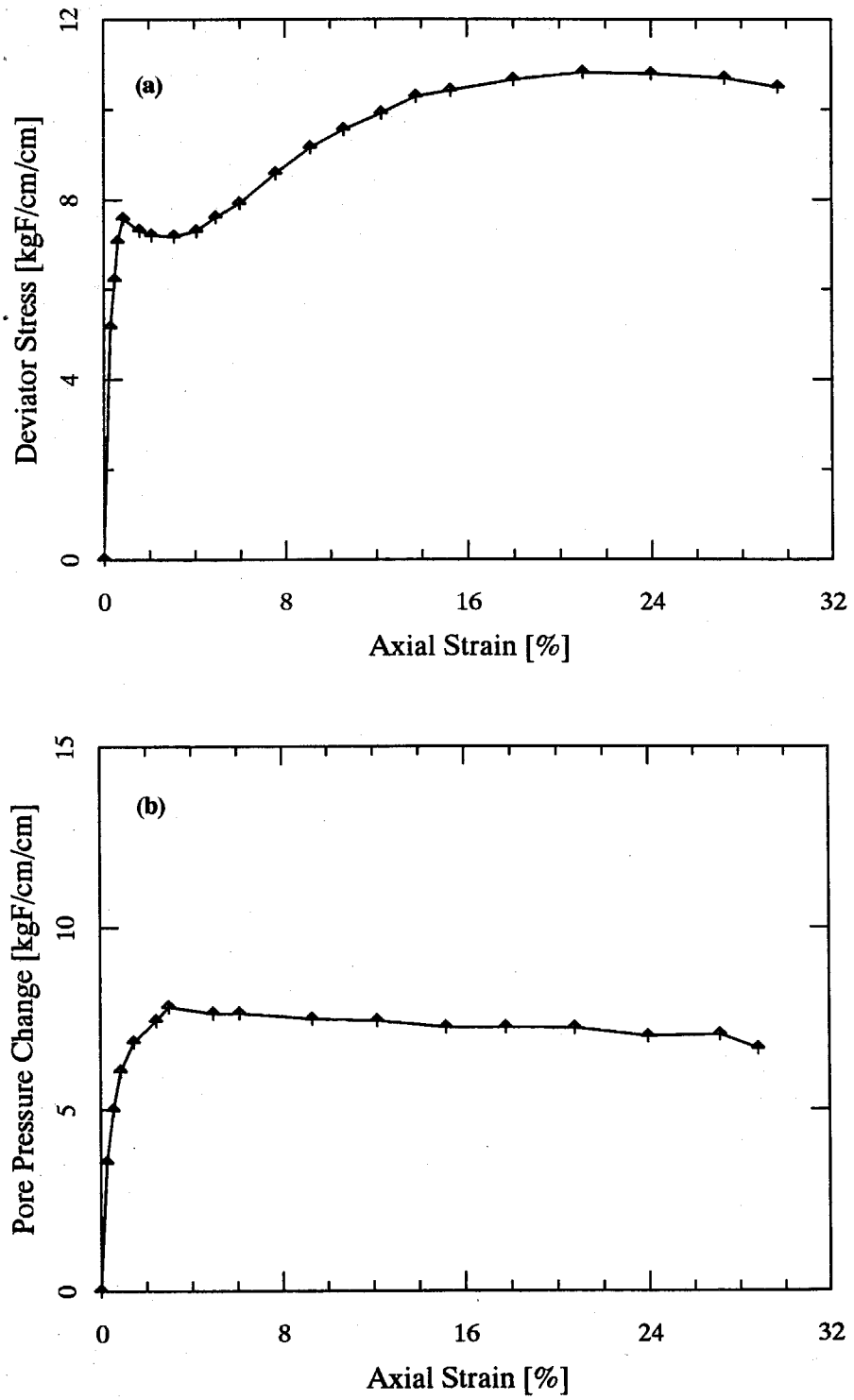

Figure 5.34: Experimental results of undrained triaxial test using loose Sacramento sand–(a) Stress-strain relationship, (b) Pore pressure change-strain relationship (after Seed, 1967)

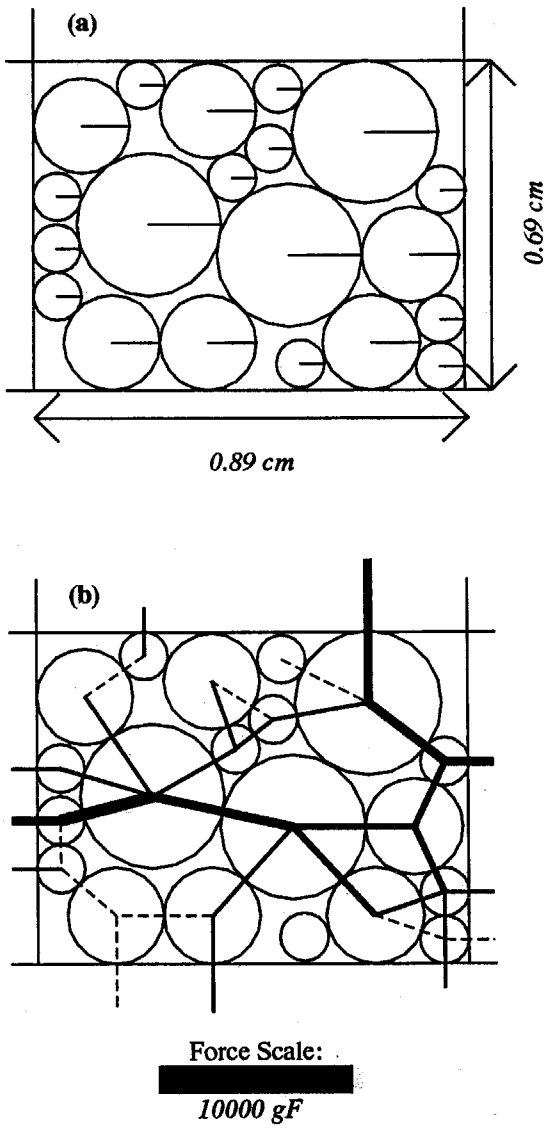

Figure 5.35: Simple shear simulations (dry, dense), end of initial compression–(a) Configuration, (b) Contact force diagram

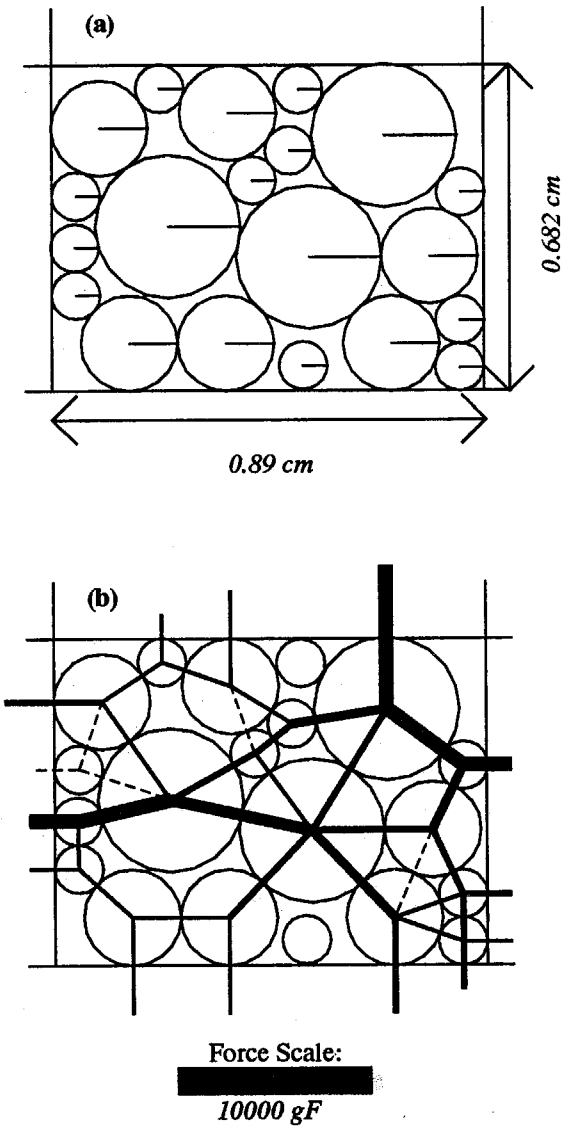

Figure 5.36: Simple shear simulations (dry, dense), end of second compression phase–(a) Configuration, (b) Contact force diagram

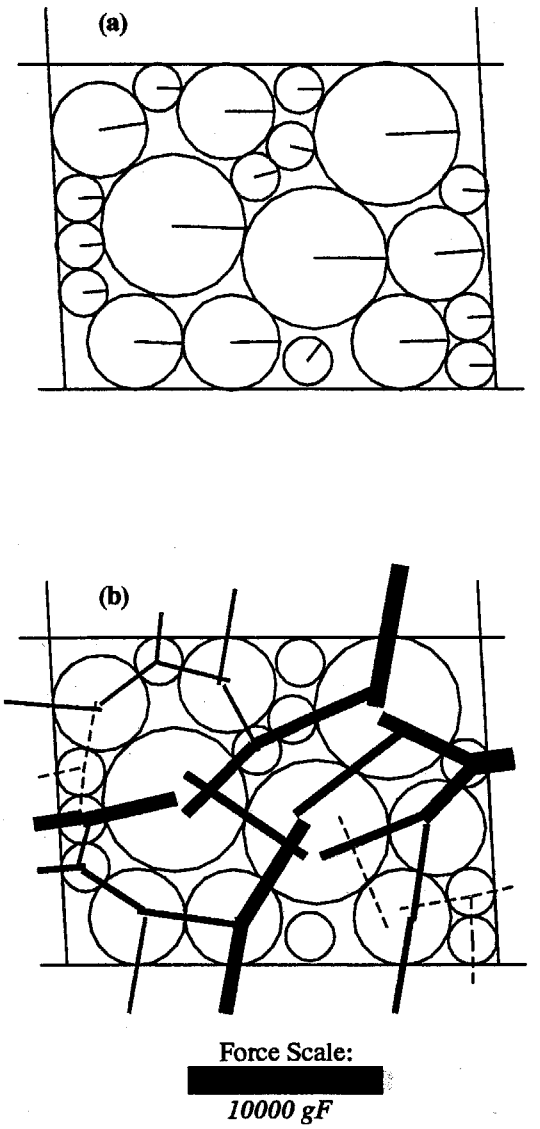

Figure 5.37: Simple shear simulations (dry, dense), γ=5%–(a) Configuration, (b) Contact force diagram

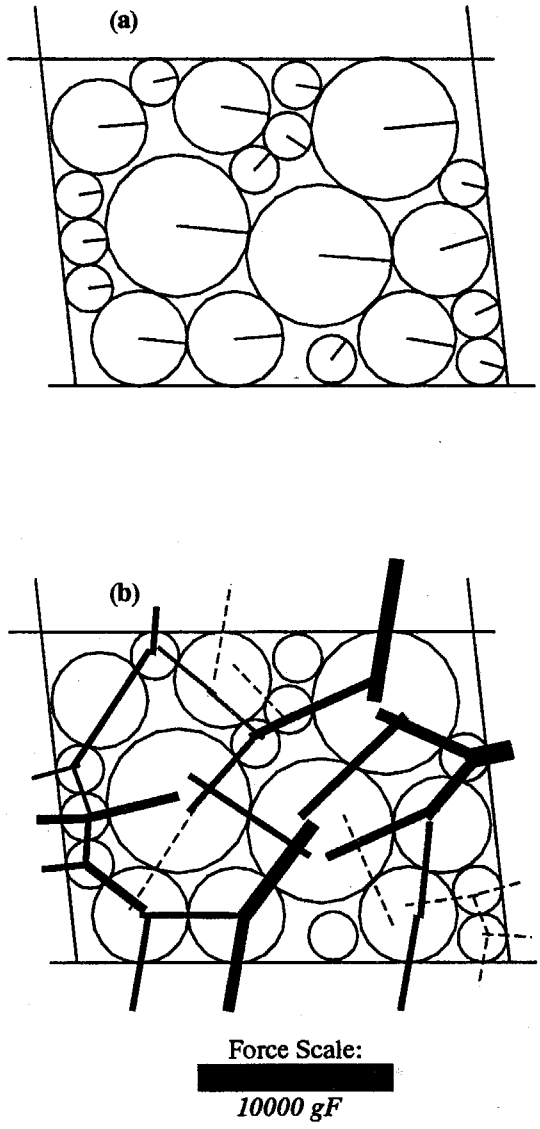

Figure 5.38: Simple shear simulations (dry, dense), γ=10.5%–(a) Configuration, (b) Contact force diagram

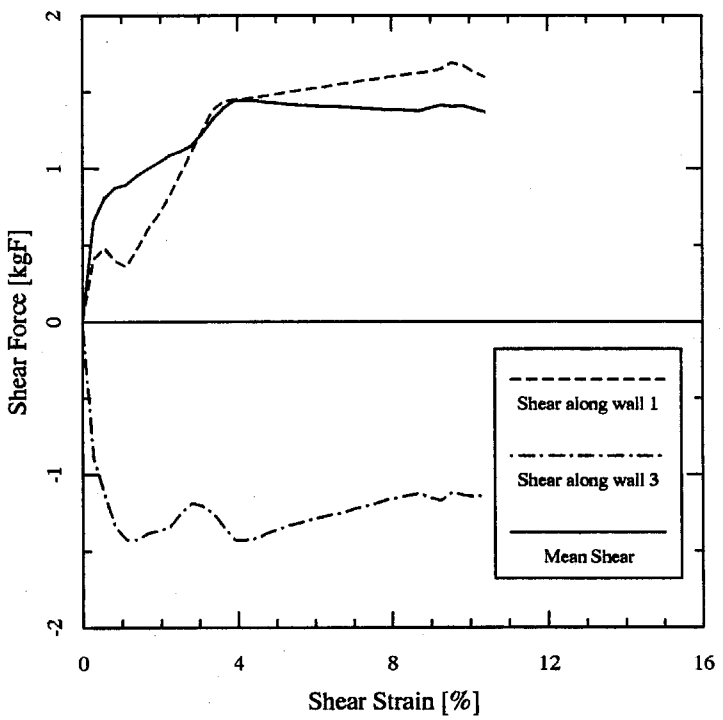

Figure 5.39: Simple shear simulations (dry, dense), Shear force along walls 1 and 3 and their average values

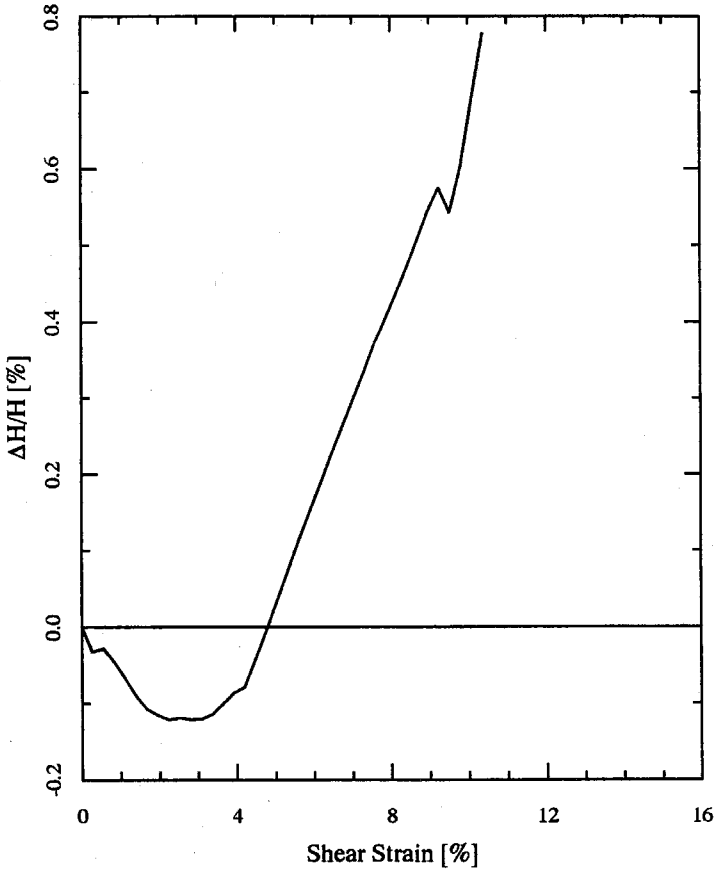

Figure 5.40: Simple shear simulations (dry, dense), Height or volume change

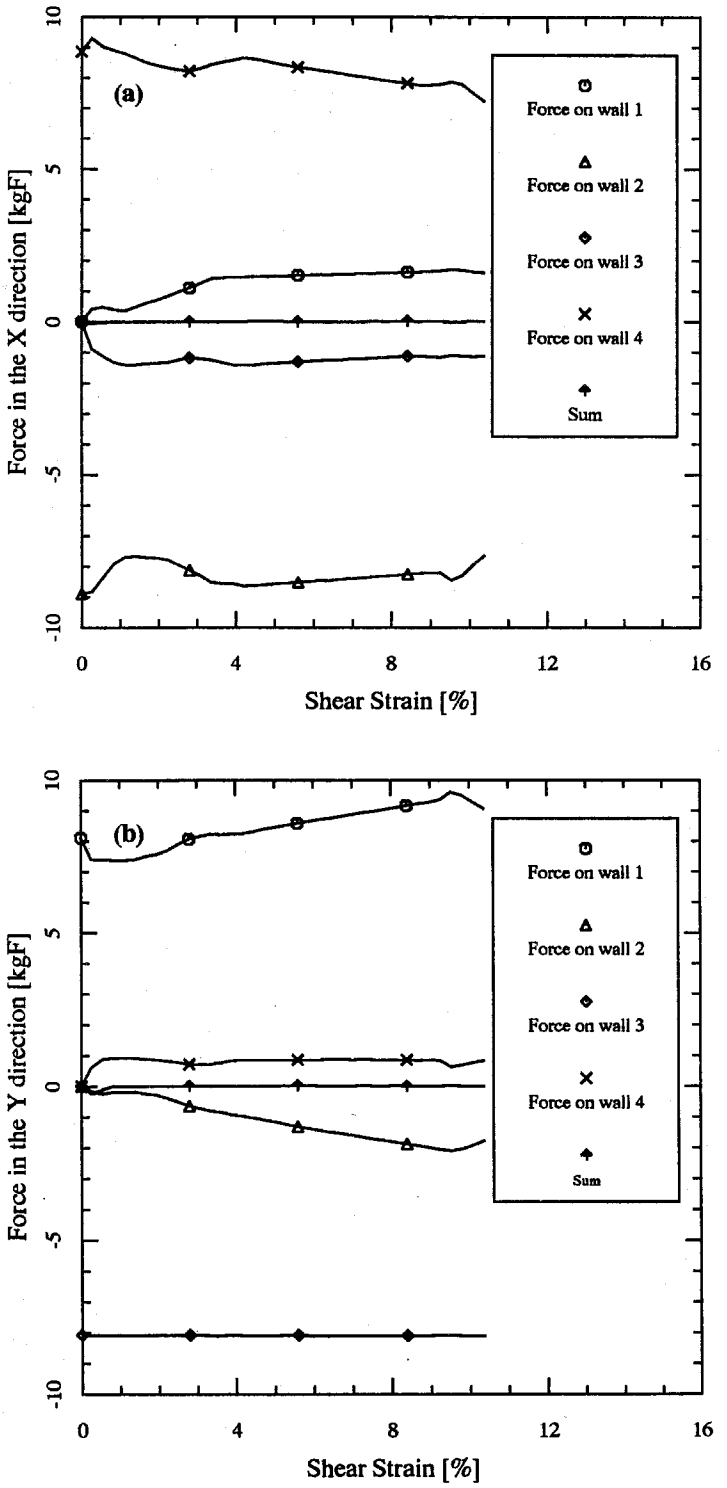

Figure 5.41: Simple shear simulations (dry, dense), Force components along the four walls and their sum–(a) in the X direction, (b) in the Y direction

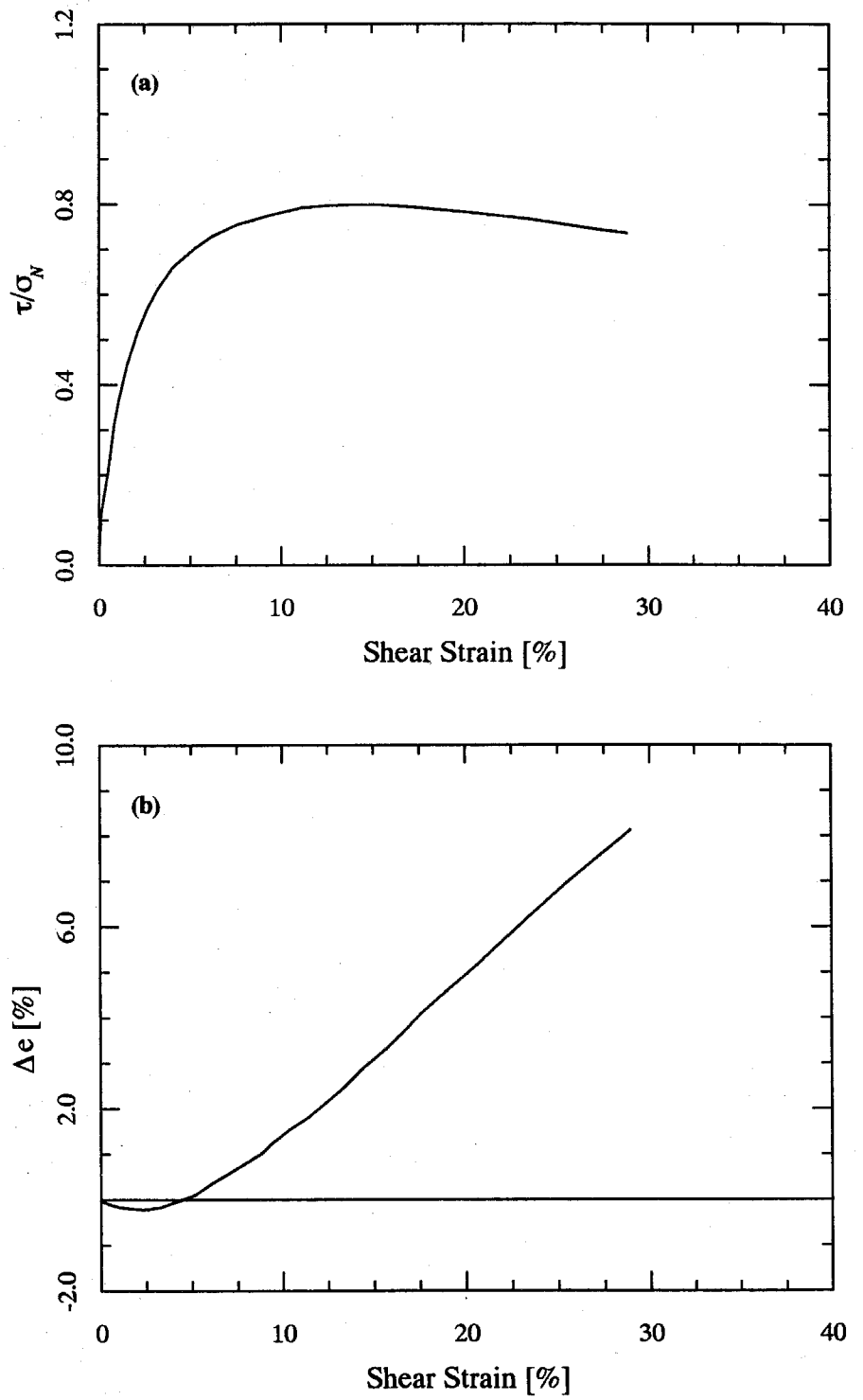

Figure 5.42: Experimental results of simple shear using dense Leighton Buzzard sand–(a) Stress ratio-shear strain relationship, (b) Void ratio change-shear strain relationship (after Cole, 1967)

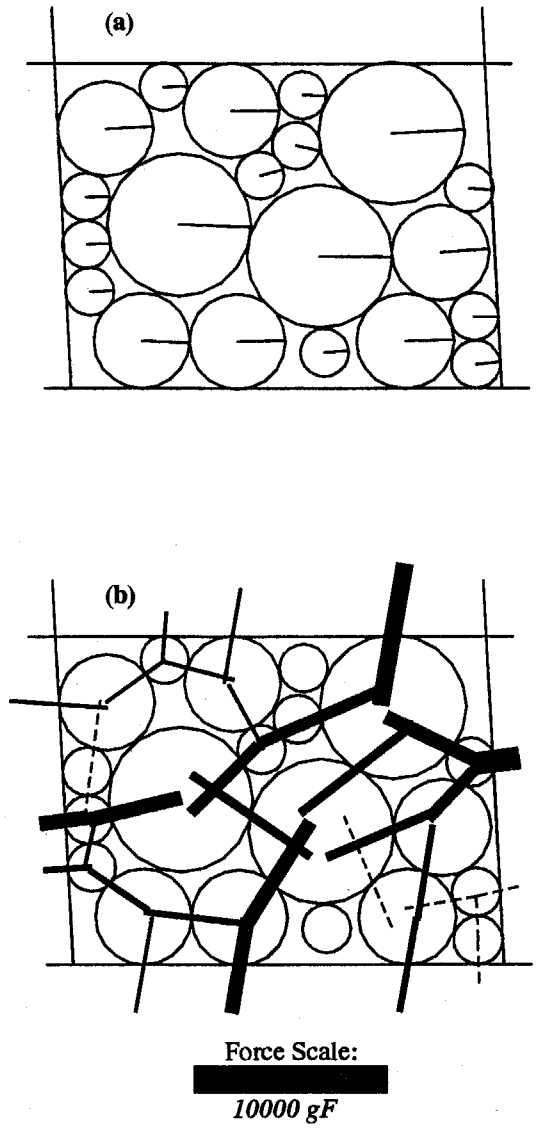

Figure 5.43: Simple shear simulations (saturated, dense), γ=5%–(a) Configuration, (b) Contact force diagram

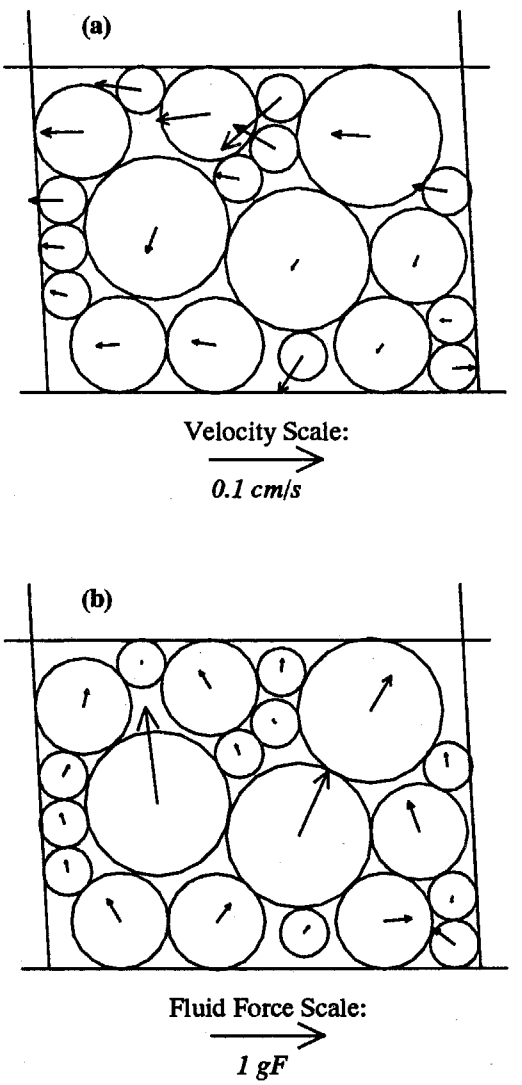

Figure 5.44: Simple shear simulations (saturated, dense), γ=5%–(a) Particles velocity, (b) Fluid force on particles

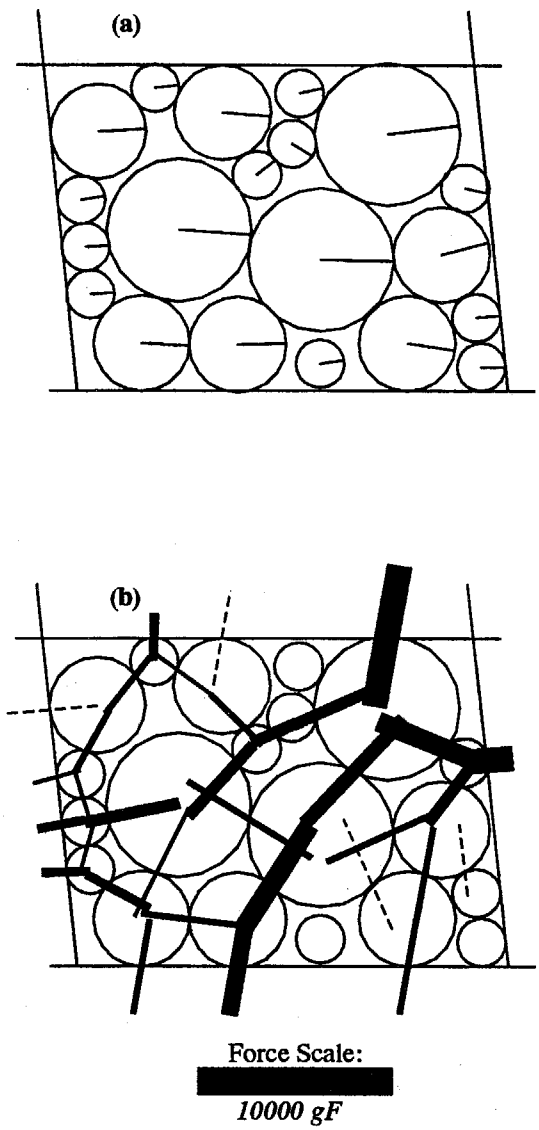

Figure 5.45: Simple shear simulations (saturated, dense), γ=10.5%–(a) Configuration, (b) Contact force diagram

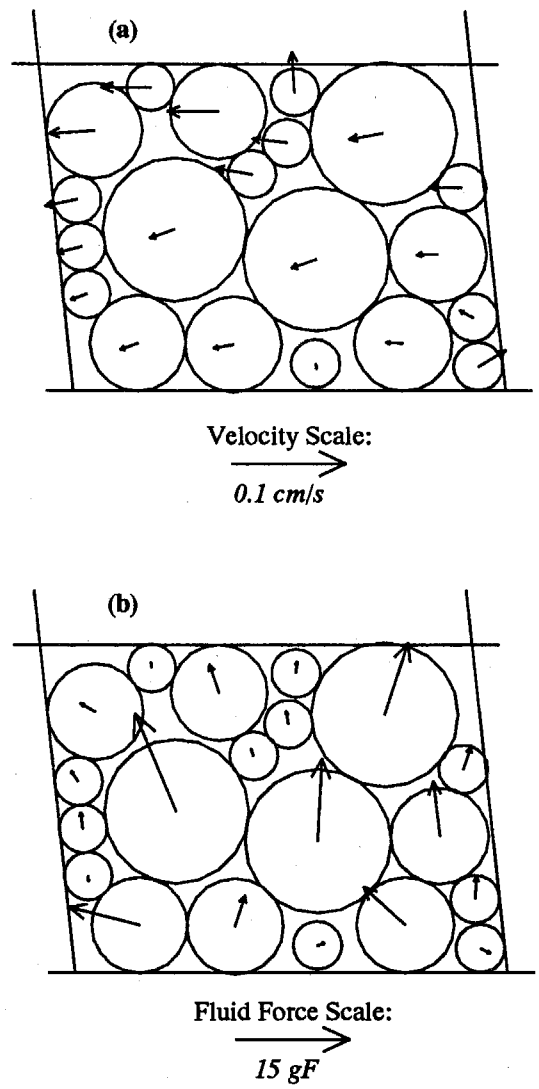

Figure 5.46: Simple shear simulations (saturated, dense), γ=10.5%–(a) Particle velocity, (b) Fluid force on particles

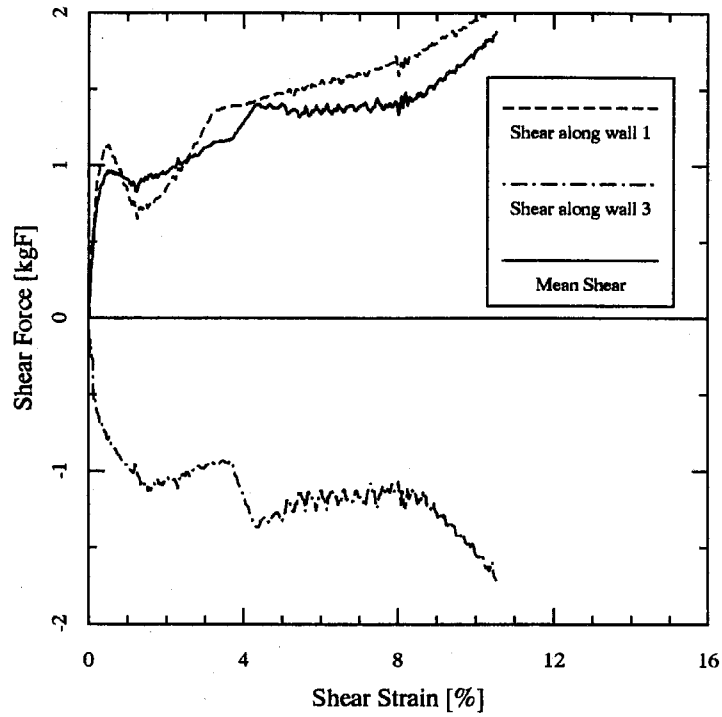

Figure 5.47: Simple shear simulations (saturated, dense), Shear force along walls 1 and 3 and their average values

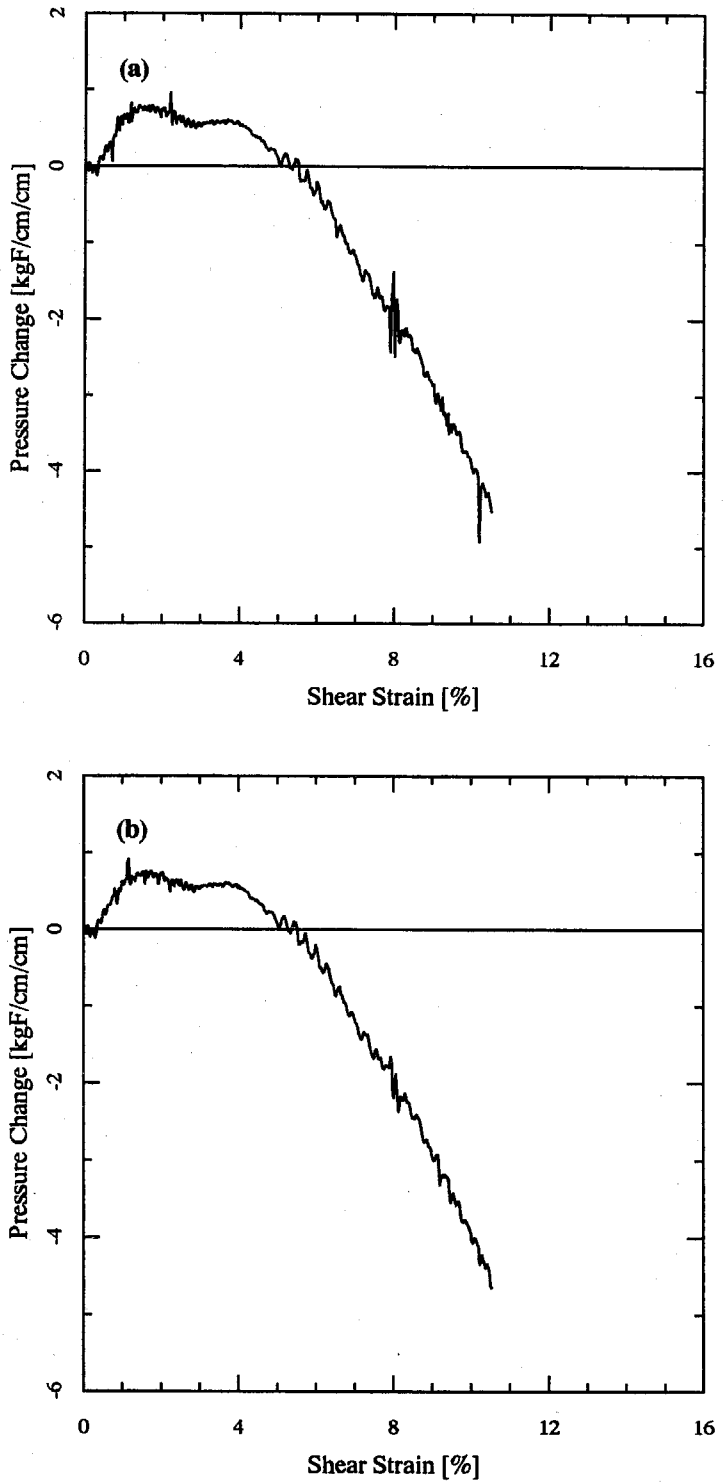

Figure 5.48: Simple shear simulations (saturated, dense), Pore pressure change–(a) along wall 1, (b) along wall 3

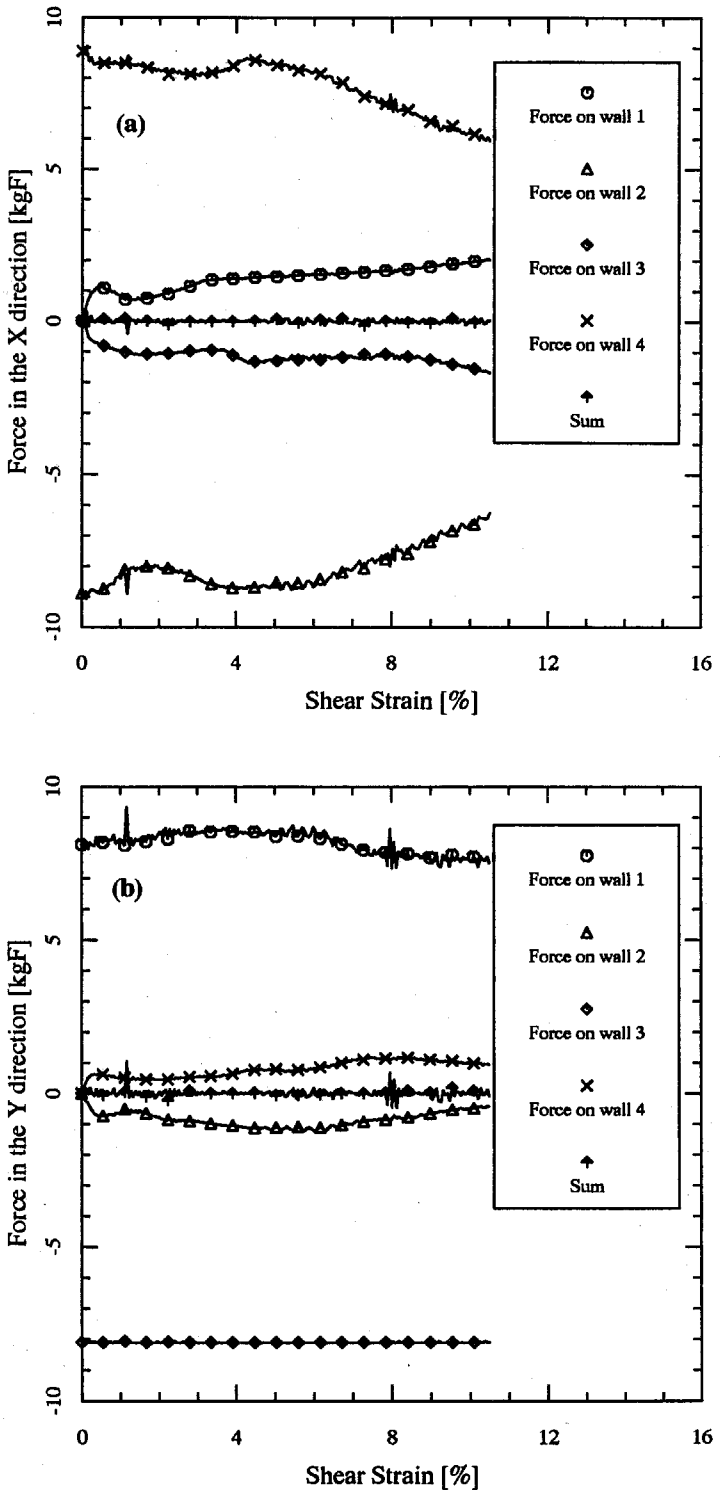

Figure 5.49: Simple shear simulations (saturated, dense), Force components along the four walls and their sum–(a) in the X direction, (b) in the Y direction

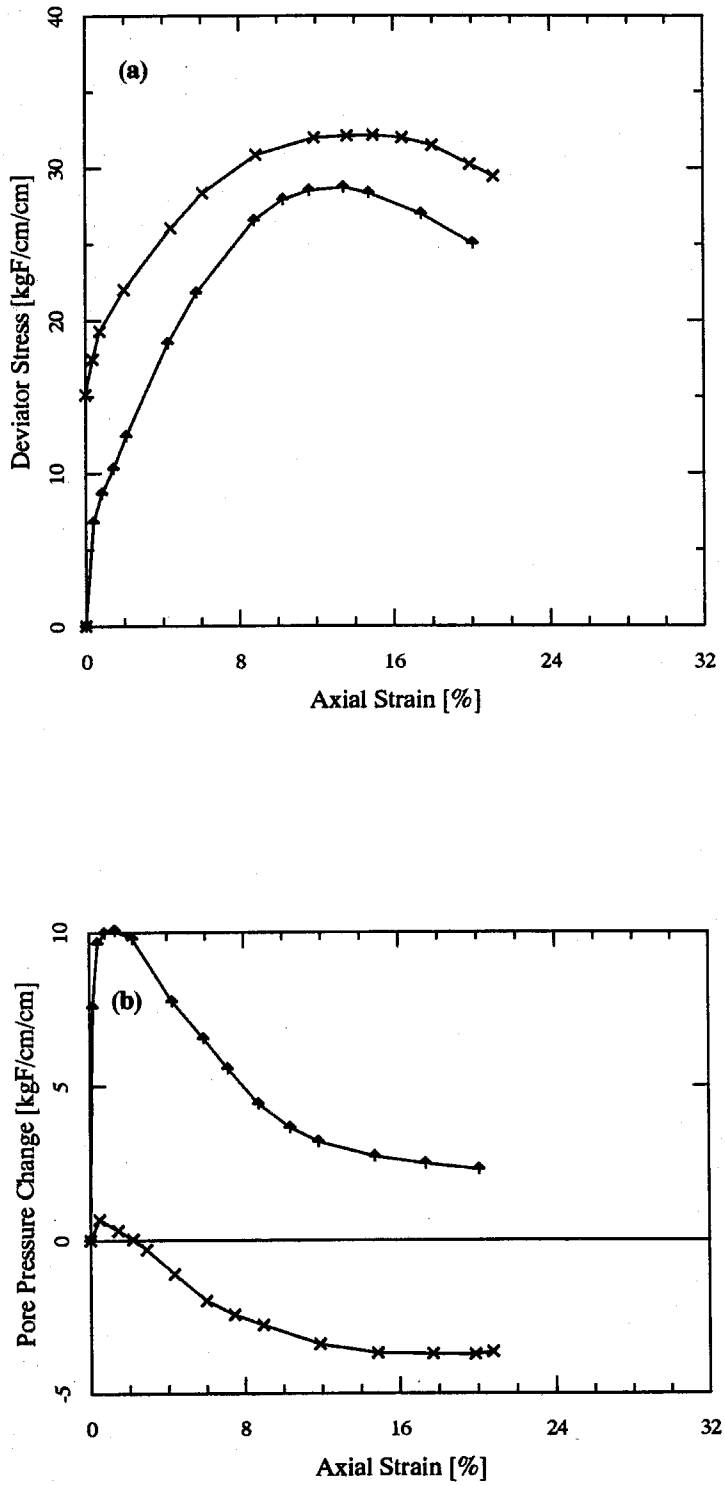

Figure 5.50: Experimental results of undrained triaxial tests using dense Sacramento sand–(a) Stress-strain relationship, (b) Pore pressure change-strain relationship (after Seed, 1967)

Chapter 6

CONCLUSIONS AND SUGGESTIONS

6.1 Conclusions

In this study we have developed a tool to simulate the behavior of a two-dimensional saturated granular medium. The treatment of the solid phase was based on Cundall's distinct element method. With this solid phase, we have incorporated a liquid phase that was modelled by the boundary element method. Because water flow processes in a porous medium occur at a low Reynolds number, the equations of motion of the fluid phase are assumed to be Stokes' equations. Furthermore, quasi-steady flow has also been assumed. This choice was based on the hypothesis that in the low velocity flow that occurs, the inertia and convection terms are negligible.

The analytical formulation of the liquid phase requirements has been described and comparisons have been made with other solutions in order to check the accuracy and validity of the algorithm used. In general these validations showed satisfactory agreement.

Finally, the developed computer code was used to simulate the simple shear of soil-like systems both for dry and saturated systems. In the course of developing the computer code, a mechanism allowing the transfer of load from the skeleton to the liquid phase has also been developed. From the numerical simple shear test results, it was found that:

1. The distinct element model is capable of modelling adequately the overall be-

havior of soil-like systems. In particular, in the dry case, the results obtained indicate that qualitatively, the overall behavior of the systems corresponds to that of a real soil. For example, the dry shearing of a loose soil is accompanied by a decrease in volume while the shearing of a dense system shows an increase in volume due to the dilation of the particles. In both cases, softening of the shear stress versus shear strain behavior was also shown.

For slow monotonic loading, the choice of the solid phase properties is not crucial to the response of the system because static equilibrium is always achieved.

2. The combined solid-fluid interaction treatment was shown to be capable of modelling adequately the overall behavior of saturated sand. We have demonstrated that the simple shearing of a loose saturated system is accompanied with an increase in pore pressure while a dense system indicated first a rise in pore pressure followed by a decrease of the pressure. This behavior has also been observed in actual soil.

3. The Stokes' flow regime used in this model is adequate for the representation of the fluid phase because the velocity of the fluid is relatively small.

4. In addition to the global behavior, a microscopic behavior is also observed that clarifies the behavior of the systems studied. The rotation of the principal stresses during the shearing process was the main characteristic of the response of the system. In the case of a dry system, this rotation is accompanied by constant increase of the interparticle contact force because the volume is allowed to change. When the system is loose, the densification process that occurs during shearing pushes the particle into closer contact, thereby increasing the contact force. In the dense, dry system, the dilation of the grain assemblage also increases the interparticle contact force; however, here the shearing occurs with an

increase in volume.

When a liquid phase is added to the system and shearing is performed at constant volume, in the loose system the forces supported by the skeleton do not change much but rotation of the direction of the load path occurs, coinciding with a decrease in solid support for the applied vertical load. Consequently, this unbalanced vertical load has to be distributed to the liquid phase, thereby increasing the pore pressure.

In the dense, saturated system, because the dilation process is not accompanied by a change of volume, the interparticle contact forces steadily increase accompanied by the same rotation of stresses. The increase of the contact forces in this case allows the skeleton to support the applied load better and leads to a decrease in loading on the liquid phase. Hence, a decrease in pore pressure is observed.

5. The fluid phase play a double role in a saturated granular medium: (1)as a transmitting medium for the pressure disturbance created at the boundary by the force unbalance due to the restructuring of the solid particles (primary effect) and (2) as a viscous medium which resists to the motion of the particles (secondary effect). For slow monotonic loading, only the primary effect contributes to the global behavior of the system.

6. At present, only a limited number of loading conditions can be performed due to the restrictions of the fluid phase model. In particular, the incompressibility of the fluid phase does not allow uniform compression on a saturated system.

6.2 Suggestions for Further Work

The modelling of saturated granular media is still in its infancy; further developments and studies are required. Possible investigations are:

1. Because an artificial gap is allowed between particles for fluid flow, the influence of this gap on the overall behavior is not yet clear and further parametric studies of the gap width are necessary to obtain some insight on the influence of this variable. Furthermore, the important role played by the fluid primary effect may be caused by the large gap width used in the simulations of this study.

2. An alternative numerical solution method for Stokes' equations is necessary because of the lengthy computation time required by the boundary integral element method. Of particular interest is the "*Lattice Cellular Gas Automata*" model [50,51,44,29], which models fluid flow using "fluid" particles with discrete velocities on a regular lattice.

3. Although it was demonstrated that the model is able to represent the liquefaction behavior, because of the limited resources available in this study, we were not able to conduct several cycles of shear loading and unloading such as is observed to produce liquefaction in real soils. Observations of the microscopic behavior resulting from this type of study would give clues as to how liquefaction is initiated.

4. In its actual form, the computer code developed for this study is not adequate for modelling uniform compression of saturated systems because of the incompressibility of the fluid phase. To overcome this restriction, further studies should take into account fluid compressibility. If this were done, general loading conditions could be applied to the system.

5. Probably the next most important step would be the study of a full three-dimensional system. Because of the plane strain assumptions used in two dimensions, several factors have been neglected. In particular, no information on stresses in the out-of-plane direction is available. When shearing occurs in two directions (as opposed to one only in two dimensions), the difference of behavior between the two- and three-dimensional cases will enable us to justify (or otherwise) the use of the two-dimensional model for certain types of problems.

6. Free surface fluid boundary conditions are needed in order to model free surface flow problems such as those found in earth dams and natural soil profiles.

7. An empirical or statistical model can be developed in order to predict the forces on particles generated by the fluid phase (i.e., a drag-like force type). From the numerical results performed here, this force is not proportional to the velocity because of the particle-fluid interactions in a closely-packed array of particles. Using such a model would allow us to describe the fluid phase without the use of any lengthy numerical solution techniques.

8. Finally, the model proposed in this study can also be used for future development of rational constitutive relations.

References

[1] Banerjee, P.K. and Butterfield, R., *Boundary Element Methods in Engineering Science,* McGraw-Hill, London, U.K..

[2] Bardet, J.P. and Scott, R.F., *Seismic Stability of Fractured Rock Mass with the Distinct Element Method,* Proc. 26th US Symposium on Rock Mechanics, E. Ashworth and A.A. Balkema, Ed., 139–149, 1985.

[3] Bathe, K.J., *Finite Element Procedures in Engineering Analysis,* Prentice-Hall, Englewood Cliffs, N.J., 1982.

[4] Bathurst, R.J. and Rothenburg, L., *Micromechanical Aspects of Isotropic Granular Assemblies with Linear Contact Interactions,* J. Appl. Mech., **55**, 17–23, 1988.

[5] Bear, J., *Dynamics of Fluids in Porous Media,* Elsevier, New York, 1972.

[6] Bézine, G. and Bonneau, D., *Integral Equation Method for the Study of Two Dimensional Stokes Flow,* Acta Mechanica, **41**, 197–209, 1981.

[7] Brebbia, C.A. and Dominguez, J., *Boundary Elements, an Introductory Course,* Computational Mechanics Publ. and Mc-Graw-Hill, N.Y., 1989.

[8] Brebbia, C.A. and Walker, S., *Boundary Element Techniques in Engineering,* Newnes-Butterworths, London, U.K..

[9] Brenner, H., *Dispersion Resulting from Flow through Spatially Periodic Porous Media,* Trans. Roy. Soc. (London), **297**, 81–133, 1980.

[10] Bush, M.B. and Tanner, R.I., *Numerical Solution of Viscous Flows using Integral Equation Methods,* Int. J. Num. Meth. Fluids, **3**, 71–92, 1983.

[11] Campbell, C.S., *Shear Flows of Granular Materials,* Ph.D. thesis, California Institute of Technology, 1982.

[12] Campbell, C.S. and Brennen, C.E., *Computer Simulation of Shear Flows of Granular Material,* Mechanics of Granular Materials: New Models and Constitutive Relations, J.T. Jenkins and M. Satake, Ed., Elsevier Science Publ., Amsterdam, 313-326, 1983.

[13] Chow, C.Y., *An Introduction to Computational Fluid Mechanics,* John Wiley & Sons, Inc., New York, N.Y., 1979.

[14] Chwang, A.T. and Wu, T.Y., *Hydrodynamics of Low-Reynolds-number Flow. Part 2. Singularity Method for Stokes Flow,* J. Fluid Mech., **67**, part 4, 787–815, 1975.

[15] Cole, E.R.L., *The Behavior of Soils in the Simple Shear Apparatus,* Ph.D. thesis, University of Cambridge, 1967.

[16] Coleman, B.D. and Mizel, V., *On the General Theory of Fading Memory,* Arch. Ration. Mech. Anal., **29**, 18–31, 1968.

[17] Coleman, B.D. and Noll, W., *Recent Results in Continuum Theory of Viscoelastic Fluids,* Ann. N.Y. Acad. Sci., **89**, 672, 1961.

[18] Collatz, L., *The Numerical Treatment of Differential Equations,* Springer-Verlag, New York, N.Y., 1966.

[19] Contenceau, M. and Bouard, R., *On the Computation of the Plane and Axisymmetric Creeping Flows Around Body in Duct,* European Mechanics Colloquium, **129**. Computation of Flow Around Systems of Airfoils, Bulgaria, 1980.

[20] Cundall, P.A., *A Computer Model for Simulating Progressive, Large-scale Movements in Blocky Rock Systems,* Proc. Symp. Int. Soc. Rock Mech., Nancy, France, **2**(8), 1971.

[21] Cundall, P.A., *A Computer Model for Rock-mass Behavior using Interactive Graphics for the Input and Output of Geometrical Data,* Report MRD-2-74 prepared at the University of Minnesota under Contract number DAWC 45-74-C-006, for the Missouri River Division, US Army Corps of Engineers, available from National Technical Information Service–report number AD/A-001 602, 1974.

[22] Cundall, P.A., *BALL–A Computer Program to Model Granular Media Using the Distinct Element Method,* Technical Note, Advanced Technology Group, Dames & Moore, London, 1978.

[23] Cundall, P.A. and Strack, O.D.L., *A Discrete Numerical Model for Granular Assemblies,* Géotechnique **29** (1), 47–65, 1979.

[24] Cundall, P.A. and Strack, O.D.L., *The Distinct Element Method as a Tool for Research,* Report to the NSF concerning Grant ENG76-20711, Dept. Civil and Mineral Engineering, University of Minnesota, Minneapolis, Minn., 1979.

[25] Cundall, P.A., Drescher, A. and Strack, O.D.L., *The Development of Constitutive Laws for Soil Using the Distinct Element Method,* Numerical Models in Geomechanics, Aachen, W. Wittke, Ed., 289–298, 1979.

[26] Cundall, P.A., Drescher, A. and Strack, O.D.L., *Numerical Experiments on Granular Assemblies: Measurements and Observations,* IUTAM Conf. on Deformation and Failure of Granular Materials, Delft, 355–370, 1982.

[27] Cundall, P.A. and Strack, O.D.L., *Modelling of Microscopic Mechanisms in Granular Material,* Mechanics of Granular Materials: New Models and Constitutive

Relations, J.T. Jenkins and M. Satake, Ed., Elsevier Science Publ., Amsterdam, 137–149, 1983.

[28] Cunningham, E., *On the Velocity of Steady Fall of Spherical Particles through a Fluid Medium,* Proc. Roy. Soc. (London), **A83**, 357–365, 1910.

[29] d'Humières, D., Lallemand, P. and Frisch, V., *Lattice Gas Models for 3D Hydrodynamics;* Europhys. Lett., **2**, 291–297, 1986.

[30] Dantu, P., *Contribution à l'Etude des Mécanique et Géométrique des Milieux Pulvérulents,* Proc. 4th Int. Conf. Soil Mech. Fdn. Eng., London, **1**, 144–148, 1957.

[31] Darcy, H.P.G., *Les Fontaines Publiques de la Ville de Dijon,* Victor Dalmont Publ., Paris, France, 1856.

[32] Davis, R.A. and Deresiewicz, H., *A Discrete Probabilistic Model for Mechanical Response of a Granular Medium,* Acta Mechanica, **27**, 69–89, 1977.

[33] De Josselin de Jong, G. and Verruijt, A., *Etude Photo-élastique d'un Empilement de Disques,* Cah. Grpe Fr. Etud. Rhéol., **2**, 73–86, 1969.

[34] De Josselin de Jong, G., *The Double Sliding, Free Rotating Model for Granular Assemblies,* Géotechnique, **21**, 155–163, 1971.

[35] Deresiewicz, H., *Mechanics of Granular Media,* Adv. Appl. Mech. 5, 233–306, 1953.

[36] Desai, C.S. and Siriwardane, M.J., *Constitutive Laws for Engineering Materials with Emphasis on Geologic Materials,* Prentice-Hall, Englewood Cliffs, N.J., 1984.

[37] Drescher, A. and De Josselin de Jong, G., *Photoelastic Verification of a Mechanical Model for the Flow of a Granular Material,* J. Mech. Phys. Solids, **20**, 337–351, 1972.

[38] Dupuit, A.J., *Traité Théorique et Pratique de la Conduite et de la Distribution des Eaux,* Paris, France, 1865.

[39] Durlofsky, L., Brady, J.F. and Bossis, G., *Dynamic Simulation of Hydrodynamically Interaction Particles,* J. Fluid Mech., **180**, 21–49, 1987.

[40] Einstein, A., *Eine neue Bestimmung der Molekül-dimensionen,* Ann. Physik, **19**, 289–306, 1906.

[41] Eringen, A.C., *Mechanics of Continua,* John Wiley & Sons, Inc., New York, 1967.

[42] Eringen, A.C., *Continuum Physics,* **2**, Academic Press, Inc., New York, 1975.

[43] Finn, W.D.L., Pickering, D.J. and Bransby, P.L., *Sand Liquefaction in Triaxial and Simple Shear Apparatus,* J. Soil Mech. and Found. Div., ASCE, **97** (SM4), 639–659, 1971.

[44] Frisch, V., Hasslacher, B. and Pomeau Y., *Lattice Gas Automata for the Navier-Stokes Equation,* Phys. Rev. Lett., **56**, 1505–1508, 1986.

[45] Gray, W.G. and O'Neil, K., *On the General Equations for Flow in Porous Media and their Reduction to Darcy's law* , Water Resour. Res., **12**, 148–154, 1976.

[46] Guiggiani, M. and Casalini, P., *On the Numerical Implementation of BEM for Axisymmetric Elasticity,* Boundary Elements VIII, M. Tanaka and C.A. Brebbia Ed., Springer-Verlag, Berlin and N.Y., 695–706, 1986.

[47] Hancock, G.J., *The Self-propulsion of Microscopic Organisms through Liquid,* Proc. Roy. Soc., A **217**, 96–121, 1953.

[48] Happel, J. and Brenner, H., *Low Reynolds Number Hydrodynamics,* Martinus Nijhoff Publ., 2nd Edition, 4th printing, 1986.

[49] Hardin, B.O. and Dronevich, V.P., *Shear Modulus and Damping in Soil: Measurement and Parameter Effects,* J. Soil Mech. Found., ASCE, **98** (SM6), 1972.

[50] Hardy, J., Pomeau, Y. and de Pazzis, O., *Time Evolution of a Two-dimensional Model System, I: Invariant States and Time Correlation Functions,* J. Math. Phys., **14**, 1746–1759, 1973.

[51] Hardy, J., de Pazzis, O. and Pomeau, Y., *Molecular Dynamics of a Classical Lattice Gas: Transport Properties and Time Correlation Functions,* Phys. Rev., **A13**, 1949–1961, 1976.

[52] Harrison, W.J., *On the motion of Spheres, Circular and Elliptic Cylinders Through Viscous Liquid,* Trans. Cambridge Phil. Soc., **23**, 71–88, 1924.

[53] Hartmann, F., *Computing C–matrix in Non-Smooth Boundary Points,* New Developments in Boundary Element Methods, C.A. Brebbia Ed., Butterworth, London, 367–379, 1980.

[54] Ishibashi, I. and Sherif, M.A., *Soil Liquefaction by Torsional Simple Shear Device,* J. Geotch. Engr. Div., ASCE, **100** (GT8), 871–888, 1974.

[55] Jaunzemis, W., *Continuum Mechanics,* Macmillan Publishing Co., Inc., New York, 1967.

[56] Kitagawa, K., Brebbia, C.A., Wrobel, L.C. and Tanaka, M., *Boundary Element Analysis of Viscous Flow by Penalty Function Formulation,* Engineering Analysis, **3** (4), 194–200, 1986.

[57] Lee, K.L., and Seed, H.B., *Undrained Strength of Anisotropically Consolidated Sand,* J. Soil Mech. and Found. Div., ASCE, **96** (SM2), 411-428, 1970.

[58] Lorentz, H.A., Zittingsverl. Akad. von Wet., **5**, 168, 1896; neu. bearb: Abhandl. Theoret. Phys., **1**, 23, 1907.

[59] Malvern, L.E., *Introduction to the Mechanics of a Continuous Medium,* Prentice-Hall, Inc., Englewood Cliffs, N.J., 1969.

[60] Marsal, R.J., *Suelos Granulares: Modelo Estadistico Teoria de Falla y Relaciones Esfuerzo-Deformacion,* Universidad Nacional Autonoma de Mexico 290, 1971.

[61] Martin, G.R., Finn, W.D.L. and Seed, H.B., *Fundamentals of Liquefaction Under Cyclic Loading,* J. Geotech. Engr. Div., ASCE, **104** (GT5), 423–438, 1975.

[62] Mindlin, R.D. and Deresiewicz, H., *Elastic Spheres in Contact under Varying Oblique Forces,* J. Appl. Mech., **20**, 327–344, 1953.

[63] Navier, L.M.H., *Mémoire sur les Lois du Mouvement des Fluides,* Mem. Acad. Sci., Paris, **6**, 389–440, 1823.

[64] Nayak, P.R., *Surface Roughness Effects in Rolling Contact,* Trans. Am. Soc. Mech. Eng., Series E, J. Appl. Mech., **39**, 456–440, 1972.

[65] Noll, W., *A Mathematical Theory of the Mechanical Behavior of Continuous Media,* Arch. Ration. Mech. Anal., **2**, 197–226, 1958.

[66] Oda, M., *A Mechanical and Statistical Model of Granular Material,* Soils and Foundations, **14** (1), 13–27, 1974.

[67] Oda, M. and Konishi, J., *Microscopic Deformation Mechanism of Granular Material in Simple Shear,* Soils and Foundations, **14** (4), 25–38, 1974.

[68] Ohmachi, T. and Arai, Y., *The Distinct Element Modelling for Earthquake Response Analysis,* 2nd International Symposium on Numerical Models in Geomechanics, Ghent, 1986.

[69] Oseen, C.W., *Hydrodynamik,* Akademische Verlag, Leipzig, 1927.

[70] Peacock, W.H. and Seed, H.B., *Sand Liquefaction Under Cyclic Loading Simple Shear Conditions,* J. Soil Mech. and Found. Div., ASCE, **94** (SM3), 689–708, 1968.

[71] Roache, P.J., *Computational Fluid Dynamics,* Hermosan Publ., Albuquerque, N.M., 1972.

[72] Rodriguez-Ortiz, J.M., *Estudio del Comportamiento de Medios Granulares Heterogéneos Mediante Modelos Discontinuos Analógicos y Matemáticos,* Ph.D. thesis, Universidad Politécnica de Madrid, 1974.

[73] Rodriguez-Ortiz, J.M., *Discussion by J.M. Rodriguez-Ortiz over Load Distribution in Granular Media,* J. Engr. Mech. Div., ASCE, **103** (EM6), 1189–1191, 1977.

[74] Rowe, P.W., *Stress-Dilatancy, Earth Pressures, and Slopes,* J. Soil Mech. and Found. Div., ASCE, **89** (SM3), 37–61, 1963.

[75] Sandhu, R.S. and Hong, S.J., *Dynamics of Fluid-saturated Soils–Variational Formulation,* Int. J. Num. Anal. Meth. Geomechanics, **11** (SM3), 241–255, 1987.

[76] Scott, R.F., *Principles of Soil Mechanics,* Addison Wesley Publishing Co., Inc., Reading, MA, 1963.

[77] Seed, H.B. and Lee, K.L., *Undrained Strength Characteristics of Cohesionless Soils,* J. Soil Mech. and Found. Div., ASCE, **93** (SM6), 333–360, 1967.

[78] Serrano, A.A. and Rodriguez-Ortiz, J.M., *A Contribution to the Mechanics of Heterogeneous Granular Media,* Proc. Symp. on the Role of Plasticity in Soil Mech., Cambridge, England, 215–227, 1973.

[79] Slichter, C.S., *Theoretical Investigations of the Motion of Ground Waters,* U.S. Geological Surveys, 19th Ann. Rep., Part 2, 301–384, 1899.

[80] Smoluchowski, M., Bull. Intern. Acad. Polonaise Sci. Lettres, **1A**, 28, 1911.

[81] Smoluchowski, M., 5th Intern. Congr. Math., **2**, 192, 1912.

[82] Stokes, G.G., *On the Theories of the Internal Friction of Fluids in Motion, and of the Equilibrium and Motion of Elastic Solids,* Trans. Cambr. Phil. Soc., **8**, Part II, 287–305, 1845.

[83] Stokes, G.G., *On the Effect of the Internal Friction of Fluids on the Motion of Pendulums,* Trans. Cambr. Phil. Soc., **9**, Part II, 8–106, 1856.

[84] Stroud, A.H. and Secrest, D., *Gaussian Quadrature Formulas,* Prentice-Hall, N.Y., 1966.

[85] Takaisi, Y., *The Drag on a Circular Cylinder Placed in a Stream of Viscous Liquid Midway Between Two Parallel Planes,* J. Phys. Soc. Japan, **11**, 1092–1095, 1956.

[86] Taylor, C. and Hood, P., *A Numerical Solution of the Navier-Stokes Equations using the Finite Element Technique,* Computers & Fluids, **1**, 73–100, 1973.

[87] Terzaghi, K. and Peck, R.B., *Soil Mechanics and Engineering Practice,* J. Wiley and sons, N.Y., 1948.

[88] Ting, J.M., Corkum, B.T. and Greco, C., *The Application of the Distinct Element Method in Geotechnical Engineering,* 2nd International Symposium on Numerical Models in Geomechanics, Ghent, Belgium, 789–798, 1986.

[89] Ting, J.M., Corkum, B.T., Kauffman, C.R. and Greco, C., *Discrete Numerical Model for Soil Mechanics,* J. Geotech. Engr., ASCE, **115** (3), 379–398, 1989.

[90] Tong, P. and Fung, Y.C., *Slow Particulate Viscous Flow in Channels and Tubes–Application to Biomechanics,* J. Appl. Mech., **38**, 721–728, 1971.

[91] Tosaka, N. and Onishi, K., *Boundary Integral Equation Formulations for Steady Navier-Stokes Equations using the Stokes Fundamental Solutions,* Engineering Analysis, **2** (3), 128–132, 1985.

[92] Truesdell, C. and Noll, W., *The Nonlinear Field Theories of Mechanics,* Encyclopedia of Physics, S. Flugge, Ed., **3** (3), Springer-Verlag, Berlin, 1965.

[93] Truesdell, C., *Continuum Mechanics–The Mechanical Foundations of Elasticity and Fluid Dynamics,* Vol.1, Gordon and Breach, Science Publishers, Inc., New York, 1966.

[94] Wakabayashi, T., *Photoelastic Method for Determination of Stress in Powdered Mass,* Proc. 7th Jap. Nat. Congr. Appl. Mech., 153–192, 1957.

[95] Werner, B.T., *A Physical Model of Wind-blown Sand Transport,* Ph.D. thesis, California Institute of Technology, 1987.

[96] Werner, B.T. and Haff, P.K., *The Impact Process in Eolian Saltation: Two Dimensional Simulations,* Sedimentology, **35**, 189–196, 1988.

[97] Whitaker, S., *Flow in Porous Media, I: A Theoretical Derivation of Darcy's Law,* Transport in Porous Media, **1**, 3–25, 1986.

[98] Zhang, Y. and Cundall, P.A., *Numerical Simulation of Slow Deformations,* Proc. Symp. on the Mechanics of Particulate Media, 10th National Congress on Applied Mechanics, Austin, Tex., 1986.

[99] Zienkiewicz, O.C. and Shiomi, T., *Dynamic Behaviour of Saturated Porous Media; The Generalized Biot Formulation and Its Numerical Solution,* Int. J. Num. Anal. Meth. Geomechanics, **8**, 71–96, 1986.